

## University of Southampton Research Repository

Copyright © and Moral Rights for this thesis and, where applicable, any accompanying data are retained by the author and/or other copyright owners. A copy can be downloaded for personal non-commercial research or study, without prior permission or charge. This thesis and the accompanying data cannot be reproduced or quoted extensively from without first obtaining permission in writing from the copyright holder/s. The content of the thesis and accompanying research data (where applicable) must not be changed in any way or sold commercially in any format or medium without the formal permission of the copyright holder/s.

When referring to this thesis and any accompanying data, full bibliographic details must be given, e.g.

Thesis: Author (Year of Submission) "Full thesis title", University of Southampton, name of the University Faculty or School or Department, PhD Thesis, pagination.

Data: Author (Year) Title. URI [dataset]





# UNIVERSITY OF SOUTHAMPTON

FACULTY OF PHYSICAL AND APPLIED SCIENCES

SCHOOL OF ELECTRONICS AND COMPUTER SCIENCE

**Dielectric Properties of  
Epoxy Based Nanocomposites Filled with Nano SiO<sub>2</sub> and BN  
and Moisture Effects**

by

**Dayuan Qiang**

Thesis for the degree of Doctor of Philosophy

Supervisors: Prof. George Chen, Dr. Thomas Andritsch

December 2017





UNIVERSITY OF SOUTHAMPTON

## **ABSTRACT**

FACULTY OF PHYSICAL AND APPLIED SCIENCES

SCHOOL OF ELECTRONICS AND COMPUTER SCIENCE

Thesis for the degree of Doctor of Philosophy

### **DIELECTRIC PROPERTIES OF EPOXY BASED NANOCOMPOSITES FILLED WITH NANO SiO<sub>2</sub> AND BN AND MOISTURE EFFECTS**

By Dayuan Qiang

Epoxy resin is one of the most commonly used thermosetting macromolecular synthetic materials, and is currently used in many areas such as casting in transformers and motors. To meet the broader usage demand for epoxy resins, many modification methods have been applied, including being filled with various nanoparticles. This has received increasing attention over recent years, because of the ability to obtain enhanced properties in the resultant nanocomposites. The investigation of this study used a range of techniques to analyse chemically and electrically the properties of epoxy resin and its nanocomposites. The first aim of the study is to develop a method of describing the morphology of nanofillers in the nanocomposites more precisely. Moreover, it will be investigated how the presence of these fillers influences the physical and chemical properties of epoxy resins by employing a number of techniques. Second, an investigation will be conducted into the consequences of the addition of nanofillers and resultant interfacial regions on the dielectric and electrical properties of epoxy nanocomposites. Third, an in-depth study into the influences of water absorption on the dielectric/electrical properties of epoxy and its nanocomposites is considered a worthwhile subject to investigate. Consequently, a number of conclusions have been made, some of which are listed below.

According to the proposed quantification method, epoxy nanocomposites with surface-treated particles achieved superior overall dispersion and distribution of particles/aggregates than those with untreated particles. Moreover, poor mixing

resulted in an adverse impact on the morphology of the epoxy matrix by creating some physical defects (such as cracks and cavities). In hBN-based samples, particles were more likely to exist solely, which resulted in many more impacts on the base material. The presence of nano-SiO<sub>2</sub> and hBN particles both resulted in a decrease in cross-linking density during the curing of epoxy resins, and further resulted in poorer thermal stability than with pure samples. Surface treatment modified the cross-linking density in the interfacial areas of SiO<sub>2</sub>-based samples by removing some surface groups, and the morphology of hBN-based nanocomposites had a significant impact on their thermal properties.

The addition of nanoparticles physically and chemically affected the base material and influenced the dielectric responses; thus, it is a solution for modifying the dielectric properties. The presence of nanoparticles resulted in morphology changes (mostly in the form of physical defects), while the surface treatment introduced deeper traps at the interface, and there were more shallow traps presented in the bulk of materials. Therefore, this hindered the charge injection and reduced the mobility of charge carriers, which consequently reduced the DC conductivity. However, with increased filler loadings, there was a greater effect on polymer structures and thus a higher density of traps. Thus, charge carriers are more easily transported by hopping or via the quantum tunnelling mechanism. This supported the concept of reduction in DC breakdown strength with the growth of filler loadings. In addition, the presence of plate-like nano-hBN created complex microstructures in epoxy resins and acted as barriers for charge injection and movement, which resulted in increased DC breakdown strength as filler loadings increased.

Studies on moisture effects have experimentally demonstrated the existence of a two-layer water shell structure, by proposing a method of estimating the average thickness of the water shell. According to the analysis of moisture uptake, surface treatment can reduce water absorption; however, there was no clear impact of modifying effects on the dielectric. The “hydrophobic” performance of BN nanocomposites is superior to silica samples, especially because of the lack of formation of water shells around the particles. According to the quantitative results from SEM and dielectric spectroscopy, the presence of water caused an increase in charge injection, higher mobility of charge carriers (both in base materials and within traps/particles,) and a clear reduction in DC breakdown results. Moreover, water shells around spherical particles contributed to higher probability of the quantum tunnelling process and the formation of conductive percolation channels.

# Table of Contents

<b>Table of Contents.....</b>	<b>i</b>
<b>Table of Tables.....</b>	<b>v</b>
<b>Table of Figures.....</b>	<b>vii</b>
<b>Thesis: Declaration Of Authorship.....</b>	<b>xix</b>
<b>Acknowledgements.....</b>	<b>xxi</b>
<b>List of Publications.....</b>	<b>xxiii</b>
<b>Abbreviations.....</b>	<b>xxv</b>
<b>Chapter 1 Introduction.....</b>	<b>1</b>
1.1 Background.....	1
1.2 Motivation and Objectives.....	1
1.3 Contributions of the Thesis .....	1
1.4 Outline of the Thesis .....	4
<b>Chapter 2 Literature Review.....</b>	<b>5</b>
2.1 Epoxy Resin.....	5
2.1.1 Definitions and Classification of Epoxy Resin.....	5
2.1.2 Curing of Epoxy Resin .....	8
2.2 Epoxy Nanocomposites.....	12
2.2.1 The Concept of Nanocomposites .....	12
2.2.2 Epoxy Nanocomposites .....	13
2.3 Particle Dispersion and Distribution of Epoxy Nanocomposites.....	15
2.4 Models for Polymer Nanocomposites .....	19
2.4.1 Dual Layer Model .....	19
2.4.2 Multi-core Model.....	20
2.4.3 Interphase Volume Model.....	21
2.4.4 Polymer Chain Alignment Model (PCAM) .....	22
2.4.5 Water Shell Model .....	23
2.5 Interfacial Characteristic .....	25
2.5.1 Inter-particle Distance and Surface Area .....	25
2.5.2 The Volume and Overlapping of Interface Region .....	27

<b>Chapter 3 Sample Preparation and Experimental Methods .....</b>	<b>31</b>
3.1 Materials.....	31
3.2 Preparation of Epoxy Nanocomposites.....	33
3.2.1 Dispersion of Nanoparticles .....	33
3.2.2 The Casting of Epoxy Films .....	35
3.2.3 Sample Composition .....	36
3.3 Sample Analysis Methods .....	37
3.3.1 Scanning Electron Microscopy (SEM).....	37
3.3.2 Thermogravimetric Analysis (TGA) .....	38
3.3.3 Differential Scanning Calorimetry (DSC) .....	39
3.3.4 Differential Scanning Calorimetry Technique.....	41
3.3.5 Experiment Set-up of AC/DC Breakdown Test .....	43
3.3.6 Dielectric Spectroscopy Measurement .....	45
3.3.7 DC Conductivity Measurement.....	46
3.3.8 Space Charge Measurement.....	46
3.4 Humidity.....	48
3.4.1 Humidity Control.....	49
3.4.2 Water Diffusion in Samples .....	50
3.4.3 Water Uptake in Samples .....	52
<b>Chapter 4 Morphology Characterisation of Epoxy Nanocomposites ....</b>	<b>57</b>
4.1 Quantification Methods .....	57
4.1.1 Equivalent Diameter .....	57
4.1.2 Nearest Neighbor Distance (NND) Method .....	59
4.1.3 Quadrat-based Method .....	59
4.2 SEM Images .....	59
4.2.1 Original Images .....	59
4.2.2 Image Processing .....	67
4.3 Data Analysis .....	71
4.4 Particle/Aggregate Dispersion and Distribution Modelling .....	73
4.5 Chapter Summary .....	79

<b>Chapter 5 Thermal Properties of Epoxy Nanocomposites.....</b>	<b>81</b>
5.1 Thermogravimetric Analysis of Epoxy Nanocomposites .....	81
5.1.1 TGA on Surface Treatment .....	81
5.1.2 TGA on Filler Loading Concentration .....	82
5.1.3 TGA on Epoxy Nanocomposites .....	83
5.2 Differential Scanning Calorimetry of Epoxy Nanocomposites .....	89
5.2.1 Free Volume Theory on Glass Transition.....	89
5.2.2 DSC Measurement Results.....	90
5.3 Chapter Summary.....	100
<b>Chapter 6 AC &amp; DC Breakdown Strength of Epoxy Nanocomposites</b>	<b>101</b>
6.1 Breakdown Theories and Weibull Distribution.....	101
6.1.1 Breakdown Theories.....	101
6.1.2 Weibull Distribution .....	103
6.2 AC Breakdown Experiments .....	105
6.2.1 Results by Weibull 7++ .....	105
6.2.2 Effect of Filler Loading Concentration and Filler Type on AC Breakdown Strength .....	110
6.3 DC Breakdown Experiments .....	115
6.3.1 Results by Weibull 7++ .....	115
6.3.2 Effect of Filler Loading Concentration and Filler Type on DC Breakdown Strength .....	119
6.3.3 Effect of Moisture on DC Breakdown Strength.....	122
6.4 Chapter Summary.....	127
<b>Chapter 7 Dielectric Spectroscopy of Epoxy Nanocomposites .....</b>	<b>129</b>
7.1 Dielectric Spectroscopy Technique .....	129
7.1.1 Dielectric Spectroscopy .....	129
7.1.2 Dielectric Response.....	130
7.2 Dielectric Spectroscopy Measurement Results .....	135

## Table of Contents

7.2.1	Dielectric Response of Pure Epoxy Resin and Temperature Effect.....	135
7.2.2	Dielectric Response of Epoxy Nanocomposites and Temperature Effect .....	140
7.2.3	Effect of Moisture on Dielectric Response of Epoxy Nanocomposites .....	145
7.3	Chapter Summary .....	152
<b>Chapter 8 DC Conductivity and Space Charge Behaviour of Epoxy Nanocomposites .....</b>		<b>153</b>
8.1	DC Conductivity of Epoxy Nanocomposites.....	153
8.1.1	DC Conductivity .....	153
8.1.2	DC Conductivity Measurement Results and Analysis .....	156
8.1.3	Effects of Moisture on DC Conductivity Measurement and Analysis .....	159
8.2	Space Charge Behaviour of Epoxy Nanocomposites.....	165
8.2.1	Space Charge and Measurement Method.....	165
8.2.2	PEA Measurement Results and Analysis-Dry .....	167
8.2.3	Effects of Moisture on PEA Measurement and Analysis .....	181
8.3	Chapter Summary .....	191
<b>Chapter 9 Conclusions and Future Work.....</b>		<b>193</b>
9.1	Conclusions .....	193
9.2	Future Work .....	196
<b>Appendix A SEM Image Processing and Histograms of Main Data...</b>		<b>199</b>
<b>Appendix B Particle/Aggregate Dispersion and Distribution Matlab Code .....</b>		<b>215</b>
<b>Appendix C DC Breakdown Strength of Epoxy and its Nanocomposites with Moisture .....</b>		<b>221</b>
<b>Appendix D Space Charge Decay in Epoxy and its Nanocomposites</b>		<b>225</b>
<b>Bibliography.....</b>		<b>231</b>

# Table of Tables

Table 2-1 Bonding distance and energy of common bonds in the polymer [51]..	16
Table 3-1 Product data of D.E.R. 332 .....	32
Table 3-2 Product data of JEFFAMINE D-230.....	32
Table 3-3 Product data of nanoparticles .....	32
Table 3-4 The coding of samples.....	37
Table 4-1 Quantitative data of SEM images, EPS and EPST samples in 1, 3, 5 wt% .....	72
Table 4-2 Weighted surface distance of EPS and EPST samples in 1, 3 and 5 wt% .....	73
Table 4-3 Simulated Quantification data of SEM images, EPS and EPST samples in 1, 3, 5 wt% by PDF and Histogram method .....	78
Table 5-1 Sample code and filler loading concentrations .....	83
Table 5-2 $T_{IDT}$ and $T_{max}$ of epoxy and its nanocomposites .....	87
Table 5-3 Onset, end and glass transition temperature of pure epoxy resins.	92
Table 5-4 Average glass transition temperature of BN epoxy nanocomposites in each loading concentration.....	94
Table 5-5 Glass transition temperature of EPS in each filler loading concentration. ....	95
Table 5-6 Glass transition temperature of EPST in each filler loading concentration. ....	97
Table 6-1 Weibull parameters of epoxy and its nanocomposites, AC BD tests	107
Table 6-2 Particle information .....	114
Table 6-3 Weibull parameters of epoxy and its nanocomposites, DC BD tests, dry .....	117

## Table of Tables

Table 6-4 Weibull parameters of epoxy and its nanocomposites, DC BD, 60RH and saturated .....	123
Table 6-5 Reduction percentage of DC breakdown strength .....	124
Table 7-1 Charge transport activation energy. ....	144
Table 7-2 Average thickness of water shell under different RH environment. ....	150
Table 8-1 Weighted surface distance of EPS and EPST samples in 1, 3 wt% in each RH condition. ....	162
Table 8-2 Percentage of weighted surface distance <10 nm of EPS and EPST samples in 1, 3 wt% in each RH condition. ....	162
Table 8-3 Space charge decay rate ( $C \cdot s^{-1}$ ) of epoxy and its nanocomposites, dry. ....	181
Table 8-4 Space charge decay rate ( $C \cdot s^{-1}$ ) of epoxy and its nanocomposites with moisture. ....	190



# Table of Figures

Figure 2-1 Diagram of the epoxy group. ....	5
Figure 2-2 Polycondensation reactions between epichlorohydrin and bisphenol-A. .....	7
Figure 2-3 Molecular structure of bisphenol-A type epoxy resin. ....	7
Figure 2-4 Three-dimensional net structure of epoxy resins [23]. ....	8
Figure 2-5 Chemical network building during curing process [25]. ....	8
Figure 2-6 Stages of curing process. ....	9
Figure 2-7 Impedance-time characteristic of epoxy resin curing with important curing process stages [26]. ....	11
Figure 2-8 Impedance and sensor and chamber temperature under dynamic temperatures [29]. ....	12
Figure 2-9 Relationship between surface atom number and size of particles [36]. .....	13
Figure 2-10 Hydroxyl group on the surfaces of SiO <sub>2</sub> and BN nanoparticles. ....	17
Figure 2-11 Electrical double layer between nanoparticles. ....	18
Figure 2-12 Schematic of the Dual Layer Model. ....	19
Figure 2-13 Schematic of multi-core model [56]. ....	20
Figure 2-14 Illustrations of the interphase region surrounding the filler particles in a composite system [59]. ....	21
Figure 2-15 Particle surface with and without surface modification in PCAM [68]. .....	23
Figure 2-16 Schematic of the Water Shell Model. ....	24
Figure 2-17 (a) Water shells in numerical modelling results [19]; (b) charge carrier transport through overlapped areas of water shells [70]. ....	24
Figure 2-18 Illustration of the inter-particle and particle surface distance. ....	25

## Table of Figures

Figure 2-19 Illustration of how RPS changes from particle to surrounding polymer [68]. .....	28
Figure 2-20 Probability of the interface region overlapping [74]. .....	29
Figure 3-1 (a) (b): Illustration of chemical structure of D.E.R. 332 and JEFFAMINE D-230; (c) photo of experimental materials .....	31
Figure 3-2 SiO <sub>2</sub> particles surface without (left) and with (right) modification. ...	33
Figure 3-3 Sample preparation facilities: (a) scale; (b) vacuum oven; (c) electric magnetic stirrer; (d) fan oven; (e) probe sonicator. ....	34
Figure 3-4 (a) Closed mould (Photograph); (b) Mould diagram showing gasket... ..	35
Figure 3-5 Revised mould for sample preparation. ....	36
Figure 3-6 EVO 50 scanning electron microscopy. ....	38
Figure 3-7 Perkin-Elmer TGA 7 thermogravimetric analyser. ....	39
Figure 3-8 Illustration of Glass Transition Temperature.....	40
Figure 3-9 Schematic diagram of DSC [4]. ....	41
Figure 3-10 Differential scanning calorimetry device. ....	42
Figure 3-11 Schematic of AC breakdown device [89]. ....	43
Figure 3-12 AC dielectric breakdown kit. ....	44
Figure 3-13 Illustration of the ball bearing electrodes used for breakdown measurements. ....	44
Figure 3-14 Schematic diagram of a dielectric spectroscopy measurement....	45
Figure 3-15 Test cell and temperature control system.....	46
Figure 3-16 Illustration of PEA method [93]. ....	47
Figure 3-17 Diagram of the pulsed electro-acoustic (PEA) system [4]. ....	48
Figure 3-18 Photographs of the PEA system used in this project. ....	48
Figure 3-19 TGA traces of dried and water saturated pure epoxy samples. ....	49

Figure 3-20 Water Diffusion of EP0, EPS, EPST and EPB samples (a) EPS, 60% RH; (b) EPS, Saturated; (c) EPST, 60% RH; (d) EPST, saturated; (e) EPB, 60% RH; (f) EPB, saturated, 293K. ....	50
Figure 3-21 Water diffusion in epoxy and its nanocomposites of 3 wt% loadings (a) 60% RH; (b) saturated, 293K.....	51
Figure 3-22 Water uptake of epoxy and its nanocomposites in 0.5 wt% loading concentration, 293K. ....	53
Figure 3-23 Water uptake of epoxy and its nanocomposites in 1 wt% loading concentration, 293K. ....	54
Figure 3-24 Water uptake of epoxy and its nanocomposites in 3 wt% loading concentration, 293K. ....	54
Figure 3-25 Water uptake of epoxy and its nanocomposites in 5 wt% loading concentration, 293K. ....	55
Figure 4-1 Illustration of the equivalent diameter of particles/aggregates.....	58
Figure 4-2 Histogram used to generate weighted average of equivalent diameter. ....	58
Figure 4-3 SEM image of pure epoxy resin: $\times 5000$ . ....	60
Figure 4-4 SEM image of EPS05, $\times 5000$ .....	60
Figure 4-5 SEM image EPS1: (a) and (b) $\times 5000$ .....	61
Figure 4-6 SEM image of EPS3: (a) and (b) $\times 5000$ . ....	61
Figure 4-7 SEM image of EPS5: (a) and (b) $\times 5000$ . ....	61
Figure 4-8 SEM image of EPST05, $\times 5000$ .....	62
Figure 4-9 SEM image of EPST1: (a) and (b) $\times 5000$ . ....	62
Figure 4-10 SEM image of EPST3: (a) and (b) $\times 5000$ . ....	63
Figure 4-11 SEM image of EPST5: (a) and (b) $\times 5000$ . ....	63
Figure 4-12 SEM image of EPS1, $\times 15000$ : (a) original; (b) featured. ....	64
Figure 4-13 SEM image of EPS3, $\times 15000$ : (a) original; (b) featured. ....	64
Figure 4-14 SEM image of EPB05, $\times 5000$ . ....	65

## Table of Figures

Figure 4-15 SEM image of EPB1, $\times 5000$ .....	65
Figure 4-16 SEM image of EPB3, $\times 5000$ .....	66
Figure 4-17 SEM image of EPB5: (a) $\times 1000$ ; (b) $\times 5000$ .....	66
Figure 4-18 SEM image of EPB5, $\times 10000$ (inset, $\times 50000$ ). ....	67
Figure 4-19 Original SEM images of EPS3 samples, $\times 15000$ .....	68
Figure 4-20 Binary SEM images of EPS3 samples, $\times 15000$ . ....	69
Figure 4-21 Processed SEM images with highlighted particles of EPS3 samples, $\times 15000$ .....	70
Figure 4-22 Histogram of measured particle/aggregate size of EPS3 samples.	71
Figure 4-23 Histogram of measured 1 <sup>st</sup> Nearest Neighbour Distance of EPS3 samples. ....	71
Figure 4-24 Occurrence probability of measured particle/aggregate size and fitting curve. ....	74
Figure 4-25 Histogram of simulated particle/aggregate size of EPS3 samples.	75
Figure 4-26 Occurrence probability of measured 1 <sup>st</sup> Nearest Neighbour Distance and fitting curve.....	75
Figure 4-27 Histogram of simulated 1 <sup>st</sup> Nearest Neighbour Distance of EPS3 samples, PDF Method. ....	76
Figure 4-28 Simulated particles/aggregates dispersion and distribution in the cubic area of EPS3 samples, PDF Method. ....	76
Figure 4-29 Histogram of simulated 1 <sup>st</sup> Nearest Neighbour Distance of EPS3 samples, Histogram Method.....	77
Figure 4-30 Simulated particles/aggregates dispersion and distribution in the cubic area of EPS3 samples, Histogram Method.....	77
Figure 5-1 TGA result of (a) untreated and C8-treated $\text{SiO}_2$ particles with DCM; (b) detailed loss of weight in C8-treated $\text{SiO}_2$ particles. ....	82
Figure 5-2 TGA traces of EPB in each loading concentration: (a) whole; (b), (c) and (d) zooming in to different temperature ranges. ....	84

Figure 5-3 Derivative traces of EPB in each loading concentration: (a) whole; (b) zooming in on the temperature range at the maximum rate.	84
Figure 5-4 TGA traces of EPS in each loading concentration: (a) whole; (b), (c) and (d) zooming in to different temperature ranges. ....	85
Figure 5-5 Derivative traces of EPS in each loading concentration: (a) whole; (b) zooming in on the temperature range at the maximum rate.	85
Figure 5-6 TGA traces of EPST in each loading concentration: (a) whole; (b), (c) and (d) zooming in to different temperature ranges. ....	86
Figure 5-7 Derivative traces of EPST in each loading concentration: (a) whole; (b) zooming in on the temperature range at the maximum rate.	86
Figure 5-8 Comparison of $T_{IDT}$ of EP0, EPS, EPST and EPB in different loading concentrations.....	87
Figure 5-9 Comparison of $T_{max}$ of EP0, EPS, EPST and EPB in different loading concentrations.....	88
Figure 5-10 DSC results of pure epoxy resins: (a) the whole curve of the DSC process; (b) zooming in on the glass transition process. ....	91
Figure 5-11 3-Time-Scan DSC results of pure epoxy resins. ....	92
Figure 5-12 DSC results of EPB in each filler loading concentration. ....	93
Figure 5-13 DSC results of EPB in different filler loading concentrations with error bars.....	94
Figure 5-14 DSC results of EP0 and EPS in each filler loading concentration: (a) the whole curves of the DSC process; (b) zooming in on the glass transition process.....	95
Figure 5-15 DSC results of EPS in different filler loading concentrations with error bars.....	96
Figure 5-16 DSC results of EP0 and EPST in each filler loading concentration: (a) the whole curves of the DSC process; (b) zooming in on the glass transition process.....	96
Figure 5-17 DSC results of EPST in different filler loading concentrations with error bars. ....	97

## Table of Figures

Figure 5-18 Comparison of the $T_g$ of EP0, EPS, EPST and EPB samples in different filler loading concentrations.....	98
Figure 5-19 Illustration of exfoliated and intercalated macroscopic layer structures of hBN-based epoxy nanocomposites.....	99
Figure 6-1 Example of Weibull distribution of AC breakdown strength with confidence bound [4]. .....	104
Figure 6-2 Weibull plot of EPS samples in different filler loading concentrations on AC breakdown strength.....	105
Figure 6-3 Weibull plot of EPST samples in different filler loading concentrations on AC breakdown strength.....	106
Figure 6-4 Weibull plot of EPB samples in different filler loading concentrations on AC breakdown strength.....	106
Figure 6-5 Shape parameter $\beta$ of EPS in different filler load concentrations...	108
Figure 6-6 Shape parameter $\beta$ of EPST in different filler load concentrations.	109
Figure 6-7 Shape parameter $\beta$ of EPB in different filler load concentrations. .	109
Figure 6-8 Scale parameter $\eta$ ( $\text{kV} \cdot \text{mm}^{-1}$ ) of EPS in different filler load concentrations. ....	111
Figure 6-9 Scale parameter $\eta$ ( $\text{kV} \cdot \text{mm}^{-1}$ ) of EPST in different filler load concentrations. ....	111
Figure 6-10 Scale parameter $\eta$ ( $\text{kV} \cdot \text{mm}^{-1}$ ) of EPB in different filler load concentrations. ....	112
Figure 6-11 Illustration of the enhancements of the electric field caused by agglomerations of nanoparticles [3]. .....	113
Figure 6-12 Weibull plot of EPS samples in different loading concentrations on DC breakdown strength, dry. ....	115
Figure 6-13 Weibull plot of EPST samples in different loading concentrations on DC breakdown strength, dry. ....	116
Figure 6-14 Weibull plot of EPB samples in different loading concentrations on DC breakdown strength, dry. ....	116

Figure 6-15 Shape Parameter $\beta$ of EPS in different filler load concentrations, dry.	118
Figure 6-16 Shape parameter $\beta$ of EPST in different filler load concentrations, dry.	118
Figure 6-17 Shape parameter $\beta$ of EPB in different filler load concentrations, dry.	119
Figure 6-18 Scale parameter $\eta$ ( $\text{kV} \cdot \text{mm}^{-1}$ ) of EPS in different filler load concentrations, dry.	120
Figure 6-19 Scale parameter $\eta$ ( $\text{kV} \cdot \text{mm}^{-1}$ ) of EPST in different filler load concentrations, dry.	120
Figure 6-20 Scale parameter $\eta$ ( $\text{kV} \cdot \text{mm}^{-1}$ ) of EPB in different filler load concentrations, dry.	121
Figure 6-21 Scale parameter $\eta$ ( $\text{kV} \cdot \text{mm}^{-1}$ ) of EP0, EPS, EPST and EPB in different filler load concentrations, 60RH.	124
Figure 6-22 Shape parameter $\beta$ of EP0, EPS, EPST and EPB in different filler load concentrations, 60RH.	125
Figure 6-23 Scale parameter $\eta$ ( $\text{kV} \cdot \text{mm}^{-1}$ ) of EP0, EPS, EPST and EPB in different filler load concentrations, saturated.	125
Figure 6-24 Shape parameter $\beta$ of EP0, EPS, EPST and EPB in different filler load concentrations, Saturated.	126
Figure 6-25 Scale parameter $\eta$ ( $\text{kV} \cdot \text{mm}^{-1}$ ) of EP0, EPS, EPST and EPB in different relative humidity conditions, 3 wt%.	126
Figure 7-1 The polarisation spectrum with orientation, ionic and electronic polarisation mechanisms [3].	130
Figure 7-2 Illustration of orientation polarisation: (a) without electric field; (b) after applying electric field.	131
Figure 7-3 Illustration of the ionic polarisation.	132
Figure 7-4 Heterogeneous material contains the matrix and fillers, which both have complex permittivity.	133

## Table of Figures

Figure 7-5 Curve fitting of the experimental $\varepsilon''$ to the sum of the $\alpha$ relaxation, MWS relaxation, and the DC conductivity [163].....	133
Figure 7-6 Illustration of loss tangent. ....	135
Figure 7-7 Relative permittivity (real) of pure epoxy resins, 293K-333K.....	136
Figure 7-8 Relative permittivity (imaginary) of pure epoxy resins, 293K-333K.....	136
Figure 7-9 $\tan\delta$ of pure epoxy resins, 293K-333K.....	137
Figure 7-10 Real and imaginary relative permittivity curve versus frequency and temperature [165]. ....	139
Figure 7-11 $\tan\delta$ curves versus frequency and temperature [165].....	139
Figure 7-12 Relative permittivity in EP0, EPS, EPST, and EPB samples, filler loading concentration of 0.5 wt%, dry, 293K. ....	141
Figure 7-13 Relative permittivity in EP0, EPS, EPST, and EPB samples, filler loading concentration of 1 wt%, dry, 293K. ....	142
Figure 7-14 Relative permittivity in EP0, EPS, EPST, and EPB samples, filler loading concentration of 3 wt%, dry, 293K. ....	142
Figure 7-15 Comparison of real relative permittivity between EP0, EPS, EPST, and EPB samples at 50Hz, filler loading concentrations of 0.5, 1 and 3 wt%, dry, 293K. ....	143
Figure 7-16 Relative permittivity in EP0, EPS samples, filler loading concentration of 3 wt%, dry, at 293, 313, 333K. ....	144
Figure 7-17 Relative permittivity in EP0, EPST samples, filler loading concentration of 3 wt%, dry, at 293, 313, 333K. ....	144
Figure 7-18 Relative permittivity in EP0, EPB samples, filler loading concentration of 3 wt%, dry, at 293, 313, 333K. ....	145
Figure 7-19 Relative permittivity in EP0, EPS, EPST, and EPB samples, filler loading concentration of 3 wt%, 60 RH, 293K.....	146
Figure 7-20 Relative permittivity in EP0, EPS, EPST, and EPB samples, filler loading concentration of 3 wt%, saturated, 293K. ....	146



Figure 7-21 Relative imaginary permittivity in EP0, EPS, EPST, and EPB samples, filler loading concentration of 1 wt%, 293K: (a) 60 RH; (b) saturated. ....	146
Figure 7-22 Measured and calculated relaxation time of silica nanocomposites: (a) 60 RH; (b) saturated. ....	149
Figure 7-23 Illustration of water shell under different relative humidity conditions. ....	151
Figure 8-1 DC conductivity of EP0 and EPS samples in each filler loading concentration, dry, 293K. ....	157
Figure 8-2 DC conductivity of EP0 and EPST samples in each filler loading concentration, dry, 293K. ....	157
Figure 8-3 DC conductivity of EP0 and EPB samples in each filler loading concentration, dry, 293K. ....	158
Figure 8-4 DC conductivity of epoxy and its nanocomposites (1 wt%), dry, 293K. ....	159
Figure 8-5 DC conductivity of epoxy and its nanocomposites (3 wt%), dry, 293K. ....	159
Figure 8-6 DC conductivity of pure epoxy resins in each RH condition, 293K.	160
Figure 8-7 DC conductivity of EP0 and EPS samples in 1 and 3 wt%, 60RH, 293K. ....	160
Figure 8-8 DC conductivity of EP0 and EPST samples in 1 and 3 wt%, 60RH, 293K. ....	161
Figure 8-9 DC conductivity of EP0 and EPS3 in each RH condition, 293K. ....	163
Figure 8-10 DC conductivity of EP0 and EPST3 in each RH condition, 293K. .	163
Figure 8-11 DC conductivity of EP0 and EPB samples in 1 and 3 wt%, 60RH, 293K. ....	164
Figure 8-12 DC conductivity of epoxy and its nanocomposites (3 wt%), 60RH.	164
Figure 8-13 Illustration of (a) Homocharge and (b) heterocharge. ....	167
Figure 8-14 A typical waveform of space charge measurement [4]. ....	168

## Table of Figures

Figure 8-15 Original space charge profile of EP0 at 40 kV·mm <sup>-1</sup> , dry.....	169
Figure 8-16 Subtracted space charge profile of EP0 at 40 kV·mm <sup>-1</sup> , dry.....	170
Figure 8-17 Original space charge profile of EPS at 40 kV·mm <sup>-1</sup> , dry. ....	171
Figure 8-18 Subtracted space charge profile of EPS at 40 kV·mm <sup>-1</sup> , dry (dash curves indicate the ideal charge distributions without neutralization). ....	172
Figure 8-19 Total charge amount in bulk of EP0 and EPS in each filler loading concentration, dry. ....	172
Figure 8-20 Original space charge profile of EPST at 40 kV·mm <sup>-1</sup> , dry. ....	173
Figure 8-21 Subtracted space charge profile of EPST at 40 kV·mm <sup>-1</sup> , dry. ....	174
Figure 8-22 Total charge amount in bulk of EP0 and EPST in each filler loading concentration, dry. ....	175
Figure 8-23 Original space charge profile of EPB at 40 kV·mm <sup>-1</sup> , dry. ....	175
Figure 8-24 Subtracted space charge profile of EPB at 40 kV·mm <sup>-1</sup> , dry. ....	176
Figure 8-25 Total charge amount in bulk of EP0 and EPB in each filler loading concentration, dry. ....	177
Figure 8-26 Comparison of total charge amount in epoxy and its nanocomposites samples at 40 kV·mm <sup>-1</sup> , dry. ....	178
Figure 8-27 Decay of total charge amount in bulk of EP0 and EPS in each filler loading concentration, dry. ....	179
Figure 8-28 Decay of total charge amount in bulk of EP0 and EPST in each filler loading concentration, dry. ....	179
Figure 8-29 Decay of total charge amount in bulk of EP0 and EPB in each filler loading concentration, dry. ....	180
Figure 8-30 Comparison of decay of total charge amount in bulk of epoxy and its nanocomposites in each filler loading concentration, dry. ....	180
Figure 8-31 Subtracted space charge profile of EP0 at 40 kV·mm <sup>-1</sup> : (a) A.RH; (b) 60RH. ....	182

Figure 8-32 Total charge amount in bulk of pure samples in different RH conditions. ....	182
Figure 8-33 Subtracted space charge profile of EPS at 40 kV·mm <sup>-1</sup> : (a) 1 wt%, A.RH; (b) 1 wt%, 60RH; (c) 3 wt%, A.RH; (d) 3 wt%, 60RH. ....	183
Figure 8-34 Total charge amount in bulk of EP0 and EPS in each filler loading concentration: (a) A.RH; (b) 60RH.....	184
Figure 8-35 Subtracted space charge profile of EPST at 40 kV·mm <sup>-1</sup> : (a) 1 wt%, A.RH; (b) 1 wt%, 60RH; (c) 3 wt%, A.RH; (d) 3 wt%, 60RH.....	184
Figure 8-36 Total charge amount in bulk of EP0 and EPST in each filler loading concentration: (a) A.RH; (b) 60RH.....	185
Figure 8-37 Subtracted space charge profile of EPB at 40 kV·mm <sup>-1</sup> : (a) 1 wt%, A.RH; (b) 1 wt%, 60RH; (c) 3 wt%, A.RH; (d) 3 wt%, 60RH. ....	186
Figure 8-38 Total charge amount in bulk of EP0 and EPB in each filler loading concentration: (a) A.RH; (b) 60RH.....	186
Figure 8-39 Comparison of total charge amount in epoxy and its nanocomposites samples at 40 kV·mm <sup>-1</sup> : (a) 1 wt%, A.RH; (b) 1 wt%, 60RH; (c) 3 wt%, A.RH; (d) 3 wt%, 60RH.....	187
Figure 8-40 Decay of total charge amount in bulk of EP0 and EPS in each filler loading concentration: (a) A.RH; (b) 60RH. ....	188
Figure 8-41 Decay of total charge amount in bulk of EP0 and EPST in each filler loading concentration: (a) A.RH; (b) 60RH. ....	188
Figure 8-42 Decay of total charge amount in bulk of EP0 and EPB in each filler loading concentration: (a) A.RH; (b) 60RH. ....	189
Figure 8-43 Comparison of decay of total charge amount in bulk of epoxy and its nanocomposites: (a) 1 wt%, A.RH; (b) 3 wt%, A.RH. ....	189
Figure 8-44 Comparison of decay of total charge amount in bulk of epoxy and its nanocomposites: (a) 1 wt%, 60RH; (b) 3 wt%, 60RH. ....	190



# Thesis: Declaration Of Authorship

I, **Dayuan Qiang**

declare that this thesis and the work presented in it are my own and has been generated by me as the result of my own original research.

*Dielectric Properties of Epoxy Based Nanocomposites Filled with Nano SiO<sub>2</sub> and BN and Moisture Effects.*

I confirm that:

1. This work was done wholly or mainly while in candidature for a research degree at this University;
2. Where any part of this thesis has previously been submitted for a degree or any other qualification at this University or any other institution, this has been clearly stated;
3. Where I have consulted the published work of others, this is always clearly attributed;
4. Where I have quoted from the work of others, the source is always given. With the exception of such quotations, this thesis is entirely my own work;
5. I have acknowledged all main sources of help;
6. Where the thesis is based on work done by myself jointly with others, I have made clear exactly what was done by others and what I have contributed myself;
7. Parts of this work have been published.

Signed: .....

Date: .....



## Acknowledgements

I would like to express sincerest thanks to my supervisors Prof. George Chen and Dr. Thomas Andritsch, who have given me persistent supports and help on expertise skills, experiment designs, inspiration of ideas and treasury suggestions. Without their patience and encouragement both on study and life, this work would not have been possible.

I would also like to sincerely appreciate the help from my colleagues: Dr. Ian Hosier, Dr. Matt Praeger and Dr. Celia Yeung spent hours training me on sample preparation and experiment devices; Dr. Suvi Virtanen gave lots of advice on chemical property analysis; Mr. Neil Palmer and Mr. Michael Smith provided numbers of technical support during my whole project in Tony Davis High Voltage Laboratory.

My special thanks will be given to all my kindest friends, Mr. Wang Yan, Mr. Ziyun Li, Dr. Churui Zhou, Dr. Xuan Wang and Mr. Miao He, for their instructions, discussions and friendship throughout my five-year study in the UK.

Finally, I will cherish the liveliest feeling of affection and gratitude: for my mother and grandpa who have given me endless and unconditional support, encouragement over past twenty years; for my dearest girlfriend, Miss. Yujia Chang, who accompanies and understands me with full heart and soul. Thus, I would like to dedicate this thesis in token of affection to them and wish a wonderful future we share together.





# List of Publications

## Article:

[1] Qiang, Dayuan, Wang, Yan, Chen, George and Andritsch, Thomas “Dielectric properties of epoxy SiO<sub>2</sub> and BN nanocomposites and moisture/ temperature influence.” (IET Nanodielectrics, Published)

## Conference Item:

[2] Qiang, D., He, M., Chen, G. and Andritsch, T. (2015) “Influence of nano-SiO<sub>2</sub> and BN on space charge and AC/DC performance of epoxy nanocomposites.” In, 2015 IEEE Electrical Insulation Conference (EIC), Seattle, US, 07 - 10 Jun 2015. IEEE, 492-495. (oral presentation).

[3] Qiang, Dayuan, Chen, George and Andritsch, Thomas (2015) “Influence of water absorption on dielectric properties of epoxy SiO<sub>2</sub> and BN nanocomposites.” In, IEEE Conference on Electrical Insulation and Dielectric Phenomena, Ann Arbor, US, 18 - 20 Oct 2015. IEEE 4pp (oral presentation).

[4] Qiang, Dayuan, Wang, Yan, Chen, George and Andritsch, Thomas (2016) “Influence of water absorption on space charge behaviour of epoxy nanocomposites.” In, IEEE Conference on Electrical Insulation and Dielectric Phenomena, Toronto Canada, 16 - 19 Oct 2016.

[5] He, M., Qiang, D., Liu, N., Chen, G. and Lewin, P.L. (2015) “Investigation of charge injection threshold field in epoxy resin.” In, 2015 IEEE Electrical Insulation Conference (EIC), Seattle, US, 07 - 10 Jun 2015. IEEE, 49-52.



# Abbreviations

<b>AC</b>	Alternating current
<b>AFM</b>	Atomic force microscope
<b>APS</b>	Average particle size
<b>ASTM</b>	American society for testing and materials
<b>ATWS</b>	Average thickness of water shell
<b>BCC</b>	Body-centred cubic
<b>BD</b>	Breakdown
<b>BET</b>	Particle analytical method by BET ( <i>Brunauer, Emmett and Teller</i> )
<b>h-/BN</b>	Hexagonal-/Boron nitride
<b>DC</b>	Direct current
<b>DCM</b>	Dichloromethane
<b>DGEBA</b>	Diglycidyl ether of bisphenol-A type epoxy resin
<b>DMA</b>	Dynamic mechanical analysis
<b>DSC</b>	Differential scanning calorimetry
<b>EDL</b>	Electrical double layer
<b>ESR</b>	Equivalent series resistance
<b>Free volume</b>	A small amount of unfilled volume is associated with the end of a polymer chain
<b>IDT</b>	Initial decomposition temperature
<b>MLE</b>	Maximum likelihood estimation
<b>MDS</b>	Multidimensional Scaling method

## Abbreviations

<b>MWS</b>	Maxwell-Wagner-Sillars
<b>NND</b>	Nearest neighbor distance
<b>PCAM</b>	Polymer chain alignment model
<b>PD</b>	Partial discharge
<b>PDF</b>	Probability distribution function
<b>PE</b>	Polyethylene
<b>PEA</b>	Pulse electroacoustic technique
<b>QDC</b>	Quasi-dc process
<b>SCA</b>	Silane coupling agent
<b>SCLC</b>	Space charge limited current
<b>SEM</b>	Scanning electron microscope
<b>SSA</b>	Specific surface area: total surface area per unit of mass
<b>STM</b>	Scanning tunnelling microscope
<b>TEM</b>	Transmission electron microscope
<b>T<sub>g</sub></b>	Glass transition temperature
<b>TGA</b>	Thermogravimetric analysis
<b>THF</b>	Tetrahydrofuran
<b>WAED</b>	Weighted average equivalent diameters
<b>WASD</b>	Weighted average surface distance
<b>wt</b>	Weight fraction: The weight of a constituent divided by the weight of all constituents of the mixture before mixing
<b>XLPE</b>	Cross-linked polyethylene

# Chapter 1 Introduction

## 1.1 Background

The term epoxy resin generally refers to a thermosetting epoxy polymer containing two or more epoxy groups, and most of the resins do not have high molecular mass. Because they contain reactive epoxy groups, they can react with many curing agents/hardeners and form three dimensional cross-linking network structures. Epoxy resins display good adhesiveness, good dielectric and mechanical property properties, chemical stability [1] and other advantages such as low cost and easy shaping. Consequently, they have been widely used in many areas as dielectric materials, anti-corrosion coating materials, and cementation between metals and non-metals. Furthermore, they are used extensively in the manufacture of composite materials, and are considered essential materials for industrial applications [2]. However, because of the broader usage demand on epoxy resins, it is challenging to meet the growing requirements of industrialisation and commercialisation. Hence, researchers have started to look for new modification methods to improve the properties of epoxy resins. There are many of these modifications, including the use of different hardeners, liquid crystal, and the addition of nanofillers, which is one of the most promising methods [3].

## 1.2 Motivation and Objectives

Nanotechnology is the study of properties and applications of materials having a structure size between 1 and 100 nm, a concept first introduced by *Richard Feynman* in his 1959 lecture. Research on nanomaterials initially started from areas in ceramics as inorganic and metal powders [4]. Today, nanotechnology has been introduced into many fields, including high voltage and power engineering and some related industrial areas [5]. For example, the Juno spacecraft, which recently entered orbit around Jupiter, utilised a layer-structured CNT (carbon nanotube) based nanocomposite paper to protect several critical components of the flight system attitude control motor struts (and the main engine housing) against electrostatic discharge [6]. To provide more knowledge to meet the increasing demands of current nanocomposites in industrial applications, many researchers have conducted research on polymer nanocomposites of certain filler loadings (normally 0.5-10 wt% [7]). Some of the results demonstrate that the thermal and dielectric properties of nanocomposites are superior to pure epoxy resins. However,

other research has displayed unexpected results, with worse properties of epoxy nanocomposites. Because of the extremely large specific surface area of nano-sized particles, even in a small loading concentration [2, 8], the interfacial characteristics between nanoparticles and base polymer materials play an important role in determining the dielectric properties [9]. Moreover, the changes in base materials due to the presence of particles would also affect the trap depths and density, which is related to the electrical properties [10]. However, the mechanisms behind these phenomena remain unclear, and some specific areas still lack research. Because many properties of epoxy resins are influenced by adding types of nanofillers that vary in shapes and dielectric properties [11-14], it is necessary to identify the differences between their influences upon the properties of polymer composites. In addition, a large number of new nanofillers appear. Thus, trials and comparisons between traditional and new fillers become increasingly meaningful. For this thesis, nano SiO<sub>2</sub> and hBN particles were selected as fillers, which have different shapes and different thermal, mechanical, and dielectric properties.

However, poor morphology of dispersion and distribution of particles has been reported, rendering the dielectric properties of polymer nanocomposites worse. Mostly, researchers tend to use imprecise descriptions to describe these two factors through SEM/TEM images, which was the initial prompt for this research. Although quantitative methods were used in some studies [15], there was still no quantification method for results of the SEM technique, and no direct relationship between quantified morphology characteristics and dielectric/electrical properties of polymer nanocomposites in different filler loadings. Another important motivation for this thesis is the well-known property that epoxy and some of its fillers are hydrophilic, and will absorb moisture from the environment during applications. This will result in the overall deterioration of insulation properties [16]. Several studies on the influence of moisture on dielectric properties of polymer nanocomposites have been reported [17-19]. However, these focused on polyethylene (PE) based nanocomposites, and some of the conclusions may not be applicable to epoxy nanocomposites. There are still some gaps in the research that are worthwhile to study, especially focusing much more on epoxy and its nanocomposites. Thus, the main objectives of this thesis are as follows: First, a method will be developed to describe the morphology of nanofillers in the nanocomposites more precisely, and it will be determined how the presence of nano-scaled fillers influences the physical and chemical properties of epoxy resins. Second, it will be investigated how the presence of nanofillers and resultant interfacial regions between the matrix and nanofillers affects the dielectric and

electrical properties of epoxy nanocomposites. Finally, the influences of water absorption on the dielectric properties of epoxy and its nanocomposites are fully considered during tests, and thoroughly investigated.

### 1.3 Contributions of the Thesis

1. A combined method was proposed to quantitatively evaluate the dispersion and distribution of spherical/ellipsoidal particles/aggregates in epoxy nanocomposites. According to this method, surface treatment was proven to help dispersion and distribution more successfully in nanocomposites. The presence of nano SiO<sub>2</sub> and hBN particles resulted in different impacts on the morphology of epoxy and resulting composites. Moreover, two modelling methods were proposed and tested to simulate the real dispersion and distribution of particles/aggregates in polymer nanocomposites. It was possible to link the simulation of dispersion and distribution of particles/aggregates based on measured morphology to existing modelling on electrical properties of nanocomposites.
2. The effects of the presence of nanoparticles on dielectric/electrical properties were investigated. The difference between nanocomposites resulted from the interfacial areas, and the surface treatment introduced deeper traps in the interphases when compared to the untreated samples. The presence of nanoparticles resulted in morphology changes and more presence of traps in the bulk of material, which hindered the charge injection and reduced the mobility of charge carriers. However, with increased filler loadings, nanoparticles affected the polymer structures significantly; thus, creating more traps in the bulk material. This means the average distance between arbitrary traps should lower in samples with higher filler loadings, and charge carriers require less energy when moving from one to another. The higher carrier mobility subsequently results in increased conductivity. Additionally, in most cases plate-like nano-BN fillers acted as barriers for charge injection and movement.
3. The effects of moisture on the dielectric/electrical properties of epoxy and its nanocomposites are thoroughly investigated. The addition of inorganic nanoparticles increased moisture inside the specimens, and water absorption was difficult to evaluate. Water shells still appeared, even though hydroxyl groups were removed from the surface of the silica particles.

Surface treatment was able to reduce the water uptake; however, there was no obvious impact on modifying the dielectric properties, due to the limitation of the thickness of tightly bonded layers and water located in the interphases. The response of frequently reported bonded water appearing in the mid-frequency range was related to the mechanism of Maxwell-Wagner-Sillars polarisation. Regarding electrical properties, the degraded performance was mainly due to the presence of water, which caused a larger amount of mobile charge carriers and higher mobility in the bulk of material. Moreover, the formation of water shells decreased the inter-particle distances, and made the effect of hopping and the quantum tunnelling process more likely in higher relative humidity conditions.

### 1.4 Outline of the Thesis

This thesis focuses on the water absorption behaviour, thermal properties, dielectric spectroscopy measurement, AC & DC breakdown tests, DC conductivity, and space charge behaviour of epoxy nanocomposites. The main factors that affect these properties will be discussed by analysing the results of experiments. The thesis has been divided into the following chapters. Chapter 2 contains brief information on the epoxy resin and polymer nanocomposites, and summarises previous literature, particularly the models for explaining the mechanisms in polymer composites. Chapter 3 is an introduction to the preparation method and set-up of all the tests conducted on epoxy-based nanocomposites in detail. An investigation of water absorption in epoxy nanocomposites is also presented. In Chapter 4, a combined quantification method is proposed, to analyse the morphology of epoxy nanocomposites based on SEM images, and further proposes a method of modelling dispersion and distribution of particles. Chapter 5 presents TGA and DSC measurements on samples to investigate the influences of particles on thermal stability, and further presents conclusions on some possible structural impacts. Chapter 6 contains the AC and DC breakdown measurement results of epoxy nanocomposites and explains the mechanisms behind this process. In Chapter 7, dielectric spectroscopy measurements are used to ascertain how nano-filler influences the dielectric properties of epoxy. In Chapter 8, DC conductivity, “volts-on” PEA, and space charge decay measurements are used to investigate and measure the space charge behaviour of epoxy and its nanocomposites. Throughout the thesis, the influence of moisture on dielectric and electrical properties are fully considered and assimilated into the experiments. The final conclusions collate this comprehensive information regarding the effect of water on nanocomposites.



## Chapter 2 Literature Review

### 2.1 Epoxy Resin

Epoxy resins are types of epoxy oligomers, and generally refer to organic molecules without high molecular mass. The molecular structure of epoxy resin is a molecular chain containing reactive epoxy groups that locate at the end and midpoints of the molecular chain, or exist as cyclic structures. Because the molecular structure of the epoxy group contains reactive groups, epoxy resins can react with curing agents to form three-dimensional net structures. Epoxy resin has excellent adhesion, chemical and heat resistance, mechanical properties, and insulating properties. It is one of the most commonly used thermosetting materials in high voltage apparatus as insulation, owing to its good mechanical and electrical properties, and chemical stability [20]. Therefore, it has become one of the most popular thermosetting resins in industrial applications.

#### 2.1.1 Definitions and Classification of Epoxy Resin

The epoxy group contains the structure, “—CH (O) CH—”, which is formed as a ring (see in Figure 2-1). When the polymerisation degree  $n$  is zero, epoxy considered an epoxy compound (or epoxide). The simplest epoxide compound is ethylene epoxide, which can form thermosetting polyethylene oxide through ionic polymerisation. Such polyethylene oxide is known as epoxy resin [4].

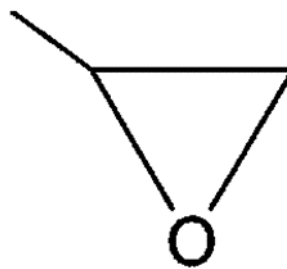


Figure 2-1 Diagram of the epoxy group.

Epoxy resin is the collective name for certain compounds. These compounds contain two or more epoxy groups in molecule structures, and can form a three-dimensional net structures when cured with an appropriate chemical reagent [21].

## Chapter 2 Literature Review

Epoxy resins can be termed epoxy oligomers, because their molecular weight is the same as an oligomer ensuring they can be distinguished from their solidified products. The main characteristic of the chemical structure of epoxy resins is that there are epoxy groups within the molecular chains. However, epoxy resin is a thermosetting resin, which is formed by applying a thermal treatment to a mixture of a base resin and a curing agent. Hence, chemical reactions are involved in the curing process, and the curing agent in addition to the base resin determines the chemical structure of a cured epoxy resin [22].

Epoxy resins can be divided into glycidyl epoxy resins and non-glycidyl epoxy resins, according to their synthesis methods [4]. Generally, the condensation reaction of a suitable dihydroxy compound, dibasic acid, or a diamine and epichlorohydrin is used for forming glycidyl epoxy resins, and the epoxidation of alkene is used for non-glycidyl epoxy resins, which are the most important reactions in organic synthesis. Moreover, glycidyl epoxy resins include glycidyl ether resin, glycidyl ester resin, and glycidyl amine resin, whereas alicyclic epoxy resin and aliphatic epoxy resin belong to the non-glycidyl epoxy resin group.

Glycidyl ether epoxy resin can be further divided into the diglycidyl ether of bisphenol-A (DGEBA) and novolac epoxy resin. Glycidyl ether type epoxy resin is produced by the polycondensation of phenols (or alcohols containing active hydrogen) with epichlorohydrin. The DGEBA epoxy resins chosen for this work are formed by polycondensation reactions between bisphenol-A and epichlorohydrin, as presented in Figure 2-2. These are mostly used in industrial applications. Products in industry are mixtures of molecules that exhibit different polymerisation degrees, and most of the structure is a linear molecule containing two epoxy groups at two ends (Figure 2-3). Owing to epoxy groups being in molecular chains, epoxy resins can react with hardeners and form three-dimensional net structures, as shown in Figure 2-4.

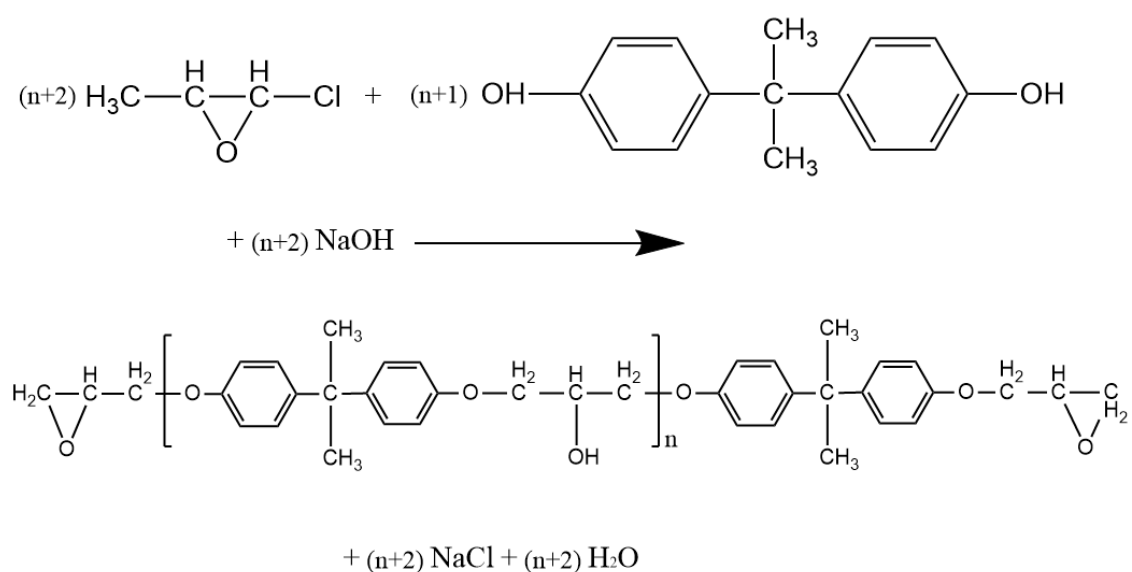


Figure 2-2 Polycondensation reactions between epichlorohydrin and bisphenol-A.

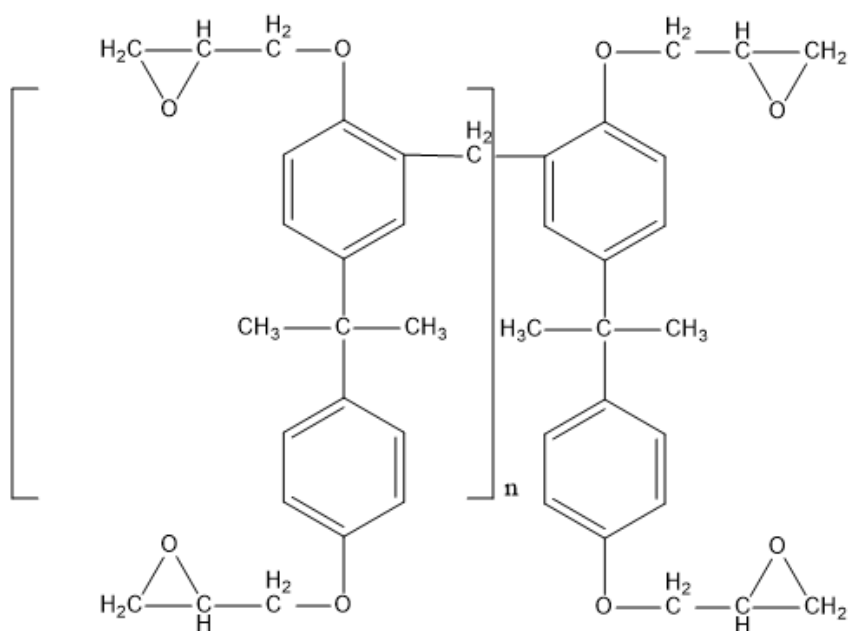


Figure 2-3 Molecular structure of bisphenol-A type epoxy resin.

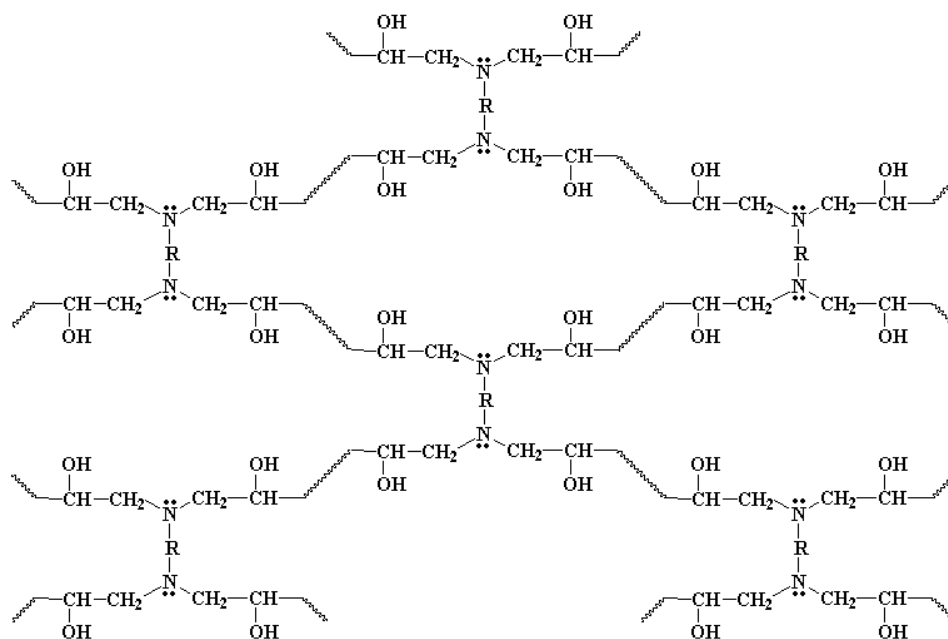


Figure 2-4 Three-dimensional net structure of epoxy resins [23].

### 2.1.2 Curing of Epoxy Resin

Before being set for use, epoxy resins need to react with a curing agent/hardener to form three-dimensional cross-linking structures, as shown in Figure 2-5; otherwise, in most cases, they are simply a type of liquid with high viscosity and without any practical value. The addition of hardener results in the start of polymerisation, which is different from curing without hardeners in room conditions [24]. Once the curing process is finished, there will be a strong net structure that is irreversible, and epoxy resins become solid and infusible solid materials, as shown in Figure 2-6.

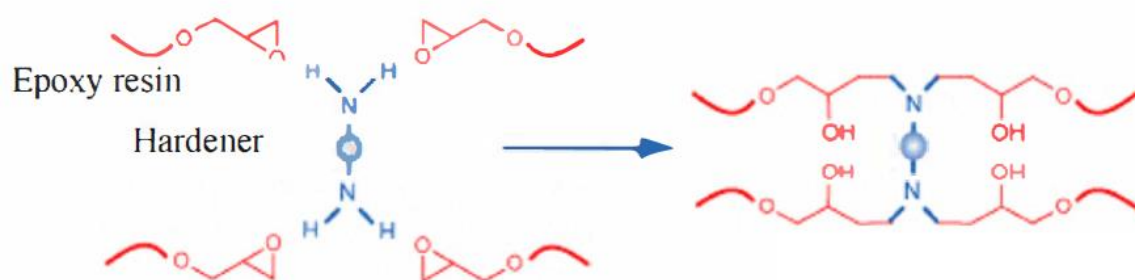


Figure 2-5 Chemical network building during curing process [25].

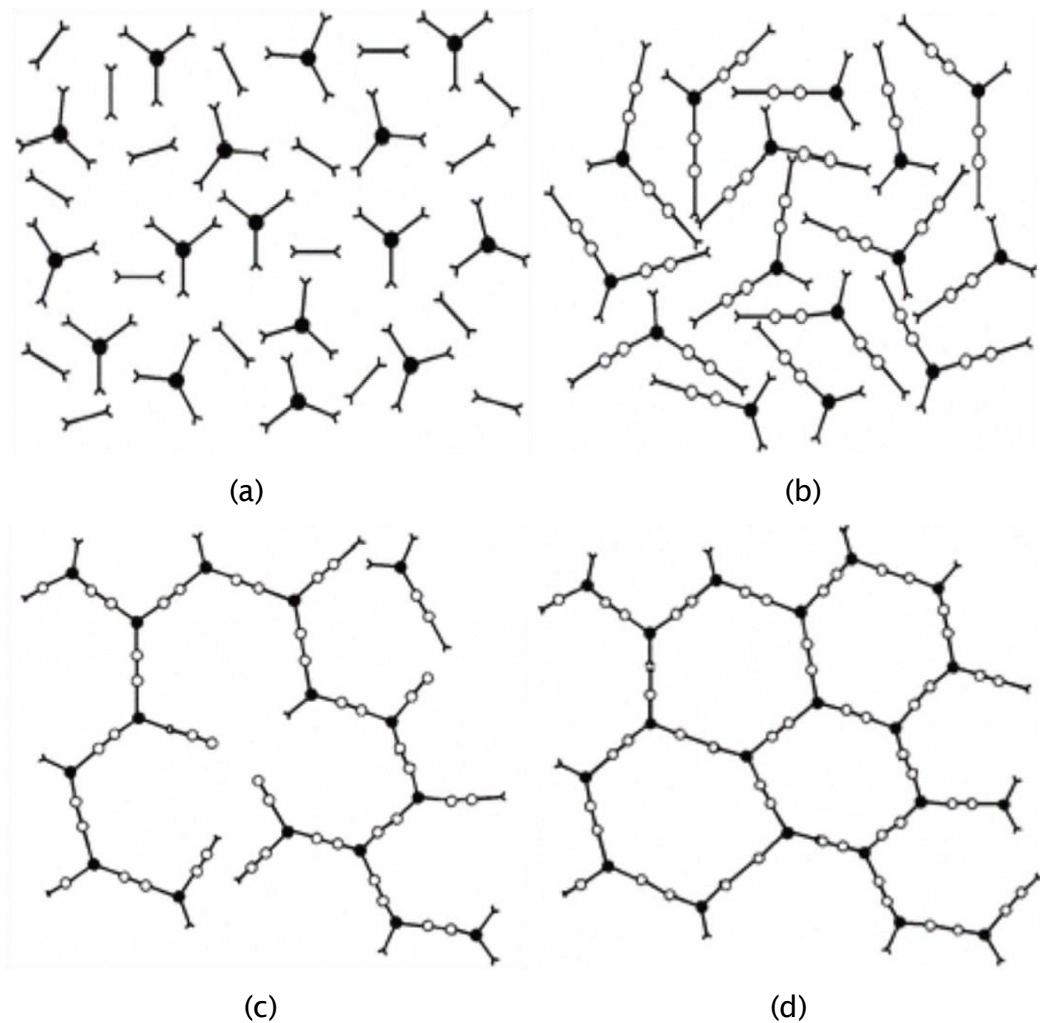


Figure 2-6 Stages of curing process: (a) Cure begins with monomers; (b) followed by linear growth and branching below the gel point; (c) continues with gelation stage but incomplete crosslinking; (d) and finishes with vitrification stage in which a fully cured state is attained[26].

Most epoxy resins can cure with hardener at room temperature or lower, but the processes will be very slow at the lower temperatures. Therefore, a high temperature is required for some certain epoxy resins. For example, bisphenol-A type epoxy resins, which have strong temperature stabilities and can remain relatively unchanged even at 200 °C, need be cured in a fan oven in the range from 100 to 150 °C [27, 28]. Different epoxy resins require different curing circumstances, not only the temperature, but also the type of hardener. This is because the resulting properties of products after curing are also influenced by the curing agent. Moreover, the hardeners also decide the glass transition temperature ( $T_g$ ) and curing kinetics [4]. Thus, each type of epoxy resin needs to react with a specific hardener, and it is essential to consider this before being applied.

## Chapter 2 Literature Review

Hardeners are usually divided into different types: alkaline, acid, explicit, amine, acid anhydride, and synthetic resin-based [4]. Among them, the explicit type is the most generally used, and can be further divided into addition polymerisation and catalytic types. The addition polymerisation type hardener is one that opens the epoxy rings and then cures with the epoxy through addition polymerisation reactions. Catalytic type curing agents are different. They share positive and negative ions to open the epoxy rings, which is followed by the addition of a polymerisation process. Hence, catalytic type hardeners are further divided into positive and negative ion types. Because the catalytic curing agent will not participate into the formation of the net structures, it will not affect the properties of cured products; however, increasing the amount of hardener can increase the speed of curing process. Therefore, if the amount of added hardener is insufficient, unreacted epoxy groups will be present in the bulk material of cured products; otherwise, there will be unreacted agents left in the composites. Regarding the mechanism of amine-type agents, it uses the active hydrogens on the nitrogen atom to open the epoxy groups to form cross-linking. In terms of easy operating of reactions and analysis in the experiments, an amine-based hardener is chosen for this work, which introduces fewer by-products and relatively simple chemical structures of final composites compared to other hardeners. The stoichiometric ratio can be calculated by Equations 2.1 and 2.2, as follows:

$$phr\ Amine = \frac{(amine\ Hydrogen\ equivalent\ weight) \times 100}{epoxide\ of\ resin} \quad (2.1)$$

where,

$$Amine\ hydrogen\ equivalent\ weight = \frac{molecular\ weight\ of\ amine}{number\ of\ active\ hydrogens} \quad (2.2)$$

Therefore, a ratio of **Resin : Hardener** is **100 : (phr Amine)**.

Moreover, the curing of epoxy resins is a chemical process, which can be greatly affected by the curing temperature. Once the temperature increases, the reaction speed will rise, and short the Arrhenius kinetics regime region, while the log of gelation time will show a linear decline with increases in curing temperature [25]. However, if the curing temperature is too high, the properties of products are often degraded because epoxy resins are heated unevenly and the cross-linking density would be asymmetric. Therefore, there must be curing temperature limits, which should be chosen carefully considering the curing speed and required properties of cured products. The chemical process of curing consists of several essential

steps within its curing time as follows: gelation point, curing, vitrification, and final solid state of the resin (also called the glass state) [12]. Generally, these steps can be identified by standard electrical measurement methods, as shown in Figure 2-7.

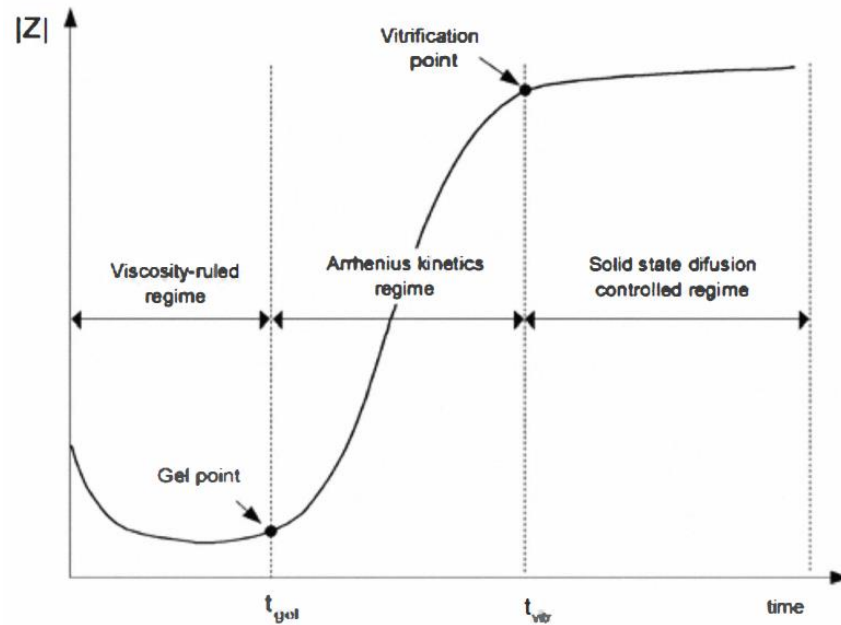


Figure 2-7 Impedance-time characteristic of epoxy resin curing with important curing process stages [26].

This dielectric response is caused by ionic conduction because of impurities, and can be used during epoxy resin manufacturing [26]. The dielectric response of impedance decreases initially when the temperature increases, which is caused by the higher mobility of ions resulting in higher conductivity. Further, the gel and vitrification points can also be detected [25], as shown in Figure 2-8. Once the resin reaches a specific temperature the viscosity rises, and as a result, the impedance increases. Therefore, it is an evaluation method (practically verified by *Pihera et al.* [29]), which can be used to identify each epoxy curing process stage and the temperature of each point. Thus, the presented results could be regarded as a supporting method when choosing the curing temperature and applied in the preparation of the epoxy resin based materials.

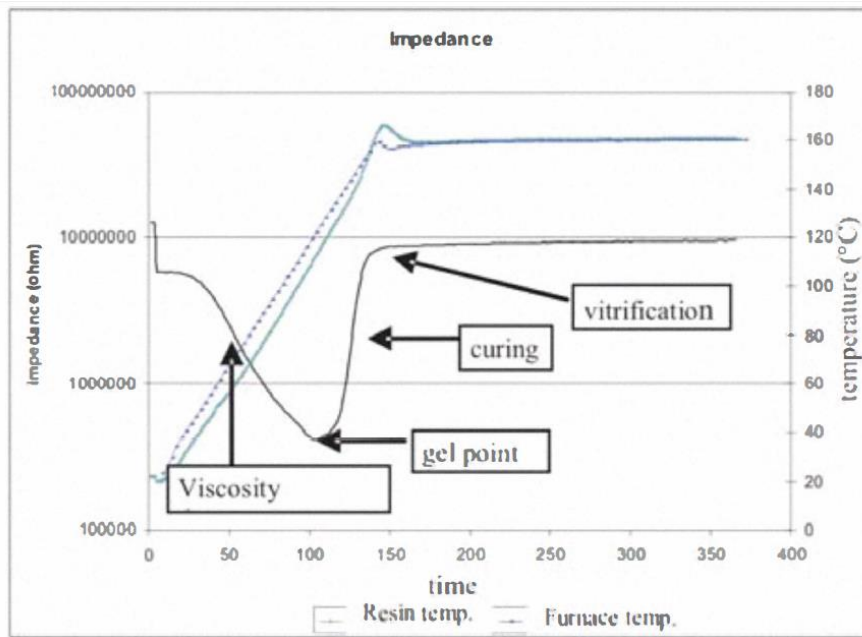


Figure 2-8 Impedance and sensor and chamber temperature under dynamic temperatures [29].

## 2.2 Epoxy Nanocomposites

### 2.2.1 The Concept of Nanocomposites

In 1984 the word “nanocomposites” was first defined by *Roy and Komarneni* [30]. The definition of nanocomposites is as follows: “A nanocomposite can be defined as a multiphase solid material where one of the phases has one, two or three dimensions of less than 100 nanometres (nm), or structures having nano-scale repeat distances between the different phases that make up the material” [31]. In other words, a nanocomposite is a material system that uses a matrix (such as resin, rubber, ceramics, and metal) as the continuous phase, and fillers (such as nano-sized metals, semiconductors, rigid particles, fibres, nanotubes, and other modifiers) as the disperse phase. These are uniformly dispersed in the matrix materials by a suitable preparation method.







As the properties of materials are changed once reaching the nano size, those materials (known as nanomaterials) always have unique optical, mechanical, thermal, magnetic, and electrical properties, which are different from ordinary materials. In the 1950s, the *Carter* group developed the method of reinforcing rubber elastomer by adding organic clay. In the 1970s, the *C. G. Granqvist* and *R.A. Burhrman* Group of the University of Cornell started to use the condensation method to prepare nanoparticles in the gas phase [32]. IBM developed the atomic



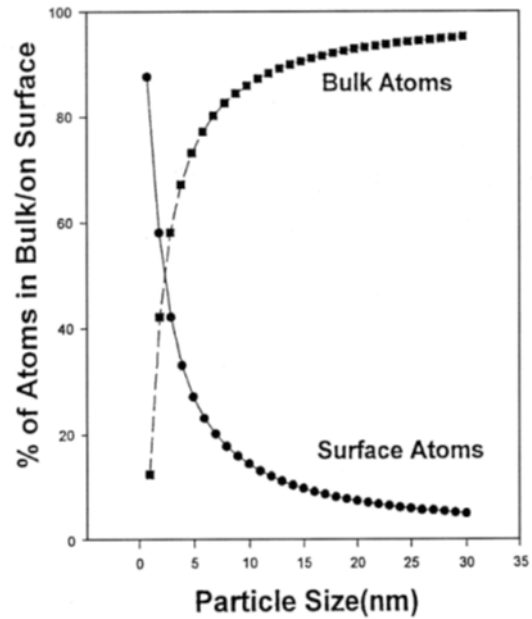
force and scanning tunnelling microscopes in 1981, which improved the development of nanotechnology. German scientist *H. Gleiter* successfully produced nano-size metal powders, which was followed by the study of nanometre-sized materials introduced in [33]. Owing to the unique properties of nanomaterials, which are mainly related to their specific surface area (SSA), the research has continued unabated in recent years [34, 35]. The SSA is the ratio between the mass of spherical particles and the surface area, as shown in Equation 2.3:

$$SSA = \frac{S_n}{m_n} = \frac{\pi \cdot d^2}{\frac{1}{6} \cdot \pi d^3 \cdot \rho_n} \quad (2.3)$$

where  $S_n$ ,  $m_n$ ,  $d$ ,  $\rho_n$ , and  $\pi$  are surface area, mass, diameter, density of particle, and a constant, respectively. It is clear that the specific surface area of the spherical particle is inversely proportional to the particle diameter, which is also shown by Figure 2-9 (a).

Full-shell Clusters		Total Number of Atoms	Surface Atoms (%)
1 Shell		13	92
2 Shells		55	76
3 Shells		147	63
4 Shells		309	52
5 Shells		561	45
7 Shells		1415	35

(a)



(b)

Figure 2-9 Relationship between surface atom number and size of particles [36].

In nanocomposites, the percentage of surface atoms will decline sharply due to particle diameter growth. For example, when the diameter of nanoparticles is 1 nm, the percentage of surface atoms is 99%. However, once the diameter increases to 5 nm, the percentage dramatically decreases to 30%, as shown in Figure 2-9 (b). Therefore, almost all the atoms will locate at the surface of particles when the diameter is small, which will result in surface atoms becoming much easier to connect to other atoms. Thus, particles with a high percentage of surface atoms,

which may lead to the high activity and unstable surface, tend to display some unique characteristics and high chemical activity. This is why it is important to consider the surface effect caused by nanoparticles, and this surface effect could become increasingly dominant as the particle size is reduced [37-39].

Therefore, nanocomposites may exhibit combined properties of the polymer matrix and nanoparticles. These combined properties are flexibility, processability, thermal resistance, and excellent mechanical characteristics. The physical properties of polymer/inorganic nanocomposites are potentially much better than conventional composites, and owing to the decreasing diameter of the particle, the surface area of nanomaterials, surface energy, and surface bonding energy would increase sharply [20].

### 2.2.2 Epoxy Nanocomposites

Because nanoparticles may reinforce epoxy properties, this phenomenon has attracted broad interest [13, 40, 41]. Further, because of the unique characteristics of nano-size fillers, nanoparticle reinforced epoxy resins display significant improvements in their properties [42, 43]. However, the introducing of nanofillers can sometimes result in a reduction of dielectric properties or insignificant changes [44, 45]. Some researchers believe that the improvements in properties of epoxy resins result from the surface effects of nanoparticles [2, 8]. The type of filler is also an important factor affecting the properties, and they must be chosen carefully. The nanoparticles introduced in this thesis are silica and boron nitride (BN), which are commonly used and relatively recently introduced, respectively. Compared with other particles, silica fillers have better insulation properties, good dielectric, and low thermal expansion coefficient [4]. Moreover, BN has higher thermal conductivity, which may potentially avoid thermal dielectric breakdown that could be required in some applications.

Some researchers have introduced these two fillers to obtain composites, and expected them to produce better properties. However, the presence of nano-sized fillers displayed no or significant improvement in the dielectric breakdown behaviour of epoxy resin composites. Similar results were also observed by *Imai et al.* (2006) [46], *Singha and Thomas* (2008) [34]. However, the addition of nanoparticles to epoxy resin significantly reduces the shape parameter ( $\beta$ ). This result is contrary to several other studies, including *Singha et al.* and *Nelson et al.* [41]. Moreover, *Wang et al.* found the surface treatment could modify the reduction of AC breakdown strength, and exhibited a higher value than pure samples in some

low filler loading concentrations (but remained worse in high loadings) [47]. He attributed this to the distribution of particles with relatively simple quantitative data.

Moreover, epoxy has the problem of absorbing water from humid ambient environments, and the loaded fillers could exacerbate or even lead to the formation of water shells, as studied by *Zou* et al. This is the result of free volume and hydroxyl groups on the surface of nanoparticles [48]. *Praeger* et al. remarked on the influence of hydroxyl groups on the SiO<sub>2</sub> surface, and displayed superior dielectric responses in calcined SiO<sub>2</sub> epoxy nanocomposites by reducing the water uptake [18]. *Lau* et al. studied the water absorption and dielectric response of polyethylene-based nanocomposites, concluding that surface treatment could reduce the water uptake and modify their dielectric properties. However, they did not link the data of water absorption and dielectric responses by mathematic methods [17]. Further, *Hosier* et al. studied the effects of water on the dielectric properties of PE nanocomposites, and based on this they simulated the water shell and resulting percolation. They concluded the dramatic effects of moisture compared to the dispersion of particles, and emphasised the importance of understanding and controlling environmental water during industrial practices [19].

Therefore, to fill the gaps found in previous research, this study mainly aims to investigate the morphology of dispersion of particles, and how moisture influences the dielectric properties of epoxy nanocomposites.

### **2.3 Particle Dispersion and Distribution of Epoxy Nanocomposites**

The mixing of particles in the composites has two aspects. The first is the dispersion of particles, which includes dispersing agglomerates into smaller aggregates and particles; the second aspect is the distribution of particles, which concerns the uniform distribution of small aggregates/particles in the polymers without influencing the size of particles [49]. When nano-sized fillers are dispersed into the epoxy resin to form composites, nanoparticles agglomerating with each other to form aggregates is unavoidable. Moreover, as a result of these interactions the dispersion is good. However, in most cases, poor dispersion was frequently observed in epoxy nanocomposites [4]. Thus, when considering dispersion, it is important to consider dispersion and distribution of particles/aggregates at the

same time. To prepare polymer nanocomposites with the high qualities of being well-dispersed and distributed, knowledge of which factors/interactions demonstrate obvious influences is required. Owing to the preparing methods and procedures, there will be many functional groups (such as “-OH”) on the surfaces of SiO<sub>2</sub> and BN, as shown in Figures 2-10 (a) and (b), or on the polymer chains, as shown in Figure 2-4 [50]. The interactions can be divided into coulomb forces, Van der Waals forces, hydrogen bonds, and covalent bonds. A list of bonding distances and energies of common bonds in the polymer is presented in Table 2-1 [51].

Table 2-1 Bonding distance and energy of common bonds in the polymer [51].

Bonding partners	Bonding distance in nm	Energy in kJ·mol <sup>-1</sup>
C-C (aliphatic)	0.154	350
C-C (aromatic)	0.140	560
C-H	0.109	413
C-O	0.143	351
C=O	0.122	708
C-N	0.147	293
C-F	0.131	485
N-H	0.102	389
Si-O	0.164	444
dipole-dipole	0.5-0.8	2-12
hydrogen bond	0.5-0.8	3-25
dispersion forces	0.5-0.8	0,3-4

Once the fillers are dispersed into the polymer matrix, the main interactions can be divided into intramolecular and intermolecular. The intramolecular interaction can be further divided into interactions between the intra-polymer chain, inter-polymer chain, and intra-filler particle. Among these three interactions, the intra-polymer chain covalent is dominant, which may determine the properties of the matrix. The other two interactions (formed via hydrogen) are usually weaker than the covalent ones, and do not play a significant role in influencing the properties of nanocomposites.

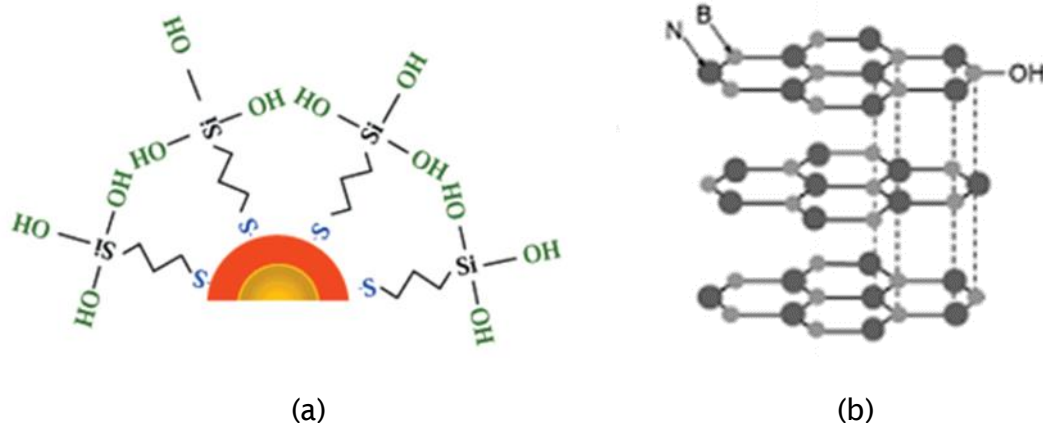


Figure 2-10 Hydroxyl group on the surfaces of SiO<sub>2</sub> and BN nanoparticles.

Among the forces of intermolecular interactions, the forces between aggregates/particles are the main factors that affect agglomeration. Once dispersed into the polymer matrix, the particles tend to move and have a chance of colliding with each other. Consequently, electrons of each nanoparticle start to avoid collisions by moving, which will lead to a non-uniform charge density distribution of nanoparticles and the formation of instantaneous dipoles. The Van der Waals forces will result in the attractions these dipoles, and thus, large agglomerations of aggregates/nanoparticles. Moreover, when the nanoparticles are placed in the liquid medium, the surface of aggregates/nanoparticles could be charged as a result of surface group dissociation or charge absorption. The charged aggregates/particles will attract charges with opposite signs from the surroundings. The region surrounding the surface of charge is known as the electrical double layer (EDL), as shown in Figure 2-11 [9]. At this stage, the Coulomb force (electrostatic force) performs a different role and repulses the aggregates/particles from each other. The combined effect of both the Van der Waals attraction force and the Coulomb repulsion force (which depends on the distance between aggregates/nanoparticles), is the key factor that determines the stabilisation of dispersion and distribution of nanoparticles [4].

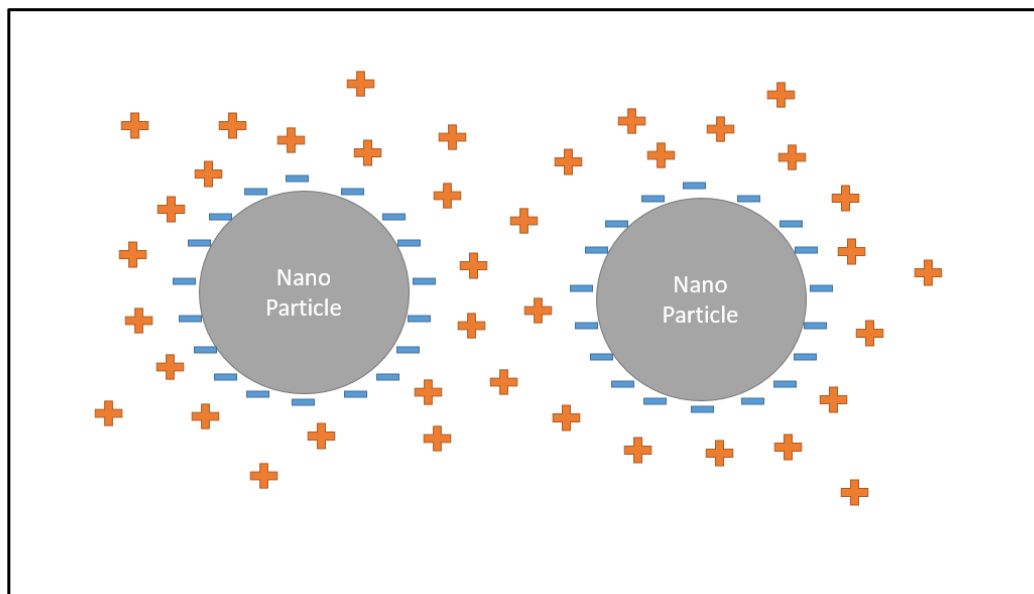


Figure 2-11 Electrical double layer between nanoparticles.

The second main intermolecular interaction resulting in agglomeration is the force between the polymer matrix and nanoparticles. As discussed in section 2.2.1, large specific surface area nanoparticles can result in high surface energy. Owing to the non-solvent system of resulting composites that contains a low ionic concentration, the Coulomb repulsion force is weak. The surface of atoms tends to interact with others and form agglomerations. Moreover, in epoxy nanocomposites, once nanoparticles are dispersed into epoxy, polymer chains and particles can form covalent bonds and interfacial regions [52, 53]. The interfacial region covers the surfaces of nanoparticles where epoxy matrix and hardener molecules are contained. If the formation of covalent bonds is not sufficient, there will be many functional groups left (such as hydroxyl groups), which will result in attraction among aggregates/particles by hydrogen bonds, and thus, agglomeration.

Uniform dispersion and distribution can be achieved if the interaction force between aggregates/nanoparticles and the polymer matrix is sufficiently strong [4]. To achieve good dispersion and distribution of nanoparticles, various mechanical and chemical methods have been developed. The purpose of the mechanical method is to reduce the interaction between the nanoparticles, thereby reducing agglomeration and modification of the surface of the nanoparticles by applying mechanical stress. Most of these methods are achieved by high-speed mixing and ultrasonic dispersion. In particular, the ultrasonic dispersion method has become increasingly popular in recent years. By applying ultrasonic waves to the mixture, the interactions will be reduced, resulting in relatively uniform

dispersion and distribution. However, it is important to note that the high energy of ultrasonic waves will result in the high surface energy and activity of nanoparticles. These are two main factors that can lead to re-agglomeration. Therefore, the energy and duration of the ultrasonic method should be controlled to a certain value to avoid new agglomeration. In this study, the high-speed mixture and ultrasonic dispersion method are both applied using a magnetic stirrer and probe sonicator, respectively, to obtain better dispersion and distribution.

## 2.4 Models for Polymer Nanocomposites

### 2.4.1 Dual Layer Model

Because the interfacial region has different properties from both nanoparticles and the polymer matrix (due to the interaction between the two phases), Dual layer model has been proposed by *Tsagarapoulos* et al. to help understand the behaviours of polymer nanocomposites. A schematic diagram of the dual layer model is shown in Figure 2-12 [54].

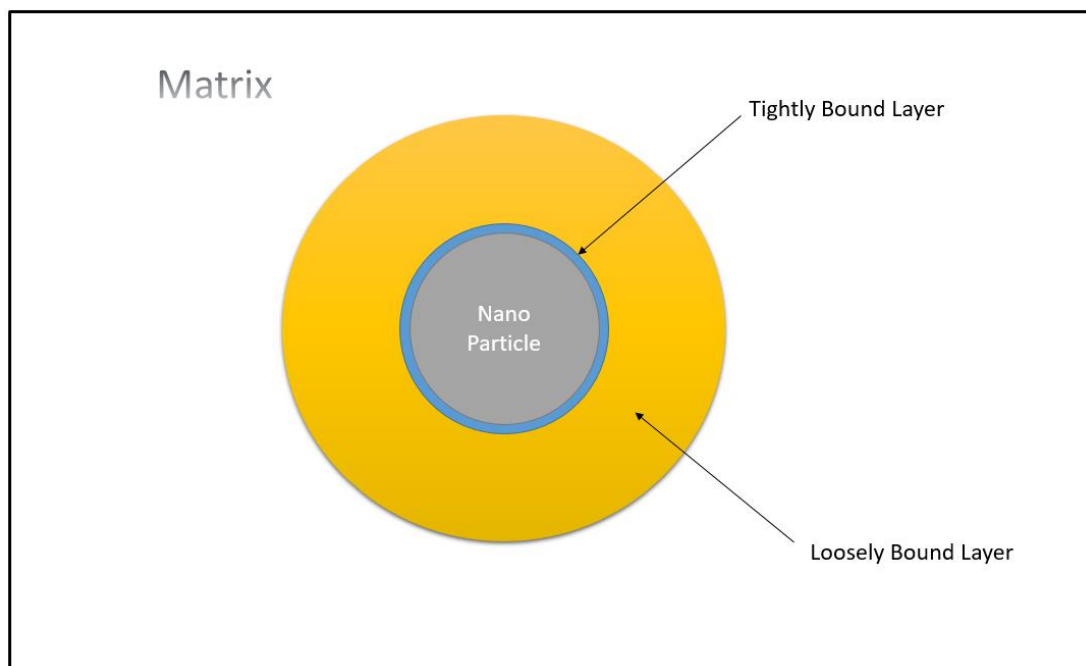


Figure 2-12 Schematic of the Dual Layer Model.

In this model, the interfacial area between nanoparticles and the polymer matrix has been divided into two different layers [54, 55]. The inner layer that covers the nanoparticle surface is formed by the tight bonds between polymer chains and the surface of nanoparticles, which are highly restricted. Therefore, the inner layer is also termed the “tightly bound layer”. The outer layer is termed the “loosely bound

layer”, which means the bonds are looser than ones in the tightly bound region. Moreover, this layer is thicker than the tightly bound one. According to these two factors, the polymer chains have higher mobility and allow charge carriers to move in and through more easily.

## 2.4.2 Multi-core Model

Based on the intensity model by *Lewis*, and dual layer model by *Tsagarapoulos* et al. [9, 54], *Tanaka* proposed a multi-core model, as shown in Figure 2-13 [56]. In this model, it is assumed the spherical nanoparticles are uniformly distributed in the base polymer materials, and the interface area between nanoparticles and polymer matrix can be classified into three different layers. The interphase thickness can range from 10–30 nm [56]. The first layer (bonded layer), which is closest to the surface of the nanoparticles, is a bonded layer consisting of molecules that are tightly bound to the nanoparticles surface by covalent, van der Waals, or hydrogen bonds. The thickness of this layer is generally to be approximately 1 nm [56]. The second layer is a bound layer containing polymer with a thickness assumed to be between 2 and 9 nm [56]. The third layer is a loose layer consisting of bulk polymer chains with different chain mobility, which is confirmed by the particles. An EDL, discussed previously, is also formed in the interface region. An effect of this electric double layer is that the opposite charge carriers are diffused outward from the interface region to the Debye shielding length.

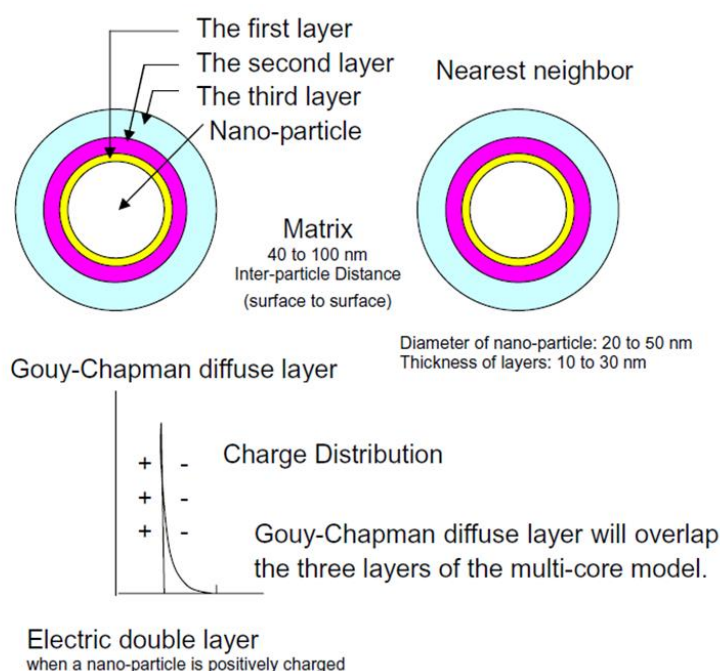


Figure 2-13 Schematic of multi-core model [56].



The multi-core model can provide an understanding of many dielectric phenomena observed in polymer nanocomposites. Moreover, the bound and loose layers are the main regions that affect the dielectric performance of polymer nanocomposites. The presence of the bound layer is believed to restrict the mobility of polymer chains and results in a decrease in permittivity. On the other hand, in the third layer, large free volumes are presented. The increase in charge mobility observed in some studies is also believed to be due to the presence of shallow traps in the loose layer [8].

### 2.4.3 Interphase Volume Model

The interphase volume model presented by *Rätzke* attempts to correlate the interfacial region with increased resistance of NC (nanocomposites) to electrical treeing, partial discharges, and HV-arcing [3, 57, 58]. It assumes that spherical particles with relatively constant average diameter are uniformly dispersed into the polymer structure, as shown in Figure 2-14.

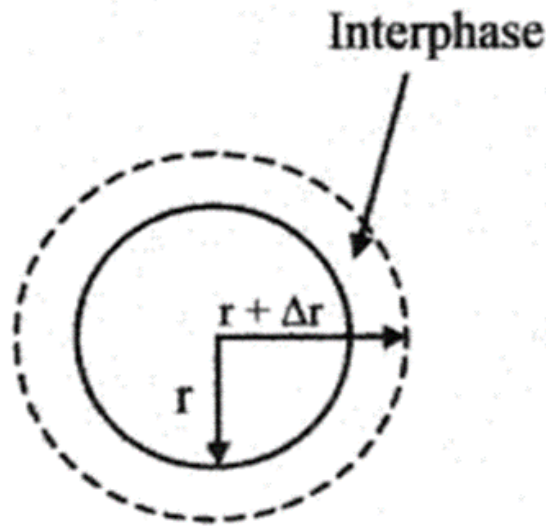


Figure 2-14 Illustrations of the interphase region surrounding the filler particles in a composite system [59].

It introduces a mathematical model based on a body-centred crystal lattice unit cell to identify the interface area fractional volume. The interphase region volume surrounding the particle can be calculated by Equation 2.4 [59] if the specific surface area of the filler is known, as follows:

$$\frac{\text{Interphase Volume}}{\text{Composite Volumes}} = (S_1 \cdot \Delta r) \cdot \rho \cdot \phi \quad (2.4)$$

where  $S_1$ ,  $\Delta r$ ,  $\rho$ , and  $\phi$  are the specific surface area of particles, the thickness of the interphase region, the density of particles and the filler volume fraction, respectively. Typically, the interphase thickness is determined by one molecular radius of gyration: ~5 to ~20 nm. The determination of the interphase thickness is described in more detail in [59-62].

Moreover, this model also introduces the overlapping of the interphase. The interphase overlap probability arises from the proximity of the individual filler particles [59]. Once the particles are close to each other, the interphase regions will be overlapped and result in a reduction of the volume fraction of the effective interphase. Therefore, the interphase overlap probability is a function of the filler volume fraction, interphase thickness, and the shape and size of the filler particles.

By using Monte Carlo simulations [63] or (alternatively) analytical solutions to percolation models [64-66], the approximations have been devised to estimate the overlapping of particles. Moreover, this model also illustrates the impact of the size of nanoparticles on nanocomposites, and explains the insignificant improvement of any property as the increase in filler loading concentrations, which are caused by the water absorption problem of nanocomposites.

### 2.4.4 Polymer Chain Alignment Model (PCAM)

The Polymer Chain Alignment Model (PCAM) by *T. Andritsch* et al. is based on experiments of epoxy-based nanocomposites, and the nanoparticles are all modified by a silane coupling agent (SCA) [12, 67]. It assumes that the material properties of nanocomposites strongly depend on processes prior to and during polymerisation [68], and all particles are spherical, the same diameter, and homogeneously distributed in the matrix. However, the hydroxyl groups of the SCA will be bonded to the surface of particles.

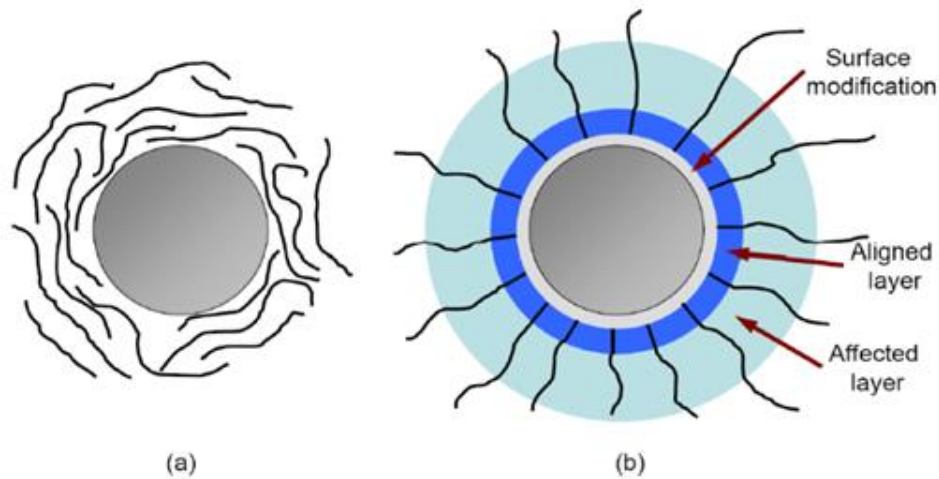


Figure 2-15 Particle surface with and without surface modification in PCAM [68]:

(a) Particle without surface modification and thus only weak interaction with the host; (b) Particle with a layer of surface modification, resulting in a layer of aligned polymer chains, further affecting the surrounding area, thus restructuring the polymer.

Once added, the curing agent will attract the epoxy groups, which may result in polymerisation of the polymer chains and silane coupling agent on the particle surfaces [69]. Moreover, each molecule of silane coupling agent will react with one polymer chain. Owing to the intermolecular forces, resulting chains will then align perpendicular to the particle surfaces, as shown in Figure 2-15 (a), and a particle has low interactions with the matrix without any modification. However, a particle with modification will demonstrate restructuring of the surrounding matrix. Therefore, a layer of aligned chains will form, as shown in Figure 2-15 (b). Because the polymer matrix often contains long chains, an affected layer will also form surrounding the aligned layer. In addition, the morphology of this model will be introduced in a later section.

#### 2.4.5 Water Shell Model

A “water shell” model was introduced to describe how water exists in epoxy nanocomposites. In this model [9, 48], a nanoparticle acts as a ‘core’. Around the ‘core’, the water in nanocomposites can form a shell-like surface, as shown in Figure 2-16, and may be divided into two layers. The first layer of water (~ 5 water molecules, 0.28 nm per water molecule) could be firmly bound to the hydroxyl groups on surfaces of nanoparticles. In the second layer, water could be loosely bound by Van der Waals forces.

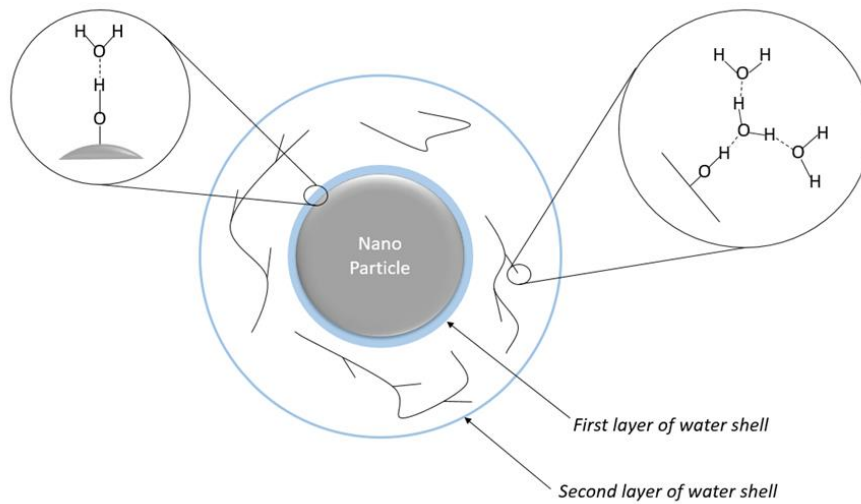


Figure 2-16 Schematic of the Water Shell Model.

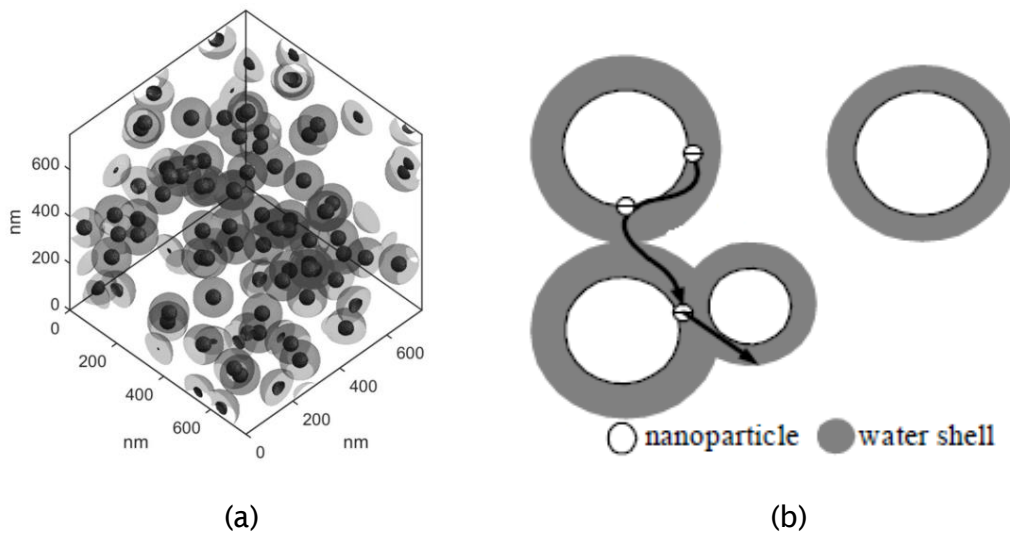


Figure 2-17 (a) Water shells in numerical modelling results [19]; (b) charge carrier transport through overlapped areas of water shells [70].

A study from *Hosier et al.* showed a simulated water shell with thickness  $\sim 50$  nm in  $\text{Si}_3\text{N}_4$  nanocomposites, with a percolation path (shown in dark grey) that can provide the paths for charges and carriers [19], as shown in Figure 2-17 (a). In this case, conducting-like (QDC behaviour) will occur at low frequencies based on the water shell model. The first and second water layers are likely to provide a channel for charge carriers to traverse, as shown in Figure 2-17 (b). Beyond the grey part, the water is lower concentration, which would not be conductive. According to the research and assumptions in the multi-core model, it can be assumed that the first layer of water shell might be overlapped with bonded layer mentioned in the multi-core model, and its second layer might be overlapped with the bound and loose layers.

## 2.5 Interfacial Characteristic

### 2.5.1 Inter-particle Distance and Surface Area

The dielectric properties of polymer nanocomposites can be enhanced because of an increase in specific surface area, or a decrease in inter-particle distance. When no significant agglomeration of particles can be observed, an assumption of ideal distribution of spherical nanoparticles can be made. According to this assumption, all particles will remain a certain distance from each other. With this homogeneous distribution of particles within the polymer host, the particles can be thought of as being arranged similarly to atoms in a crystal structure [57]. Therefore, a unit cell can be designed. This is the body-centred cubic (BCC), which describes the locations of particles on each corner and one in the centre (for polymer nanocomposites), as shown in Figure 2-18 (a). Both the inter-particle distance and the surface area have been calculated using the equation given by Rätzke [71].

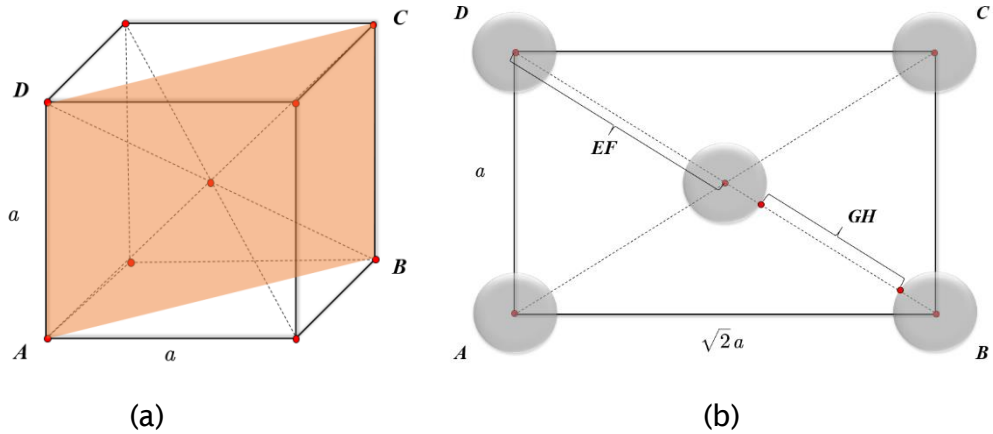


Figure 2-18 Illustration of the inter-particle and particle surface distance.

The cell length  $a$  is determined by the volume fraction of the nanoparticles  $p$  and filler sizes (as shown in Figure 2-18), described as follows:

$$p = \frac{V_{\text{Particles}}}{V_{\text{BCC}}} = \frac{\frac{\pi}{6} \cdot d^3 \left(1 + 8 \cdot \frac{1}{8}\right)}{a^3} = \frac{\pi \cdot d^3}{3 \cdot a^3} \quad (2.5)$$

Thus,

$$a = d \cdot \sqrt[3]{\frac{\pi}{3 \cdot p}} \quad (2.6)$$

## Chapter 2 Literature Review

According to Figure 2-18 (b), the inter-particle distance  $D$  and surface distance  $D_s$  ( $EF$  and  $GH$ , respectively) as a function of particle diameter  $d$  and cell length  $a$  are described as follows:

$$D = \sqrt{2}a/2 \quad (2.7)$$

$$D_s = \frac{\sqrt{3}}{2} \cdot a - d \quad (2.8)$$

Moreover, the specific surface area per unit volume  $S$  of particles is derived as follows:

$$S = \frac{\left(\frac{1}{8} \cdot \pi d^2 \cdot 8 + \pi \cdot d^2\right)}{a^3} = \frac{2\pi \cdot d^2}{a^3} = \frac{6p}{d} \quad (2.9)$$

Equations 2.8 and 2.9 can also be expressed by nanoparticle weight percentage (wt%) and nanoparticles size  $d$ , which is described in the following equation ( $\rho_p$  and  $\rho_n$  are used for describing the specific gravity of the polymer matrix and the nanoparticles, respectively):

$$wt\% = 100 \cdot \frac{\frac{\pi}{3} \cdot d^3 \cdot \rho_n}{a^3 \cdot \rho_p}, \quad a = \left[ \frac{2}{\sqrt{3}} (D_s + d) \right] \quad (2.10)$$

Thus,

$$D_s = \frac{\sqrt{3}}{2} \cdot a - d = \frac{\sqrt{3}}{2} \cdot \left( \frac{100 \cdot \pi d^3}{3 \cdot wt\%} \cdot \frac{\rho_n}{\rho_p} \right)^{\frac{1}{3}} - d \quad (2.11)$$

$$p = wt\% \cdot \rho_p / \rho_n$$

$$S = \frac{2\pi \cdot d^2}{a^3} = \frac{3\sqrt{3} \cdot d^2}{4(D_s + d)^3} \quad (2.12)$$

Further, if wt%,  $\rho_p$  and  $\rho_n$  maintain a certain value,

$$D_s = (A - 1) \cdot d \quad (2.13)$$

and

$$S = \frac{2\pi \cdot d^2}{a^3} = \frac{3\sqrt{3} \cdot d^2}{4(D_s + d)^3} = \frac{3\sqrt{3}}{4 \cdot A^3 \cdot d} \quad (2.14)$$

where  $A$  is a constant and related to wt%,  $\rho_p$ , and  $\rho_n$ .

Clearly, the particle surface distance between any two nanoparticles is proportional to the particle diameter, and the surface area per unit volume is inversely proportional to the particle diameter [4]. Moreover, the previous equations can be used to calculate the inter-particle surface distance and the surface area of nanoparticles. The inter-particles surface distance can be quantified experimentally by measuring graphs obtained by transmission electron microscopy [67]. According to the results, nanoparticles have significantly larger surface area than microparticles. Therefore, it is necessary to consider the influence of inter-areas on the properties of polymer nanocomposites.

### 2.5.2 The Volume and Overlapping of Interface Region

Before calculating the volume of the interface region, it is necessary to discuss the characteristics of the interface. Based on the PCAM, there will be two layers in the interface region: the aligned layer (inner layer), and affected layer (outer layer), as discussed in section 2.4.4. The intermolecular forces will be dominant once nanoparticles are dispersed into the polymer matrix, and are essentially constant within each particle, although they might vary with inter-particle distance [35, 72]. Therefore, these forces will attract predominantly parallel alignment of chains to the surface of particles, which will result in semi-crystalline structures around the particles. This area is the rigid polymer structure (RPS), and the degree of semi-crystallinity will decrease with increasing distance to the surface of particles, as shown in Figure 2-19.

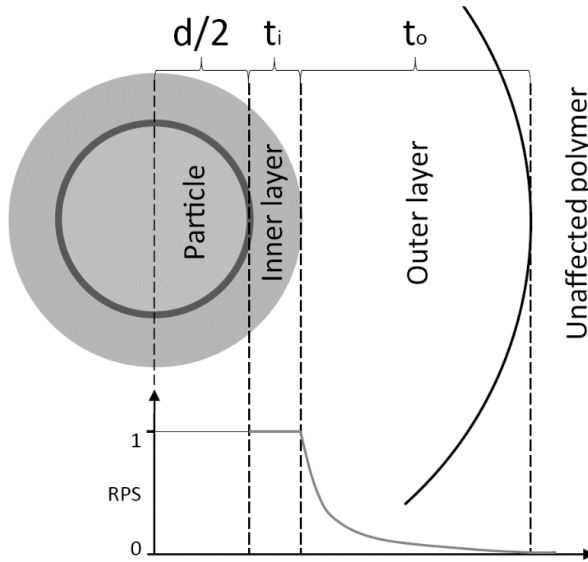


Figure 2-19 Illustration of how RPS changes from particle to surrounding polymer [68].

The equations for volumes of the inner and outer layers are also provided by PCAM, shown as follows

$$V_i = \frac{8\pi}{3} \left[ \left( \frac{d}{2} + t_i \right)^3 - \left( \frac{d}{2} \right)^3 \right] \quad (2.15)$$

$$V_o = \frac{8\pi}{3} \left[ \left( \frac{d}{2} + t_i + t_o \right)^3 - \left( \frac{d}{2} + t_i \right)^3 \right] \quad (2.16)$$

where  $t_i$ ,  $V_i$ ,  $t_o$ , and  $V_o$  are the thicknesses and volumes of the inner and outer layers, respectively. Generally, the thickness of particle layers will increase with decreasing average particle diameter  $d$ . Parameters  $t_i$  and  $t_o$  are determined by the chemical structure of the polymer matrix, surface of particles, and surface modification results of particles. Therefore, throughout Equations 2.15 and 2.16, it can be concluded that the two main characteristics of particles that determine the layer volume are the average particle diameter  $d$  and the volume fraction of particles  $p$  [68]. Moreover, as the volume fraction of particles  $p$  is related to the weight percentage via the density of nanoparticles  $\rho_p$ , weight percentage is also a very important characteristic that influences the layer volume. With increasing volume fraction of particles  $p$  and weight percentage, the interface region will increase proportionally. Moreover, the specific surface area of particles is inversely proportional to the average particle diameter, which is inversely proportional to the inter-two-layer thickness. Thus, a high specific surface area is related to a large interface region. The interface regions have different mechanical, chemical,



thermal, and insulating properties compared with the bulk materials, and have a significant influence on the overall properties of polymer nanocomposites [73].

Sufficient high volume fraction  $p$ , and significant small inter-particle distance  $b$ , will result in overlapping of layers in the interface region. If the inter-particle distance  $b$  fulfills the condition (Equation 2.17), it will result in outer layer overlapping. If fulfilling the condition (Equation 2.18), overlapping of the inner layer occurs, which only appears in very high weight percentage of particles.

$$2 \cdot t_i \leq b < (t_i + t_0) \quad (2.17)$$

$$b < 2 \cdot t_i \quad (2.18)$$

In polymer nanocomposites, if the aggregates/nanoparticles are uniformly dispersed in the base polymer materials, the inter-distance tends to be distributed according to the Poisson distribution [74]. In this case, and regarding evenly dispersed spherical nanoparticles, the probability of overlapping of the interface region of nanoparticles can be calculated by Equation 2.19 as follows:

$$P = 1 - \exp \left\{ - \frac{2(t_i + t_0)}{d} \right\} \quad (2.19)$$

where  $P$  is the probability of overlapping. For a given filler loading concentration, the probability of interface overlapping as a function of interface thickness over inter-particle distance is shown in Figure 2-20 [74].

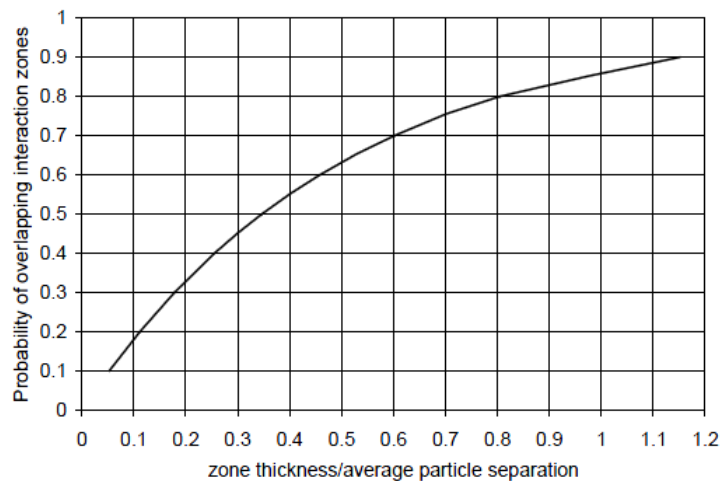


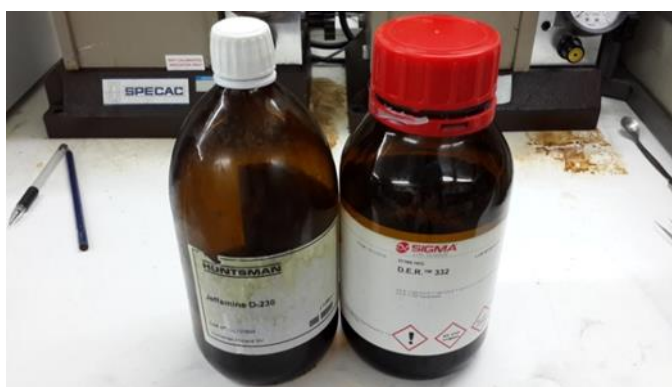
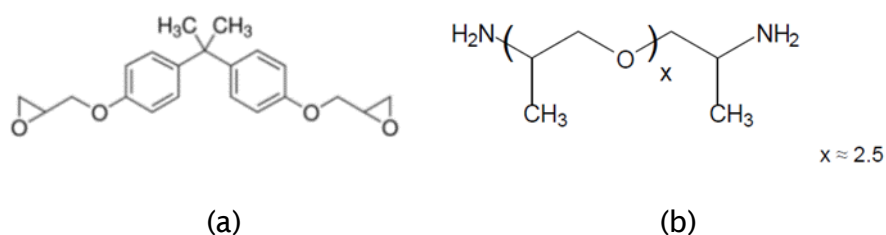
Figure 2-20 Probability of the interface region overlapping [74].



## Chapter 3 Sample Preparation and Experimental Methods

### 3.1 Materials

Samples were prepared using high purity bisphenol-A diglycidyl ether (D.E.R. 332, density  $1.16 \text{ g}\cdot\text{cm}^{-3}$ ) along with polyether amine hardener (JEFFAMINE D-230, density  $0.948 \text{ g}\cdot\text{cm}^{-3}$ ) supplied by Huntsman. The filler particles used in the present study are commercially available  $\text{SiO}_2$  and BN fillers. The average particle size (APS) of nano-silica and nano-BN is 20 nm. C8-treated Nano- $\text{SiO}_2$  was also used (this surface treatment is intended to eliminate hydroxyl groups on the surface of  $\text{SiO}_2$  nanoparticles). The chemical structures of both resin and hardener are shown below in Figure 3-1 (a) and (b) [75, 76]. The real materials are also shown in Figure 3-1 (c). A schematic diagram of nano-silica particles (with and without C8-treatment) is shown in Figure 3-2.



(c)

Figure 3-1 (a) (b): Illustration of chemical structure of D.E.R. 332 and JEFFAMINE D-230; (c) photo of experimental materials

The base resin was selected because of its high purity and low polymer fractions content. Moreover, D.E.R. 332 has low viscosity, low chloride content and light color. This epoxy resin offers better properties than standard bisphenol-A based

## Chapter 3 Sample Preparation and Experimental Methods

epoxy resins, particularly at elevated temperature (provided that certain cure conditions are met). Thus, it is mainly used in filament winding, electrical laminates and encapsulation applications.

Table 3-1 Product data of D.E.R. 332

<b>Bisphenol-A Diglycidyl Ether</b>			
<b>Colour</b>	Achromatic		
<b>Density at 25°C</b>	ASTM D-4052	(g·ml <sup>-1</sup> )	1.16
<b>Viscosity at 25°C</b>	ASTM D-445	(mPa·s)	4000 - 6000
<b>Epoxy content</b>	ASTM D-1652	(mmol·kg <sup>-1</sup> )	5710 - 5850
<b>Provided by</b>	Sigma-Aldrich		

Table 3-2 Product data of JEFFAMINE D-230

Polyether Amine Curing Agent		
Colour	pale yellow liquid with slight haze permitted	
Density at 25°C	g.ml <sup>-1</sup> (lb.gal <sup>-1</sup> )	0.948 (7.90)
Viscosity at 25°C	cSt	9.5
Provided by	Huntsman	

Table 3-3 Product data of nanoparticles

<b>Nanoparticles</b>				
	<b>Size (nm)</b>	<b>Structure</b>	<b>Shape</b>	<b>Provided by</b>
<b>Nano-SiO<sub>2</sub></b>	10-20 (BET)	Crystalline	Spherical	Sigma-Aldrich [77]
<b>C8-treated Nano-SiO<sub>2</sub></b>	10-20 (BET)	Crystalline	Spherical	Sigma-Aldrich, Pre-made by <i>Kwan Yiew Lau</i> [10]
<b>Nano-BN</b>	900 (APS) 200-500 (Crystal Size)	Hexagonal crystalline	Platelets	Momentive [78]

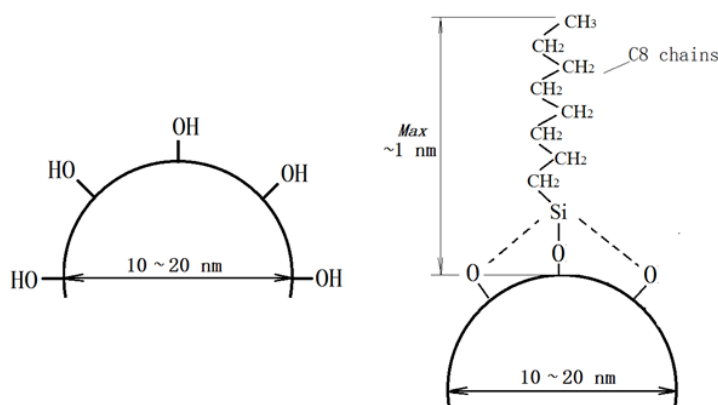


Figure 3-2  $\text{SiO}_2$  particles surface without (left) and with (right) modification.

Surface treatment of the nano-silica is performed using the following anhydrous route [17]. In a flask, 15 g of untreated nano-silica is suspended in 200 ml of dry tetrahydrofuran (THF), 7 ml of trimethoxy (octyl) silane (the silane coupling agent) is then added. At room temperature, the mixture is sonicated for 10 min, followed by stirring on a sealed rotary evaporator at 180 rpm for 20 min and subsequently 80 rpm for 40 h. During this time a fraction of the silane coupling agent reacts with the nano-silica surface; the unbound residue is then removed by using a solvent washing process. The resulting mixture is divided into flasks of equal weight which are centrifuged at 3500 rpm for 10 min. The supernatant (containing unbound coupling agent) is poured off and replaced with fresh solvent. Each container is then vigorously shaken until the nano-silica is again suspended in the solvent. The washing process is repeated three times with THF and two times with dry ether to remove. The resulting solid is washed from the containers into a round-bottomed flask. All solvent is then removed using a rotary evaporator before final drying of the white solid under high vacuum for 24 h.

## 3.2 Preparation of Epoxy Nanocomposites

### 3.2.1 Dispersion of Nanoparticles

The nanoparticles tested are nano- $\text{SiO}_2$  and nano-BN. As described in the literature review, the main methods of preparing epoxy nanocomposites are the heat blending method (performed here with a hot plate and magnetic stirrer) and the ultrasonic method (here carried out using a probe sonicator). The sample preparation devices are shown in Figure 3-3 and further details of the sample preparation method are given below:

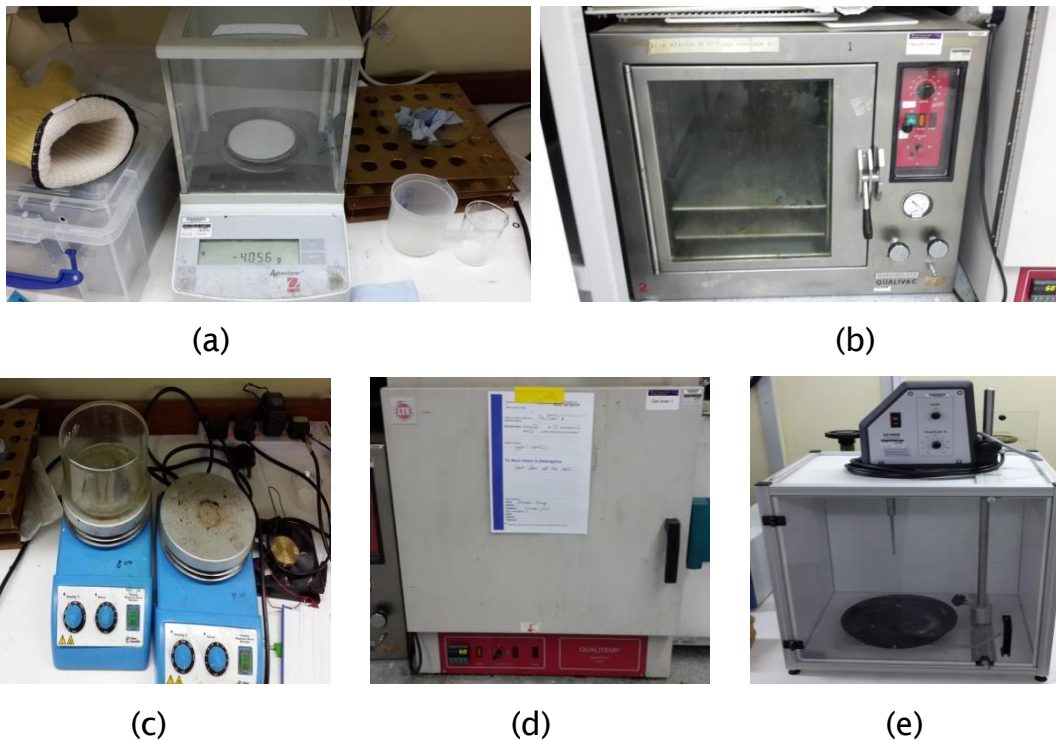


Figure 3-3 Sample preparation facilities: (a) scale; (b) vacuum oven; (c) electric magnetic stirrer; (d) fan oven; (e) probe sonicator.

1. In order to reduce its viscosity, the epoxy resin is heated to 50 °C in the oven.
2. The appropriate amounts of epoxy resin and hardener are weighed out and degassed separately using a vacuum oven (103 Pa, 50 °C for 15 min). The total amount of epoxy resin and hardener is 6 grams with a ratio of 1000:344. Therefore, the weights of the epoxy resin and hardener are 4.464 g and 1.536 g respectively.
3. The resin is injected into a small glass vessel that contains the weighed out nanoparticles this mixture is then stirred using a glass rod. (Dry nanoparticles are always handled inside a fume cupboard to prevent accidental exposure).
4. The nanoparticles are dispersed within the resin using ultrasonic vibrations from a probe sonicator at room temperature (cycle: 0.5; amplitude: 40% for 1 hour). Excessive heating from this process can lead to pre-curing or oxidation of the resin. This is avoided by holding the sample vessel in a water bath and replacing the cooling water every 15 minutes.
5. The mixture of resin and particles is combined with the hardener in a beaker. A magnetic stirrer is then used (600 rpm, 50 °C, for 15 min) with a heated water bath in order to keep the viscosity low.

6. The mixed solution is then put into a vacuum oven (103Pa, 50 °C) to degas for a further 30 min.

### 3.2.2 The Casting of Epoxy Films

The mould used for preparing epoxy resin composite films was designed by Dr. Steve Dodd from the University of Leicester. This mould consists of two metal plates which are bolted together as shown in Figure 3-4 (a) and a plastic film gasket that is positioned between the two plates as shown in Figure 3-4 (b). The gasket thickness defines the thickness of the resulting sample. Release agent QZ13 is uniformly wiped over the inner surfaces of the upper and lower plates. Care is taken to ensure that no excess release agent is left as this could affect the properties of samples. Resin (either with or without filler) is poured into one of the slots in the upper plate and the mould is then held at an angle. The resin flows (with the aid of gravity) through the mould with air and excess resin escaping at the lower slot. Once the mould is completely filled it can be held level during curing.

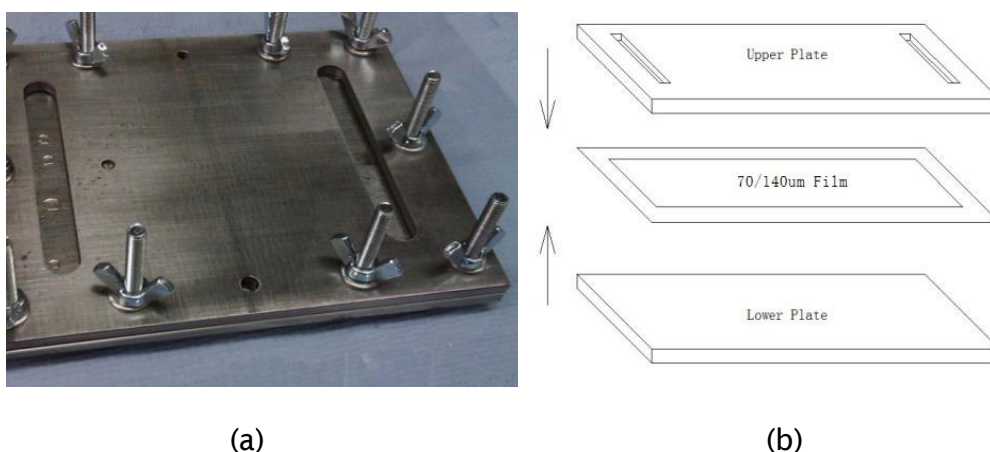


Figure 3-4 (a) Closed mould (Photograph); (b) Mould diagram showing gasket.

#### Improved Method:

It was found that many samples (especially those with high filler loading) did not flow through the mould due to their increased viscosity [43]. Consequently, a revised method has been involved where pressurised nitrogen gas is used to push the mixture through the mould [4]. In order to connect the gas supply a rubber plastic plate and a rigid plastic plate are installed over the resin filling slot as shown in Figure 3-5 (a).

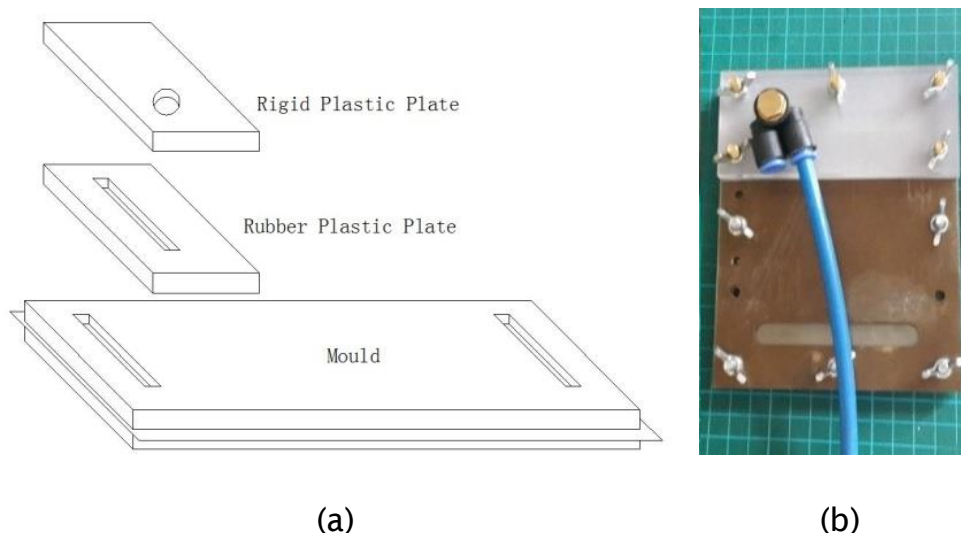


Figure 3-5 Revised mould for sample preparation.

1. The mould is assembled as before. At this point the mixture is ready to be poured into the mould for casting. The resin input slot is filled with the sample mixture and the gas connection plates and pipe are then connected to the mould. The nitrogen gas pressure is gradually increased and as before the mould is held at an angle so that gravity assists the flow of resin. Once the mixture is seen coming out of the other slot the gas regulator is closed and the pipe is disconnected. The sample is now ready for curing.
2. Once the mould is filled the epoxy can be cured by placing the entire mould in the fan oven at 120 °C for 4 hours (conditions previously established by *Zhiqiang Xu* et al. [79]).
3. The fan oven is then switched off and allowed to cool gradually; waiting 12 hours before the mould is removed.
4. The sample is then released from the mould and stored in a vacuum desiccator to keep it in a relatively dry condition.

### 3.2.3 Sample Composition

Table 3-4 provides details of the samples produced using the methods described above. In the sample code the following abbreviations are used: EP for epoxy resin, S for untreated nano silica composites, ST for treated silica, B for boron nitride and the number represents the filler loading. For example, EPS05 represents epoxy nanocomposites loaded with 0.5 wt% untreated silica.



Table 3-4 The coding of samples

Sample code	Type of particles	Theoretical loading concentration (Wt%)
EP0	N/A	N/A
EPS05	untreated SiO <sub>2</sub>	0.5
EPS1	untreated SiO <sub>2</sub>	1
EPS3	untreated SiO <sub>2</sub>	3
EPS5	untreated SiO <sub>2</sub>	5
EPST05	C8-treated SiO <sub>2</sub>	0.5
EPST1	C8-treated SiO <sub>2</sub>	1
EPST3	C8-treated SiO <sub>2</sub>	3
EPST5	C8-treated SiO <sub>2</sub>	5
EPB05	hBN	0.5
EPB1	hBN	1
EPB3	hBN	3
EPB5	hBN	5

### 3.3 Sample Analysis Methods

#### 3.3.1 Scanning Electron Microscopy (SEM)

It is known that the dielectric properties of polymer nanocomposites are strongly depended on nano-filler dispersion. One of the most commonly and widely used method to observe the surface of materials is the SEM due to its simplicity of system and ease of use when compared to TEM and AFM methods. It could be used to analyse the nano-filler dispersion in polymer nanocomposites at such magnifications. Thus, the SEM has been selected for this investigation. SEM was introduced by *Max Knoll* in 1935. It can observe the surface structure of materials down to the nanoscale. Through SEM, the morphology (size and shape of particles) and the composition of material can be observed. In SEM, an electron beam is created by the electron gun positioned at the top of the sample. The beam is focused onto the selected area of the sample surface. The electrons could penetrate the sample up to 1  $\mu\text{m}$  and experience a multiple scattering, resulting in a subsequent interaction that can be detected. The interaction is usually secondary electrons that can escape from the upper 50 nm of the sample (for polymer) due

## Chapter 3 Sample Preparation and Experimental Methods

to their low energy ( $\sim 30$  eV) and result in much higher resolution. The resulting image of secondary electrons is highly sensitive to the surface topology of materials, if the surface topography can be used to represent the internal morphology, the internal morphology of the material can be observed [4].

In my thesis, an EVO 50 scanning electron microscopy was used shown in Figure 3-6. The gun voltage was set to 15 kV with a working distance of 7-12 mm. All samples had been coated with gold before the test by the Emitech K550X sputter coater at 25 mA for 3 min for each sample.



Figure 3-6 EVO 50 scanning electron microscopy.

### 3.3.2 Thermogravimetric Analysis (TGA)

Thermogravimetric analysis (TGA) is a thermal analysis method. When the temperature changes, the mass loss of the sample is measured with time/temperature. This measurement provides information about physical phenomena, such as phase transitions, absorption and desorption and chemical phenomena which includes chemisorption, thermal decomposition and solid gas reaction (such as oxidation or reduction) [80]. In most cases, TGA is used to evaluate the thermal stability of the material including polymers [81-83]. Within the desired temperature range, if a species is thermally stable, there will be no observable mass change. However, once the temperature is beyond the threshold, mass loss will be presented on TGA traces. Through analysis by TGA, the maximum use temperature of a material can be provided.

TGA was performed on a Perkin-Elmer Pyris 1 thermogravimetric analyser as shown in Figure 3-7. Samples with a mass of around 2-5 mg were tested by measuring the weight loss under air gas flow of  $20 \text{ ml min}^{-1}$  at a rate of  $10 \text{ }^{\circ}\text{C}\cdot\text{min}^{-1}$  from 50 to  $850 \text{ }^{\circ}\text{C}$ .



Figure 3-7 Perkin-Elmer TGA 7 thermogravimetric analyser.

### 3.3.3 Differential Scanning Calorimetry (DSC)

Thermosetting materials are those that are irreversibly hardened during the curing process; the curing reaction may require the material to be held at elevated temperature [84]. The chemical formulation or composition and conditions (e.g., temperature and time that the resin is exposed to) will determine the properties of a thermosetting material. In order to avoid production problems, thermal characterisation of thermosetting resins should be undertaken as this is often very useful. For polymer dielectric materials, once the temperature reaches the glass transition temperature ( $T_g$ ), a significant change is observed in the dielectric properties of the material. Therefore, it is necessary to know the glass transition temperature and in order to use it to do further study on materials. Differential scanning calorimetry (DSC) is a good and popular method to analyse the properties of the unreacted material and the cured end products. For example, DSC can characterise changes in the physical state of a material, such as crystallisation, melting and glass transition, which lead to the enthalpies that can be detected by DSC [85, 86].

$T_g$  is not a certain temperature, but a temperature range, this is because the glass transition encompasses a range of processes which combine to produce a significant change in the mobility of the polymer chains. Ultimately the  $T_g$  is determined by factors including the chemical structure of the epoxy resin, the hardener and the cure degree. A diagram of a DSC trace featuring a glass transition is shown in Figure 3-8. Temperature is plotted on the x-axis and the heat flow (sometimes as heat capacity) is plotted on the y-axis. As  $T_g$  is a temperature range, one can define an onset temperature for the glass transition  $T_{ig}$  and the end temperature of the glass transition,  $T_{eg}$ . Generally, the midpoint of the temperature range is reported and used to represent the glass transition temperature [87].

" $T_{ig}$  is the temperature at the intersection of the straight line formed by extending the baseline on the low-temperature side to the high-temperature side and the tangent drawn to the curve showing a stepped change of glass transition at the point of the maximum gradient.  $T_{eg}$  is the temperature at the intersection of the straight line formed by extending the baseline on the high-temperature side to the low-temperature side and the tangent drawn to the curve showing a stepped change of glass transition at the point of maximum gradient", as shown in Figure 3-8 [28].

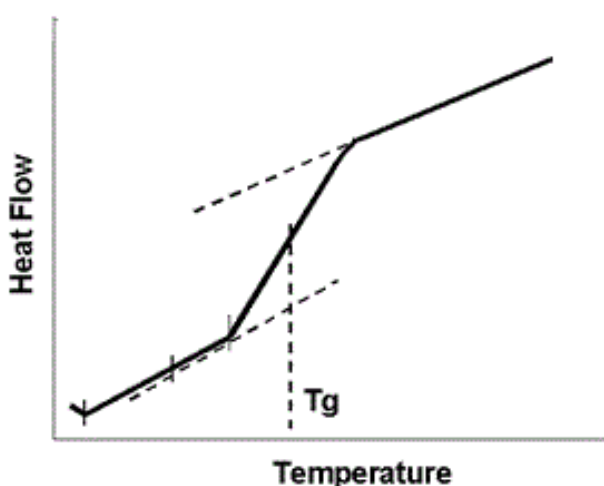


Figure 3-8 Illustration of Glass Transition Temperature.

That is to say  $T_g$  is equal to the average of  $T_{ig}$  and  $T_{eg}$ .  $T_g$  spans a temperature range, rather than occurring at a specific temperature, due to the cross-linked polymer chains having multiple degrees of freedom and modes of polymer chain

movement in response to any applied thermal energy. The  $T_g$  value can also vary depending on its cure degree and is proportional to it. Generally, the reported  $T_g$  is based on fully cured materials.

### 3.3.4 Differential Scanning Calorimetry Technique

The basic principle of DSC technology is heating and measuring the difference in heat flow between the sample and reference with the increase or decrease of temperature. If some physical state change occurs in the sample material, its heat flow will change relative to the stable reference which shows as exothermic or endothermic peaks on the curve. For example, when a material changes its state from solid to liquid, a peak corresponding to the melting temperature is produced. Since melting is an endothermic process, the sample requires higher heat flow in order to follow the same temperature profile as the reference, the DSC trace, therefore, shows an endothermic peak. Figure 3-9 shows a schematic diagram of DSC.

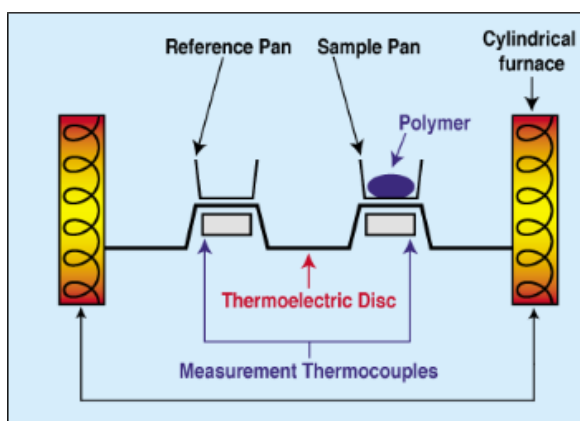


Figure 3-9 Schematic diagram of DSC [4].

The DSC instrument can measure heat flow changes of a sample under heating, cooling or isothermal conditions. DSC measures the quantitative heat flow which can be plotted either directly as a function of time or against the sample temperature. This heat flow-temperature data can provide useful information about thermosetting materials including: glass transition or softening temperature, onset and completion of glass transition and cure, the heat of cure, the maximum degree of cure, percent cure and heat capacities ( $C_p$ ).

Analysis of the properties listed above can be helpful for manufacturers or users of thermosetting resins. For example, for quality assurance testing, the establishment of optimal processing conditions, estimating the cure degree of end

### Chapter 3 Sample Preparation and Experimental Methods

products, verifying product integrity and for comparison of alternative materials [88]. In this project, a power-compensated Perkin-Elmer DSC 7 was used with a nitrogen gas feed. This system was controlled by Perkin-Elmer Pyris software which was also used for data analysis. The DSC 7 system is shown in Figure 3-10.



Figure 3-10 Differential scanning calorimetry device.

Samples with a mass of approximately 5 mg (between 4.8 mg and 5.2 mg) were prepared for DSC testing by sealing them in an aluminum can. An empty aluminum can (also sealed) is used as the reference. The reference aluminum and the sample are placed into separate compartments inside the DSC. Control electronics inside the DSC ensure that the sample and reference materials follow the same temperature profile. The difference in heat flow into the two cans is measured as a function of temperature or time by DSC.

The melting temperature of indium is known to be very stable at 156.6 °C. An indium sample was therefore used to calibrate the temperature axis of the DSC measurements. Care must be taken during these measurements as rate of temperature change can affect the calibration.

In this project, for each loading concentration and particle type, five samples were taken from uniformly spaced locations on the moulded film. The selected rate of temperature change was 10 °C·min<sup>-1</sup> for all the measurements. As given in the datasheet, the glass transition temperature of D.E.R. 332 used in this project is around 85 °C, therefore, for all the measurements, the temperature was swept from 40 °C to 150 °C.

### 3.3.5 Experiment Set-up of AC/DC Breakdown Test

The electrical breakdown strength of epoxy composites is an important factor for many industrial applications. Therefore, it is necessary and essential to study the extent that the presence of nanofillers influences the breakdown strength of epoxy-based nanocomposites. The AC breakdown test was performed with apparatus based on ASTM standard D149-87. The schematic diagram of this kit is shown in Figure 3-11. A photograph of the breakdown kit used in this project is also shown in Figure 3-12. The breakdown strength of epoxy samples was measured by the ramp testing method. The process was simply to apply a 50 Hz AC voltage with linearly increasing RMS magnitude to the tested sample. The voltage is increased from 0 kV at a rate of  $0.05 \text{ kV}\cdot\text{s}^{-1}$  until breakdown occurs. At breakdown, sound and arcs could usually be observed. The breakdown strength  $E \text{ (kV}\cdot\text{mm}^{-1}\text{)}$  is related to the thickness of the sample film and can be calculated by the following Equation 3.1:

$$E = V_{BD}/d \quad (3.1)$$

Respectively,  $V_{BD}$  and  $d$  are the breakdown voltage and the sample thickness.  $d$  can be measured using a micrometer.

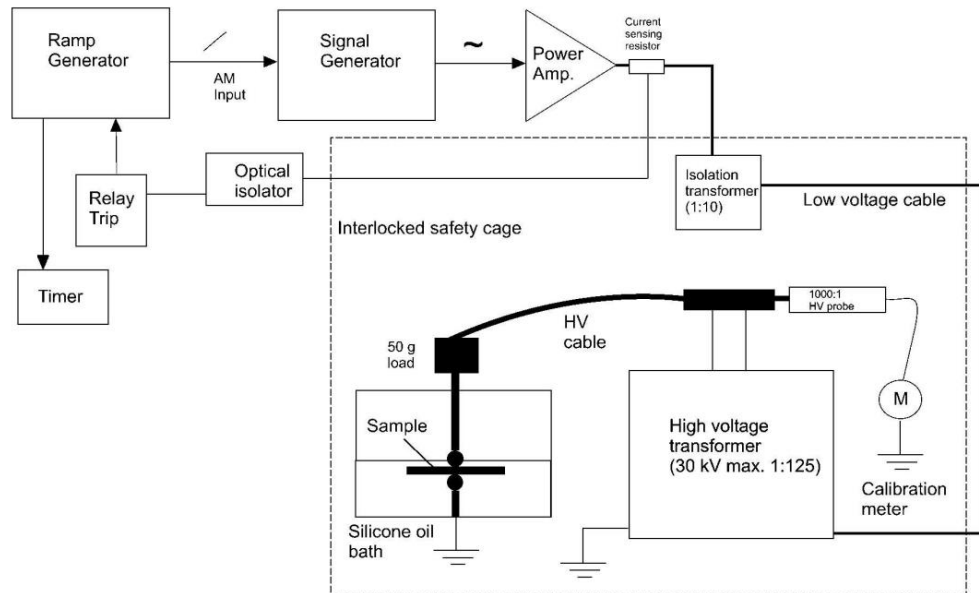


Figure 3-11 Schematic of AC breakdown device [89].





Figure 3-12 AC dielectric breakdown kit.

Samples with greater than 200  $\mu\text{m}$  thickness cannot breakdown because the upper limit of voltage for the kit (25 kV) does not produce a sufficiently high electric field within the sample. Epoxy resin films with approximately 70  $\mu\text{m}$  thickness were used in this test. Since the thickness of the epoxy sample films varies slightly, testing points (25 in total) were uniformly spaced over each epoxy film. The thickness at each test point was measured with a micrometer before the breakdown. During the measurement, the sample film is immersed in silicone oil and held between two steel ball bearings with a diameter of 0.635 cm as shown in Figure 3-13. It has been found that about 15 breakdowns will cause pitting on electrodes [4]. Therefore, during the test, the ball bearings were changed after every 10 breakdown tests.

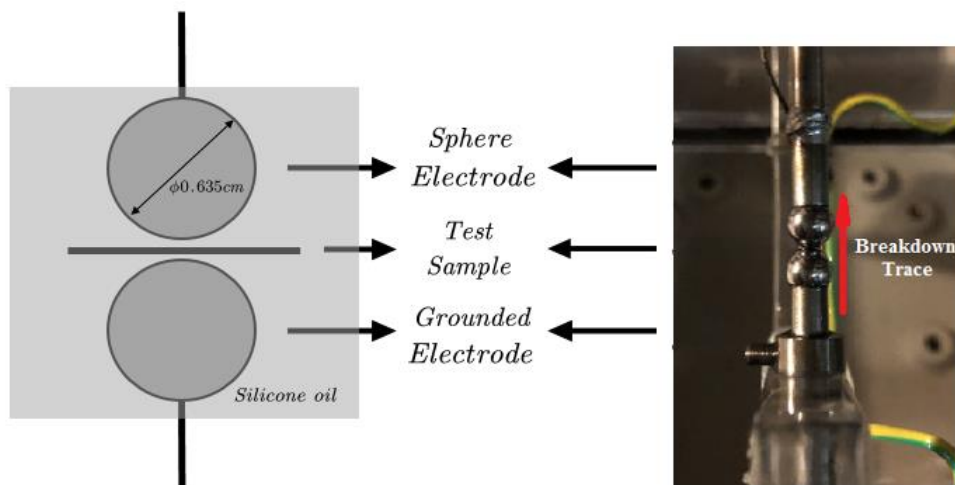


Figure 3-13 Illustration of the ball bearing electrodes used for breakdown measurements.



DC breakdown strength was measured with a ramp of  $100 \text{ V}\cdot\text{s}^{-1}$ . The test points selected were uniformly distributed on each sample with a total of 25 breakdown measurements being collected for each type of sample. The average thickness of the samples is  $\sim 70 \text{ }\mu\text{m}$ . All of the samples were visually checked after breakdown testing and they all had a puncture hole caused by the breakdown.

In this project, measurements of the breakdown strength of epoxy resin and its nanocomposites were made in order to study the effect of inorganic nanofillers, the differences between different particle types and between different filler loadings of the same particles. All the experiments were carried out at room temperature.

### 3.3.6 Dielectric Spectroscopy Measurement

Dielectric spectroscopy is a method to measure the dielectric properties of materials as a function of frequency [90]. The magnitude of the applied electric field and the temperature can also be variables in this type of measurement. Dielectric spectroscopy is based on the interaction of the electric dipole moments within the sample and provides dielectric properties of materials [91], such as relative permittivity and loss factor that can reflect the mobility of polymer chains. Thus, dielectric spectroscopy has been widely carried out to study material structures. A schematic diagram of a dielectric spectroscopy measurement is shown in Figure 3-14.

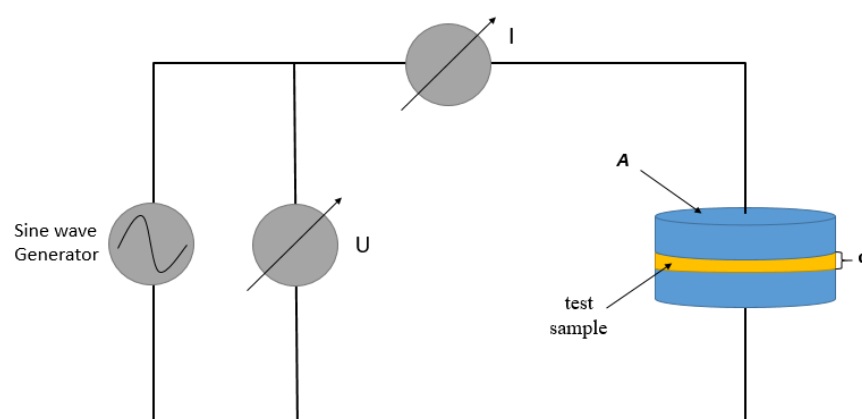


Figure 3-14 Schematic diagram of a dielectric spectroscopy measurement.

Dielectric spectroscopy measurements were made over the frequency range from  $10^{-2}$  to  $10^5$  Hz using a Solartron 1260 Analyser and 1296 Dielectric Interface. Measurements were taken at 293, 313 and 333K (20, 40 and 60 °C)  $\pm 1$  K using the

system shown in Figure 3-15. During testing the samples were placed between two disc-shaped electrodes each with a diameter of 32 mm. The thickness of the samples is  $145 \pm 10 \mu\text{m}$ . A voltage of 1 V RMS was used. The accuracy of real capacitance values is  $<2\%$  (typical) according to the instrument manual.

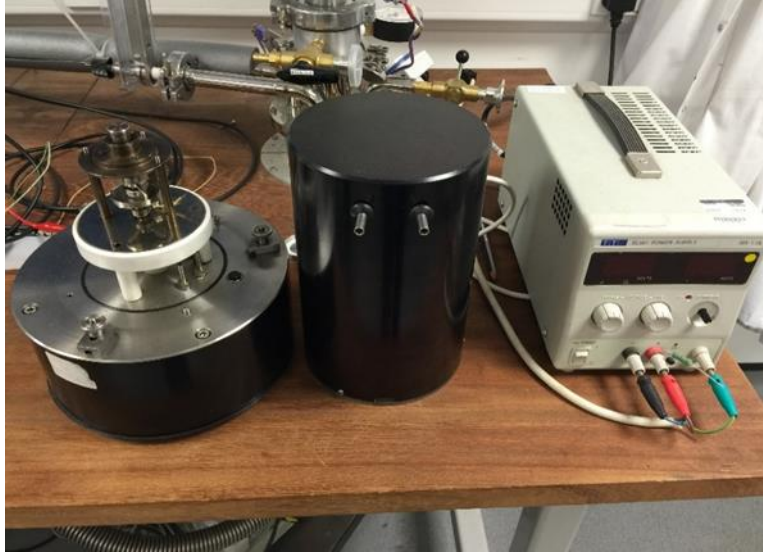


Figure 3-15 Test cell and temperature control system.

### 3.3.7 DC Conductivity Measurement

In this project, DC conductivity measurements were carried out on samples that were pre-conditioned in different humidity environments. Before DC conductivity testing the thin film samples were sputter coated with gold to create electrodes on both sides with a diameter of 30 mm. The sample was then placed between two parallel electrodes (20 mm in diameter) and a voltage between 5 and 6 kV was applied in order to achieve an average electric field of  $\sim 40 \text{ kV}\cdot\text{mm}^{-1}$  inside the sample. A Keithley 6487 pico-ammeter was used to measure the current through the specimen as a function of time, the DC conductivity was then calculated from this data by software running on the experiment control computer. The thickness of each sample is  $145 \pm 10 \mu\text{m}$ . All the tests were carried out at  $20^\circ\text{C}$  under ambient RH conditions.

### 3.3.8 Space Charge Measurement

In this project, PEA was used to measure the space charge distribution in the samples [92]. The principle of the PEA measurement is to apply a short pulse voltage across the sample and then to record the acoustic vibrations that are

caused by the motions of space charge that is distributed within the sample. This is shown diagrammatically in Figure 3-16.

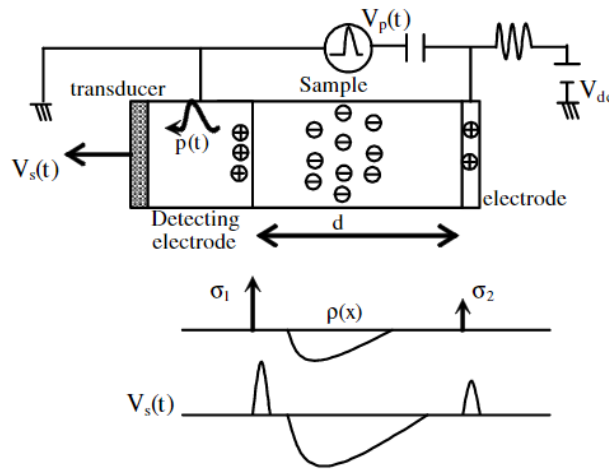


Figure 3-16 Illustration of PEA method [93].

In the PEA measurement, the dielectric sample is clamped between two electrodes. In order to help propagation of the pressure wave signals silicone oil is applied at the interfaces between electrodes and the samples. A dc voltage is applied to the sample (causing a gradual accumulation of space charge), the PEA signal waveform is then measured by repeatedly applying a short pulse voltage  $V_p(t)$  to the sample. The space charges experience an acceleration due to the electric field and a sound wave is produced with an amplitude that is proportional to the local charge density. This sound wave propagates through the samples and is detected by a piezoelectric sensor. The piezoelectric sensor transforms the acoustic wave into an electrical signal that is recorded on an oscilloscope as a function of time. The schematic diagrams of the PEA system and photographs of the PEA system used in this project are shown in Figures 3-17 and 3-18 respectively.

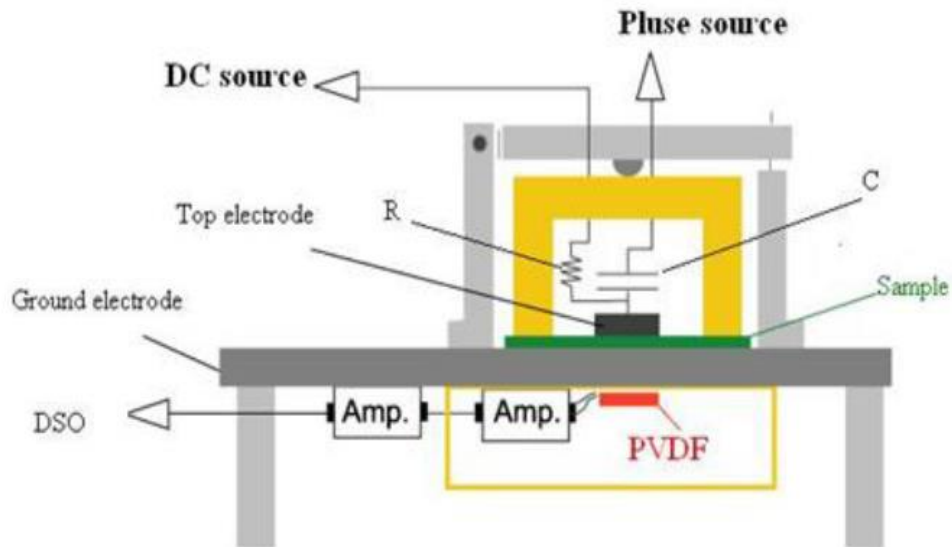


Figure 3-17 Diagram of the pulsed electro-acoustic (PEA) system [4].

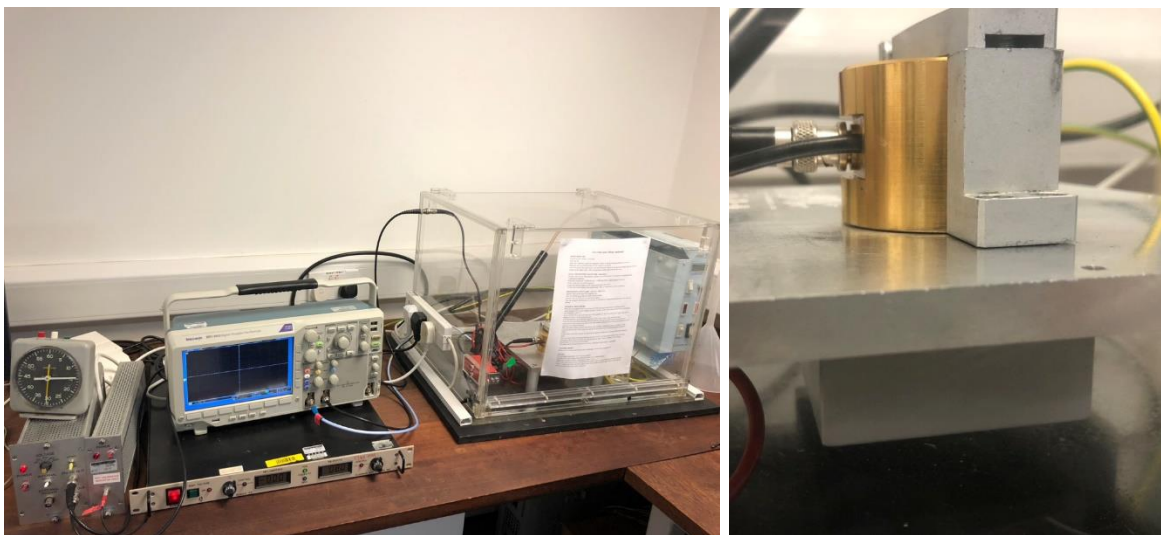


Figure 3-18 Photographs of the PEA system used in this project.

### 3.4 Humidity

Water absorption has a huge effect on the dielectric properties of polymers, this should, therefore, be considered when polymer dielectrics materials are used as insulators [15, 16, 19, 48, 94, 95]. Water absorption occurs in any humid environment and results in an overall deterioration in dielectric properties. The maximum amount of water absorbed by epoxy resins can be as high as several weight percent. Due to free volume and hydroxyl groups at the surface of nanoparticles, absorbed water in epoxy nanocomposites tends to locate at the

interface between the polymer matrix and the nano-sized fillers [4] the additional trapped moisture further increases total absorption.

### 3.4.1 Humidity Control

There are four relative humidity conditions in the test.

1. All dry samples were held in the vacuum oven (103 Pa, 60 °C, for 72 h) and then stored in a vacuum desiccator with dried silica gel at 293 K.
2. Ambient Humidity (A.RH): These samples were exposed to the laboratory environment for 10 days where temperature and RH were controlled at 293 K and  $(36.1 \pm 6.7) \%$ .
3. 60% RH: These samples were stored in a RH controlled chamber at 293 K, where actual RH is in the range from 56 to 62%.
4. Saturated: These samples were immersed in de-ionised water for 10 days before testing at 293 K.

The TGA traces, shown in Figure 3-19, of EP0 shows there is a weight loss of 1.92% in saturated one which is almost same with gained weight% (1.86%) obtained from the later experiments, and the initial decomposition temperature (5 wt% loss ignoring the loss of moisture) of dry and saturated samples are 389.31 °C and 385.23 °C. That is to say the samples were relatively dried before and all other samples were conditioned and stored under the same method.

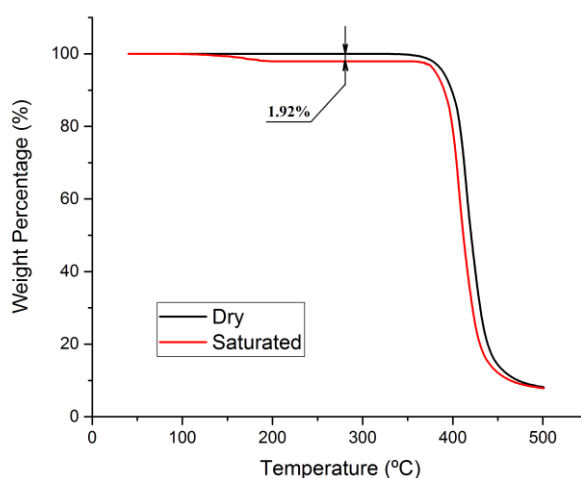
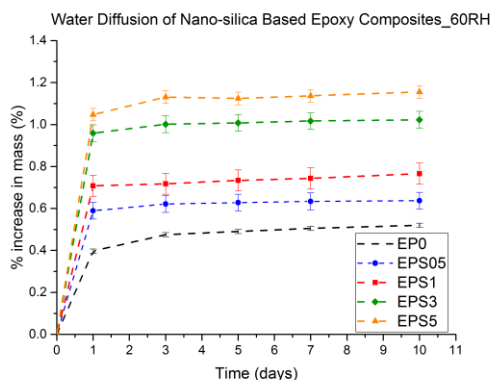


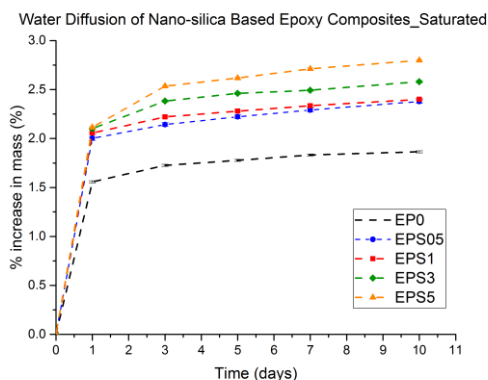
Figure 3-19 TGA traces of dried and water saturated pure epoxy samples.

## 3.4.2 Water Diffusion in Samples

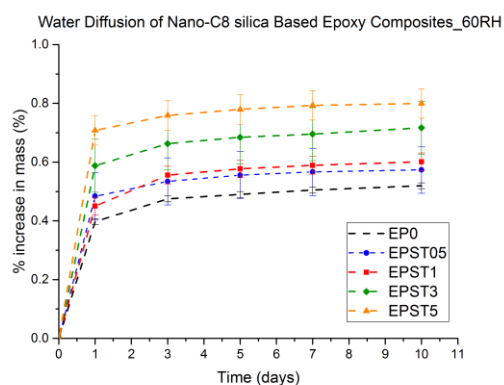
Water diffusion in epoxy and its nanocomposites was measured at 293 K (20 °C).



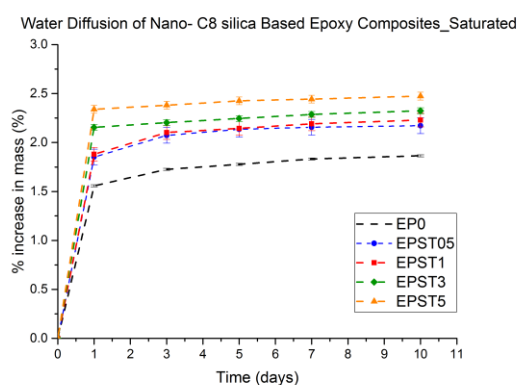
(a)



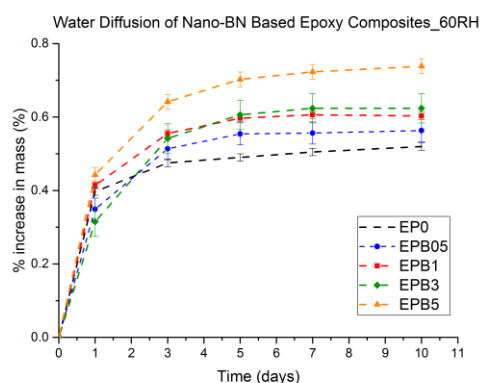
(b)



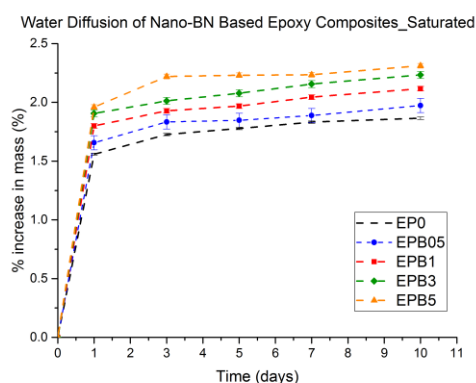
(c)



(d)



(e)

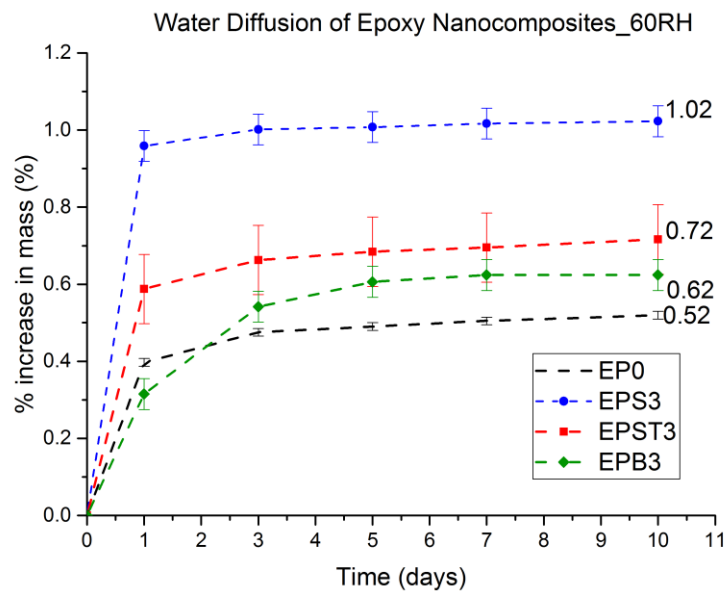


(f)

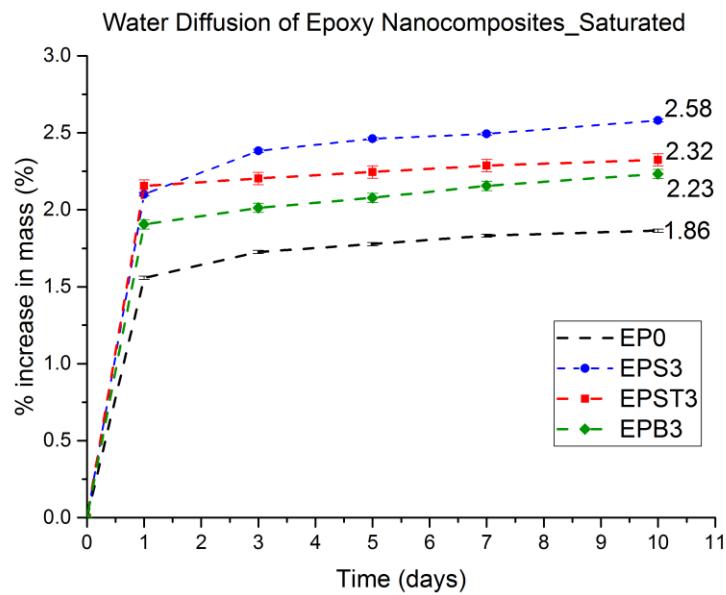
Figure 3-20 Water diffusion of EP0, EPS, EPST and EPB samples (a) EPS, 60% RH; (b) EPS, Saturated; (c) EPST, 60% RH; (d) EPST, saturated; (e) EPB, 60% RH; (f) EPB, saturated, 293K.

The samples were held in a humid environment but were periodically removed and weighed using a microbalance. The measurements were continued until the weight becomes stable. This took about 10 days in both the 60% RH and totally saturated

environments. The water diffusion into epoxy and its nanocomposites is shown in Figure 3-20 (expressed as the percentage increase in mass versus time). Most of the mass change occurs on the first day of the experiment; this is true for all of the samples at both 60% RH and saturated. Water diffusion reaches a quasi-equilibrium after three days. Samples with higher filler loading clearly undergo a larger increase in mass; the presence of nanoparticles, therefore, seems to increase the moisture holding capacity of the samples. In order to study the influence of filler type on the diffusion process, the data from all of the of 3 wt% samples at both 60% RH and saturated is compared in Figure 3-21.



(a)



(b)

Figure 3-21 Water diffusion in epoxy and its nanocomposites of 3 wt% loadings  
(a) 60% RH; (b) saturated, 293K.

As shown in Figure 3-21 (a), both the EPS and EPST samples reach their quasi-equilibrium state more quickly than the EPB samples. This may be caused by the fact that  $\text{SiO}_2$  particles are more hydrophilic than BN ones. The lower equilibrium state of EPST samples probably indicates the effective removal of hydroxyl groups by the surface treatment. Unfilled epoxy (EP0) exhibits the lowest mass change. This confirms that adding nanoparticles provides additional sites for physical adsorption of moisture which cannot be completely removed by surface treatment or that the elimination of surface hydroxyl groups from the nanoparticles is incomplete. Comparison between Figure 3-21 (a) and Figure 3-21 (b) shows that under saturated conditions most samples reach their quasi-equilibrium state on the first day and all the samples contain much more water on the 10th day compared to ones held in the 60% RH environment. Thus, it can be concluded that a higher RH environment helps water to diffuse into materials faster and results in a higher state of equilibrium.

### 3.4.3 Water Uptake in Samples

The water uptake,  $M_w$ , can be calculated by Equation 3.2:

$$M_w = \left| \frac{M_{wet} - M_{dry}}{M_{dry}} \right| \times 100\% \quad (3.2)$$

where  $M_{wet}$  is the weight of water absorbed samples and  $M_{dry}$  is the weight of dry samples. The increases in the mass of all epoxy samples in each humidity are shown in Figures 3-22 to 3-25.

As shown in Figures 3-22 to 3-25, water uptake in all samples increases with the relative humidity and filler concentration. However, under A.RH conditioning, the water uptake of all epoxy nanocomposites is very similar and close to that of the pure epoxy samples. Moreover, under A.RH conditioning there is little increase in water uptake with the growth of filler concentration. This could indicate that for low levels of moisture uptake, water can be absorbed into the matrix with the nanoparticles having little effect. This is contrary to the findings of Figure 3-21 where (under higher RH conditions) increased nanoparticle concentration clearly increases water absorption capacity. There are two main forms of water that appear in epoxy nano-composite samples: free water and bound water [70, 96, 97]. Free water must first permeate through the matrix in order to find sites where it can bind. The polymer matrix therefore has a certain capacity for free water and this capacity may be high enough to carry the majority of water under A.RH conditions.



As bonded water is formed prior to the relatively free ones [97], considering hydroxyl groups and interfacial areas introduced by nanofillers which would lead to more water, no obvious difference in A.RH conditions between pure epoxy and nanocomposites should indicate the present water is mainly bound to chains of the matrix. As the environmental RH is increased more and more free water will become bound at surface hydroxyl groups and interfacial areas introduced by nanofillers. Once the available sites for chemical bonding have been saturated a different kind of free water (loosely associated with the nanoparticle sites) can accumulate.

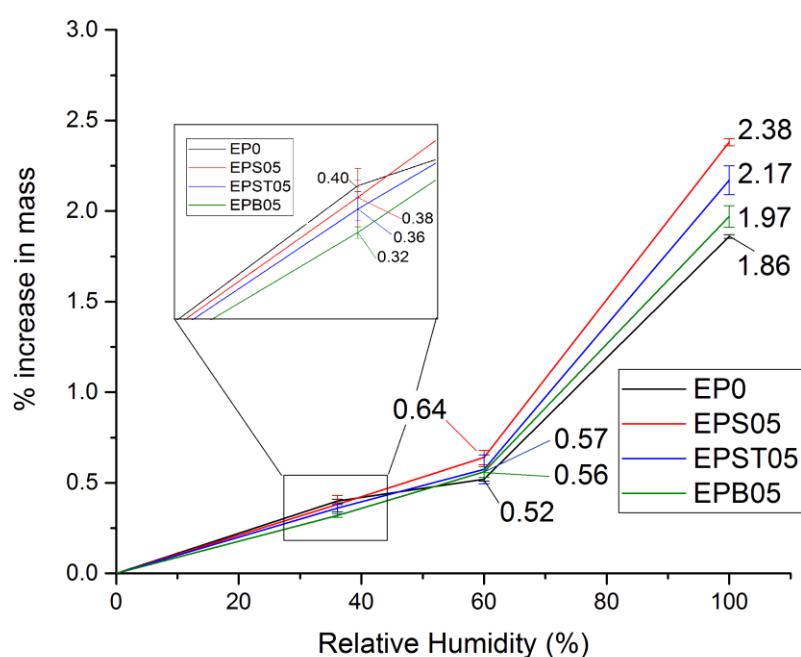


Figure 3-22 Water uptake of epoxy and its nanocomposites in 0.5 wt% loading concentration, 293K.

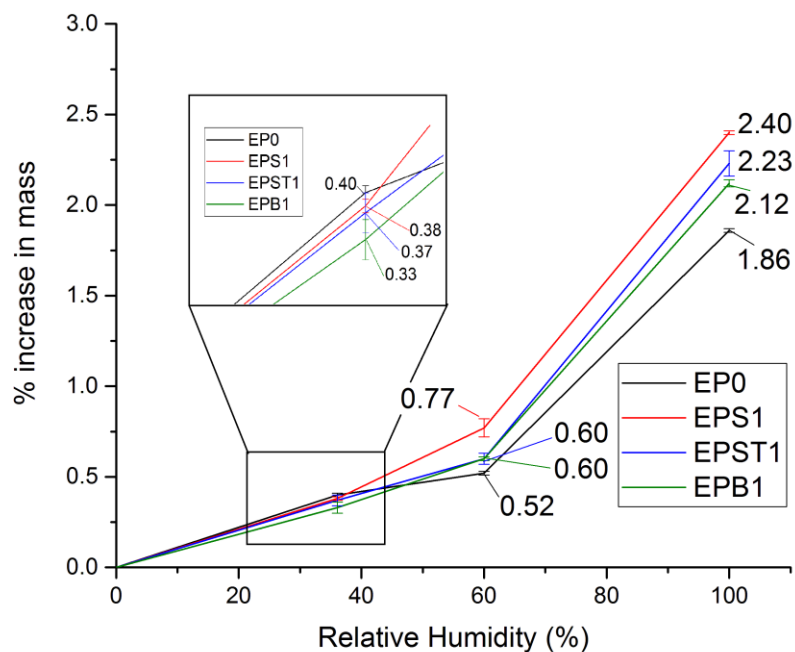


Figure 3-23 Water uptake of epoxy and its nanocomposites in 1 wt% loading concentration, 293K.

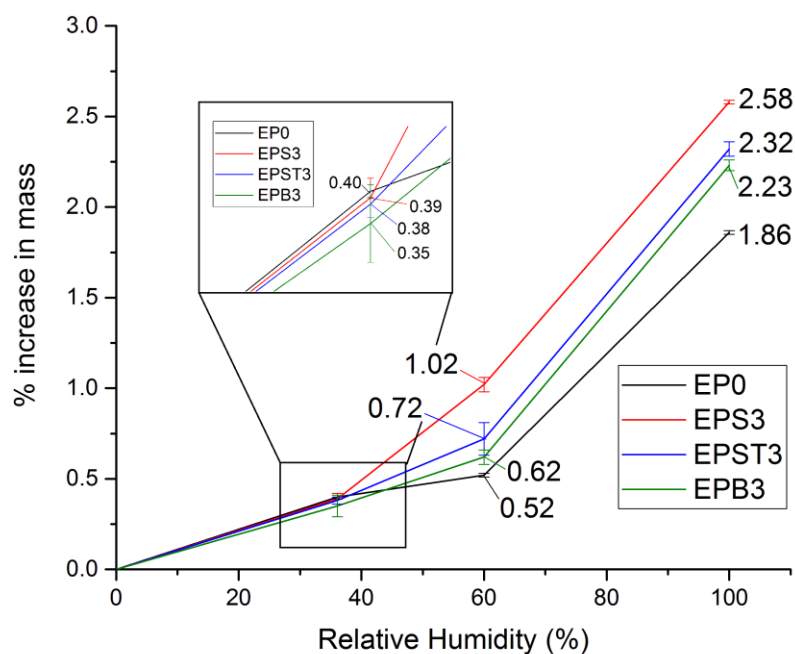


Figure 3-24 Water uptake of epoxy and its nanocomposites in 3 wt% loading concentration, 293K.

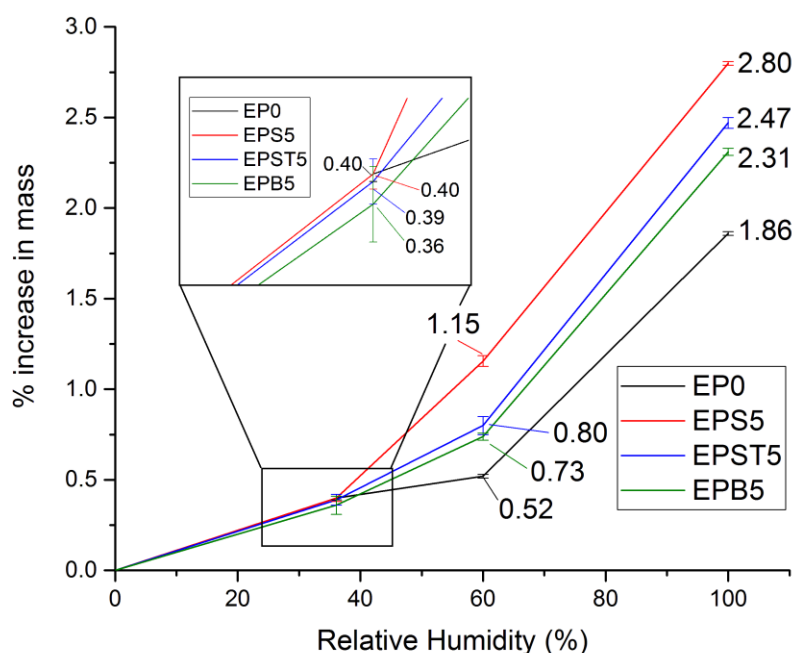


Figure 3-25 Water uptake of epoxy and its nanocomposites in 5 wt% loading concentration, 293K.

The behaviour is entirely different in 60% RH conditioned samples. There is more water present in all samples, with the highest levels being found in untreated  $\text{SiO}_2$  nanomaterials. Relative to the pure samples, EPS, EPST and EPB all have increased water uptake. In the case of the silica-based nanocomposites, this effect may be caused by increased free volume in the interfacial regions surrounding the nanoparticles. Here, the effects of surface tension make it favourable for water to accumulate [41] allowing the second layer of the water shell to form.

The increased water uptake of the EPS samples relative to the EPST ones can be attributed to higher availability of hydroxyl groups on the nanoparticle surfaces [70]. Although the EPST samples show a reduced amount of water bonded to their particle surfaces, they still exhibit higher water absorption than EPB and pure epoxy samples. The EPB samples have a higher moisture uptake than the pure epoxy ones. This may be for similar reasons to the increased free volume effect seen near to silica nanoparticles, however, differences exist due to the shape of the hBN nanoparticles. In other words, the morphology of the epoxy will be changed once hBN particles are introduced, this leads to stress concentration sites, that allow more water to accumulate due to initiation of cracks [98].



## Chapter 4 Morphology Characterisation of Epoxy Nanocomposites

### 4.1 Quantification Methods

The morphology and mixing state of particles in polymers is reported to affect the insulating properties of nanocomposites. Many researchers have, therefore, sought to achieve good mixing states by applying different treatment methods [49, 99]. *Kim* et al. identified two aspects that are key in understanding the morphology and mixing state of particles [49]. The first is the dispersion of particles; this involves reducing the size of agglomerations of particles with the aim of yielding well-separated individual nanoparticles. The second is the distribution of particles/aggregates; this is concerned with the uniformity of spreading of particles/aggregates throughout the polymer matrix. *Hui* et al. then quantified the mixing in nanocomposites with these two aspects by analyzing TEM images of XLPE nanocomposites [99]. SEM images are widely used for nanocomposite characterisation. However, most SEM analysis is based on imprecise descriptions. This chapter will apply quantitative methods and analysis to existing SEM images in order to relate morphological features to the dielectric/electrical properties.

#### 4.1.1 Equivalent Diameter

The following method can be used to evaluate the first aspect of particle mixing; dispersion. Most particles observed by SEM are not the primary ones but rather exist as aggregates. The degree of dispersion can, therefore, be related to the particle count of aggregates and particles [99]. In this research, equivalent diameter is chosen to estimate the dispersion degree as shown in Figure 4-1 and can be calculated via Equation 4.1 as below:

$$D_E = 2 \cdot \sqrt{A_a / \pi} \quad (4.1)$$

where  $D_E$  is the equivalent diameter and  $A_a$  is the measured area of aggregates.

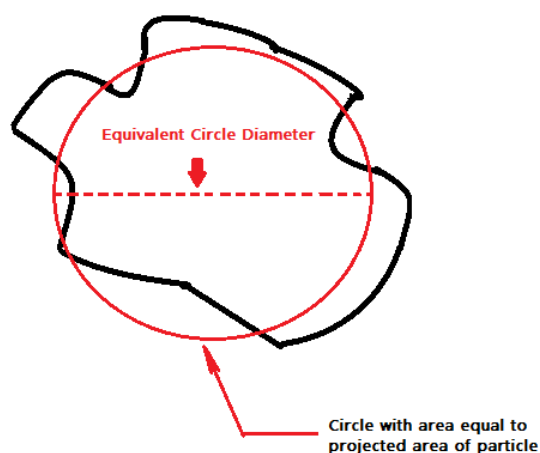


Figure 4-1 Illustration of the equivalent diameter of particles/aggregates.

The arithmetic mean of equivalent diameters is not precise enough for use as a measure of dispersion due to the variation of particle numbers in specific areas. Improved dispersion metrics can be obtained by considering the probability distribution of the equivalent diameter data which is to generate some squares as bins and then to collect numbers of into each bin based on the fulfillment condition of each square. The area of each square is proportional to the count numbers and a histogram can be generated according to the existing data as shown in Figure 4-2 which also includes the ideal Poisson distribution, shown by the red curve. The weighted average of equivalent diameter seems to be a good metric of the dispersion degree of particles in nanocomposites [100]. The standard deviation or the weighted standard deviation of the equivalent diameter data can also be used to evaluate the dispersion degree [99].

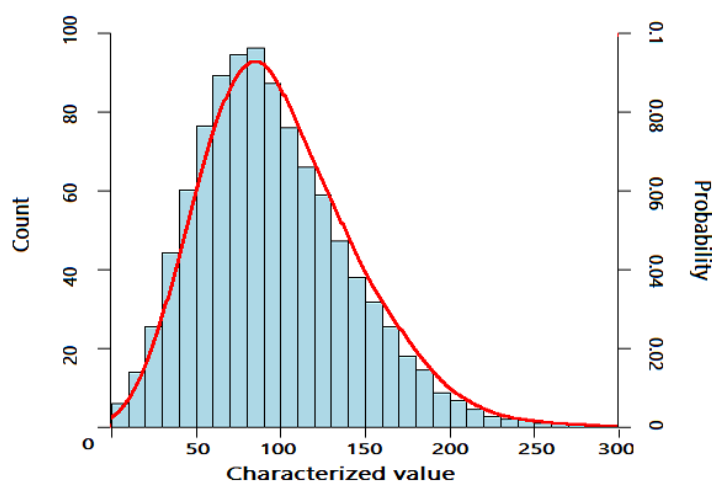


Figure 4-2 Histogram used to generate weighted average of equivalent diameter.

### 4.1.2 Nearest Neighbour Distance (NND) Method

The nearest neighbour distance (NND) method is based on a calculation of the distance between the centre of mass of each particle/aggregate and its nearest neighbour; it has been widely used by many researchers [101]. For an arbitrary particle/aggregate, the distance between this one and others can be calculated and sorted descendingly. In the resulting distances, the 1<sup>st</sup> nearest neighbor distance is usually used to estimate the distribution of particles/aggregates. Moreover, according to the discussion on the dispersion of particles, the 1<sup>st</sup> NND data is best interpreted via Histogram by evaluating the weighted parameters.

### 4.1.3 Quadrat-based Method

The Quadrat test of randomness is a widely used method to investigate the distribution of points in a specific area [102] and can calculate the deviation of particles/aggregates in different parts of polymer nanocomposites. The principle of the method is first to divide the area into equal quadrats of small size based on the scale of particle/aggregate [49]. Then the number of particles in each quadrat is collected and an index called skewness is calculated using Equation 4.2 below:

$$skewness = \frac{N}{(N-1)(N-2)} \sum_i^N \left( \frac{x_i - \bar{x}}{\sigma} \right)^3 \quad (4.2)$$

where  $N$  is total number of particles,  $x_i$  is the number of particles in  $i^{th}$  quadrat and  $\bar{x}$  and  $\sigma$  are the average and standard deviation of  $x_i$  respectively. As particles/aggregates would sometimes form vast agglomeration of particles/aggregates and leave most of the quadrats empty, only using 1<sup>st</sup> NND is not accurate enough. Non-zero values of skewness indicate non-uniformity of particle distribution, with higher values implying a poorer distribution of particles/aggregates.

## 4.2 SEM Images

### 4.2.1 Original Images

The SEM images of pure, EPS, EPST and EPB samples with different filler concentrations are shown in Figures 4-3 to 4-18.

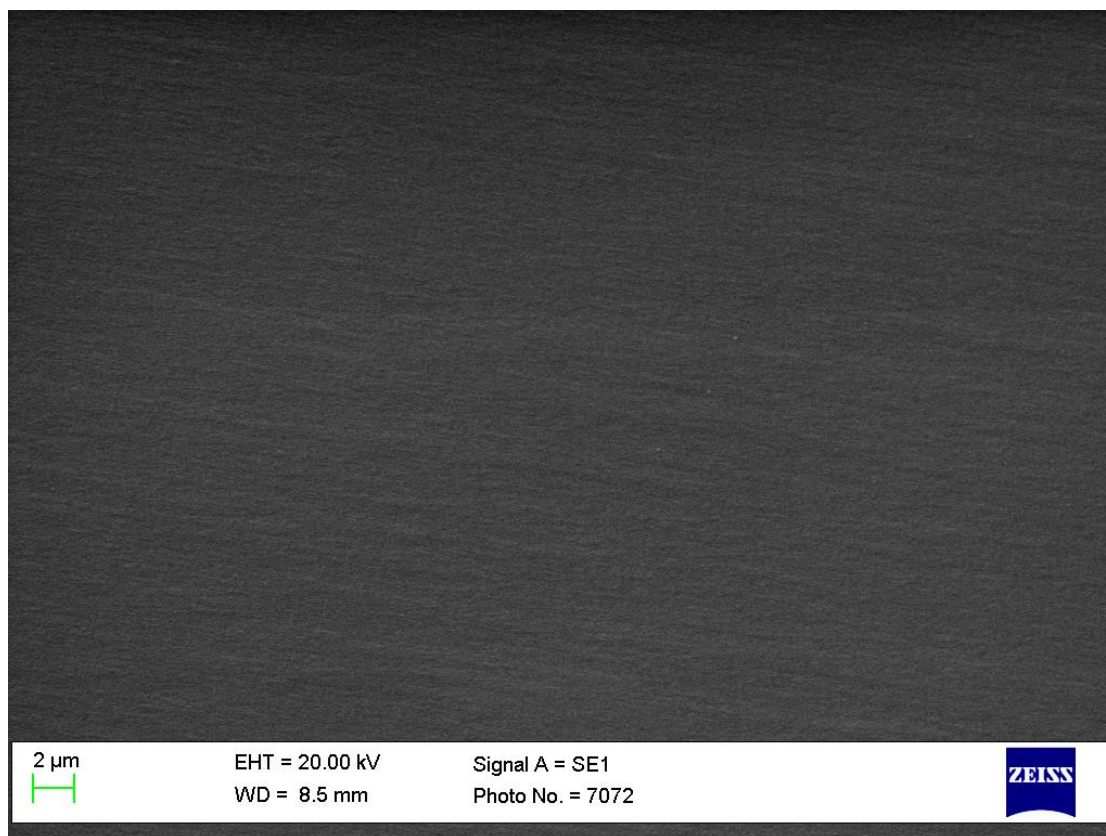


Figure 4-3 SEM image of pure epoxy resin:  $\times 5000$ .

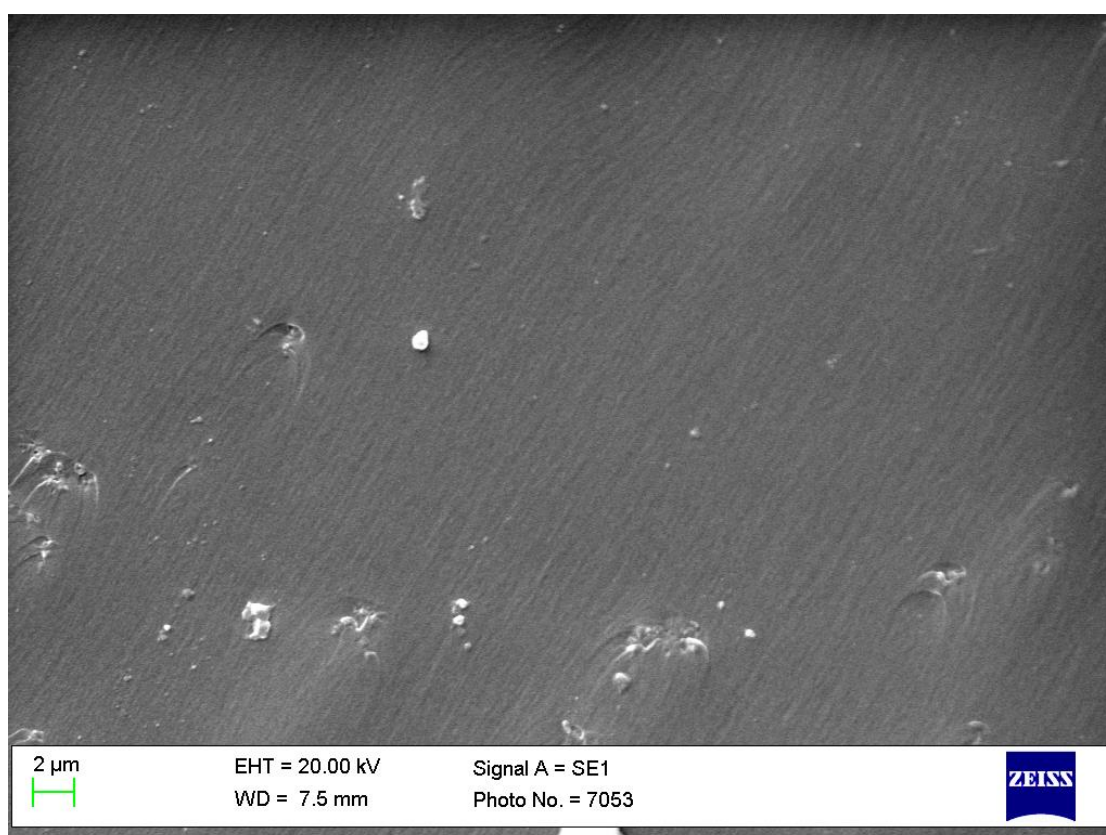


Figure 4-4 SEM image of EPS05,  $\times 5000$ .



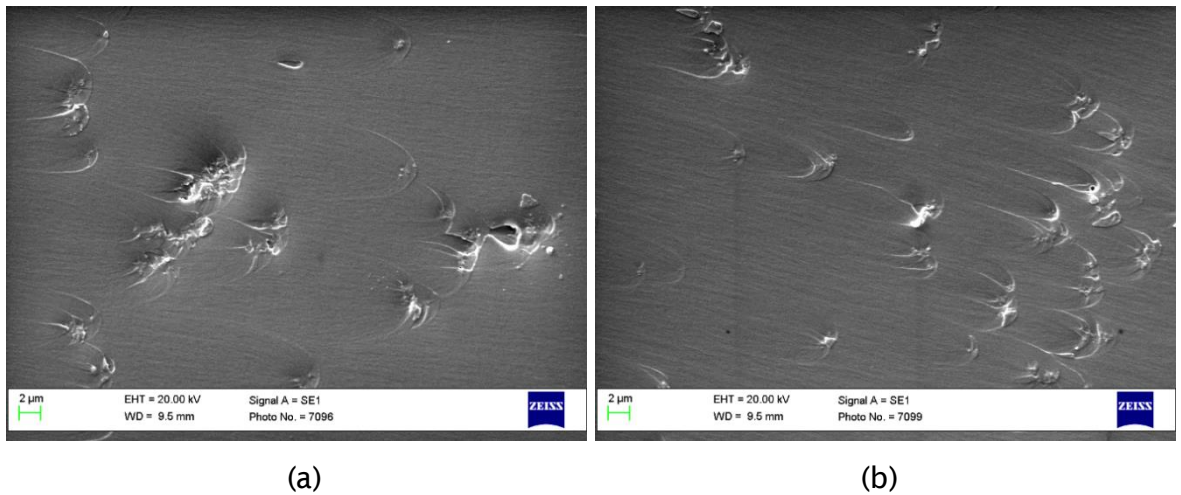


Figure 4-5 SEM image EPS1: (a) and (b)  $\times 5000$ .

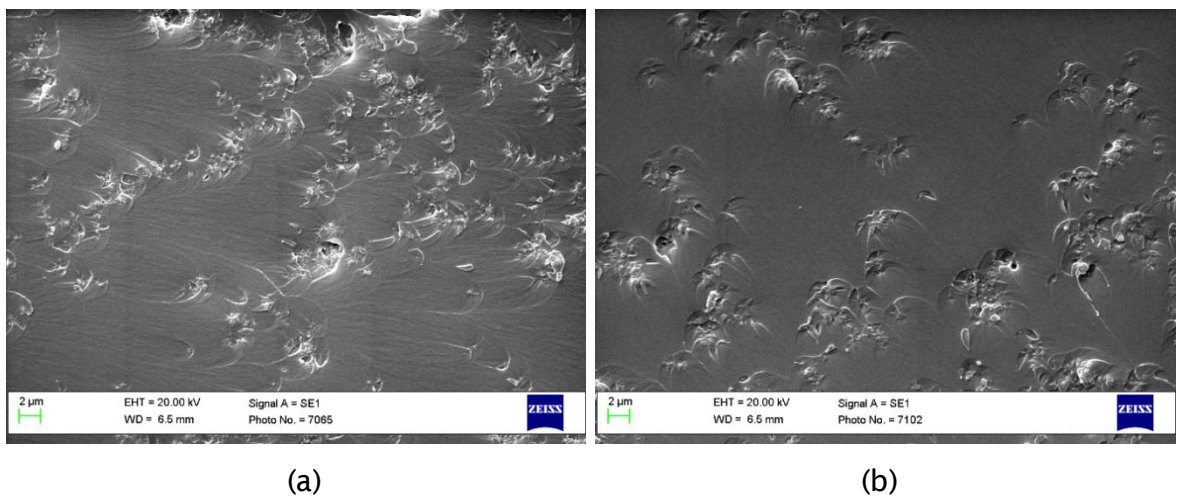


Figure 4-6 SEM image of EPS3: (a) and (b)  $\times 5000$ .

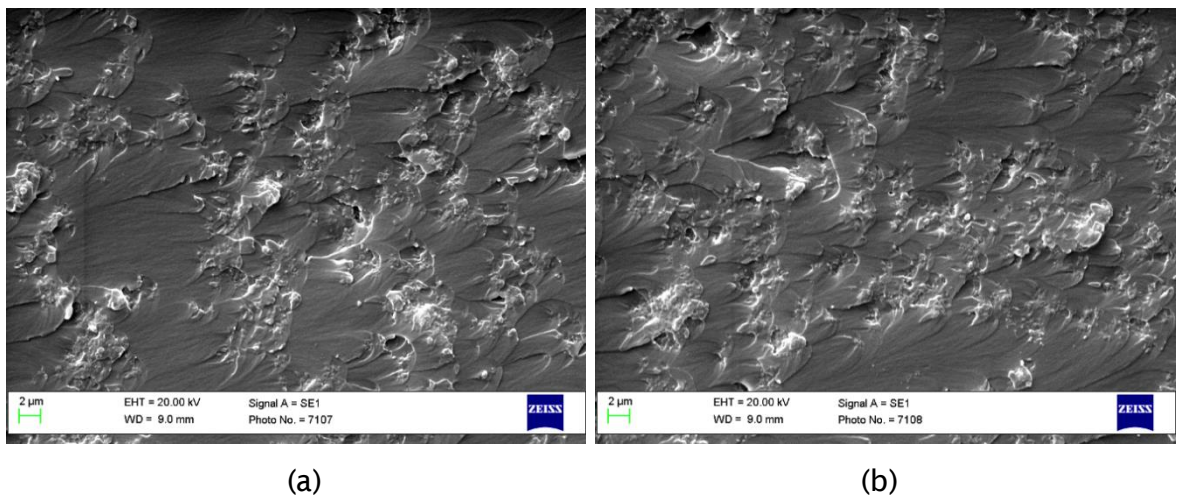


Figure 4-7 SEM image of EPS5: (a) and (b)  $\times 5000$ .

It can be observed that the number of particles visible in both the EPS and EPST samples increases with filler concentration. From 3 wt% of EPS and EPST samples, obvious agglomerations of particles/aggregates have appeared and it seems that the fillers have had a significant impact on the structure of the matrix, especially

## Chapter 4 Morphology Characterisation

in EPS samples shown in Figures 4-6 and 4-7. The more perturbed matrix morphology may lead to deteriorated insulation properties in epoxy nanocomposites. Comparing EPS and EPST samples, it is easy to note that the surface treatment acts to reduce disturbance of the polymer matrix, this is especially clear for high filler concentrations of  $\text{SiO}_2$  samples. EPST3 and EPST5 samples seem to show relatively good dispersion and distribution (Figures 4-10 and 4-11).

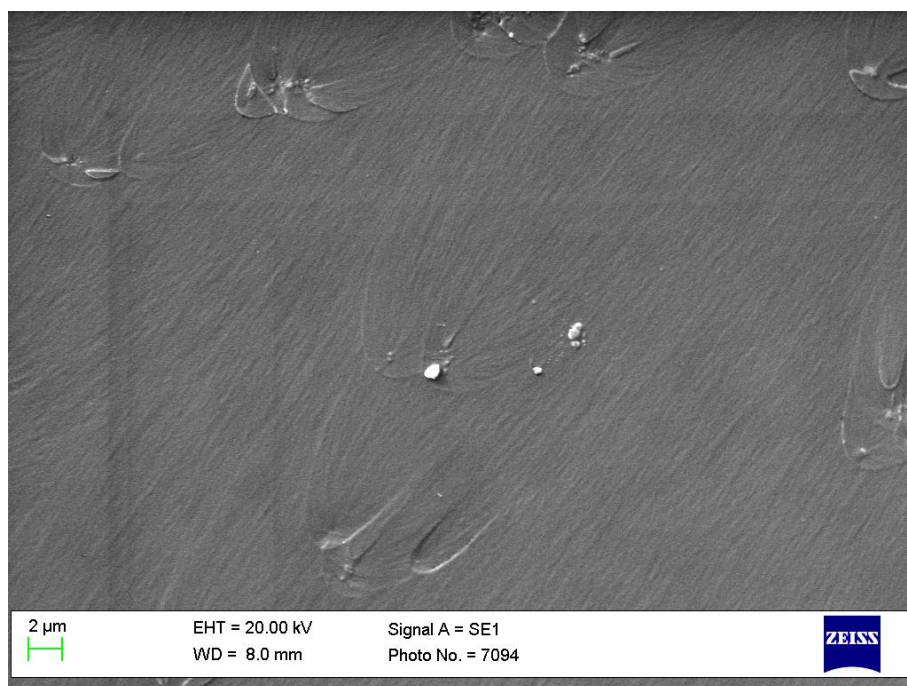


Figure 4-8 SEM image of EPST05,  $\times 5000$ .

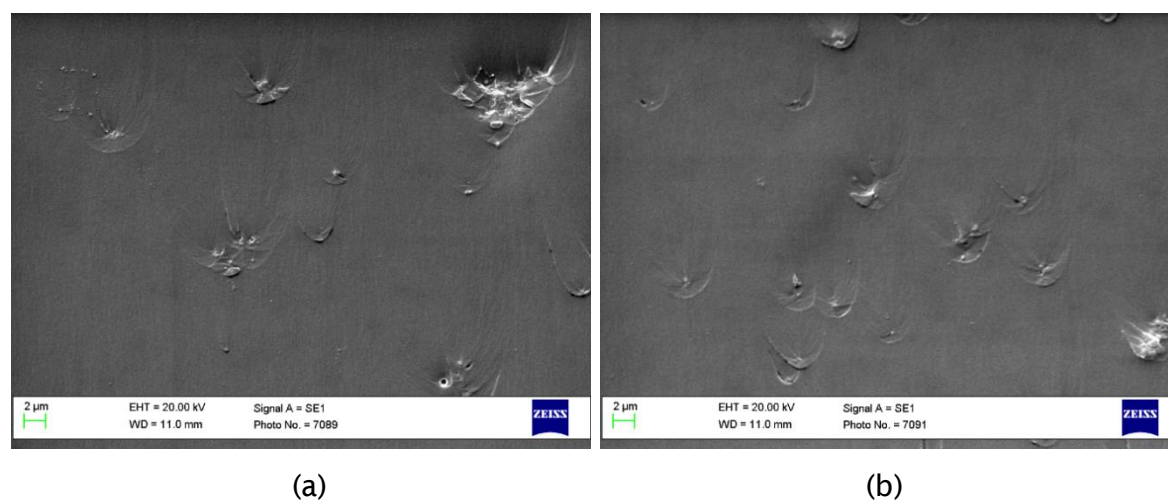


Figure 4-9 SEM image of EPST1: (a) and (b)  $\times 5000$ .

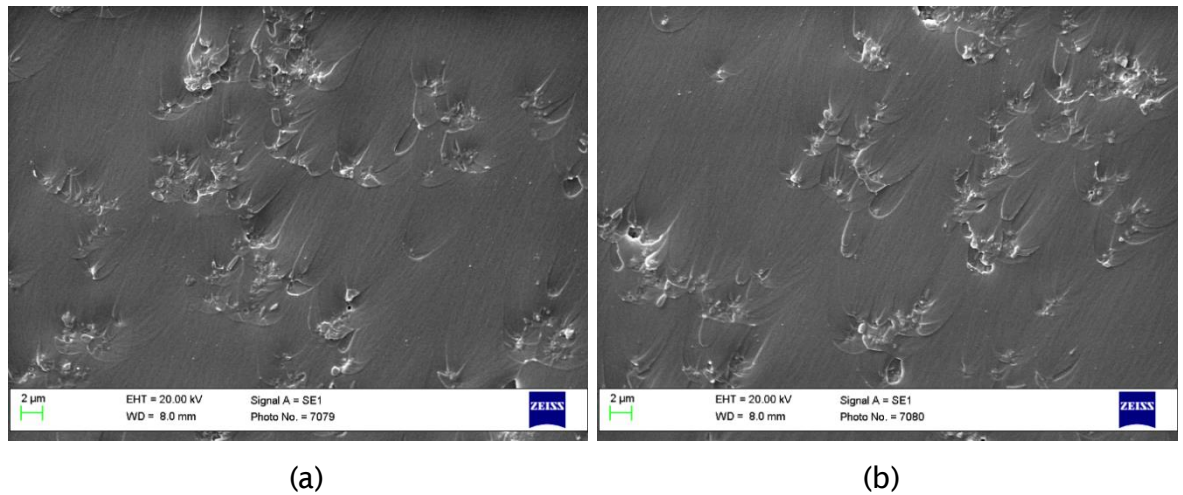


Figure 4-10 SEM image of EPST3: (a) and (b)  $\times 5000$ .

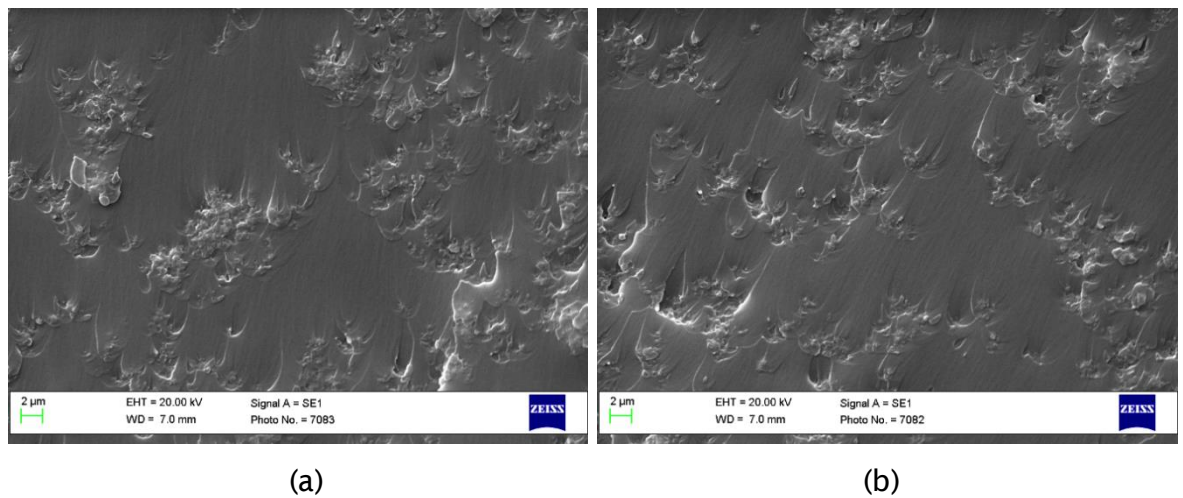


Figure 4-11 SEM image of EPST5: (a) and (b)  $\times 5000$ .

Another interesting phenomenon that can be observed relates to traces formed around particles/aggregates in both EPS and EPST samples, most of which spread in the same directions (see, for example, Figures 4-12 and 4-13). These are assumed to be due to the propagation of forces applied at the boundary of materials while preparing the samples for SEM. In Figures 4-12 and 4-13, the black circles highlight particles/aggregates and red arrows might be regarded as the thickness of the interphases between fillers and matrix. With the growth of filler loadings, these interphase areas tend to overlap as shown in Figure 4-13 (b). This relatively naive analysis could be improved by methods mentioned in [103] which is one potential area for future research.



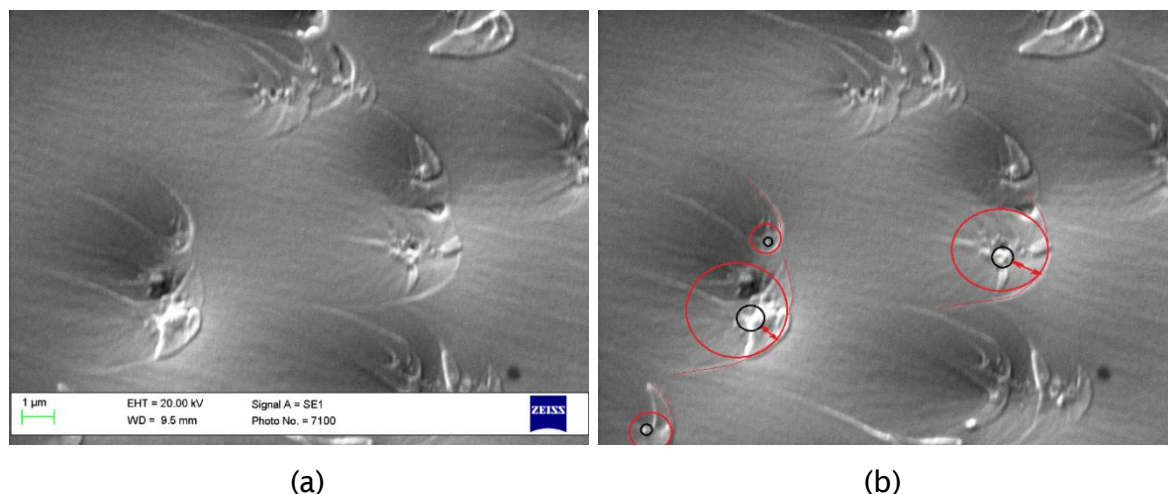


Figure 4-12 SEM image of EPS1,  $\times 15000$ : (a) original; (b) featured.

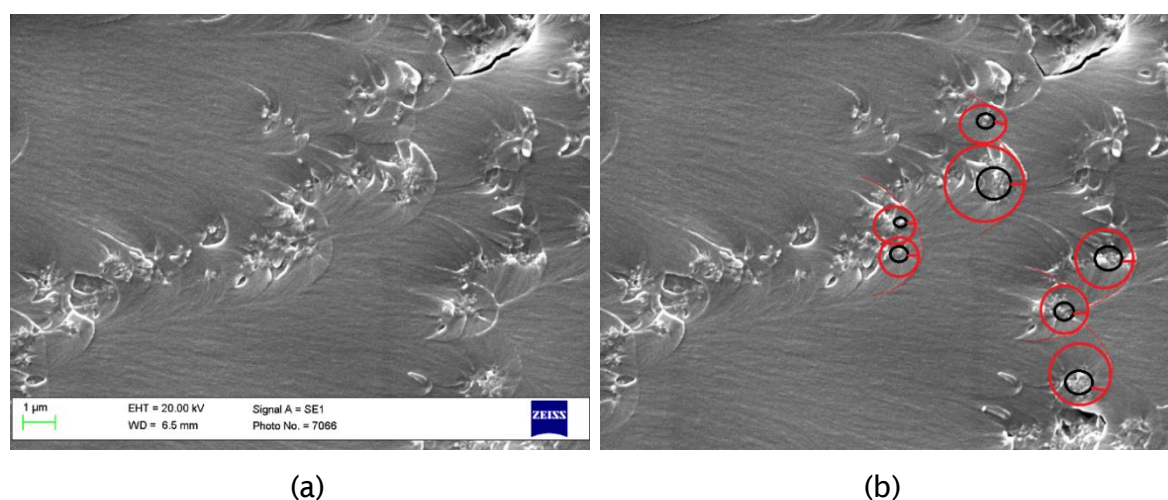


Figure 4-13 SEM image of EPS3,  $\times 15000$ : (a) original; (b) featured.

The SEM images of EPB samples are shown in Figures 4-14 to 4-18. For this type of nanoparticles it can be concluded there are three distinct forms, which have also been observed in clay platelet-based nanocomposites [104]: First, due to the sonication process, particles can be exfoliated and solely dispersed in the matrix as shown in Circle B of Figure 4-16. Second, some exfoliated particle plates could intercalate with the chains or their segments [104] as shown in Circle B of Figure 4-15. Third, particles are also agglomerated as sphere-like aggregates as shown in Circle A of Figure 4-15 (a) and in the high magnification insets within Figure 4-18.

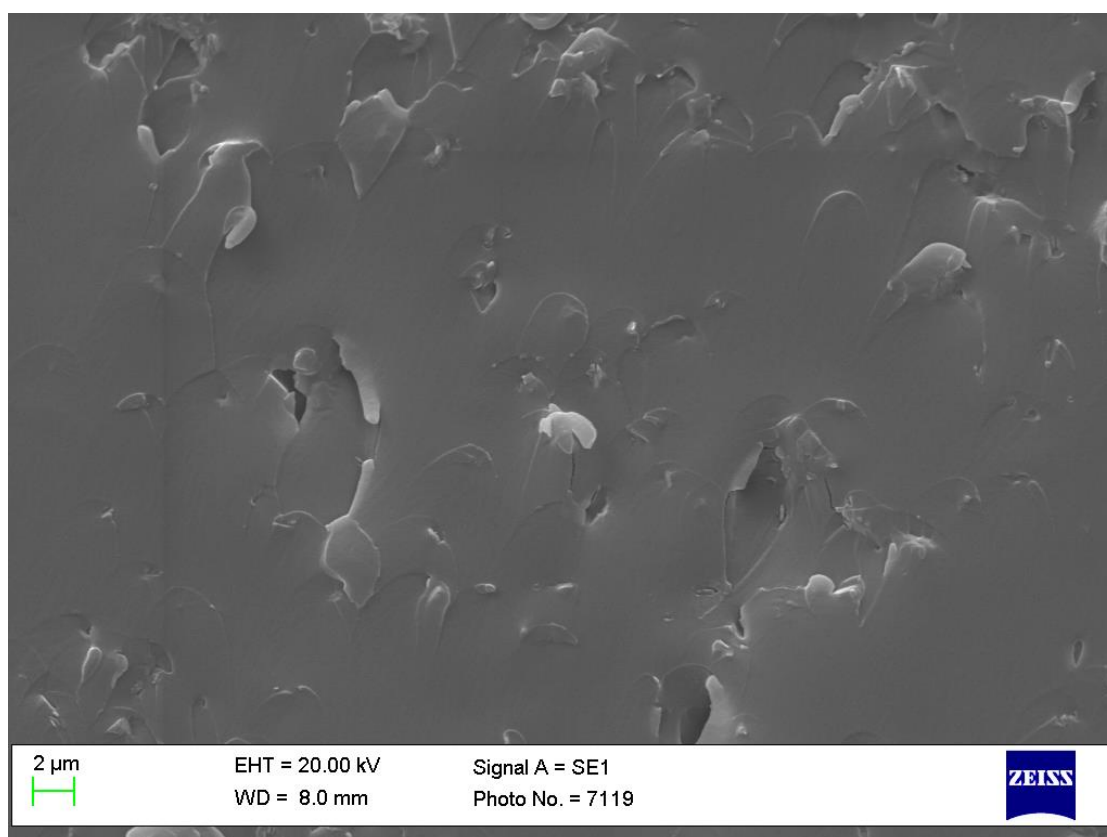


Figure 4-14 SEM image of EPB05, ×5000.

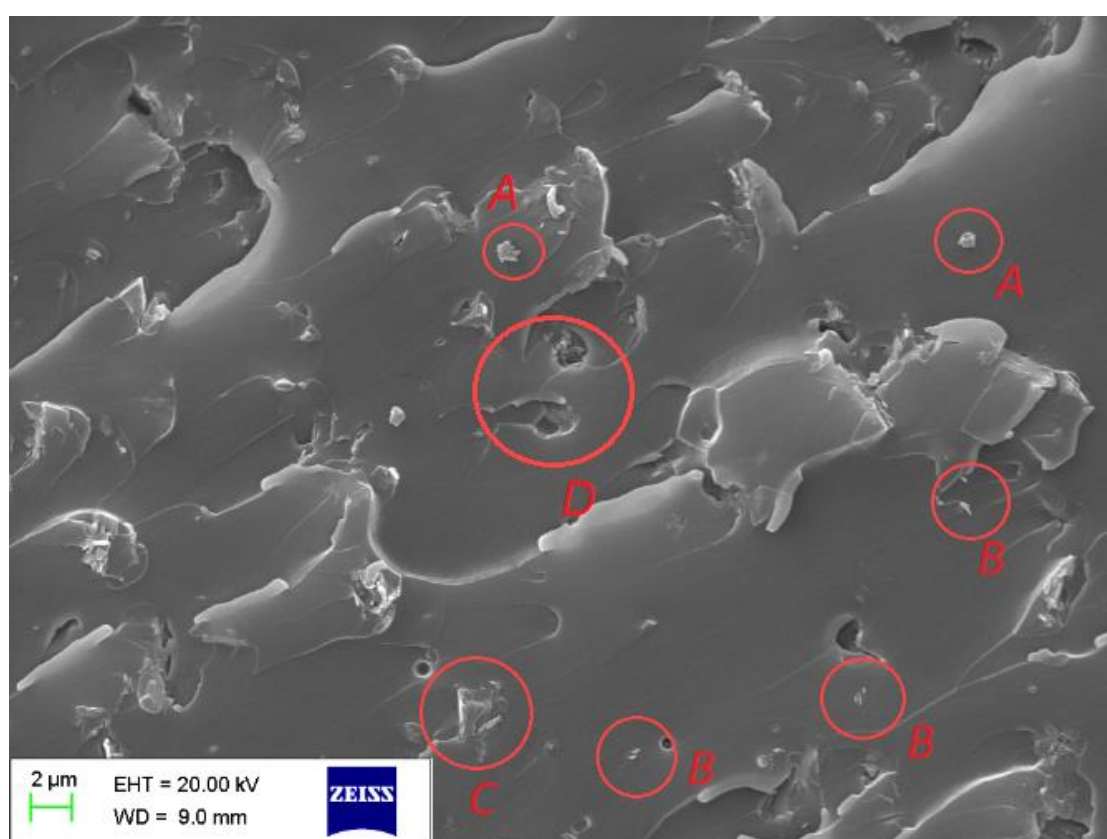


Figure 4-15 SEM image of EPB1, ×5000.

## Chapter 4 Morphology Characterisation

Moreover, the presence of hBN particles could lead to some stress concentration sites and initiation of cracks [98]. This type of feature is shown in Circle D of Figure 4-15 and Circle C of Figure 4-16. The cracking and disruption of the matrix becomes more severe in samples of higher filler loading. It is obvious that hBN particles have a much more noticeable impact on the morphology of base material than  $\text{SiO}_2$  nanoparticle and tend to produce a layered structure in the matrix as shown in Circle C of Figure 4-15, in Circle A of Figure 4-16 and in Figure 4-17.

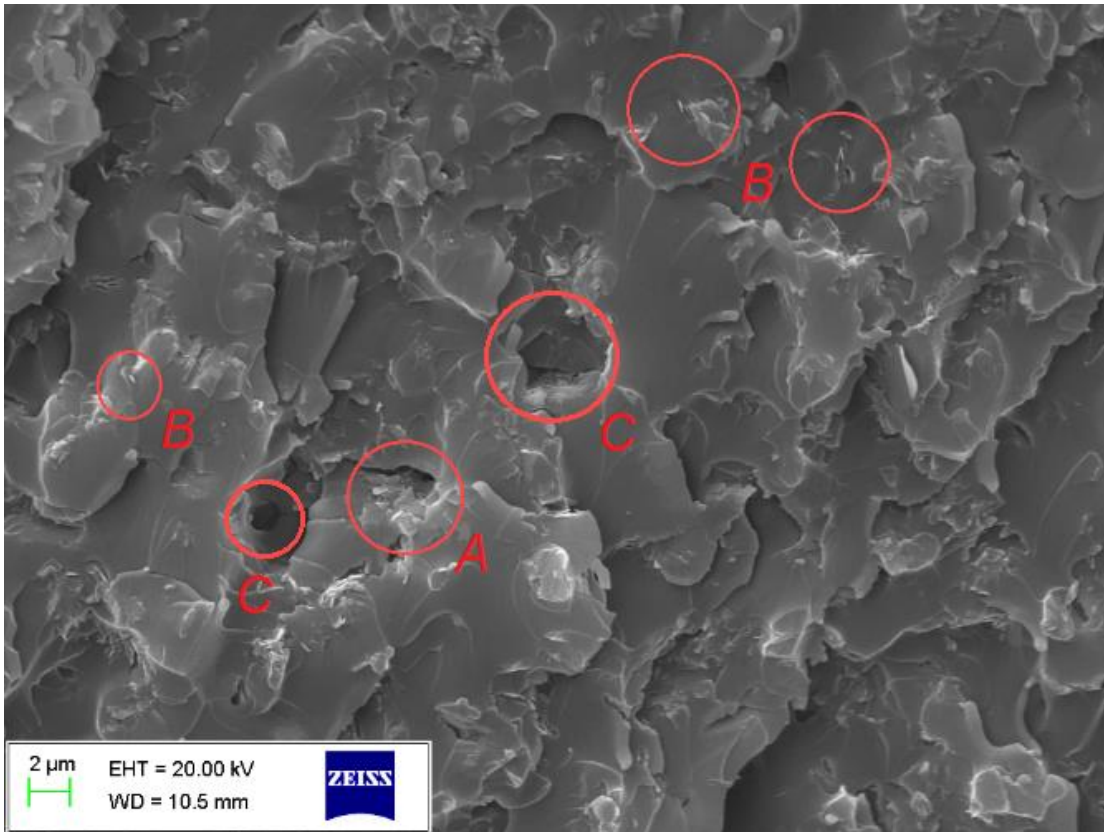


Figure 4-16 SEM image of EPB3,  $\times 5000$ .

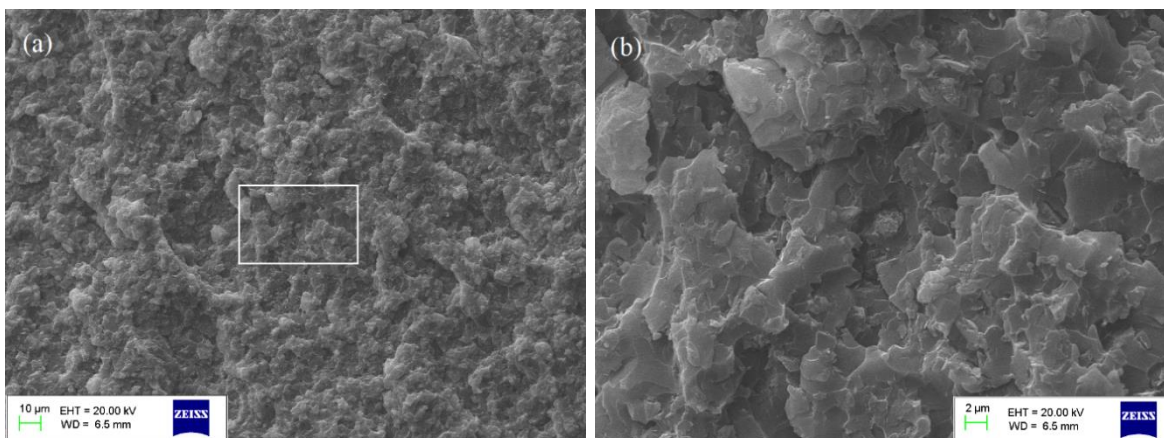


Figure 4-17 SEM image of EPB5: (a)  $\times 1000$ ; (b)  $\times 5000$ .



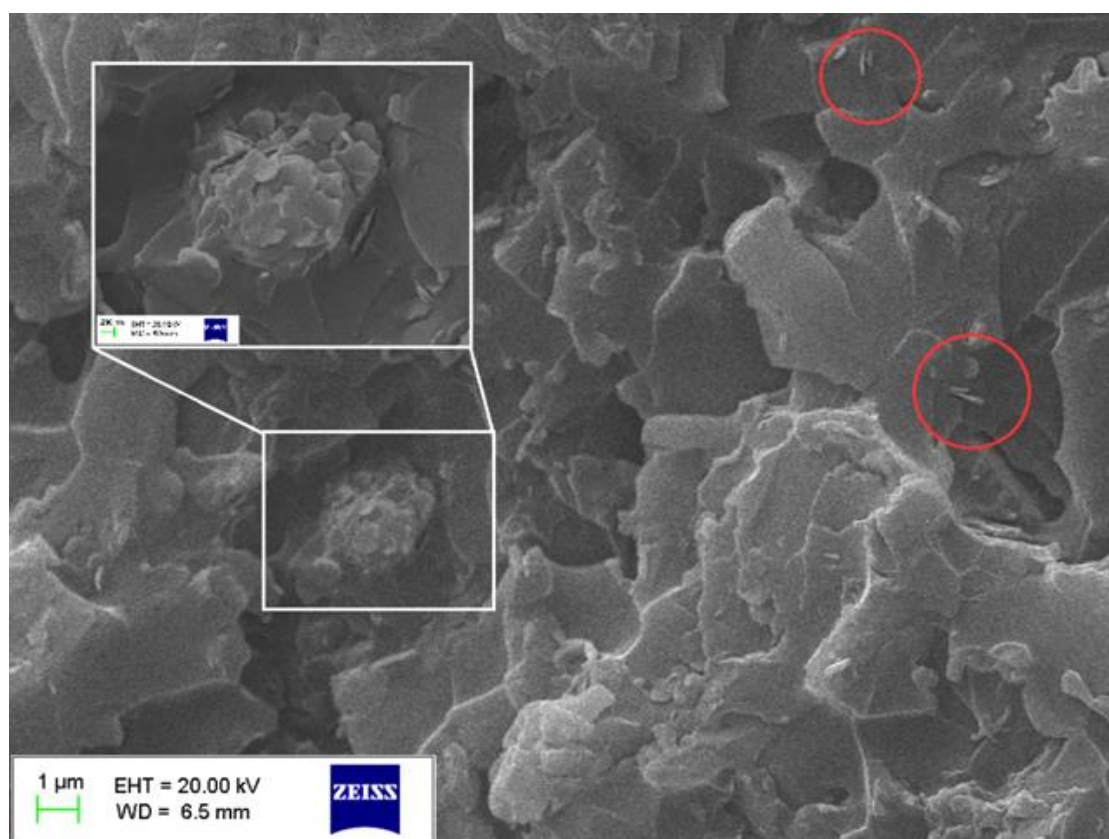
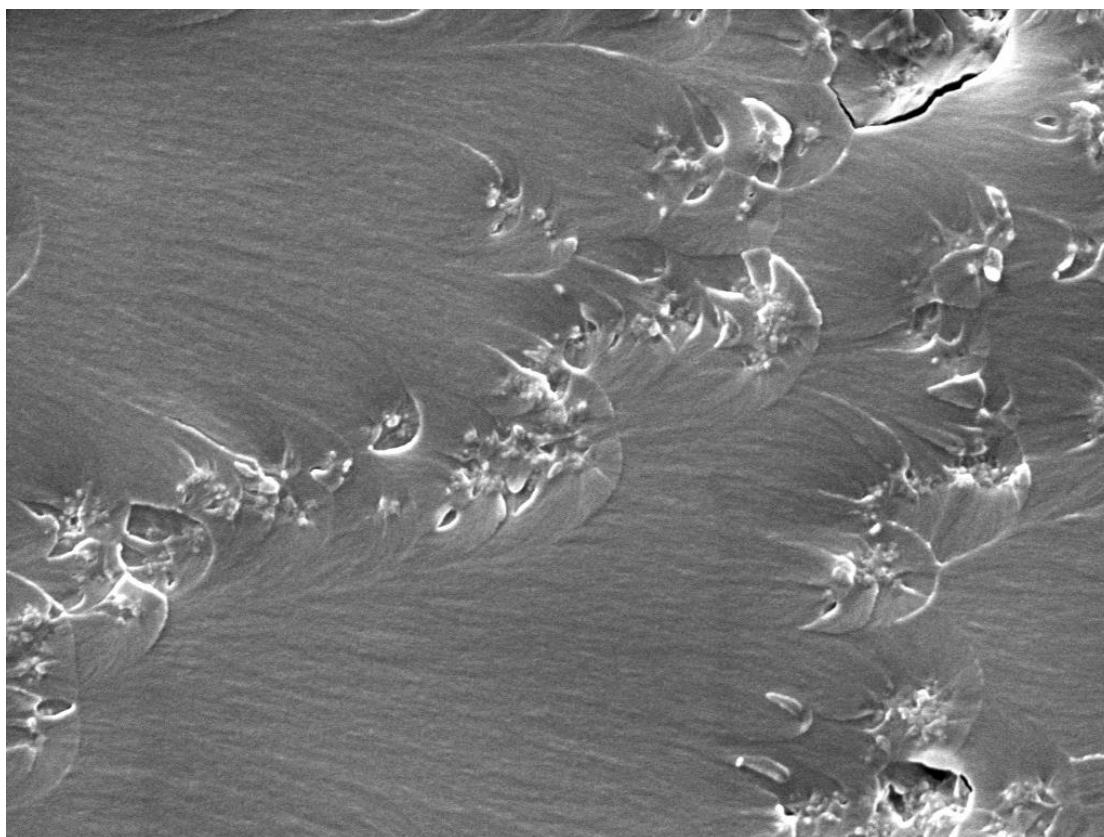


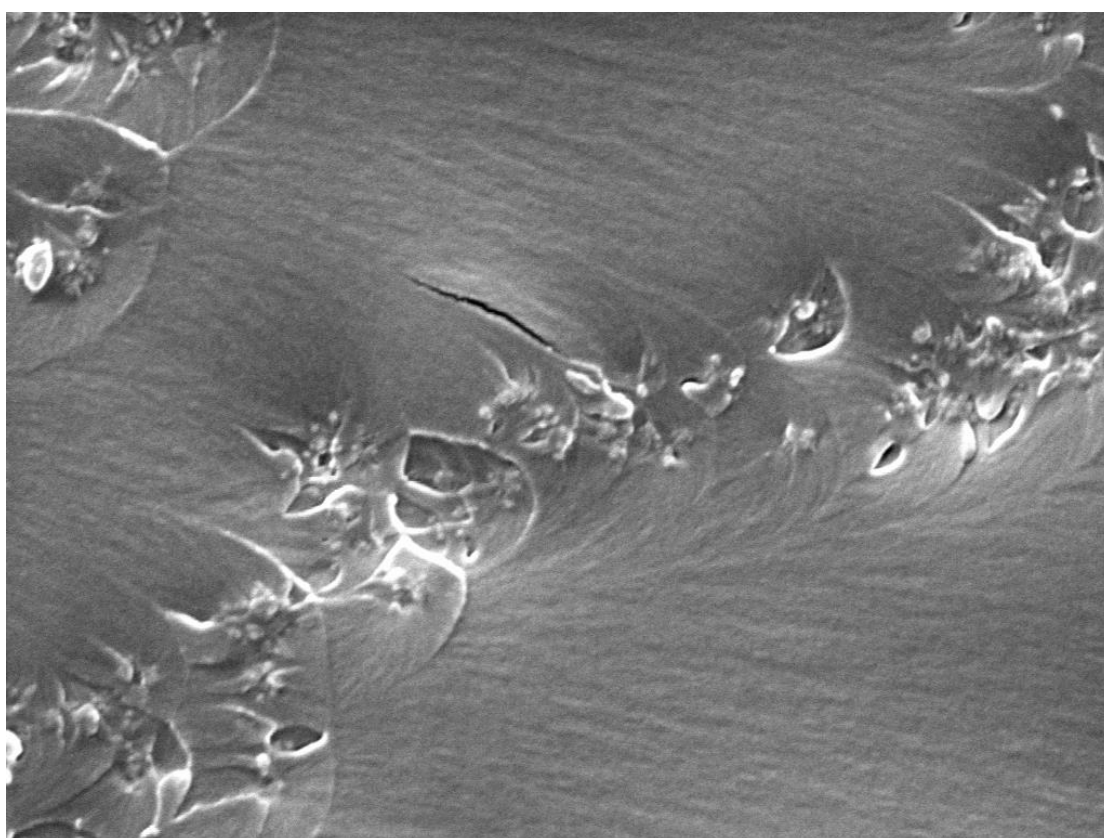
Figure 4-18 SEM image of EPB5,  $\times 10000$  (inset,  $\times 50000$ ).

#### 4.2.2 Image Processing

The analysis above is informative but is not precise enough, therefore, this section introduces image processing methods for a more quantitative analysis. The EPS and EPST samples of 1, 3, 5 wt% were chosen for quantitative analysis with the EPS3 sample shown as an example in Figure 4-19 (Normally at least 2 SEM images were processed for each kind of sample). SEM image processing for the other samples is included in Appendix A. In order to get sufficient spatial resolution to resolve individual nano-particles (10-20 nm), SEM images recorded at a magnification of  $\times 15000$  were used (16-17 nm spatial resolution). ImageJ® software, is used to digitalize images and generate data such as, the coordinates of mass centers and the areas of each particle/aggregate (example binary images are shown in Figure 4-20). Particles that could be clearly recognized were selected and their circularity was calculated; it was found that this ranged between 0.3 and 0.6. Features in the binary images can then be filtered based on their circularity so that structures of the matrix, like cracks shown in Figure 4-19 (b) are ignored. In this manner particles/aggregates within an image can be identified (blue circled) as shown in Figure 4-21.



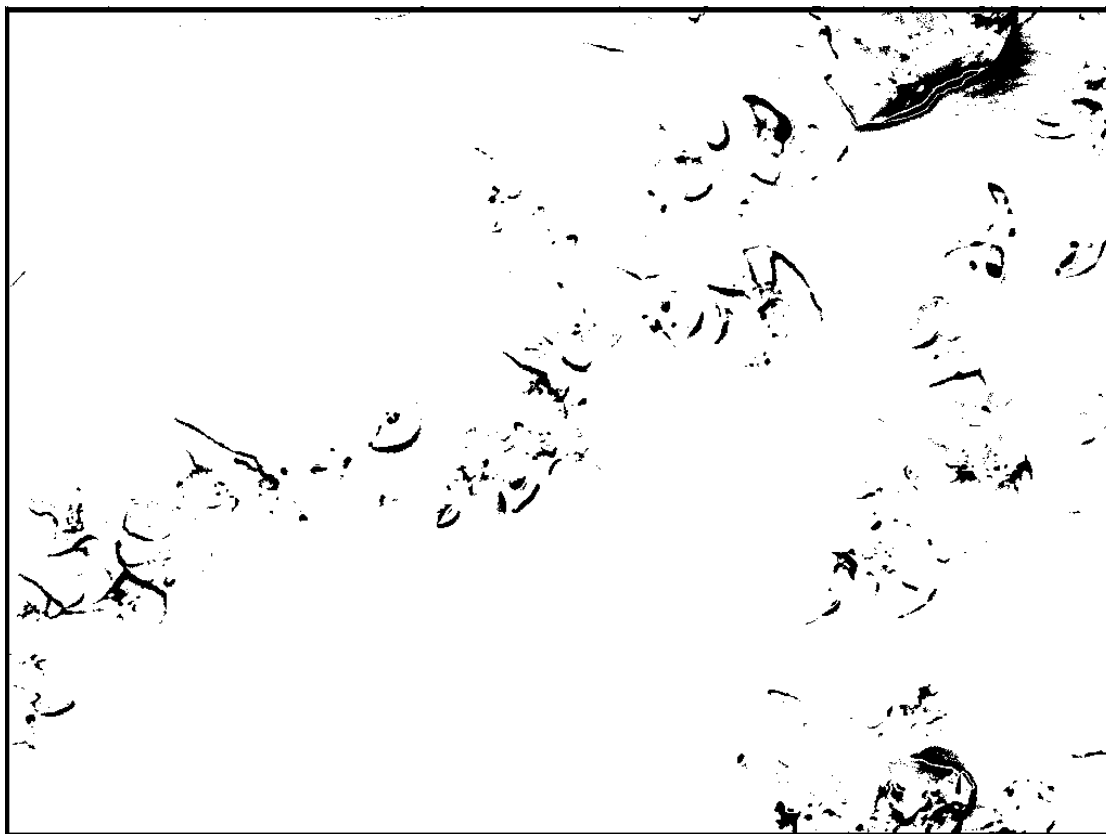
(a)



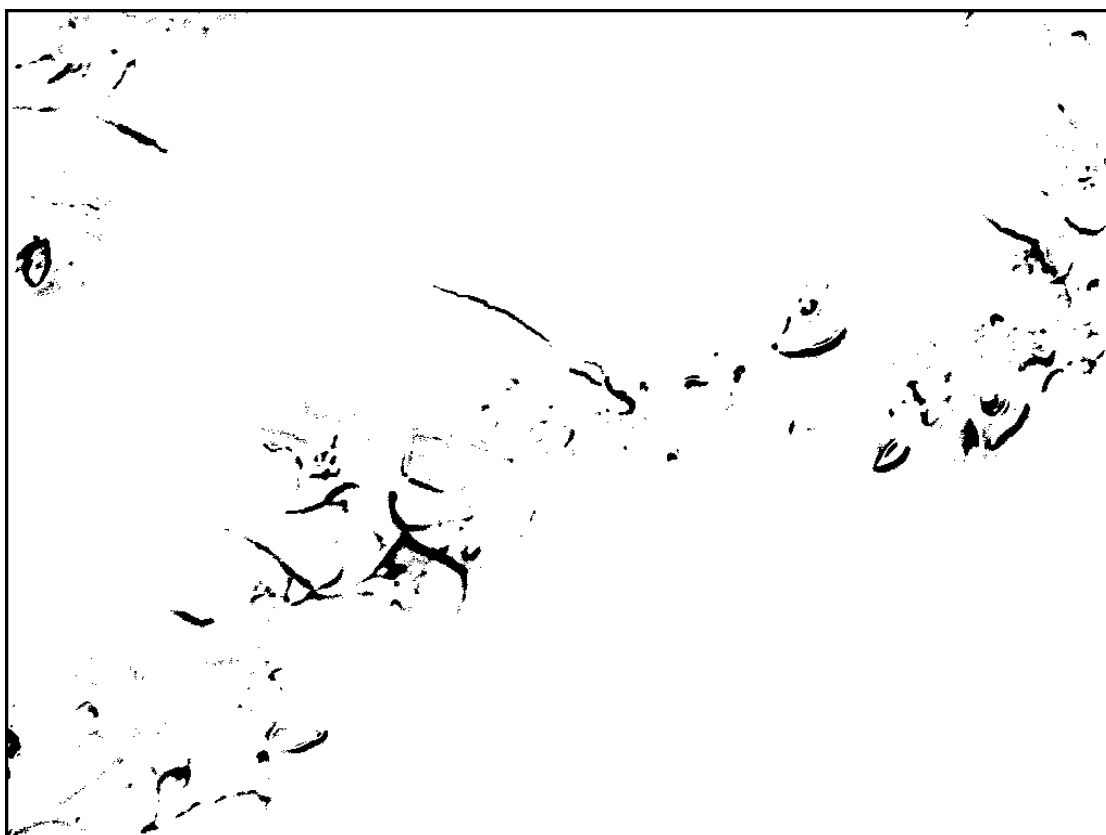
(b)

Figure 4-19 Original SEM images of EPS3 samples,  $\times 15000$ .



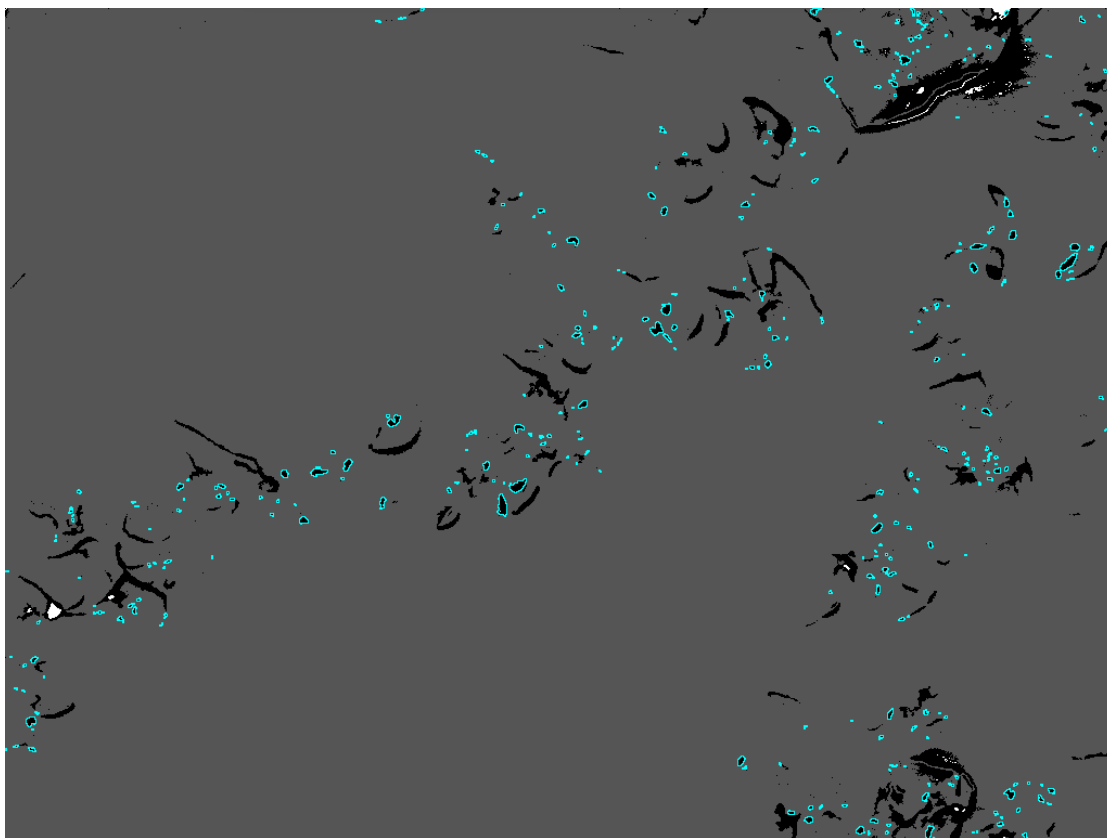


(a)

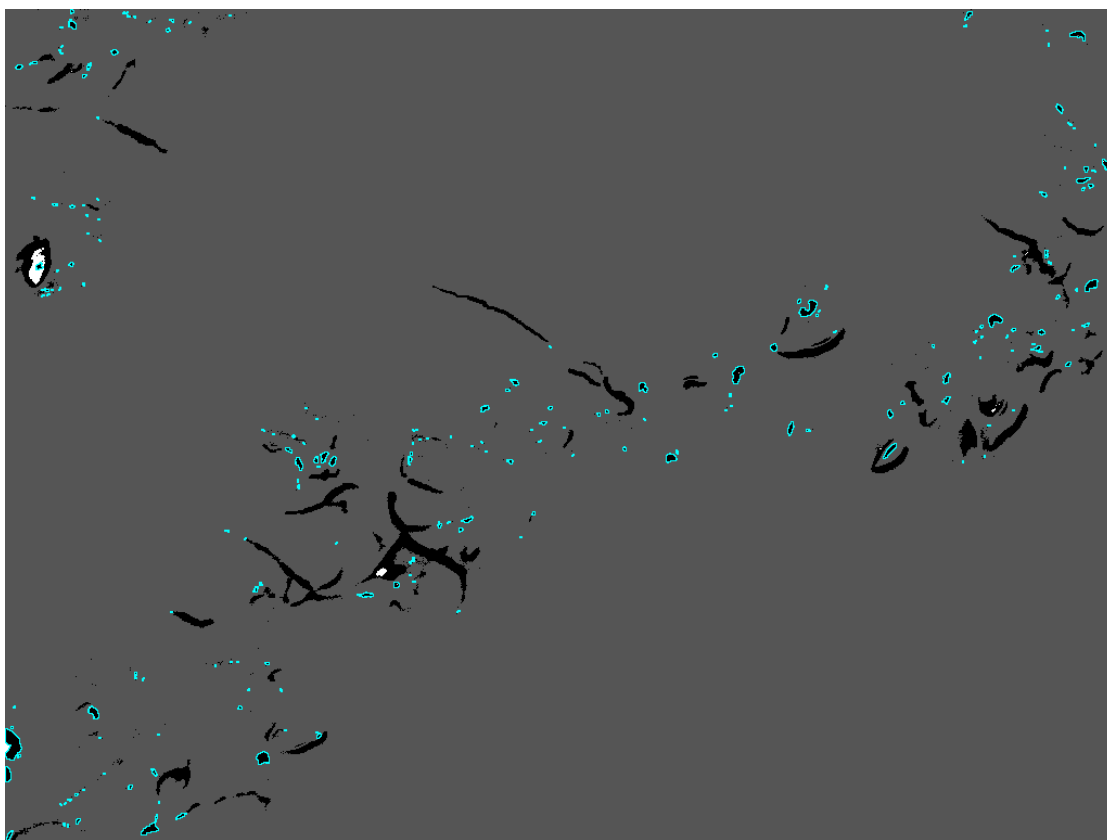


(b)

Figure 4-20 Binary SEM images of EPS3 samples,  $\times 15000$ .



(a)



(b)

Figure 4-21 Processed SEM images with highlighted particles of EPS3 samples,  $\times 15000$ .

### 4.3 Data Analysis

Figures 4-22 and 4-23 show example histograms of the measured particle/aggregate size and the 1<sup>st</sup> NND respectively (for 3 wt% untreated SiO<sub>2</sub>). From the image data, the weighted average equivalent diameters (WAED) and their deviations, the 1<sup>st</sup> NND and the skewness of particles are all calculated; these data are shown in Table 4-1. For skewness, a quadrat size of 32000 nm<sup>2</sup> is chosen [49]. The generated data are shown in Table 4-1.

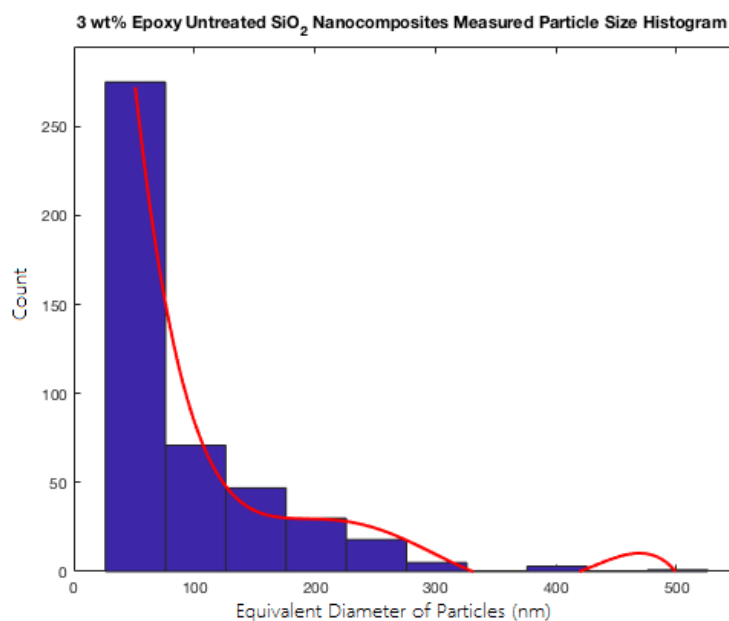


Figure 4-22 Histogram of measured particle/aggregate size of EPS3 samples.

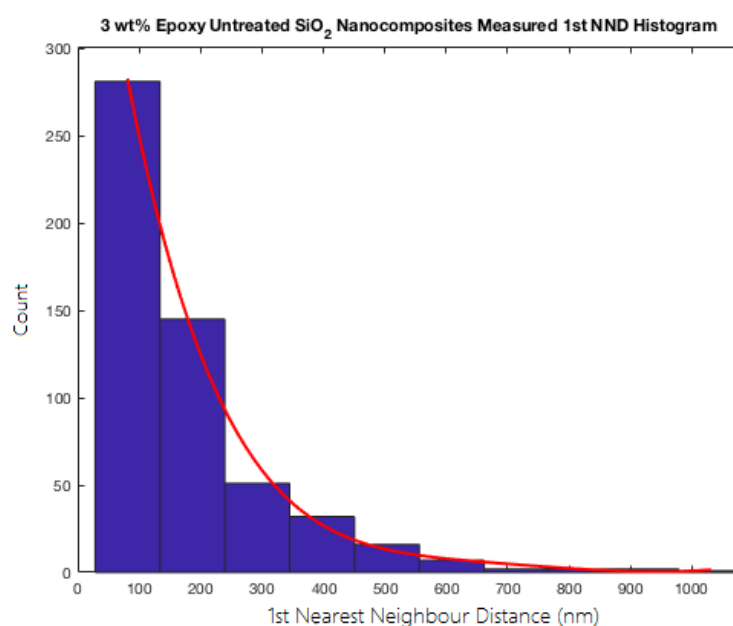


Figure 4-23 Histogram of measured 1st Nearest Neighbour Distance of EPS3 samples.

Table 4-1 Quantitative data of SEM images, EPS and EPST samples in 1, 3, 5 wt%

Sample Code	Weighted Average Equivalent Diameter (nm)	Weighted Average Equivalent Diameter Deviation	Weighted 1st NND (nm)	Skewness
EPS1	169.39	165.60	291.11	12.66
EPS3	93.58	68.54	218.48	8.05
EPS5	100.79	70.22	177.60	6.25
EPST1	160.27	120.65	353.12	11.69
EPST3	75.12	51.14	277.10	6.44
EPST5	89.55	66.66	245.16	5.71

For EPS samples: In the case of EPS3 and EPS5 WAED and its deviation increase with the growth of filler loadings. Smaller WAED and deviation means smaller aggregates and better dispersion of particles [99]. The lower value in EPS3 than EPS5 could be due to the probe sonication, since there are fewer particles but they are subjected to the same amount of sonication energy. However, EPS1 samples show a much larger value in WAED. This is probably because there is a much lower number of particles with many of them being agglomerated together. This is also reflected in the larger value in deviation of WAED (165.60) and skewness of 12.66 for the EPS1 samples.

The weighted 1<sup>st</sup> NND and the skewness in EPS samples both decrease as the filler loading is increased. For a given filler loading lower weighted 1<sup>st</sup> NND and lower skewness together indicates better dispersion and more even distribution. However, the relatively low value of weighted 1<sup>st</sup> NND for EPS3 could be due to the asymmetry of distributions which leaves many areas blank as shown in Figure 4-13. This asymmetry is also reflected in its relatively large value of skewness (8.05). For the EPST samples, the overall values indicate better dispersion and distribution when compared with EPS samples of the same filler loadings; this is the expected result of effective surface treatment.

Moreover, if particles/aggregates are regarded as recombination centers for charge transport [105], then another interesting value, Weighted Average Surface Distance

(WASD), can be considered as a method to relate morphology to dielectric properties. Thus, these values are shown for EPS and EPST samples in Table 4-2.

Table 4-2 Weighted surface distance of EPS and EPST samples in 1, 3 and 5 wt%

Sample Code	Weighted Average Surface Distance (nm)
EPS1	180.43
EPS3	155.27
EPS5	121.59
EPST1	257.35
EPST3	200.08
EPST5	157.97

#### 4.4 Particle/Aggregate Dispersion and Distribution Modelling

In order to gain a deeper understanding of epoxy SiO<sub>2</sub> nanocomposites and to give a foundation in the simulation of dielectric properties based on the measured morphology of nanocomposites, this section proposes two methods to simulate the dispersion and distribution of particles/aggregates based on our measured data. These two methods (implemented in Matlab® 2017b) are referred to here as the PDF method and the Histogram method. Simulated results of EPS3 are presented here to provide an example. In both simulation methods the measured equivalent diameter data is fitted in order to generate a probability distribution function (PDF) as shown in Figure 4-24. The required number of particles/aggregates are assigned with randomly generated sizes that conform to the PDF determined in the previous step (see Figure 4-25). The total volume fraction of simulated particles/aggregates is equal to that in EPS3. The two methods differ in their treatment of the 1<sup>st</sup> NND data. In the PDF method a probability distribution function is fitted to the NND data (as was done with the particle size data, see Figure 4-26). The simulation code then finds a set of random particle positions that satisfy that PDF (see Figure 4-27 and Figure 4-28 for a visualisation of one such distribution). In the Histogram method the 1<sup>st</sup> NND data is loaded into the code and

the Multidimensional Scaling Method (MDS) is applied in order to find a set of simulated particle locations that conform to the histogram of measured 1<sup>st</sup> NND data (see Figure 4-29 and Figure 4-30 for a visualisation of the distribution).

Using the Monte Carlo approach, 100 runs were carried out for each simulation method to generate the resulting distribution metrics shown in Table 4-3. According to Figure 4-28, Figure 4-30 and the data in Table 4-3, simulated WAEDs of particle size fulfills the relationship between EPS and EPST samples, and between different filler loadings. The simulated value are, however, a bit higher that may be due to the randomness of simulation and errors in the curve fitting. The distribution quantification data from the PDF method deviates further from the measured values than those derived from the Histogram method, however, the simulated particle distribution from the PDF method appears visually to be more realistic. This could be caused by the random generation of 1<sup>st</sup> NND data in the PDF method whereas the Histogram method attempts to conform as closely as possible to the measured data. Matlab code for both methods is included in Appendix B.

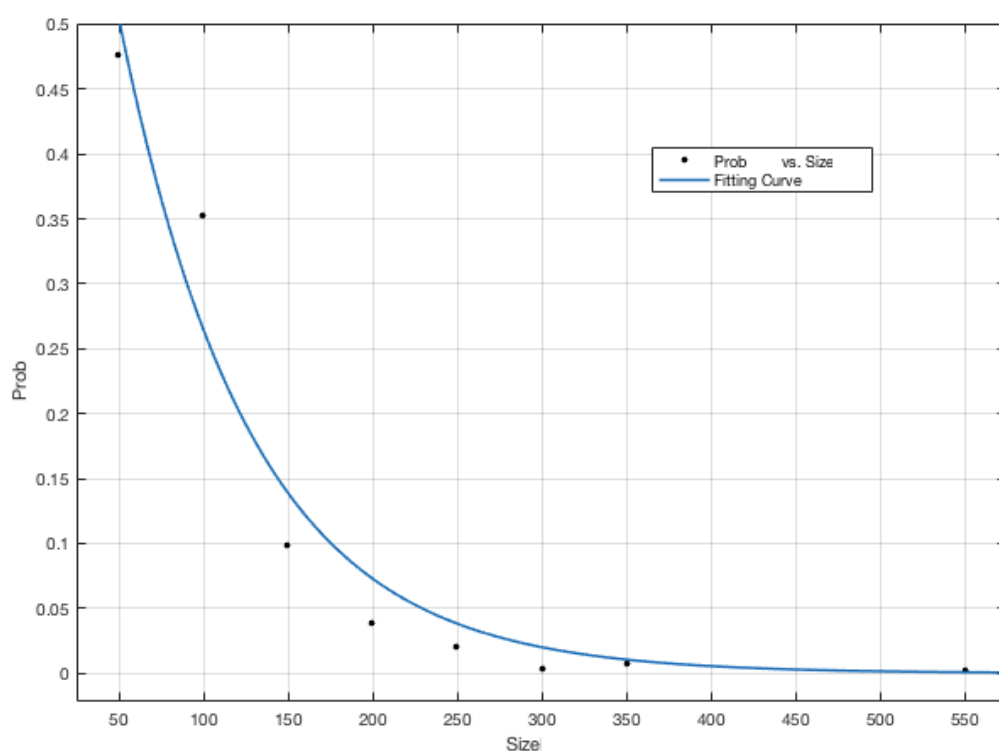


Figure 4-24 Occurrence probability of measured particle/aggregate size and fitting curve.

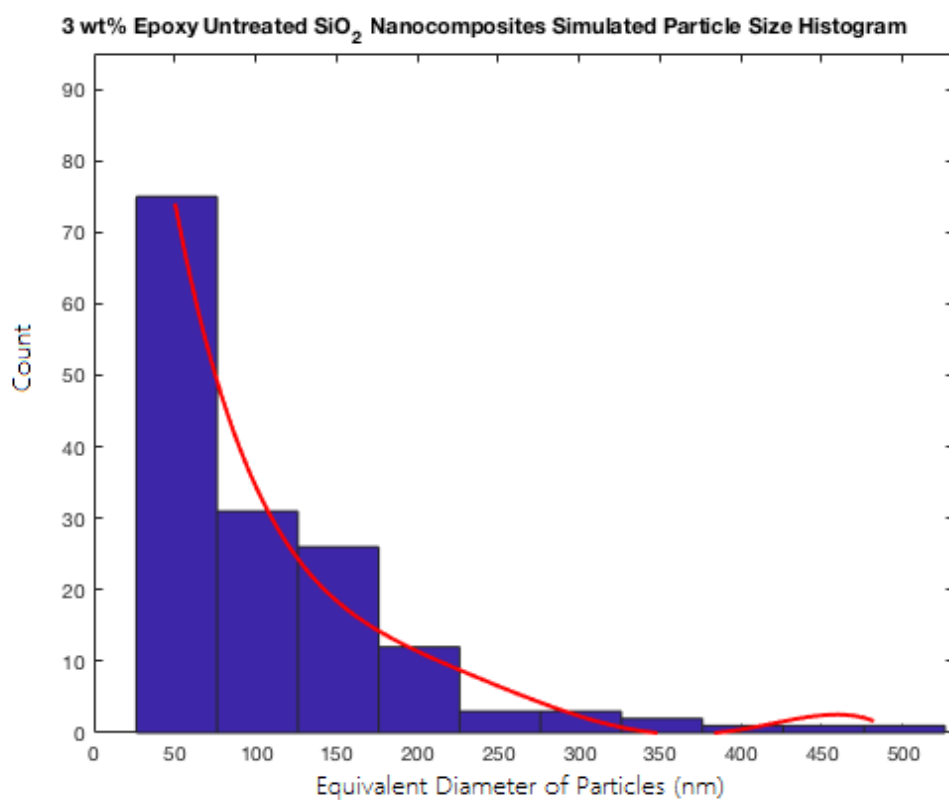


Figure 4-25 Histogram of simulated particle/aggregate size of EPS3 samples.

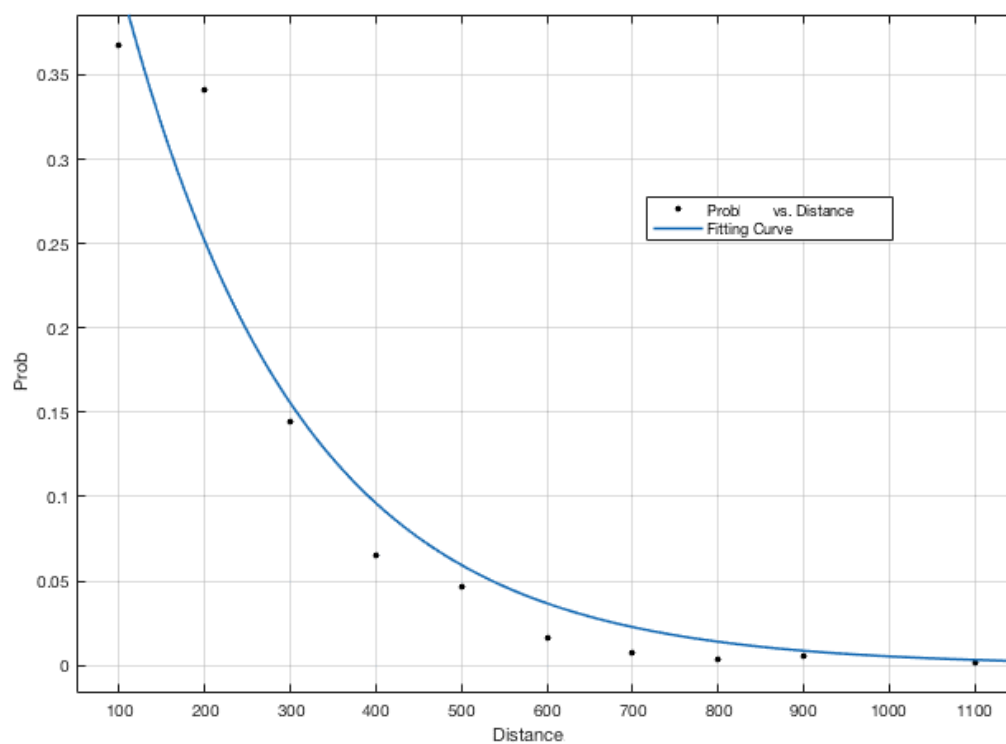


Figure 4-26 Occurrence probability of measured 1<sup>st</sup> Nearest Neighbour Distance and fitting curve.

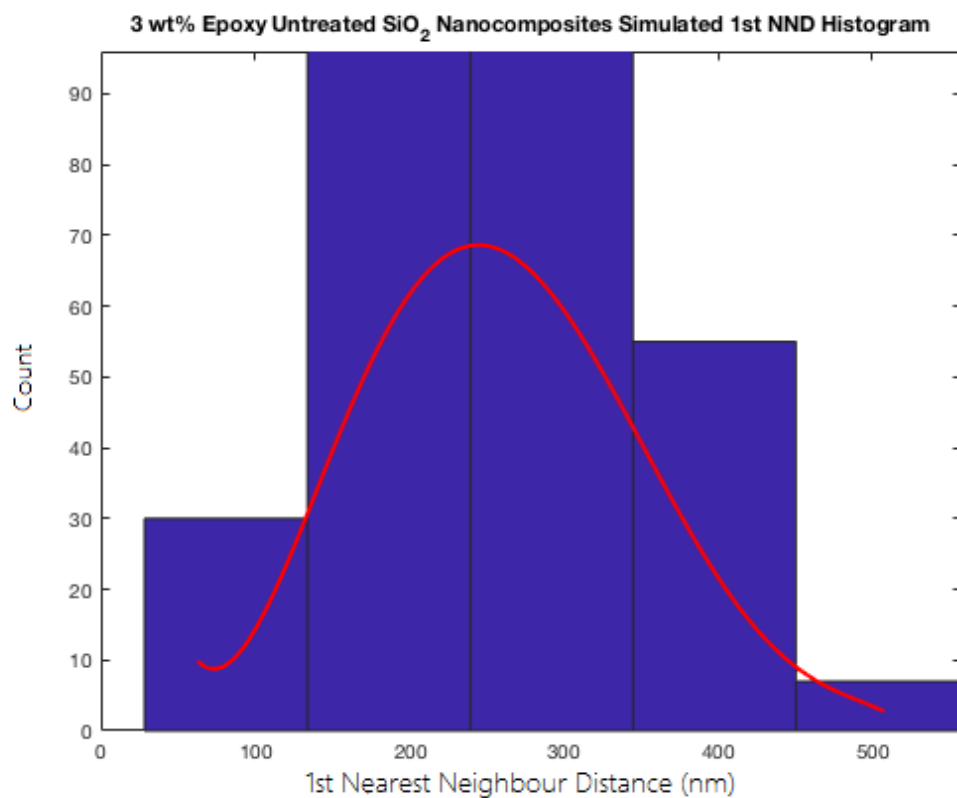


Figure 4-27 Histogram of simulated 1<sup>st</sup> Nearest Neighbour Distance of EPS3 samples, PDF Method.

**3 wt% Epoxy Untreated SiO<sub>2</sub> Nanocomposites Particle Simulated Dispersion and Distribution**

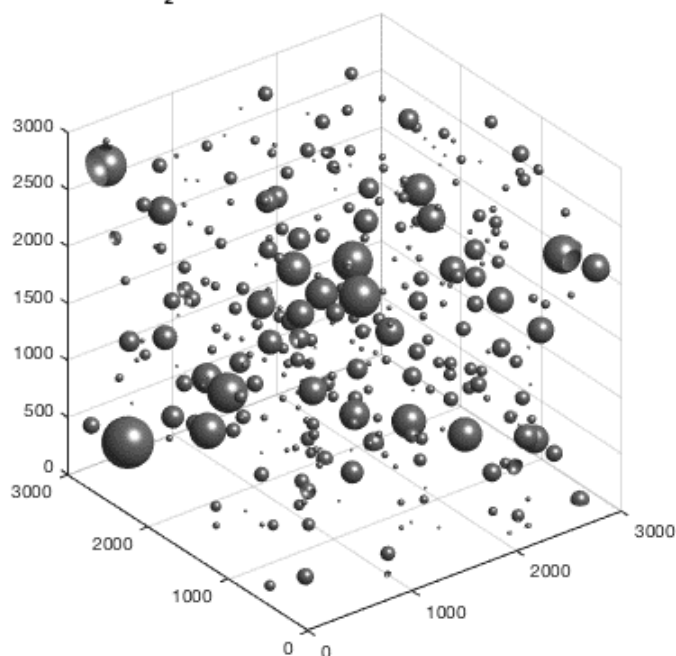


Figure 4-28 Simulated particles/aggregates dispersion and distribution in the cubic area of EPS3 samples, PDF Method.



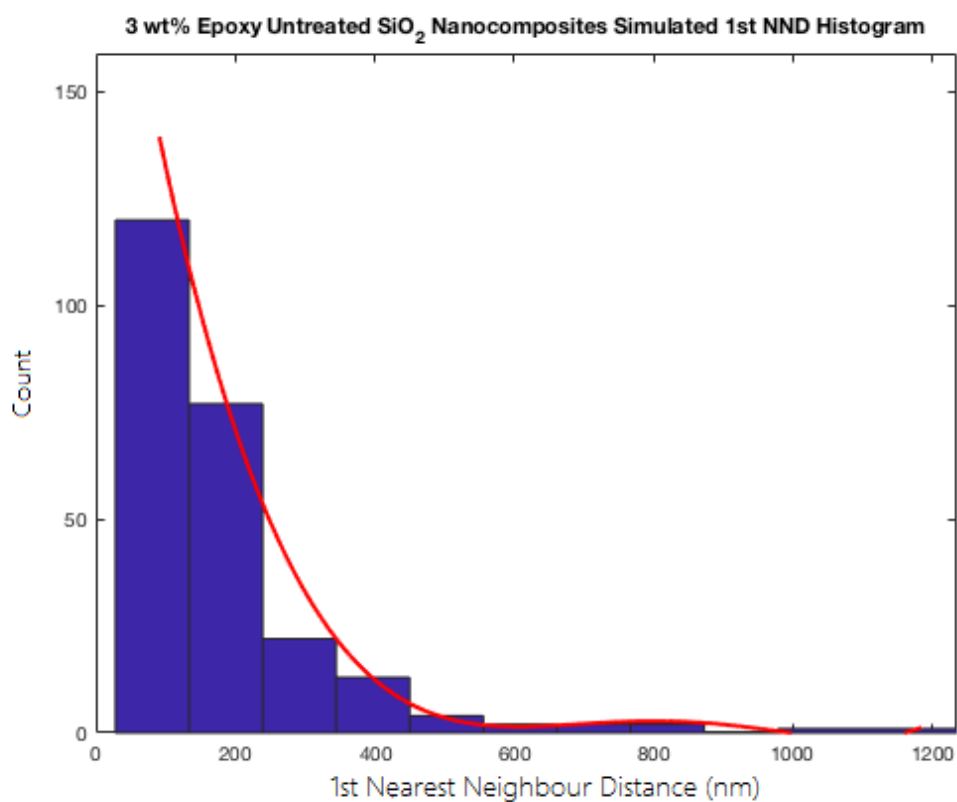


Figure 4-29 Histogram of simulated 1<sup>st</sup> Nearest Neighbour Distance of EPS3 samples, Histogram Method.

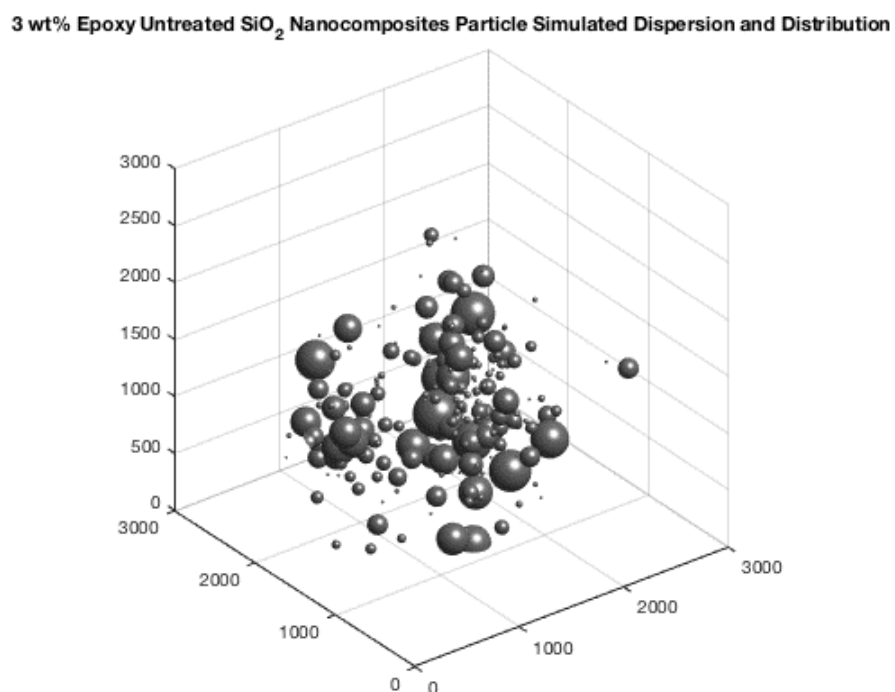


Figure 4-30 Simulated particles/aggregates dispersion and distribution in the cubic area of EPS3 samples, Histogram Method.

Table 4-3 Simulated Quantification data of SEM images, EPS and EPST samples in 1, 3, 5 wt% by PDF and Histogram method

Sample code	WAED (nm)	WAED Deviation	PDF Method		Histogram Method	
			1 <sup>st</sup> NND (nm)	skewness	1 <sup>st</sup> NND (nm)	skewness
EPS1	179.33	62.52	819.56	25.26	324.26	28.77
EPS3	114.74	7.57	283.89	5.79	214.80	7.93
EPS5	125.36	6.67	258.48	5.12	183.69	7.25
EPST1	171.81	36.04	714.16	22.47	373.59	27.84
EPST3	97.27	5.04	338.76	4.65	247.34	6.71
EPST5	90.04	4.73	298.36	4.21	220.33	6.09

## 4.5 Chapter Summary

This Chapter proposed a combined method to quantitatively evaluate the dispersion and distribution of particles/aggregates in epoxy nanocomposites. This method is based on Equivalent Diameter measurement, 1<sup>st</sup> Nearest Neighbour Distance measurement and Quadrat-based Skewness measurements. The method was applied to nanocomposites with approximately spherical SiO<sub>2</sub> particles, however, quantifying the mixing state of nano-hBN based epoxy nanocomposites was not possible due to their highly perturbed morphology and the unclear SEM images this caused. Based on the proposed quantification method, epoxy nanocomposites with surface treated particles showed an overall better dispersion and distribution of particles/aggregates than those with untreated ones. Moreover, the worse mixing state of the EPS samples resulted in an adverse impact on the morphology of the epoxy matrix. In hBN-based samples, particles were more likely to exist individually and they therefore have a larger effect on the matrix which was observed in SEM results. These results will be used to help the investigation of structural and dielectric/electrical properties of epoxy nanocomposites in the following chapters.

Two modeling methods were also presented where Matlab was used to generate simulated distributions of particles/aggregates based on the quantification parameters defined in the previous part of this chapter. These methods aim to give a deeper understanding of epoxy SiO<sub>2</sub> nanocomposites and act as a foundation for simulation-based research into dielectric properties and their relationship with the measured morphology of nanocomposites.



## Chapter 5 Thermal Properties of Epoxy Nanocomposites

### 5.1 Thermogravimetric Analysis of Epoxy Nanocomposites

Thermal stability is one of the essential properties of polymers for some applications, such as structural parts in a high-temperature environment. Thermogravimetric analysis (TGA) has been widely used to investigate the epoxy nanocomposites [81, 106, 107]. In this chapter, the TGA technique was used to firstly investigate the differences between untreated and C8-treated SiO<sub>2</sub> particles. Then, the real filler loading concentrations of all epoxy nanocomposites were checked followed by an investigation into how nanoparticles would influence the thermal stability of epoxy composites.

#### 5.1.1 TGA on Surface Treatment

Figure 5-1 shows the TGA results of untreated and C8-treated particles which were immersed in dichloromethane (DCM) solutions. The first peak A is caused by evaporation of DCM. The second peak B is believed due to the loss of trimethoxy (octyl) chains on particle surfaces. Then, the surface density of C8 chains can be calculated as Equation 5.1 [108]:

$$\#C8 \cdot nm^{-2} = \frac{WT_2 - WT_1}{\frac{M_{C8}}{N_A}} / (SSA \times WT_1) \quad (5.1)$$

where  $WT_1$  is the sample weight at the temperature at the beginning of losing C8 chains and  $WT_2$  is the weight at the end temperature.  $M_{C8}$  is the molecular weight of C8 chains equal to 113 g·mol<sup>-1</sup>,  $N_A = 6.02 \times 10^{23}$  is Avogadro's constant, and  $SSA$  is the specific surface area as shown in Equation 5.2 [109]. Thus, the calculated surface density of C8 chains is ~10.67 nm<sup>-2</sup>.

$$SSA (m^2 \cdot g^{-2}) = \frac{6000}{d(nm) \times \rho(g \cdot cm^{-3})} \quad (5.2)$$

Moreover, if it is assumed that the density of the layers of C8 chains is equal to that of PE, which is 0.94 g·cm<sup>-3</sup>, then the weight of C8 per nm<sup>2</sup>,  $m_{C8}$ , can be

calculated according to Equation 5.3, and further the average thickness of layer of C8 chains,  $d_{C8}$ , can be obtained which is  $\sim 2.13$  nm.

$$d_{C8} = m_{C8} / (\rho \cdot S) = \frac{[(\#C8 \cdot nm^{-2}) \times M_{C8}]}{N_A} / (\rho \cdot S) \quad (5.3)$$

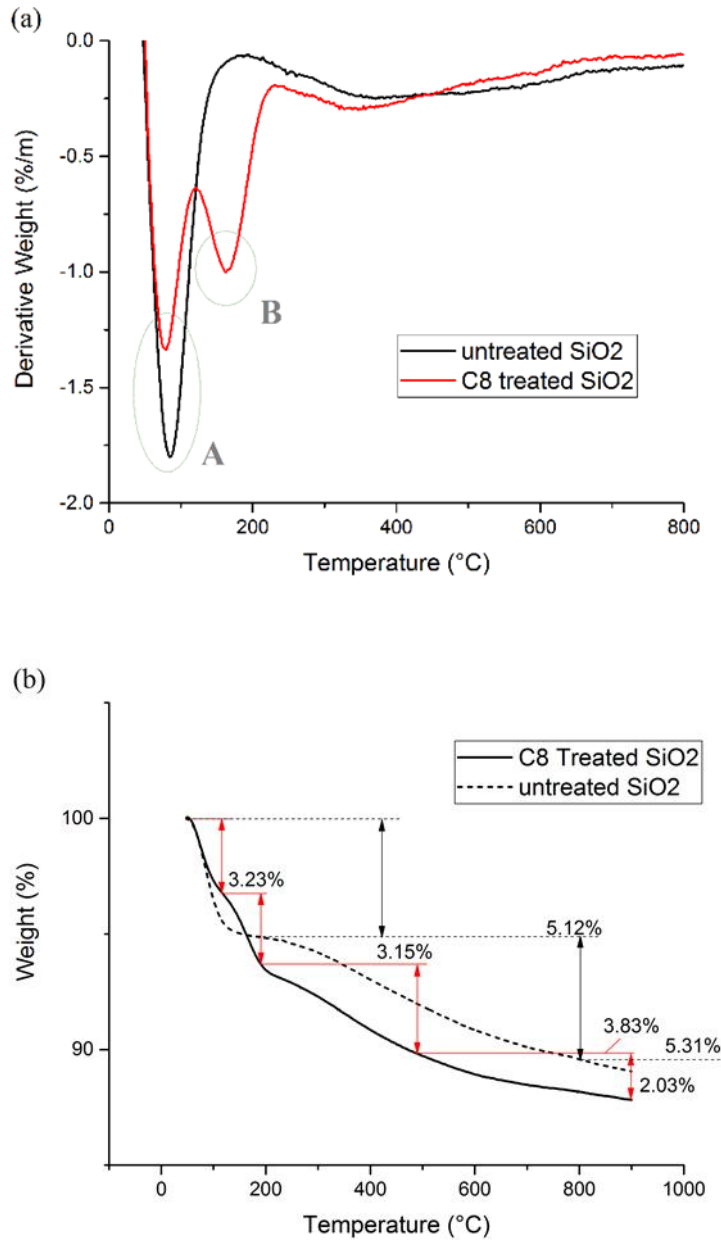


Figure 5-1 TGA result of (a) untreated and C8-treated SiO<sub>2</sub> particles with DCM; (b) detailed loss of weight in C8-treated SiO<sub>2</sub> particles.

### 5.1.2 TGA on Filler Loading Concentration

The measured filler loading concentrations of each type of sample are shown below in Table 5-1.

Table 5-1 Sample code and filler loading concentrations

Sample code	Type of particles	Theoretical loading concentration (wt%)	Real loading concentration (wt%)
EP0	N/A	N/A	N/A
EPS05	untreated SiO <sub>2</sub>	0.5	0.751 ± 0.090
EPS1	untreated SiO <sub>2</sub>	1	1.236 ± 0.081
EPS3	untreated SiO <sub>2</sub>	3	2.837 ± 0.021
EPS5	untreated SiO <sub>2</sub>	5	4.750 ± 0.078
EPST05	C8-treated SiO <sub>2</sub>	0.5	0.634 ± 0.096
EPST1	C8-treated SiO <sub>2</sub>	1	1.110 ± 0.136
EPST3	C8-treated SiO <sub>2</sub>	3	2.551 ± 0.047
EPST5	C8-treated SiO <sub>2</sub>	5	4.468 ± 0.090
EPB05	hBN	0.5	0.713 ± 0.028
EPB1	hBN	1	0.967 ± 0.062
EPB3	hBN	3	3.211 ± 0.038
EPB5	hBN	5	5.161 ± 0.086

### 5.1.3 TGA on Epoxy Nanocomposites

The purpose of study in this section is to investigate the influence of nanoparticles on the thermal stability of epoxy composites. Normally, two temperature indexes are used to clarify the thermal stability: one is initial decomposition temperature (IDT)  $T_{IDT}$  which indicates the 5% weight loss of total mass, another is the maximum rate loss temperature  $T_{max}$  [81, 82, 106]. Those most representative results of EP0, EPS, EPST and EPB samples are shown in Figures 5-2 to 5-7.

## Chapter 5 Thermal Properties of Epoxy Nanocomposites

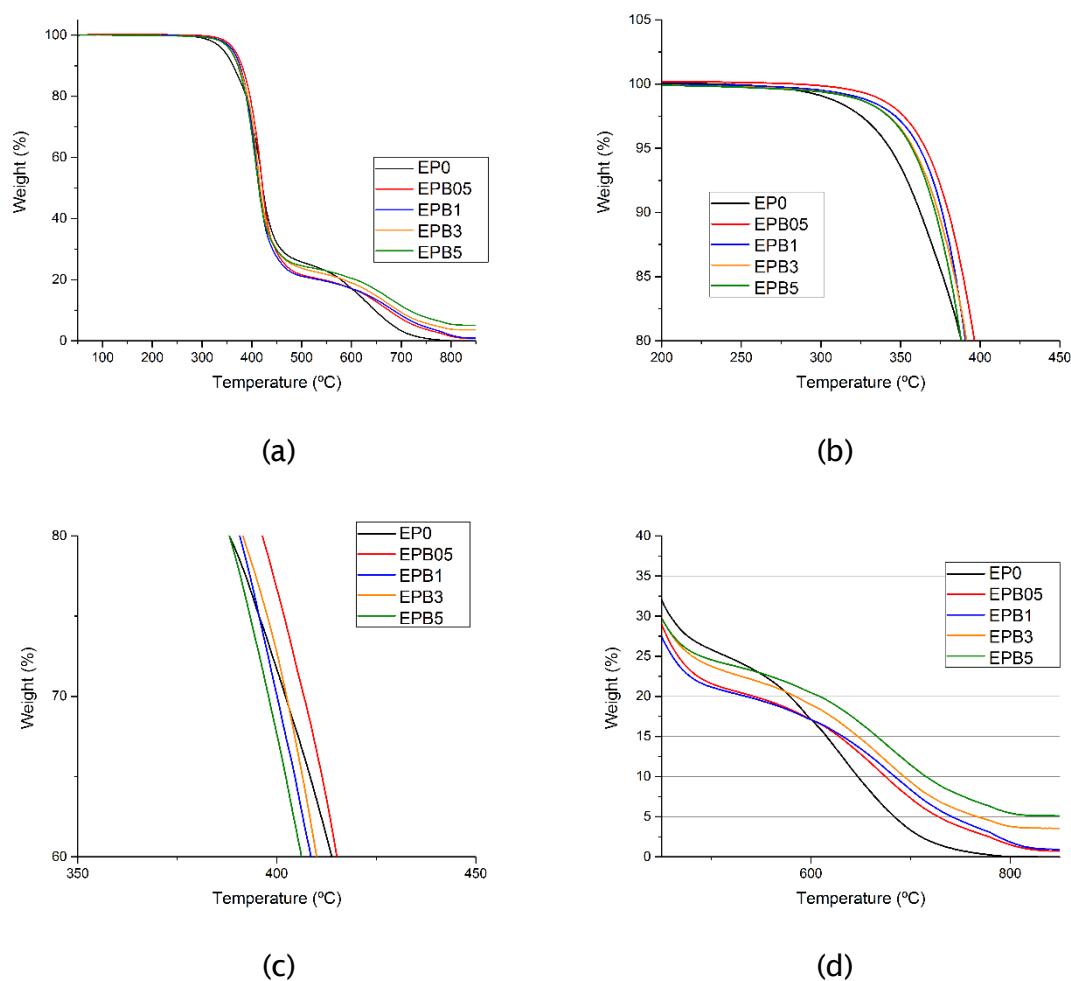


Figure 5-2 TGA traces of EPB in each loading concentration: (a) whole; (b), (c) and (d) zooming in to different temperature ranges.

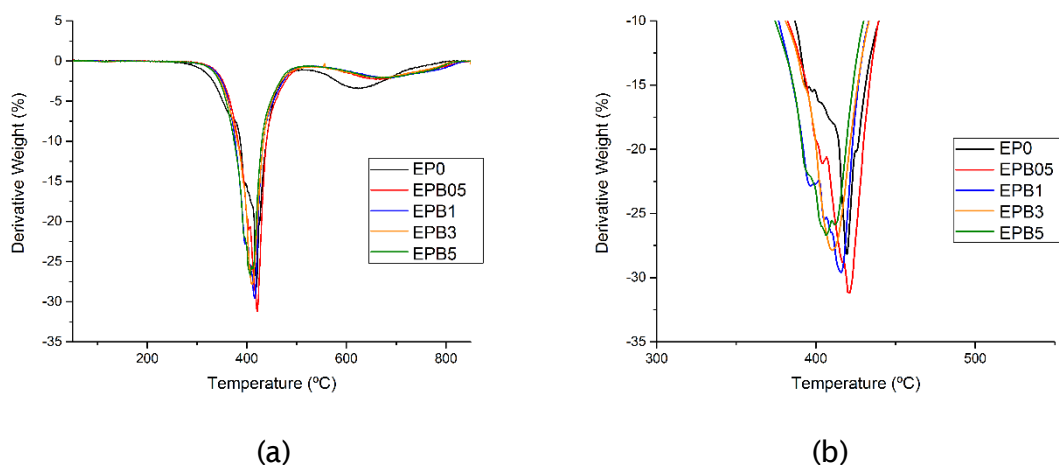


Figure 5-3 Derivative traces of EPB in each loading concentration: (a) whole; (b) zooming in on the temperature range at the maximum rate.



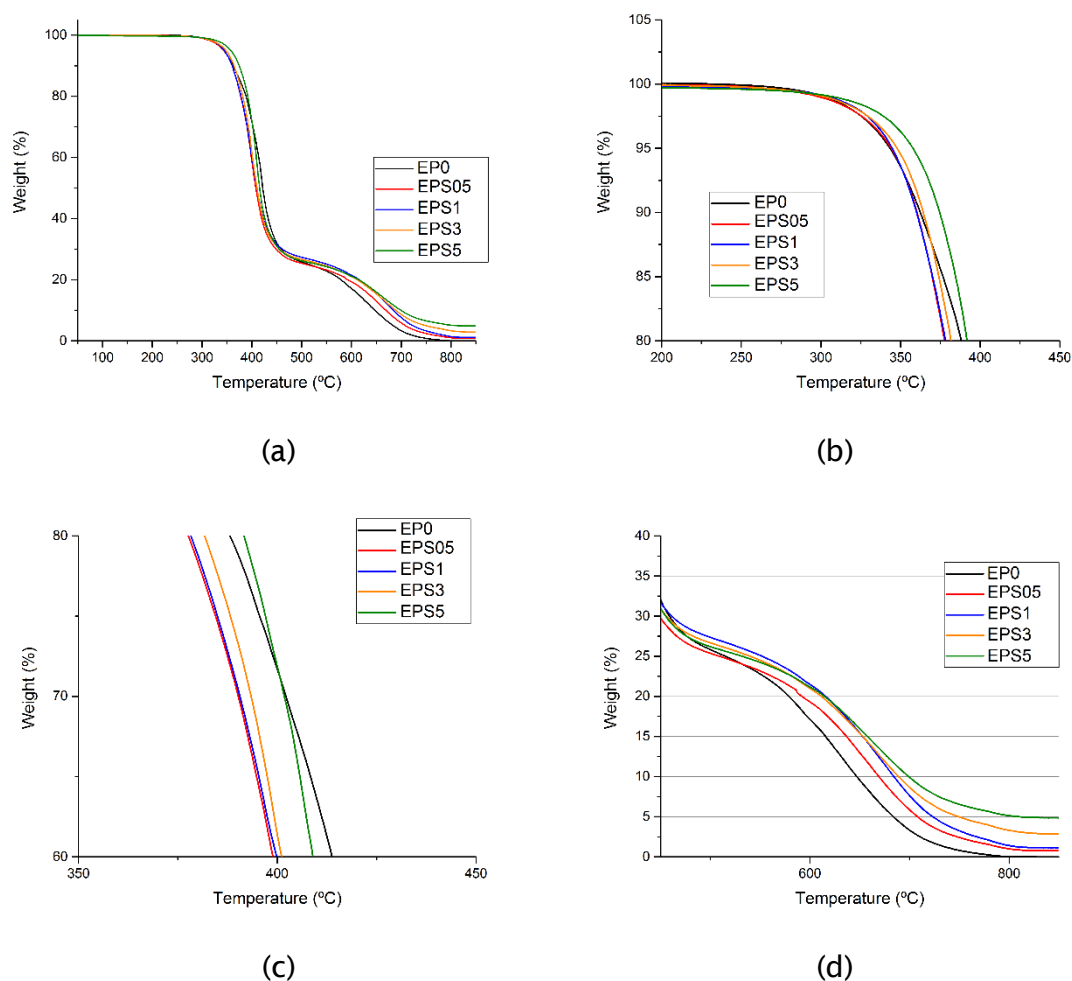


Figure 5-4 TGA traces of EPS in each loading concentration: (a) whole; (b), (c) and (d) zooming in to different temperature ranges.

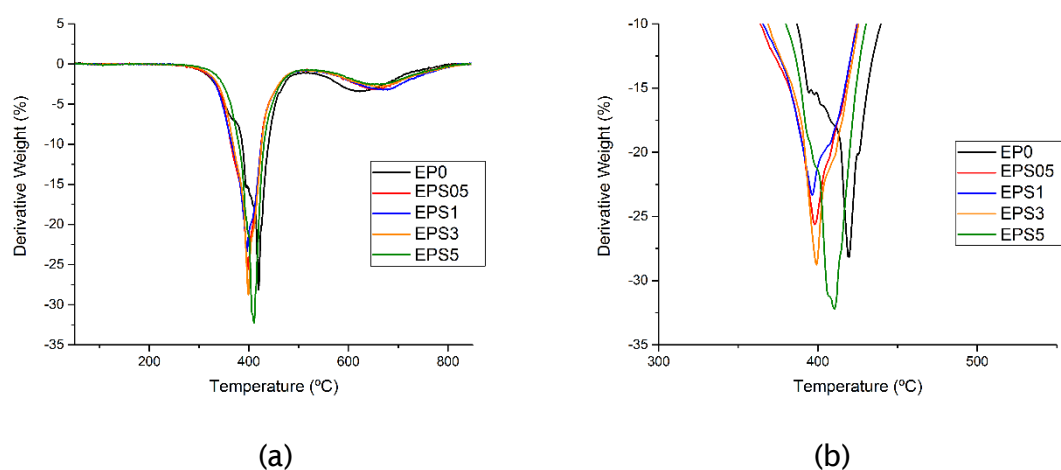


Figure 5-5 Derivative traces of EPS in each loading concentration: (a) whole; (b) zooming in on the temperature range at the maximum rate.

## Chapter 5 Thermal Properties of Epoxy Nanocomposites

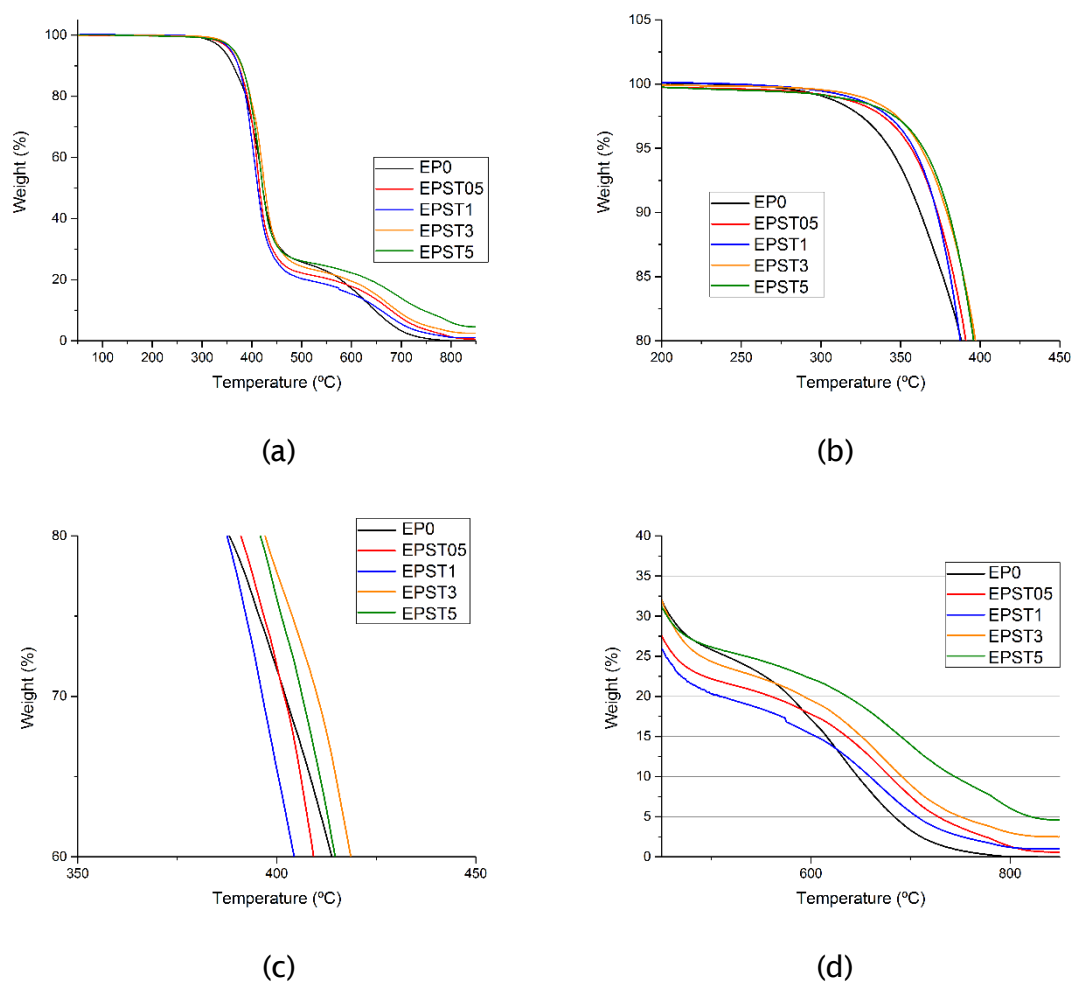


Figure 5-6 TGA traces of EPST in each loading concentration: (a) whole; (b), (c) and (d) zooming in to different temperature ranges.

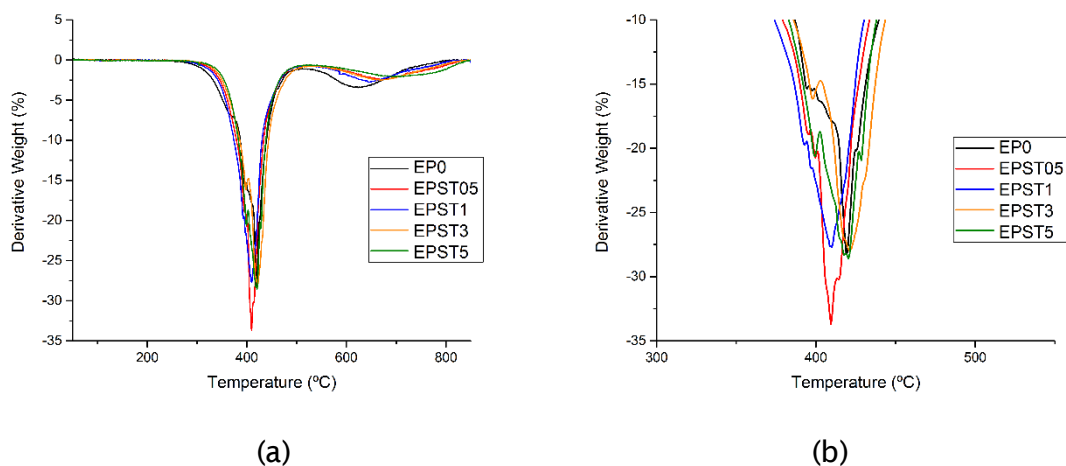


Figure 5-7 Derivative traces of EPST in each loading concentration: (a) whole; (b) zooming in on the temperature range at the maximum rate.

$T_{IDT}$  and  $T_{max}$  data of all the samples are collected and summarised in Table 5-2, and further compared in Figures 5-8 and 5-9.

Table 5-2  $T_{IDT}$  and  $T_{max}$  of epoxy and its nanocomposites

Samples	$T_{IDT}$ (°C)	$T_{max}$ (°C)
EP0	$343.35 \pm 2.06$	$419.63 \pm 3.58$
EPS05	$342.02 \pm 7.07$	$397.87 \pm 3.12$
EPS1	$344.46 \pm 3.55$	$396.51 \pm 2.77$
EPS3	$347.77 \pm 1.36$	$399.18 \pm 2.62$
EPS5	$357.99 \pm 2.37$	$410.55 \pm 3.27$
EPST05	$356.41 \pm 2.22$	$409.30 \pm 3.87$
EPST1	$358.28 \pm 3.95$	$408.71 \pm 1.63$
EPST3	$362.80 \pm 1.87$	$420.99 \pm 2.24$
EPST5	$364.45 \pm 0.87$	$420.37 \pm 2.78$
EPB05	$365.63 \pm 5.11$	$421.31 \pm 4.35$
EPB1	$361.96 \pm 1.50$	$417.28 \pm 1.34$
EPB3	$358.21 \pm 0.98$	$410.27 \pm 1.44$
EPB5	$357.25 \pm 0.90$	$406.78 \pm 1.06$

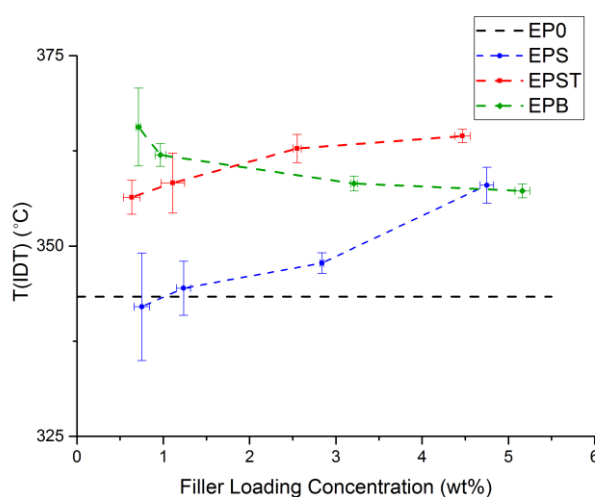


Figure 5-8 Comparison of  $T_{IDT}$  of EP0, EPS, EPST and EPB in different loading concentrations.

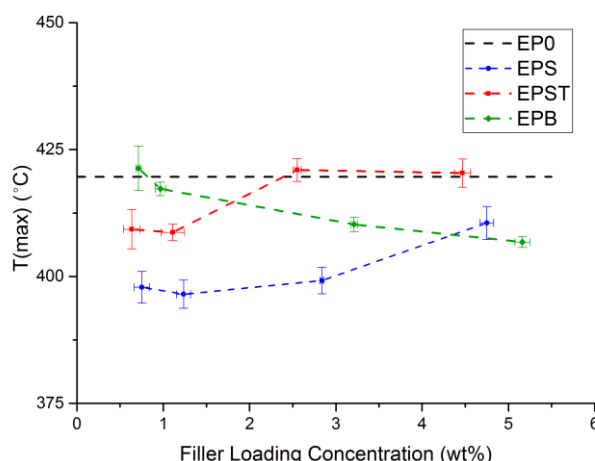


Figure 5-9 Comparison of  $T_{max}$  of EP0, EPS, EPST and EPB in different loading concentrations.

As shown in Figure 5-8, the initial decomposition temperature in EPS and EPST samples increases when compared to EP0, which is reportedly due to the filled silica restricting the mobility of polymer chains and acting as flame retardants for polymers [81, 83, 110]. The filled silica particles near the surface would form a layer to protect the materials from oxidizing [81, 111]. For EPS, there is a lower value in 0.5 wt% samples than the EP0 and may result from a lower cross-linking degree [112]. With the increase in filler loadings, the surface protective effect becomes dominant again. EPST shows similar increasing trends of  $T_{IDT}$ , however, results in most filler loadings are higher than the EPS samples. This phenomenon may be caused by the hydroxyl groups being left on silica particles in EPS samples that will lead to the formation of hydrogen bonds, then low cross-linking density at the interface and further lowering the  $T_{IDT}$ .

In EPB samples, as mentioned in section 4.2, hBN particles could have a significant impact on base material and lead to very low curing density. Such low curing density will create large numbers of short chains. As short chains are more thermally stable than longer ones which should exist more in EPS and EPST,  $T_{IDT}$  of EPB samples is higher than that of silica nanocomposites at 0.5 and 1 wt% and EP0. However,  $T_{IDT}$  of EPB decreases with the growth of filler loadings. This should be due to the much higher thermal conductivity of hBN when compared to silica particles, which are  $20\text{--}400\text{ W} \cdot \text{m}^{-1} \text{K}^{-1}$  [113] and  $1.4\text{ W} \cdot \text{m}^{-1} \text{K}^{-1}$  [114]. The higher thermal conductivity of nanocomposites in high loadings results in much more thermal energy transported into bulk and enhances the decomposition of polymers, despite the protective effect of particles near the materials' surface still working.

As shown in Figure 5-9, because most surface protective layers have been removed due to longtime decomposition,  $T_{\max}$  reflects the thermal stability of composites in bulk. Owing to the lower cross-linking density resulting from adding particles, all nanocomposites show lower  $T_{\max}$  than EP0 [81, 106], whereas EPB05 shows higher value due to the higher stability of short chains. For EPS and EPST, the increasing  $T_{\max}$  in high loadings should be caused by the formation of carbonaceous-silicate char that hinders/slows the oxidization of bulks [115]. In addition, the difference between them shares the same mechanism in that of  $T_{\text{IDT}}$ . Most  $T_{\text{IDT}}$  and  $T_{\max}$  results of EPB samples are little higher than EPS samples, which may indicate that the thermal stability in the high temperature of epoxy BN nanocomposites is better than untreated silica samples. However, the stability of EPB becomes worse while increasing the filler loadings.

## 5.2 Differential Scanning Calorimetry of Epoxy Nanocomposites

### 5.2.1 Free Volume Theory on Glass Transition

In polymer chemistry, the Flory-Fox equation is a simple empirical formula that indicates the relationship between the molecular weight and the glass transition temperature of a polymer system. The equation was first introduced in 1950 by *Paul J. Flory* and *Thomas G. Fox* [116]. They built and demonstrated a new theory that the glass transition temperature is the temperature at which the free volume available for molecular motions achieved a minimum value, which is named the Free-Volume Theory. The concept of free volume can be most easily understood as a polymer chain's 'elbow room' in relation to the other polymer chains surrounding it [117].

The assumptions of free volume theory are listed below:

1. When the temperature is higher than  $T_g$ , the free volume will increase with the increase in temperature in order to ensure the polymer chains can move in the larger space.
2. When the temperature is close to  $T_g$ , the free volume will decrease with the decrease in temperature, and reach the lowest volume once the temperature is equal to  $T_g$ . Then, the movement of chains will be at a stage of freezing-like structure and morphology. With the decrease in free volume to the lowest value,

the process of chains freezing is also the process of the glass transition.

3. In the glass transition stage, the fraction of free volume in the total volume of the polymer matrix system will maintain a certain value.
4. Once transformed into the glass state, the free volume fraction will not change within the increase or decrease of the temperature and, therefore, the glass state can be regarded as an 'Equilibrium Free Volume State'.

In sum, the free volume may be able to help explain the results of DSC and thermal behaviour of the epoxy and its nanocomposites.

### 5.2.2 DSC Measurement Results

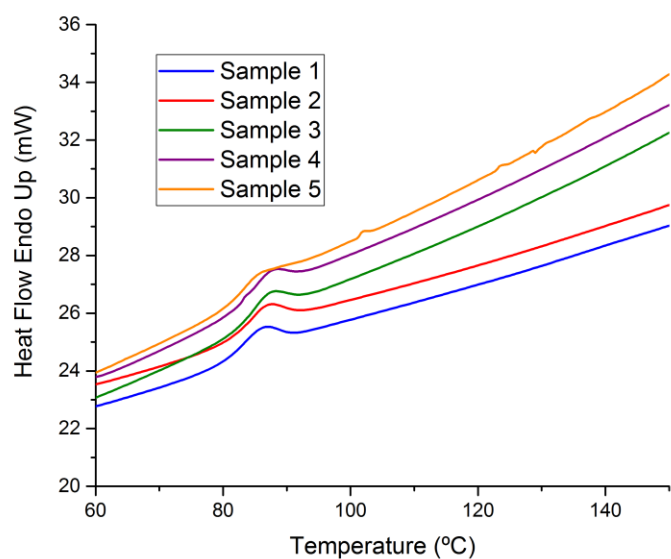
DSC has been used to study epoxy nanocomposites with nano-SiO<sub>2</sub> and nano-BN in different loading concentrations. In order to help understand the effect of the presence of nanofillers on  $T_g$  of epoxy composites, EPS, EPST and EPB samples were prepared.

#### 5.2.2.1 DSC results of Each Kind of Sample

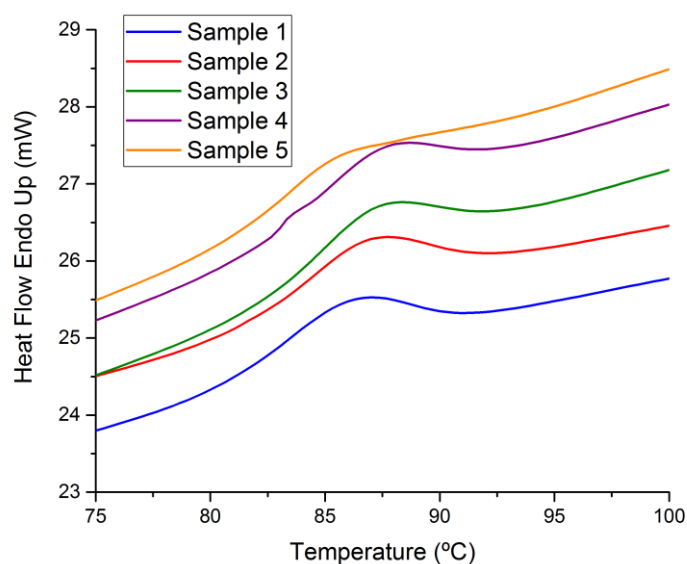
The glass transition temperature of epoxy and its nanocomposites have been measured by DSC and calculated by the method mentioned in section 3.3.4.  $T_g$  is equal to the average of the onset and end temperature of the glass transition.

##### ***A. Pure Epoxy Resin***

DSC results for all five small pieces (five-test) from one pure epoxy resin specimen are shown in Figure 5-10. From Figure 5-10 (b), first, it can be concluded that the cure degree of each part of the epoxy resin is uniform according to the similar  $T_g$ . Moreover, the sample was almost totally cured because of no significant exothermic peak being observed after glass transition which represents the post cure of the resin as shown in Figure 5-10 (a). Both indicate a good integrity of the sample.



(a)



(b)

Figure 5-10 DSC results of pure epoxy resins: (a) the whole curve of the DSC process; (b) zooming in on the glass transition process.

In order to further verify the curing process and ensure the accuracy of the measured  $T_g$ , each specimen was scanned 3 times and the results are shown in Figure 5-11. The  $T_g$  of the second scan becomes consistent and standard derivation shows the lowest value. Thus, the data of  $T_g$  for all the samples come from the second scan of each kind of composite. The results of EP0 samples are summarised in Table 5-3.

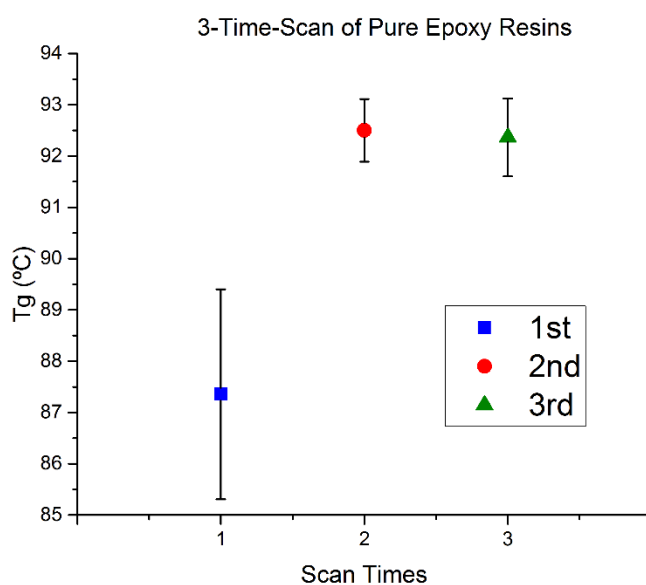


Figure 5-11 3-Time-Scan DSC results of pure epoxy resins.

Table 5-3 Onset, end and glass transition temperature of pure epoxy resins.

Sample code	Onset temperature (°C)	End temperature (°C)	T <sub>g</sub> (°C)
EPO-1	82.611	91.719	87.165
EPO-2	83.511	91.483	87.497
EPO-3	84.398	92.913	88.656
EPO-4	83.912	92.276	88.094
EPO-5	83.560	92.242	87.901
<b>Average</b>	83.608	92.127	87.863
<b>Std. Dev</b>	0.757	0.556	0.571

The average  $T_g$  is 87.863 °C which is similar to the  $T_g$  given by the datasheet about 85 °C, and the standard deviation of the onset and end temperature is small. Thus, it can be concluded that the glass transition process of pure samples is uniform.



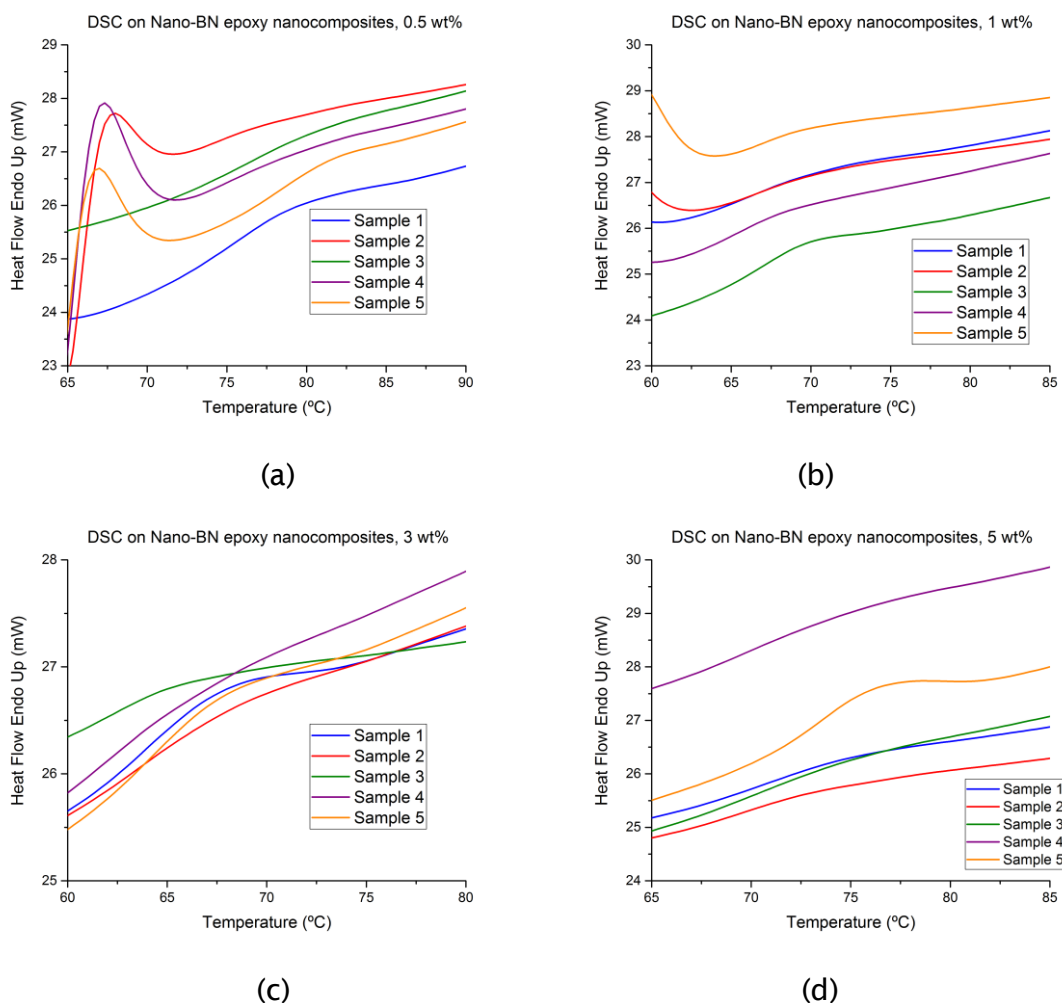
**B. Nano-BN Based Epoxy Nanocomposites**

Figure 5-12 DSC results of EPB in each filler loading concentration.

DSC results of five pieces (five-test) from epoxy nano-BN composites in each loading concentration are shown in Figure 5-12. From the figures, it can be concluded that the curing degree of samples is relatively high enough so that there is no significant exothermic peak being observed after glass transition which represents the post cure. Moreover, the 3-Time-Scan was applied to BN samples as well and data from the second scan is used. By using the method of calculating glass transition temperature mentioned in section 3.3.3, the  $T_g$  of the BN epoxy nanocomposites in each loading concentration is given in Table 5-4 and plotted in Figure 5-13 with error bars (standard deviation).

Table 5-4 Average glass transition temperature of BN epoxy nanocomposites in each loading concentration.

Sample code	Aver. T <sub>g</sub> (°C)	Std. Dev
EP0	87.863	0.571
EPB05	80.124	1.581
EPB1	72.424	0.696
EPB3	68.485	1.442
EPB5	75.685	1.330

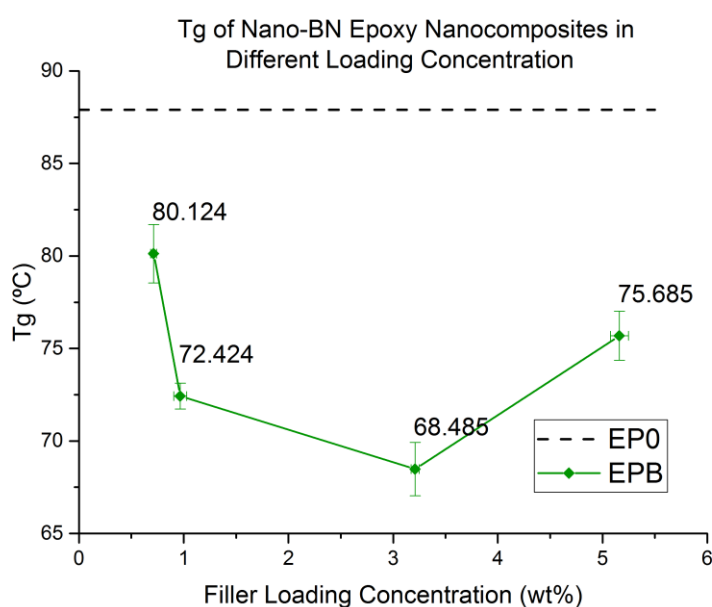


Figure 5-13 DSC results of EPB in different filler loading concentrations with error bars.

### C. Untreated Nano-SiO<sub>2</sub> Based Epoxy Nanocomposites

The most representative curves of each loading, which means the  $T_g$  of them is the closest ones to the average values of each five-test, are plotted in Figure 5-14. The glass transition temperature results of untreated nano-SiO<sub>2</sub> samples are calculated and summarised by using the same method for BN samples, as shown in Table 5-5 and plotted in Figure 5-15.

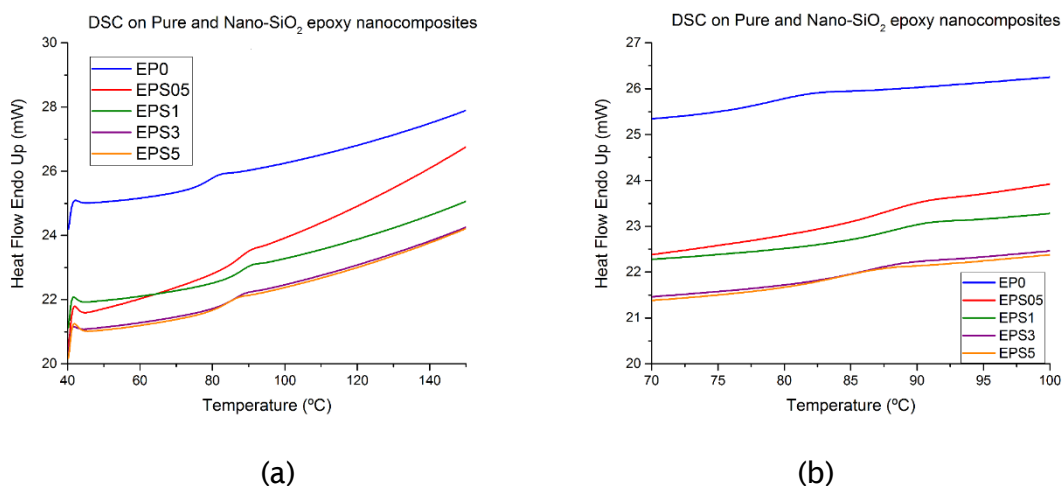


Figure 5-14 DSC results of EP0 and EPS in each filler loading concentration:  
 (a) the whole curves of the DSC process; (b) zooming in on the glass transition process.

Table 5-5 Glass transition temperature of EPS in each filler loading concentration.

Sample code	Aver. Tg (°C)	Std. Dev
EP0	87.863	0.571
EPS05	87.044	0.111
EPS1	86.825	0.443
EPS3	85.552	0.100
EPS5	83.794	0.254

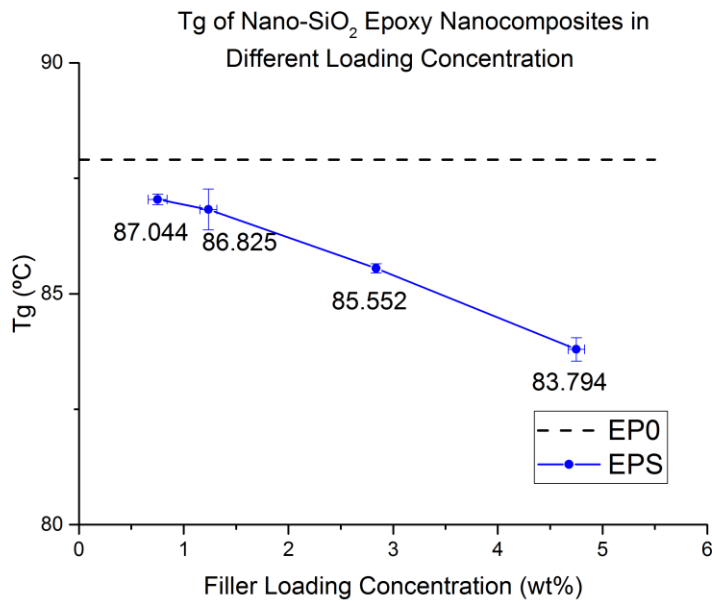


Figure 5-15 DSC results of EPS in different filler loading concentrations with error bars.

**D. C8-Treated Nano-SiO<sub>2</sub> Based Epoxy Nanocomposites**

The most representative curves of each loading, which means *T<sub>g</sub>* is the closest values to the average one of each five-test, and they are plotted in Figure 5-16. The glass transition temperature results of C8-treated nano-SiO<sub>2</sub> samples are calculated and summarised as shown in Table 5-6 and plotted in Figure 5-17.

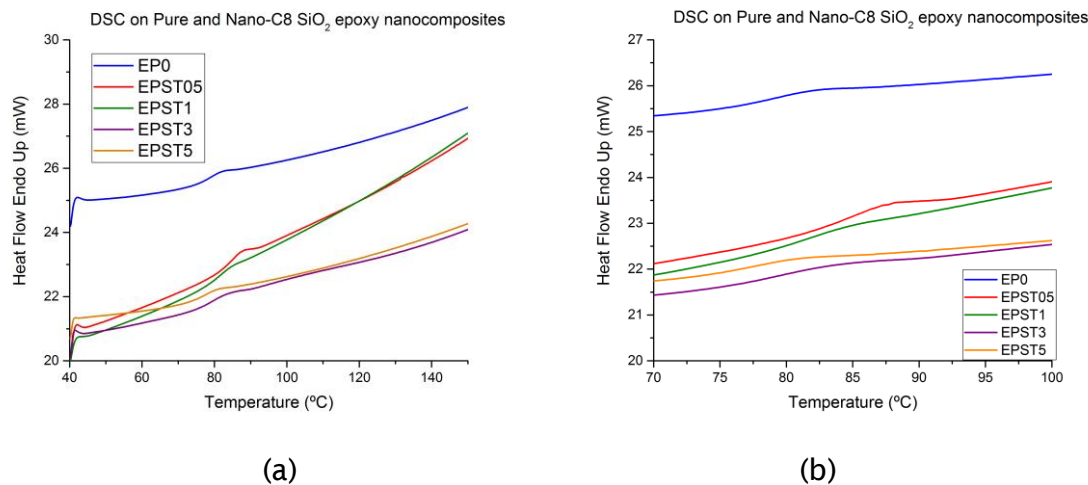


Figure 5-16 DSC results of EP0 and EPST in each filler loading concentration:  
(a) the whole curves of the DSC process; (b) zooming in on the glass transition process.

Table 5-6 Glass transition temperature of EPST in each filler loading concentration.

Sample code	Aver. Tg (°C)	Std. Dev
EP0	87.863	0.571
EPST05	85.674	1.605
EPST1	81.674	0.248
EPST3	79.116	0.356
EPST5	76.626	0.225

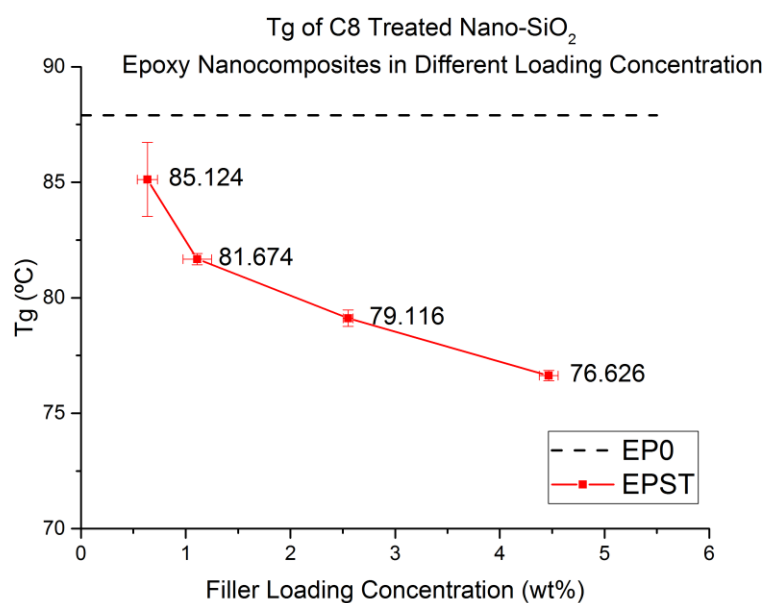


Figure 5-17 DSC results of EPST in different filler loading concentrations with error bars.

#### 5.2.2.2 DSC Study on the Effect of Filler Loading Concentration and Filler Type on Glass Transition Temperature

The glass transition temperature of a polymer system depends on various factors, including changes of the molecular weight, chain segment mobility, density of crosslinking, and the amount of reaction residue acting as a plasticiser [118]. In

this project, the ingredients and curing conditions of the nanocomposites were the same for all the samples. Thus, it is possible to make sure the changes in  $T_g$  are mainly due to the different loading concentrations, properties of the fillers and their influences upon the base material.

As shown in Figure 5-18, it is obvious that the  $T_g$  of epoxy nanocomposites is overall lower than that of EP0 and decreases with the growth of filler loading concentrations, though EPB5 shows an enhancement of  $T_g$ . This phenomenon should be, first, due to the lower cross-linking density of epoxy nanocomposites [106, 119].

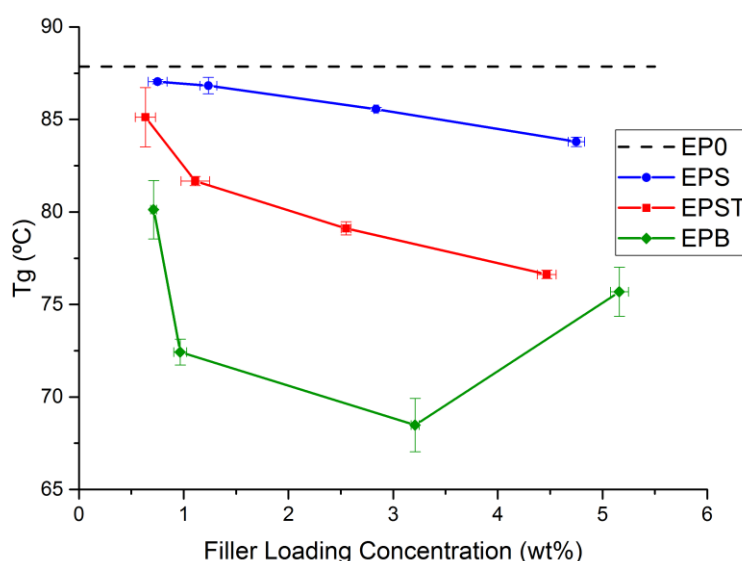


Figure 5-18 Comparison of the  $T_g$  of EP0, EPS, EPST and EPB samples in different filler loading concentrations.

Second, the surface characteristics of nanoparticles and the interfacial region between the polymer matrix and nanofillers can be used to explain the behaviours of  $T_g$ . Early studies indicated that the interfacial region was the most critical factor that influenced the  $T_g$  of polymer nanocomposites by *Starr et al.* [55, 120]. *Santanu* and *Thomas* then introduced the Dual Layer Model to explain the behaviours of  $T_g$  [55, 120]. In this model, the interfacial region around the nanofillers is divided into a tightly and loosely bound layer. The tightly bound region is the inner layer and it is tightly bound between nanoparticles and polymer chains by weak hydrogen bonds and thus limits the movements of the chains, which could increase the  $T_g$ . However, as the surface treatment of EPST samples is

not suitable, there is no tightly bound chain and this results in a higher mobility of chains in the interfacial areas. Thus, the  $T_g$  of EPST samples is lower than that of EPS. With the increase in filler loadings, the volume fraction of the interfacial area between the  $T_g$  matrix and particles increases significantly, especially the loosely bound layer where free volumes are more likely to locate, and this leads to the increase in free volume and the further reduction of  $T_g$  [54, 120, 121]. This has also been observed in [122, 123].

Regarding the EPB samples, the obvious lower value of  $T_g$  than pure and silica-based composites should be mainly due to the significant low cross-linking density of curing, which should become worse with the increase in filler loadings. Moreover, the higher thermal conductivity of hBN could play a role as well. However, it is noticed there is a smaller reduction of  $T_g$  in EPB3 and even increase in EPB5. This should be due to a mix of the exfoliated and intercalated macroscopic layer structures of hBN-based nanocomposites [124-126] as shown in Figure 5-19 which would impair the mobility of chain segments in the vicinity of particles, and thus increase the glass transition temperature [119, 127].

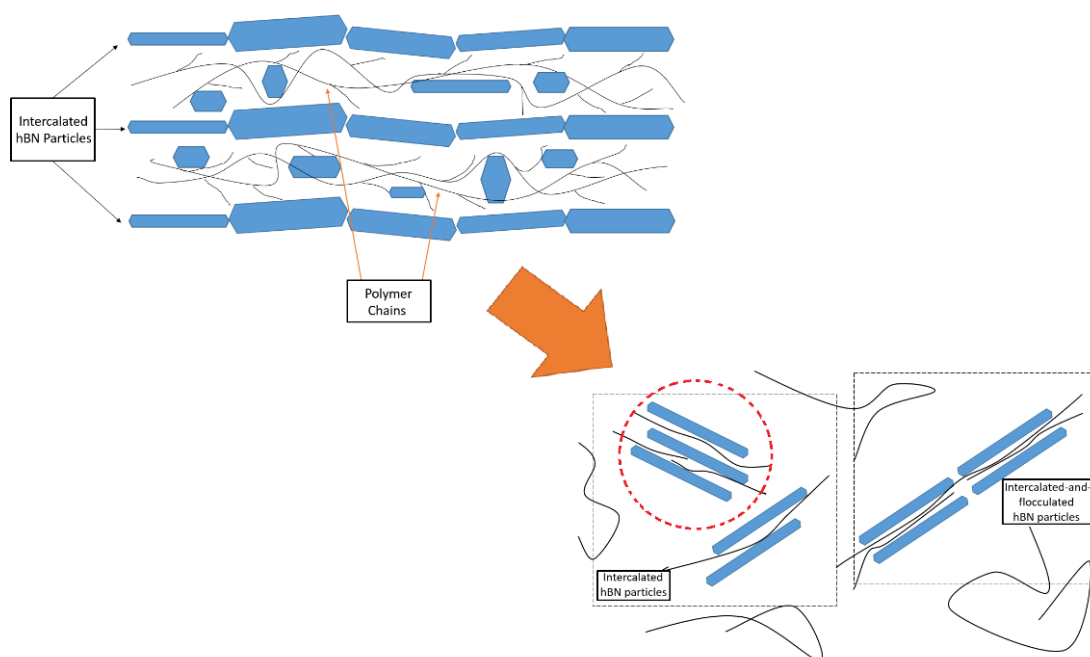


Figure 5-19 Illustration of exfoliated and intercalated macroscopic layer structures of hBN-based epoxy nanocomposites.

### 5.3 Chapter Summary

According to work in this chapter, the chemical structures and thermal properties of epoxy and its nanocomposites were investigated by TGA and DSC measurements, and the following conclusions can be made

1. The presence of nano-SiO<sub>2</sub> and hBN particles both led to the decrease in cross-linking density during curing of epoxy resins and further resulted in worse thermal stability than pure samples. However, particles acted as flame retardants for polymers and postponed the initiation of decomposition by hindering/slowing the oxidization.
2. When compared within two SiO<sub>2</sub>-based samples, surface treatment modified the cross-linking density in the interfacial areas by getting rid of some surface groups, like hydroxyl groups found in EPS samples, but unsuitable surface treatment led to the higher mobility of chain segments at the interface and thus the reduction of  $T_g$  in EPST samples.
3. The morphology of EPB samples had a significant impact on its thermal properties: in TGA measurement, shorter chains resulted in improved performance when decomposing, while in the DSC measurement, exfoliated and intercalated macroscopic layer structures of hBN-based nanocomposites, which was observed in Chapter 4, restricted the mobility of chain segments in the vicinity of particles and led to the increase in  $T_g$  in samples with higher filler loadings.
4. The cross-linking density of samples should mainly affect the results of TGA, whereas the mobility of chain segments played the main role in influencing the glass transition temperature of polymer composites.

As the dielectric/electrical properties of polymer nanocomposites are highly influenced by their chemical structures, the work in this chapter is to relate the preparation method to the structures of resultant samples and help understand the mechanism behind the phenomena observed in the following chapters.



## Chapter 6 AC & DC Breakdown Strength of Epoxy Nanocomposites

### 6.1 Breakdown Theories and Weibull Distribution

#### 6.1.1 Breakdown Theories

The definition of an electrical breakdown is that insulators lose their insulation performance under an applied electric field, and it can happen in solids, liquids, gases, even in vacuum condition. This insulation breakdown usually applies to high voltage applications and the breakdown voltage is the maximum voltage that can be applied to an insulating material before it fails. It is important to note that the breakdown voltage is not a fixed value, which is mainly because the breakdown is statistical and the value will vary within the different individual samples, which usually refers to the average value of a large group of tests. Regarding the mechanisms of electrical breakdown, there is the electron impact ionization mechanism, the thermal breakdown mechanism, the avalanche breakdown mechanism, the mechanical mechanism and the space charge breakdown mechanism. However, so far, it is still not clear which mechanism is correct and whether these mechanisms can be applied to different conditions.

In this project, both electrical and chemical properties of polymers need to be considered to understand and explain the breakdown behaviours of polymer dielectric materials. However, there are still many uncertain things, even in the simplest polymer system. Thus a comprehensive understanding should be made in order to develop a material of epoxy resin nanocomposites with good dielectric properties. Although the polymer nanocomposites seem to have better dielectric properties compared to pure composite materials, there is still much work required before it is widely used in application. The most popular explanations of the mechanism will be introduced in the following section.

Impact ionization is a process where a charge carrier loses its energy through the method of creating new charge carriers. *Hippel* put forward the ionization model for this mechanism [128, 129]. According to *Von Hippel*, in a dielectric polymer, positive ions in the materials are not affected by the external field, but the electron can pass through the matrix if the electric field is high enough. Under a high electric field, electrons will move towards the anode and leave the positive ions behind.

The distribution of the electric field will be influenced by positively charged ions that may also lead to the ionization process. The repetition of the ionization process will weaken the heat insulation properties of materials and ultimately lead to the electrical failure of materials. This failure mechanism is called the electron impact ionization mechanism. As this theory only provides the theoretical hypothesis that the applied electric field was high enough to ensure electronic travel and had a sufficient possibility to traverse the maximum value of the excitation function, it is a relatively simple theory [130].

The electrons can knock other electrons out from molecules if they have enough energy. When the applied field is sufficiently high, the repetition of impact ionization will make material lose their insulation properties. This mechanism is called an avalanche breakdown. Avalanche breakdown usually involves long-term partial discharge (PD) that leads to the formation of a conductive channel in insulating materials. Once the channel is formed, then breakdown occurs [131]. Moreover, *Sharbaugh* developed a model that combines both avalanche and bubble theory [132]. He believed that these two theories could be put together to create a new theory to describe both theories and phenomenon in order to give accurate predictions of a breakdown in insulating materials before application.

Owing to their inherent properties, the insulation properties of lots of dielectric materials change with the temperature. When the dielectric material is applied to the electric field, the temperature will continue to increase if heat is generated due to the conductivity and eventually this will lead to the loss of insulation material. This process is called thermal breakdown. The thermal breakdown strength is much lower when compared with the electrical breakdown. *Nagao* investigated the influences of thermal conditions on the breakdown strength of polyethylene (PE) samples [133]. In his study, PE was prepared as film samples. Once samples of PE breakdown at room temperature, the presence of local joule heat could be observed and there would be high-temperature points in the films. Then, with the continuation of time, conduction current at those points could be observed and thus led to a dielectric breakdown. These phenomena suggest that a thermal breakdown process has taken place, which refutes the idea that the dielectric breakdown is a pure electronic process at room temperature [134]. Moreover, owing to the observation of local Joule heating, some defects should appear at the high-temperature point in the film sample resulting from cracks, cavities or impurities. *Nagao* assumed that the dielectric molecules would leave the region of the electrode due to the heating effects. Thus, the dielectric breakdown will make

the sample thinner at those points. The charging current can be described by Equation 6.1 as shown below:

$$I = I_0 \cdot \exp\left(-\frac{H}{\kappa T}\right) \quad (6.1)$$

where  $I$ ,  $I_0$ ,  $\kappa$ , and  $T$  are the charging current, a constant, the activation energy, the Boltzmann constant, and the absolute temperature respectively.

Moreover, the understanding of the effective magnitude of the thermal process on dielectric breakdown is still unclear. *Hikita* found that the breakdown strength of PVDF decreased when the temperature was higher than 50 °C [135]. The rate of decrease is mainly determined by the applied electric field rate rather than sample thickness. Therefore, the ionic conduction controlled the breakdown. However, the thermal effect on the breakdown is still ambiguous. One primary problem is that there is no supporting evidence on the relationship between the increase in temperature and current. So far, most researches tend to agree that the overheating will lead to a current increase [136].

The theories above are a summary that can provide a basic understanding of the mechanisms of the dielectric breakdown to give explanations on experimental results.

### 6.1.2 Weibull Distribution

During the test, a voltage with a certain ramping rate is applied to the sample with breakdown voltages being recorded, and the breakdown strength can be then calculated. Then, the Weibull 7++ software package (supplied by Reliasoft®) was used to analyse the results of the BD data. The Weibull distribution was firstly introduced by *Weibull* in 1951 and has developed into a viral continuous probability distribution that is widely used in describing the reliability and life tests. Owing to its flexibility, it is the most commonly used probability distribution in breakdown studies and also recommended by the Institute of Electrical and Electronics Engineers (IEEE) as the standard probability distribution.

The Weibull distribution allows either one, two or three parameters to describe the breakdown distribution [135, 137]. The studies by *C. Green* showed that using one-parameter Weibull could not meet the requirement of the accuracy of experiments. Moreover, improvements by using three parameters did not make a big difference compared with two-parameters [138] and most researchers were more likely to the

select two-parameter Weibull to analyse their data. Therefore, the two-parameter Weibull was introduced in this project. Equation 6.2, the two-parameter Weibull is shown below:

$$P_f(x) = 1 - \exp\left[-\frac{E}{\eta}\right]^\beta \quad (6.2)$$

where  $P_f$ ,  $\eta$ , and  $\beta$  represent the cumulative failure probability, the scale, and shape parameters, respectively. The scale parameter  $\eta$  is the electric field strength for which the probability for failure is 63.2% and is widely and commonly used. Moreover, the shape parameter  $\beta$  is analogous to the inverse of the standard deviation. The results are shown in the form of a probability plot, whose x-axis shows the AC breakdown strength while the y-axis is the probability of failure for tested samples at certain AC field strength.

Moreover, by using the upper and lower confidence bounds, the results can be described much more accurately as shown in Figure 6-1 [139].

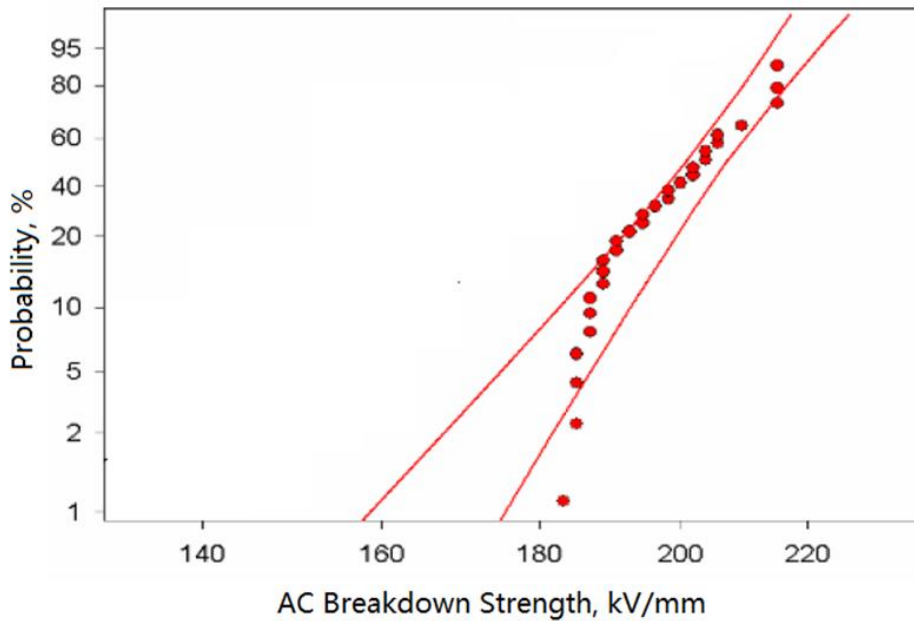


Figure 6-1 Example of Weibull distribution of AC breakdown strength with confidence bound [4].

## 6.2 AC Breakdown Experiments

### 6.2.1 Results by Weibull 7++

The Weibull distribution plots for epoxy nanocomposites filled with untreated nano-SiO<sub>2</sub>, C8-treated nano-SiO<sub>2</sub> and nano-hBN are shown in Figures 6-2, 6-3 and 6-4 respectively. Moreover, the results of pure epoxy resins are also shown as a control group in each plot. The maximum likelihood estimation (MLE) is used as the parameter estimator for the breakdown data, and the parameters of the Weibull distribution of nano-SiO<sub>2</sub> and hBN-based samples are also shown in Table 6-1.

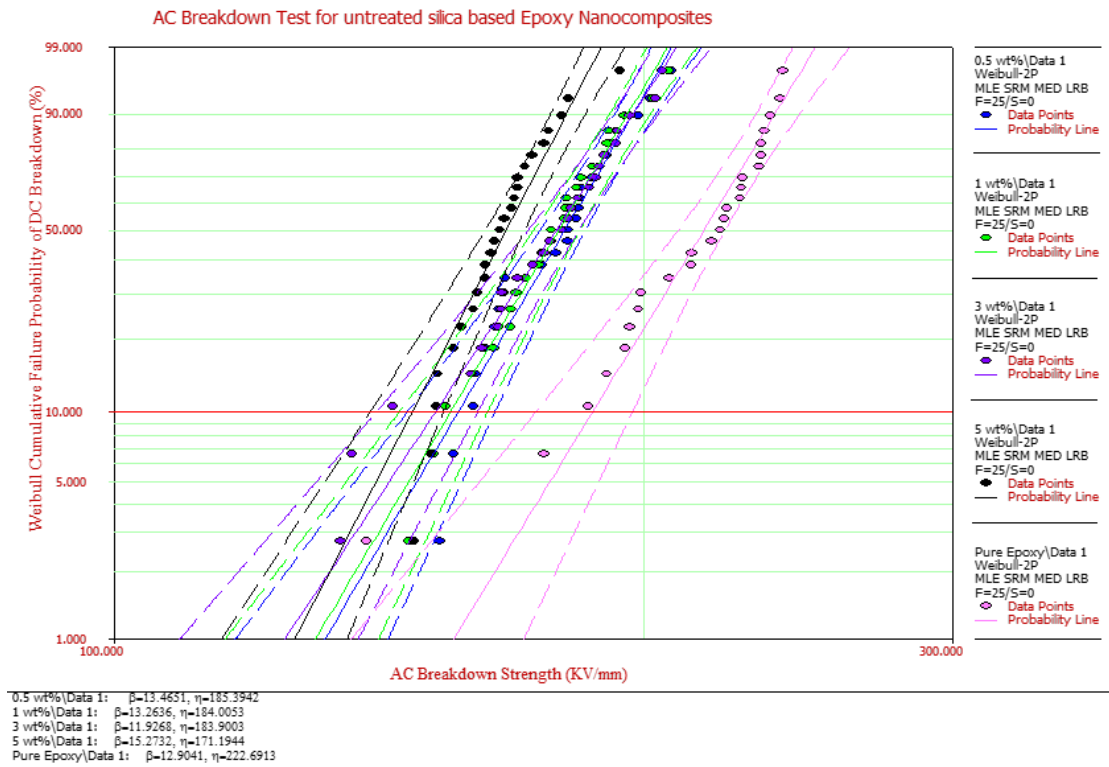


Figure 6-2 Weibull plot of EPS samples in different filler loading concentrations on AC breakdown strength.

## Chapter 6 AC and DC Breakdown Strength

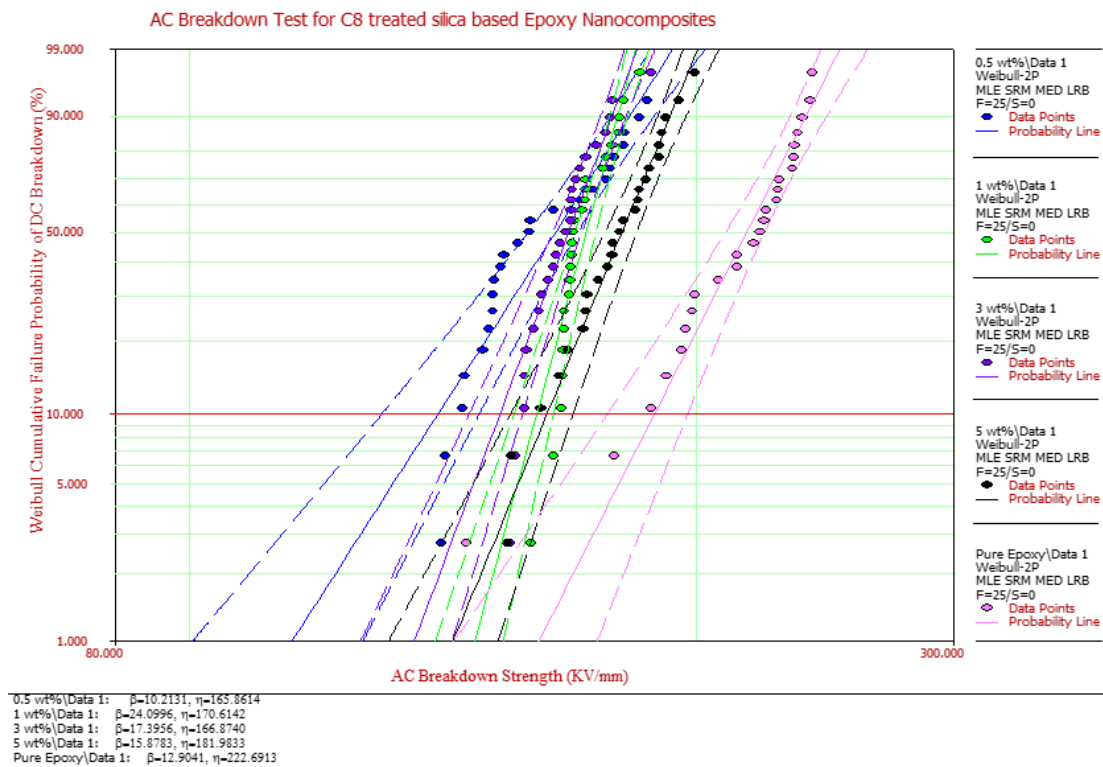


Figure 6-3 Weibull plot of EPST samples in different filler loading concentrations on AC breakdown strength.

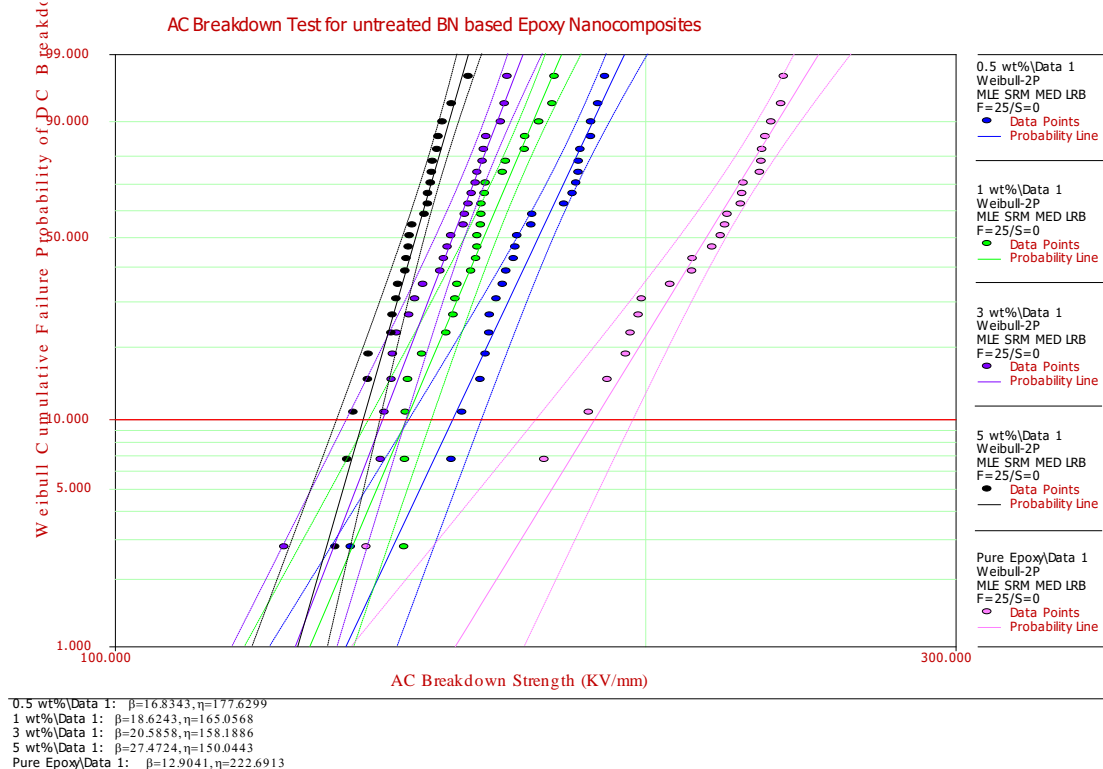


Figure 6-4 Weibull plot of EPB samples in different filler loading concentrations on AC breakdown strength.

According to the testing results, the AC breakdown strength of EP0 is  $222.7 \text{ kV} \cdot \text{mm}^{-1}$ . For EPS samples, a decrease in breakdown strengths with the growth of the loading concentration is observed, and EPS show an obvious reduction in breakdown strength when compared to EP0. As shown in Figure 6-2, EPS05 shows a significantly lower breakdown strength ( $\eta$ ) and slightly lower scatter ( $\beta$ ). The BD further decreases with the increase in filler loading concentration. The reduction in the breakdown strength of EPS samples is at least  $37.7 \text{ kV} \cdot \text{mm}^{-1}$ , and EPS5 shows the worst characteristics that BD strength is  $51.5 \text{ kV/mm}$  lower than EP0 at  $171.2 \text{ kV} \cdot \text{mm}^{-1}$ , which is much lower than samples with other filler loading concentrations. Compared to EPS, EPST shows lower AC breakdown strength in samples with low filler loading concentrations but the enhanced value in ones with higher filler loadings.

Table 6-1 Weibull parameters of epoxy and its nanocomposites, AC BD tests

Sample code	Scale Parameter ( $\eta$ ) ( $\text{kV} \cdot \text{mm}^{-1}$ )	Shape Parameter ( $\beta$ )
EP0	$222.7 \pm 6.1$	12.9
EPS05	$185.4 \pm 4.9$	13.5
EPS1	$184.0 \pm 5.0$	13.2
EPS3	$183.9 \pm 5.5$	11.9
EPS5	$171.2 \pm 4.0$	15.3
EPST05	$165.9 \pm 5.8$	10.2
EPST1	$170.6 \pm 2.5$	24.1
EPST3	$166.9 \pm 3.4$	17.4
EPST5	$182.0 \pm 4.1$	15.9
EPB05	$177.6 \pm 3.8$	16.8
EPB1	$165.1 \pm 3.2$	18.6
EPB3	$158.2 \pm 2.7$	20.6
EPB5	$150.0 \pm 1.9$	27.5

As shown in Figure 6-4, EPB samples exhibit a reduction in breakdown strength. The lowest reduction in the breakdown strength of EPB is at  $45.1 \text{ kV} \cdot \text{mm}^{-1}$  in EPB05, and EPB5 samples show the worst properties with  $72.7 \text{ kV} \cdot \text{mm}^{-1}$  lower than EP0, at  $150.0 \text{ kV} \cdot \text{mm}^{-1}$ .

Moreover, as shown in Figures 6-5, 6-6 and 6-7, the shape parameters of EP0 and EPS samples are at a low level. EPST samples show a reduction with the growth of filler loading concentration, whereas the EPST05 shows the lowest value. In addition, EPB samples exhibit an increase with filler loadings. Thus, it seems the filler type and surface treatment have a significant influence on the shape parameter of AC breakdown results.

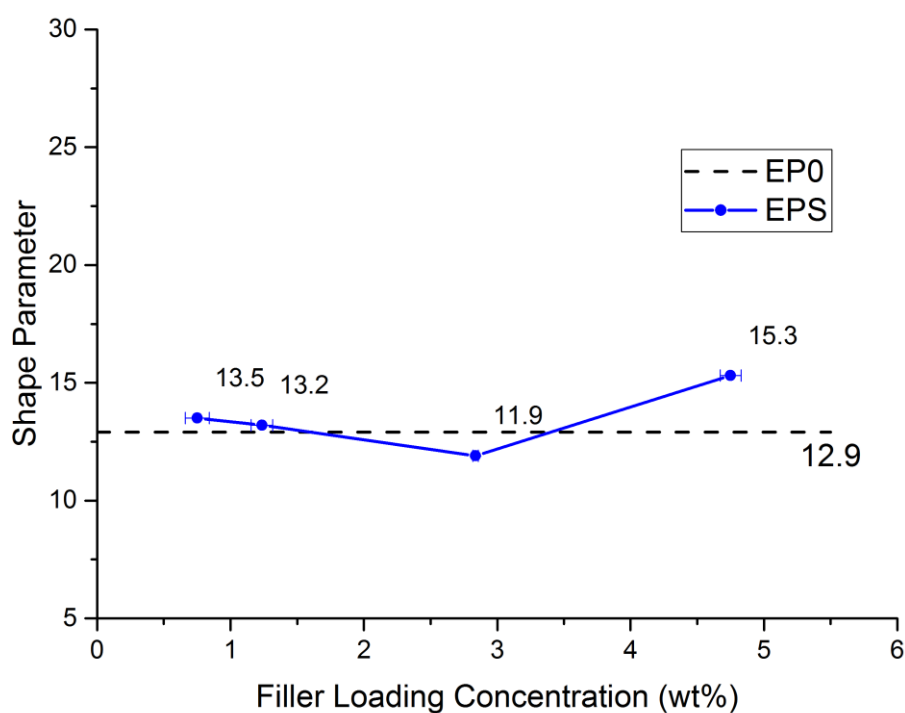


Figure 6-5 Shape parameter  $\beta$  of EPS in different filler load concentrations.



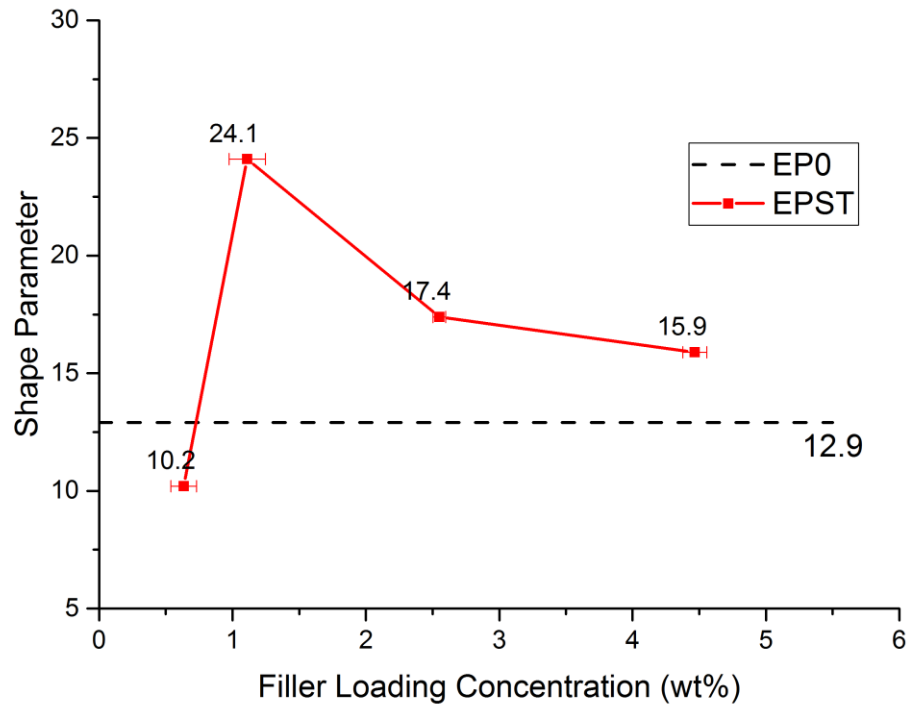


Figure 6-6 Shape parameter  $\beta$  of EPST in different filler load concentrations.

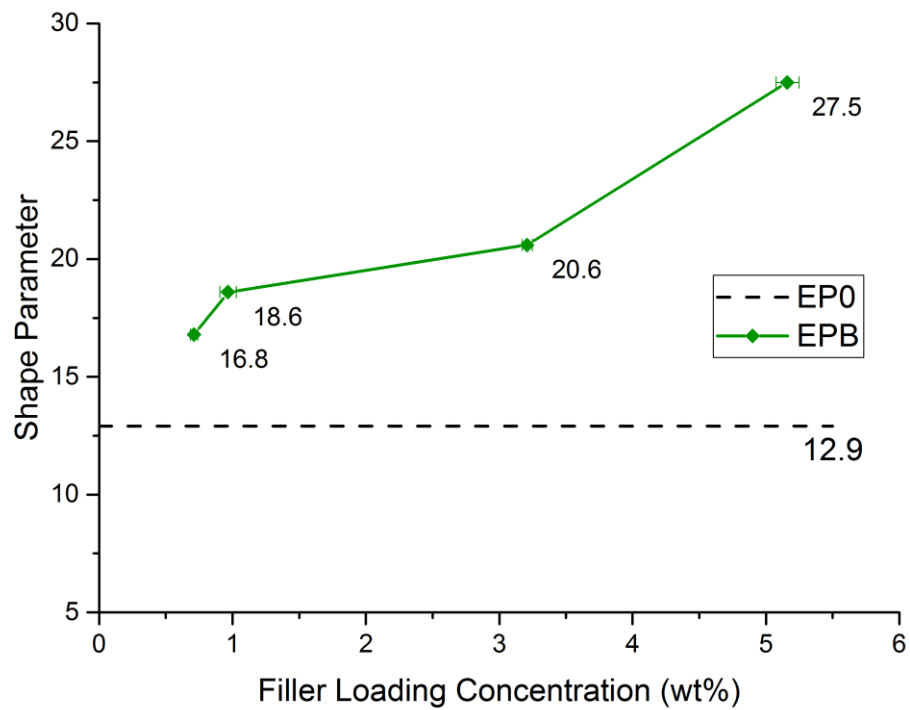


Figure 6-7 Shape parameter  $\beta$  of EPB in different filler load concentrations.

The shape parameter reflects the consistency degree of AC breakdown strength. Some studies also state that variations of  $\beta$  reflected cavities and impurities, and in samples, the large agglomeration of particles could act as impurities [38]. Therefore, based on the higher values in EPST samples than EPS samples, the surface treatment can help the nano-SiO<sub>2</sub> particles to achieve better dispersion and distribution in samples, which has already been observed in SEM results. However, with an increase in filler loading concentrations, the dispersion in EPST samples becomes worse. Moreover, the presence of nano-BN fillers enhances the consistency of the resulting AC breakdown strengths, which are worse, of epoxy composites and the effect grows with the filler loading concentration. As most of the AC BDs of hBN-based samples are at low values, the increasing shape parameter indicates the detrimental effect of hBN particles on morphology and the AC BD of composites becomes more and more obvious.

Above all, the presence of nanofillers shows no obvious improvement in epoxy composites' AC breakdown strength. Similar results were also observed by *Imai* et al. [46] and *Singha* et al. [34]. This should be because of the role of nanoparticles as impurities and the agglomeration that deteriorated the conditions. The addition of treated SiO<sub>2</sub> and hBN nanoparticles into epoxy resin relatively improve the shape parameter ( $\beta$ ), which was shown in several other studies, including ones from *Singha* et al. and *Hu* et al. [140].

### **6.2.2 Effect of Filler Loading Concentration and Filler Type on AC Breakdown Strength**

#### **6.2.2.1 Effect of Filler Loading Concentration on AC Breakdown Strength**

In order to understand how filler loading concentration influences the AC breakdown of EPS, EPST and EPB samples, Figures 6-8 to 6-10 are given below.

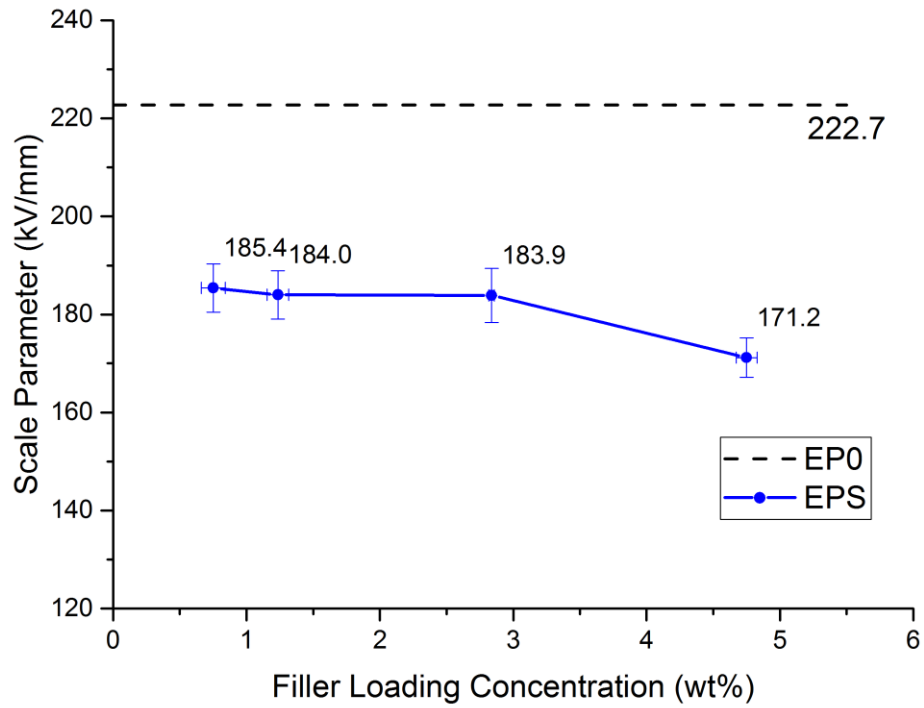


Figure 6-8 Scale parameter  $\eta$  ( $\text{kV} \cdot \text{mm}^{-1}$ ) of EPS in different filler load concentrations.

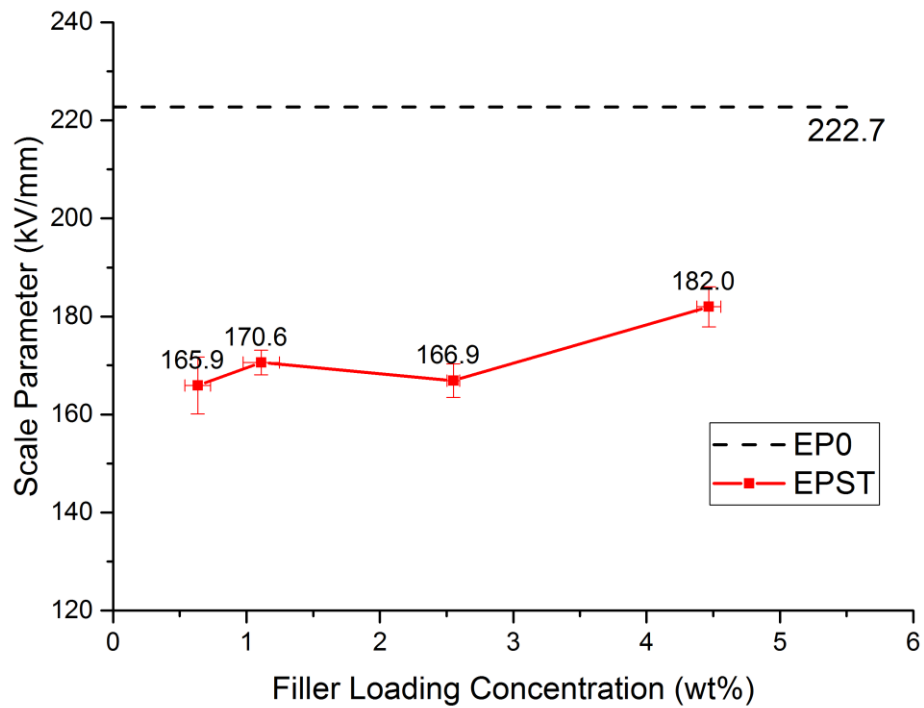


Figure 6-9 Scale parameter  $\eta$  ( $\text{kV} \cdot \text{mm}^{-1}$ ) of EPST in different filler load concentrations.

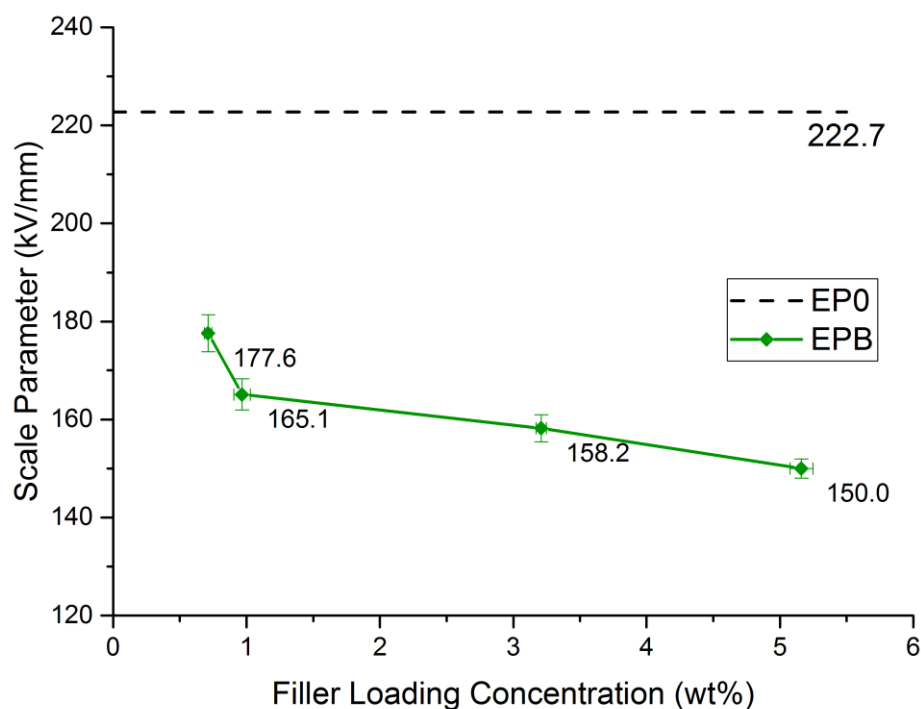


Figure 6-10 Scale parameter  $\eta$  ( $\text{kV} \cdot \text{mm}^{-1}$ ) of EPB in different filler load concentrations.

The results of the AC breakdown in EPS and EPB samples show similar trends. There are two possible reasons why AC breakdown strength in epoxy nanocomposites reduces with the growth of filler loading concentrations.

First, spherical nanoparticles can sometimes play a role as recombination centres [105], and with the growth of filler loadings, inter-particle/aggregate distances, or in other words, these ‘recombination centres’, will decrease, as shown in the SEM analysis result. Thus, the transport of positive charges along the long chains and electrons transported via inter-chain spaces [105] become easier from one centre to another. In early studies, it also showed that mobile charge carriers could travel easier through the loosely bound region. Therefore, once applying the electric field, charge carriers are more likely to travel in the bulk of polymer nanocomposites [141]. All these phenomena will result in lowering the percolation threshold of nanocomposites [142] and lead to the final reduction in BD strength when compared to pure samples. However, according to a study by *Zhou et al.* [143], AC breakdown happens, most of the time, at layers near the surfaces of film samples rather than going through the whole bulk. Thus, the observed reduction in inter-particle/aggregate distances with filler loadings, based on a study of the whole material, cannot be directly related to the AC BD behaviour of  $\text{SiO}_2$  particles based

epoxy nanocomposites but the local dispersion and distribution in the BD regions instead. This should be the reason why there is no significant difference in AC BD strength with the growth of filler loadings.

Second, once the applied electric field and the bulk of samples are injected with charges, due to electrostatic Coulomb forces and Van der Waals forces, nanoparticles will attract ions with opposite charges around them and form EDL in the range of the Debye shielding distance, as discussed in section 2.4.2. The presence of EDL will lead to a strong inner field in the tightly bound region. Furthermore, the agglomeration of nanoparticles could further enhance the reduction in breakdown strength. As the aggregates of nano-SiO<sub>2</sub> and nano-hBN would act as impurities in the samples, the enhancement of a field can be observed around the particles, which has also been observed in studies by *T. Andritsch* and illustrated in Figure 6-11 [3, 41, 144, 145]. In addition, the presence of voids and defects, caused by the process of sample preparation, will further lead to field enhancements. Such field enhancements thus result in an overall reduction in the breakdown strength compared to pure resins.

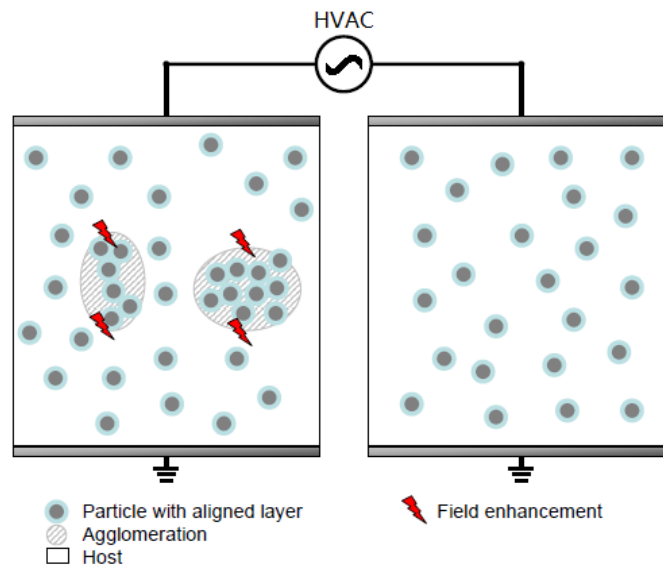


Figure 6-11 Illustration of the enhancements of the electric field caused by agglomerations of nanoparticles, compared with the situation without agglomerations [3].

In addition, in EPST samples, there is a small increase with the growth of filler loadings, which could be due to the presence of additional traps resulting from the functionalised surface at interphase [17, 146], and the density of traps at the interphase would increase with loadings and then impairs the mobility of charge

carriers. According to the results, agglomerations should have no significant effect on the AC breakdown strength of nanocomposites, which was also reported in [147]. Thus, it could be further concluded that reduction with the growth of filler loadings and the main differences between pure and nanocomposites are mainly due to the increase in the mobility of charge carriers.

### 6.2.2.2 Effect of Filler Type on AC Breakdown Strength

According to the BD strength in different filler loading concentrations in Figures 6-8 to 6-10, it can be observed that all BD strengths of the SiO<sub>2</sub> epoxy nanocomposites are higher than those of nano-hBN samples in each loading concentration. The differences between the two types of nanofillers is, first, caused by the different shape of particles. According to the modelling by *Lau* et al. and *Sharip* et al. [148, 149], the spherical particles have about 3 to 4 orders of lower electrical intensity around than that of plate-like particles. Thus, the higher value will deteriorate the breakdown strength. And based on the data shown in Table 6-2, it is hard to say if there is any relationship between permittivity of the two types of nanofillers and AC breakdown strength of resultant epoxy nanocomposites.

Table 6-2 Particle information

Type	Size (nm)	Structure	Shape	$\epsilon'$	References
SiO <sub>2</sub>	10-20 (BET)	Crystalline	Spherical	3.8-7.0	[77, 150, 151]
hBN	900 (APS) 200-500 (Crystal Size)	Hexagonal crystalline	Platelets	4.0-4.5	[78, 152, 153]

The main reason why EPST samples show worse AC BD than EPS samples would be caused by the residues of solvents introduced via surface treatment which could provide more charge carriers and was also reported in [10]. Moreover, as the surface treatment applied to nano-SiO<sub>2</sub> was not suitable for epoxy and could only get rid of the hydroxyl groups on the surface of particles, it was not able to form a tight bond in the interphase and did not modify the interphase behaviour. However, the higher BD strength in 5 wt% loading concentration is due to the better dispersion of particles and acts as the dominant mechanism instead of as described in the SEM results in section 4.3, to which the surface treatment contributed. This means the surface treatment can help SiO<sub>2</sub> particles disperse better and improve the AC breakdown strength in samples of high filler loading concentrations.

### 6.3 DC Breakdown Experiments

The data was analysed by Weibull 7++ software. In this project, the measurements of the DC breakdown strength of an epoxy and its nanocomposites shared the same purposes of AC breakdown tests, besides the effects of moisture.

#### 6.3.1 Results by Weibull 7++

The Weibull distribution plots for epoxy nanocomposites filled with untreated nano-SiO<sub>2</sub>, C8-treated nano-SiO<sub>2</sub> and nano-hBN are shown in Figures 6-12, 6-13 and 6-14 respectively. The results of pure epoxy resins are also shown as a control group in each plot. The maximum likelihood estimation (MLE) was used as the parameter estimator for the breakdown data, and the parameters of the Weibull distribution of nano-SiO<sub>2</sub> and hBN are also shown in Table 6-3.

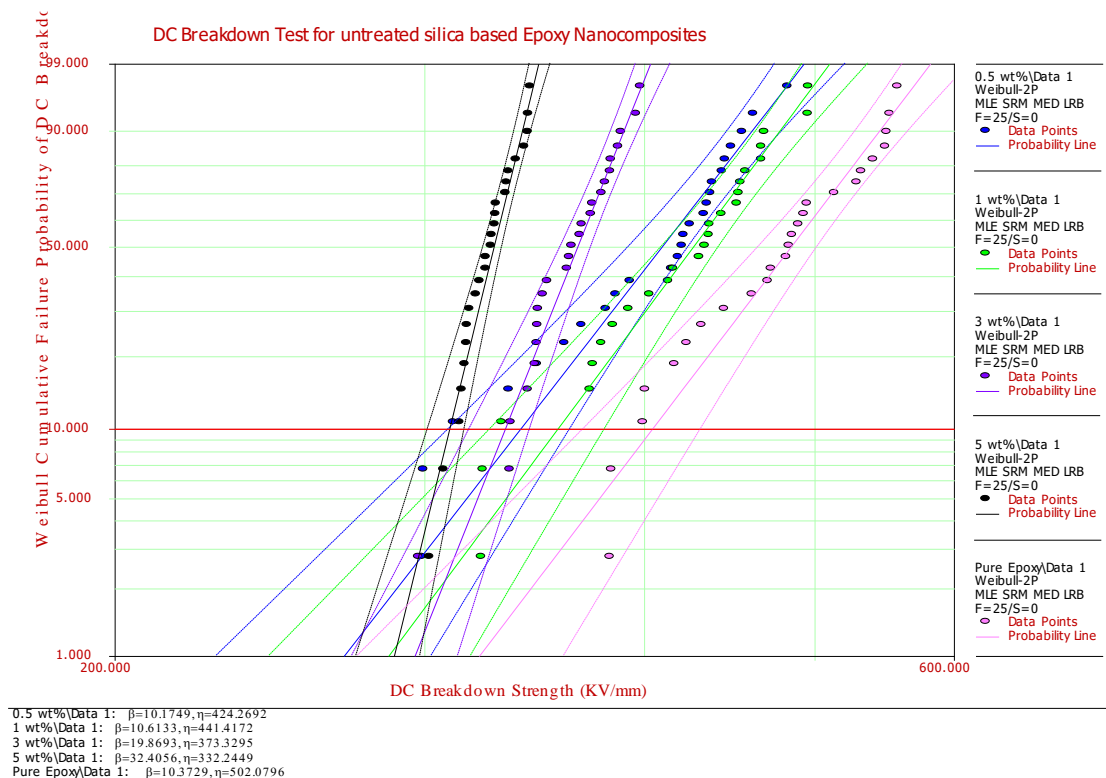


Figure 6-12 Weibull plot of EPS samples in different loading concentrations on DC breakdown strength, dry.

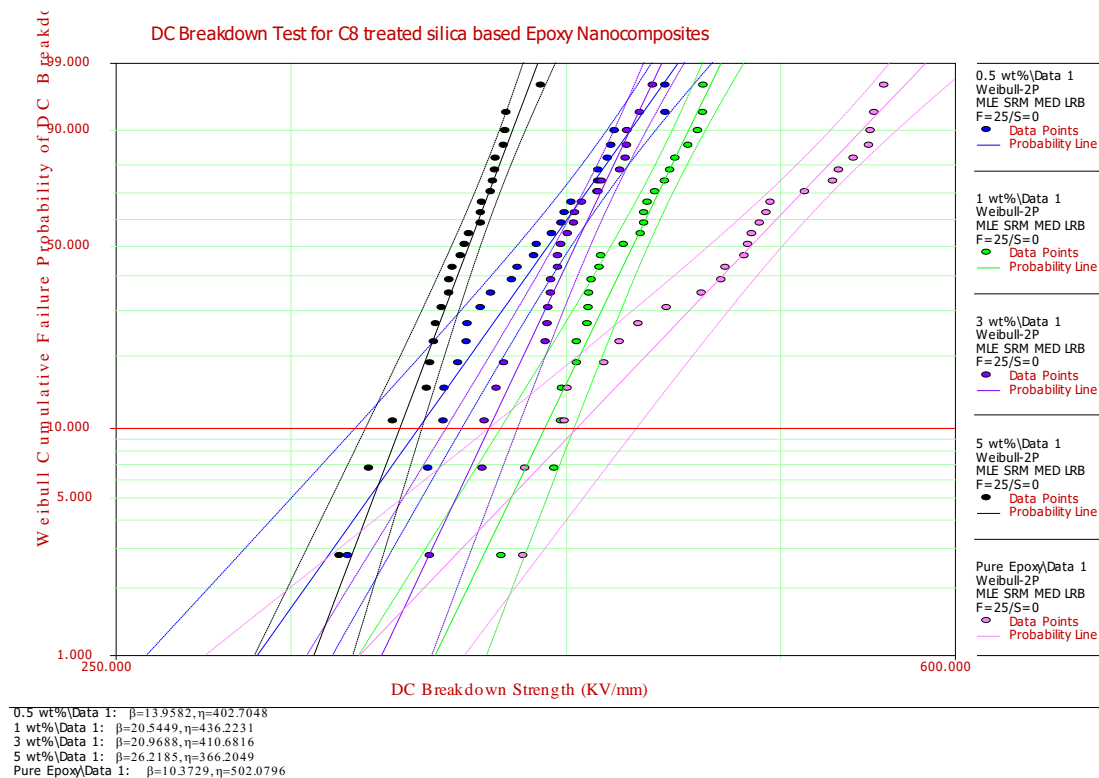


Figure 6-13 Weibull plot of EPST samples in different loading concentrations on DC breakdown strength, dry.

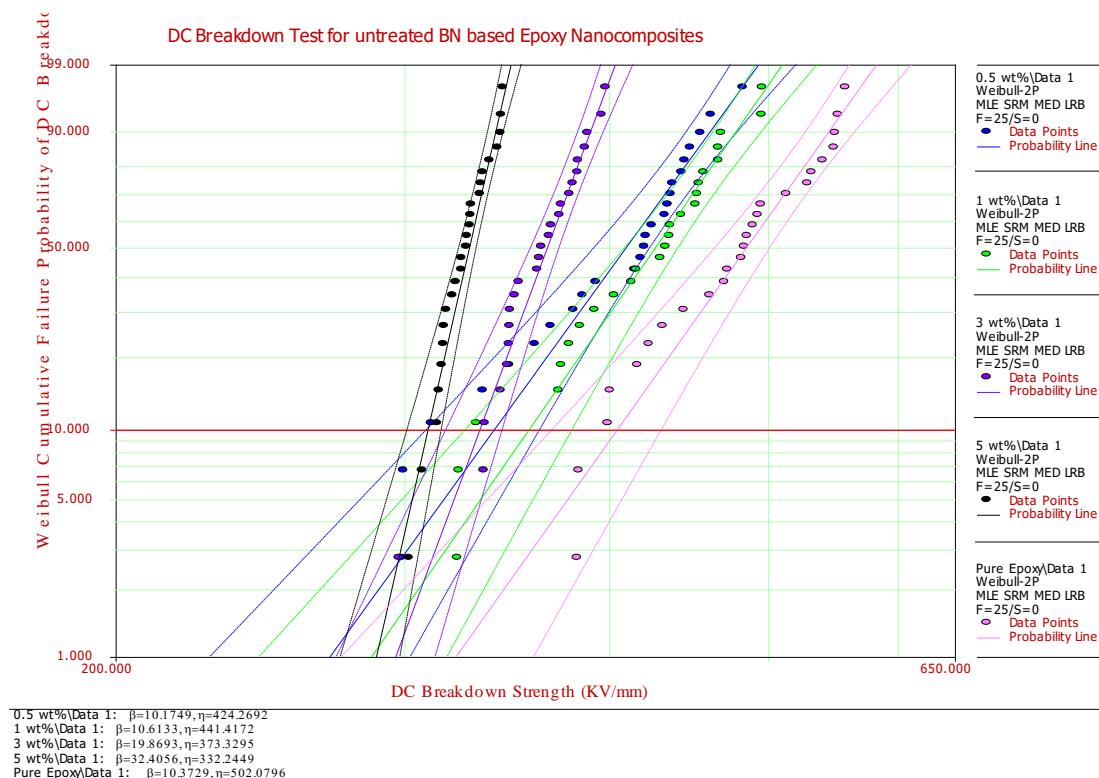


Figure 6-14 Weibull plot of EPB samples in different loading concentrations on DC breakdown strength, dry.



Table 6-3 Weibull parameters of epoxy and its nanocomposites, DC BD tests, dry

Sample code	Scale Parameter ( $\eta$ ) (kV·mm <sup>-1</sup> )	Shape Parameter ( $\beta$ )
EP0	502.1 ± 17.3	10.4
EPS05	402.7 ± 14.9	14.0
EPS1	436.2 ± 14.8	20.5
EPS3	410.7 ± 6.7	21.0
EPS5	366.2 ± 3.7	26.2
EPST05	424.3 ± 10.3	10.2
EPST1	441.4 ± 7.6	10.6
EPST3	373.3 ± 7.0	20.0
EPST5	332.2 ± 5.0	32.4
EPB05	364.8 ± 7.4	17.6
EPB1	403.3 ± 8.6	16.9
EPB3	410.9 ± 12.2	12.0
EPB5	423.3 ± 8.9	16.9

As shown in Table 6-3, the DC breakdown strength of EP0 is 502.1 kV·mm<sup>-1</sup>. For epoxy nanocomposites, an overall reduction of DC breakdown strengths is observed, which was also reported in [17, 146, 154]. The DC breakdown strength of both SiO<sub>2</sub> samples decreases with the growth of filler loadings, whereas BN samples show a slight enhancement. The overall deterioration effect on DC BD of the presence of nanofillers is due to the role of impurities/defects [147]. Moreover, the presence will also lead to the accumulation of space charges and consequently lower the DC breakdown strength [155].

Moreover, as shown in Figures 6-15, 6-16 and 6-17, the shape parameters of EP0 and EPB samples are at a low level. EPS and EPST samples exhibit an increase in filler loading concentrations. It seems the filler type has a significant influence on the shape parameter of DC breakdown results.

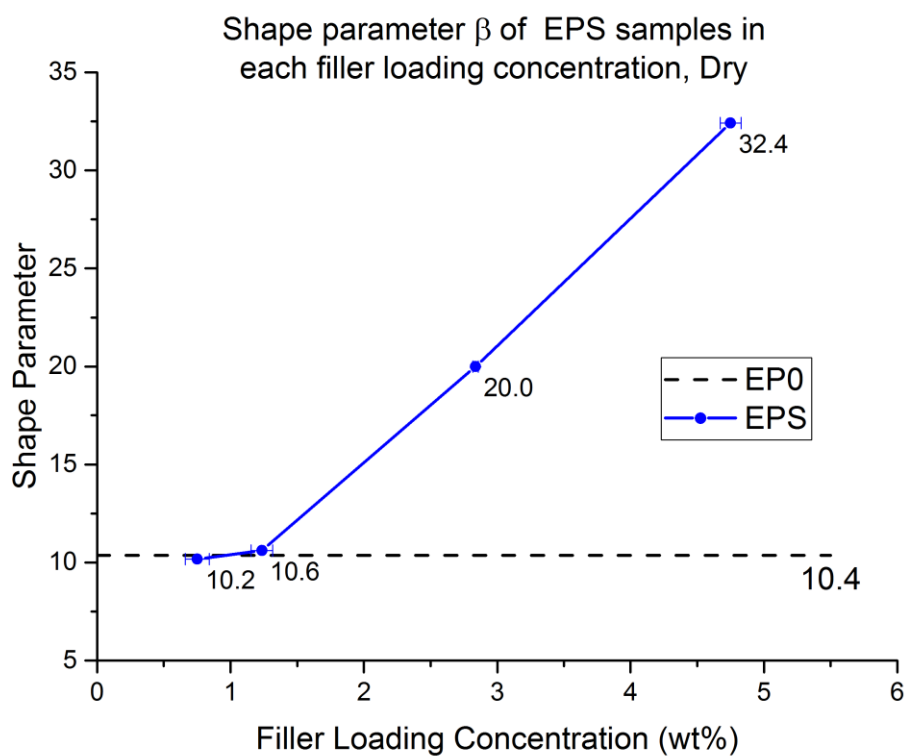


Figure 6-15 Shape Parameter  $\beta$  of EPS in different filler load concentrations, dry.

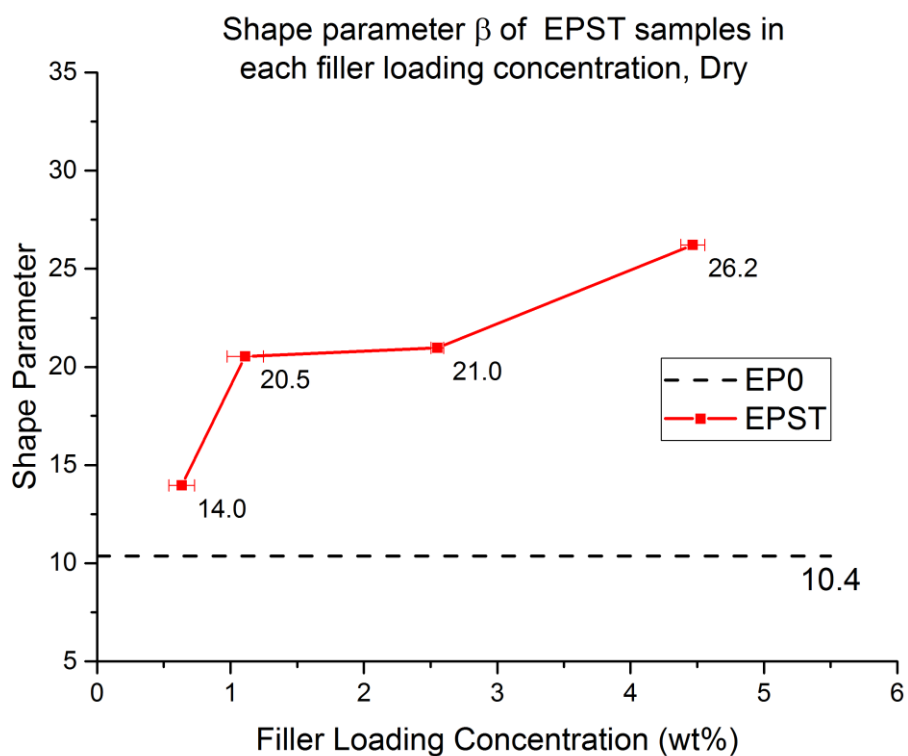


Figure 6-16 Shape parameter  $\beta$  of EPST in different filler load concentrations, dry.

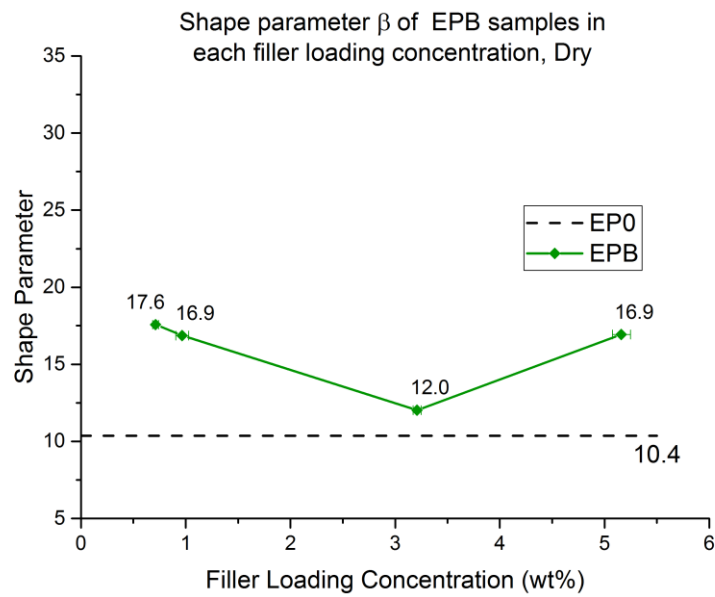


Figure 6-17 Shape parameter  $\beta$  of EPB in different filler load concentrations, dry.

### 6.3.2 Effect of Filler Loading Concentration and Filler Type on DC Breakdown Strength

#### 6.3.2.1 Effect of Filler Loading Concentration on DC Breakdown Strength

In order to understand how filler loading concentration influences the DC breakdown of EPS, EPST and EPB samples, Figures 6-18 to 6-20 are plotted as below.

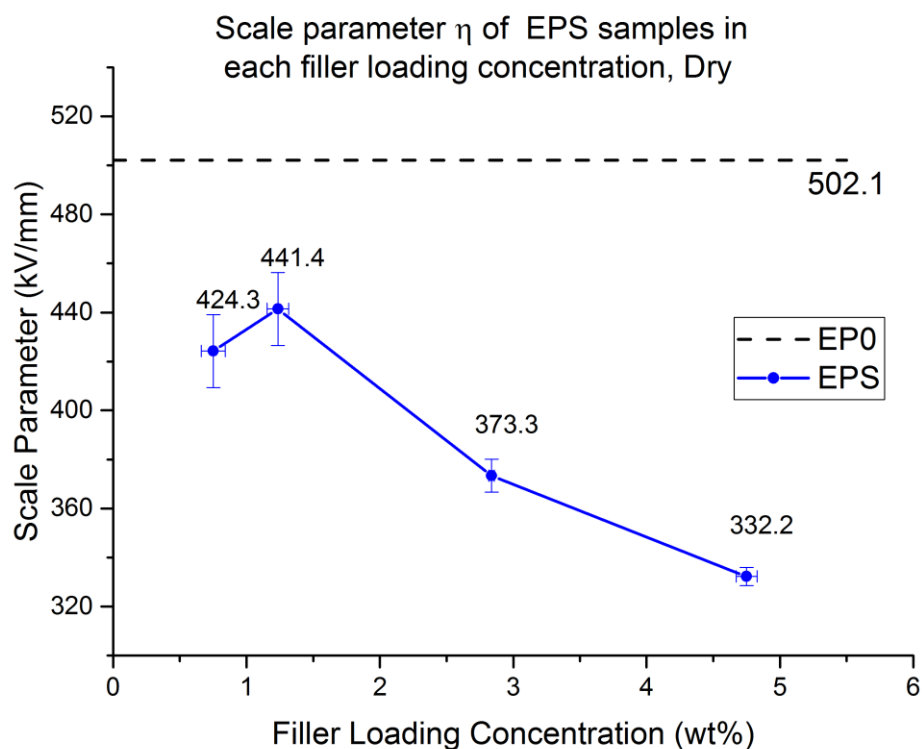


Figure 6-18 Scale parameter  $\eta$  ( $\text{kV} \cdot \text{mm}^{-1}$ ) of EPS in different filler load concentrations, dry.

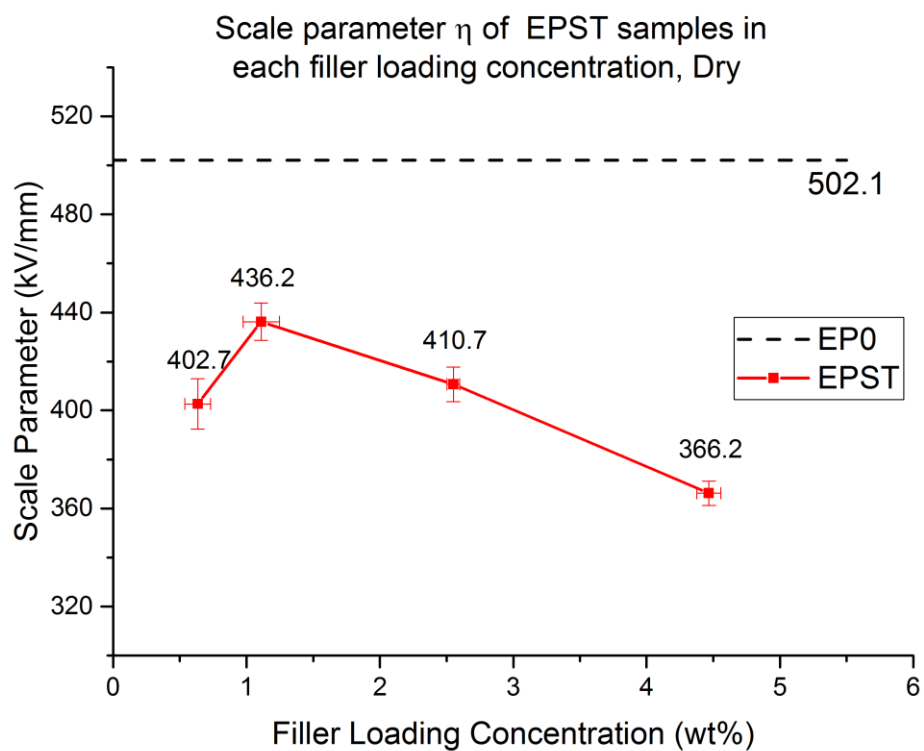


Figure 6-19 Scale parameter  $\eta$  ( $\text{kV} \cdot \text{mm}^{-1}$ ) of EPST in different filler load concentrations, dry.

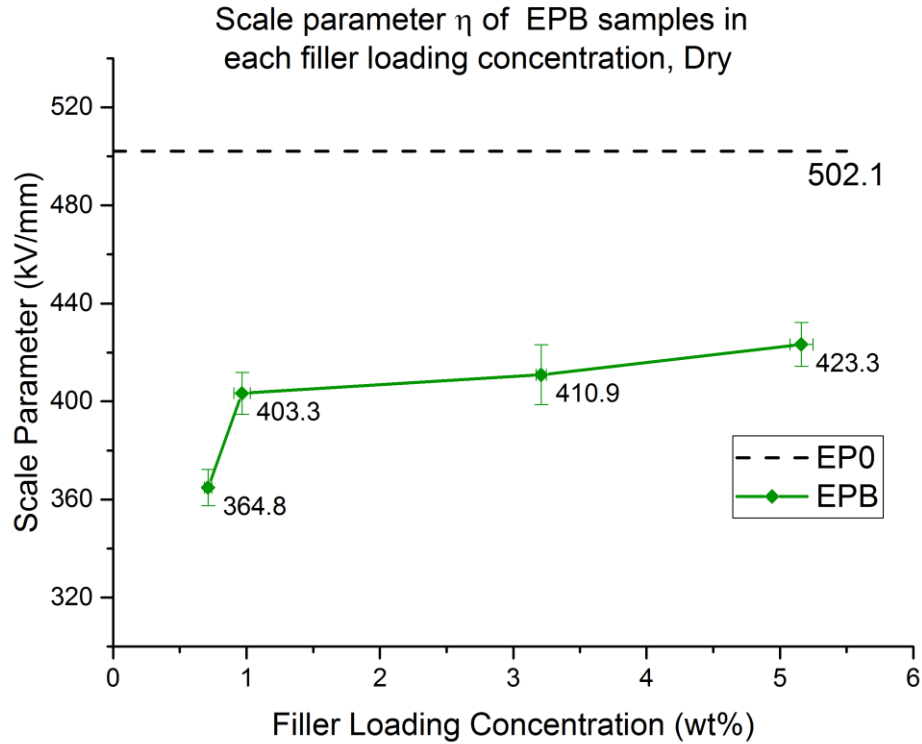


Figure 6-20 Scale parameter  $\eta$  ( $\text{kV} \cdot \text{mm}^{-1}$ ) of EPB in different filler load concentrations, dry.

The results of DC breakdown in EPS and EPST samples show very similar trends, whereas the results from the EPB samples were quite different. The higher DC BD of EPS1 and EPST1 than EPS05 and EPST05, respectively, could be mainly caused by the presence of more nano-SiO<sub>2</sub> particles introducing more traps, especially traps near the surface acting as a barrier and thus hindering the injection of charges, consequently increasing breakdown strength. However, in higher loadings, the enhancement of electrical intensity caused by aggregates and agglomerations leads to a deterioration performance of BD strength. Due to the presence of particles/aggregates, charge accumulation would happen around them. Second, the growth of loadings will lead to a decrease of inter-particle/aggregate that can be proved by SEM results in section 4.3; the percolation of charge carriers in the whole bulk become easier with increasing loadings. In other words, the mobility of charge has been increased [147].

However, there is an increase in the breakdown strength in the hBN-based samples. As discussed in section 4.2 regarding morphology of EPB, which was also considered as an influence of microstructures by *Tanaka* et al. [156], the presence of hBN particles could create very complex microstructures in epoxy resins and would result in many deeper or shallow traps near the surface and inner the bulk

of nanocomposites. Thus, this could reduce the injection of charges due to the formation of trapped charges near the surface and then act as a barrier, which becomes more obvious in higher filler loading concentrations. These analyses are supported by further investigations in later chapters.

### **6.3.2.2 Effect of Filler Type on DC Breakdown Strength**

Based on a comparison of BD strength in different filler loading concentrations shown in Figures 6-18 to 6-20, the lower BD strength of EPST and EPB samples in 0.5 wt% and 1 wt% than EPS samples should mainly result from the solvent residues of surface treatment and particle shape respectively as discussed in the section 6.2.2.2. However, with the growth of loadings, the better the dispersion and distribution of EPST samples, compared to EPS, the better performance in DC breakdown strength. In all, it could be concluded that the dispersion and distribution of particles is the main factor that influences the DC breakdown strength in epoxy nanocomposites. Moreover, as it is hard to identify the dispersion of hBN particles, the better performance of EPB samples than silica-based ones is more likely because of the microstructures mentioned before.

### **6.3.3 Effect of Moisture on DC Breakdown Strength**

As there are few investigations of the effect of moisture on the DC breakdown strength of an epoxy and its nanocomposites, this will be discussed in this section. All the samples were treated in different moisture conditions, as outlined in section 3.4.1 and tested with the same technique in the section 6.3.2 for dry samples. The Weibull plots are shown in Appendix C and their scale and shape parameters are summarised in Table 6-4.

Table 6-4 Weibull parameters of epoxy and its nanocomposites, DC BD, 60RH and saturated

Sample code	60RH		Saturated	
	Scale	Shape	Scale	Shape
	Parameter ( $\eta$ ) (kV·mm <sup>-1</sup> )	Parameter ( $\beta$ )	Parameter ( $\eta$ ) (kV·mm <sup>-1</sup> )	Parameter ( $\beta$ )
EP0	345.7 ± 9.6	13.1	287.7 ± 11.7	8.7
EPS05	326.0 ± 11.0	10.8	288.1 ± 8.9	11.1
EPS1	317.3 ± 12.4	9.1	247.1 ± 9.1	9.4
EPS3	282.4 ± 8.3	12.1	218.2 ± 4.3	17.9
EPS5	271.6 ± 4.6	20.8	193.5 ± 5.6	12.2
EPST05	320.0 ± 6.7	18.8	256.3 ± 8.2	10.9
EPST1	275.2 ± 6.6	14.8	195.1 ± 6.5	11.0
EPST3	269.5 ± 7.7	12.4	189.5 ± 5.6	12.0
EPST5	262.9 ± 4.5	20.8	183.1 ± 6.1	10.2
EPB05	332.0 ± 13.1	9.0	302.1 ± 16.6	9.6
EPB1	300.4 ± 19.1	5.6	273.2 ± 11.4	8.4
EPB3	322.2 ± 9.3	12.4	281.0 ± 14.6	6.6
EPB5	296.7 ± 14.9	6.7	291.4 ± 8.9	11.9

In order to give a more direct view of the moisture effect, these two parameters in 60RH and saturated conditions are plotted in Figures 6-21 to 6-25 as well. As shown in Figures 6-21 and 6-23, both SiO<sub>2</sub> samples show the decrease of BD strength with increasing filler loadings. First, the overall reduction of breakdown strength including pure samples is mainly caused by the presence of water in the matrix, which enhances the mobility of charges in bulk. Second, as the water shells form around spherical particles [48], if it is assumed, under a certain RH condition, the average thickness is the same in EPS or EPST according to research by *Hosier* et al. [19] and water uptakes in the matrix of all kind of samples reach a same quasi-equilibrium state, more water uptake will indicate the number/percentage of particles/aggregate surrounded by water shell will become larger with the growth of filler loadings as discussed in section 3.4. That is to say the average inter-particle/aggregate distances will decrease and be more obvious in samples of the higher filler loadings. Thus, the percolation of the bulk should become easier [15],

as lower distance will help charges hop/ tunnel from one to another if they are regarded as recombination centres, and will finally be reflected in the DC breakdown strength. This analysis can be further proved by the values in Table 6-5. Compared under same RH condntions, the reduction percentages of BD strength are highly related to the variation of filler loadings. The less influenced value of EPST could be because of its better disperison and distribution of particles than that of EPS. Moreover, in EPB samples, which microstructures were discussed in section 6.2.2.1 would impair the injection of charges and thus lead to an increase in breakdown strength with the growth of filler loadings with moisture inside. Another reason could be the non-formation of the water shell around hBN particles. However, there is a reduction in EPB5 samples; it is assumed to be caused by the poor morphology in bulk due to filler loadings of 5 wt%, which can be proved by its much lower shape parameter in Figure 6-22.

Table 6-5 Reduction percentage of DC breakdown strength

	Dry	60RH	Saturated	Dry	60RH	Saturated
	From 0.5 wt% to 3 wt%			From 0.5 wt% to 5 wt%		
EPS	12.02%	13.38%	24.25%	21.71%	16.69%	32.82%
EPST	-1.99%	15.76%	26.07%	9.06%	15.12%	28.56%

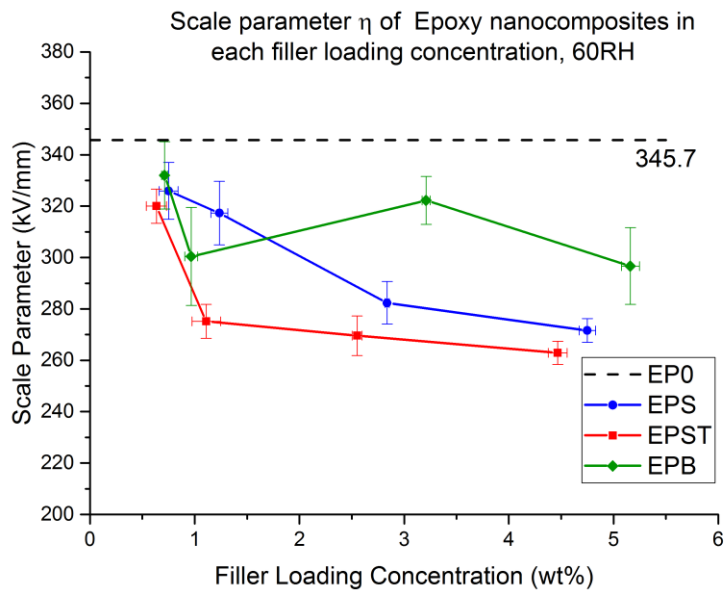


Figure 6-21 Scale parameter  $\eta$  ( $\text{kV} \cdot \text{mm}^{-1}$ ) of EP0, EPS, EPST and EPB in different filler load concentrations, 60RH.



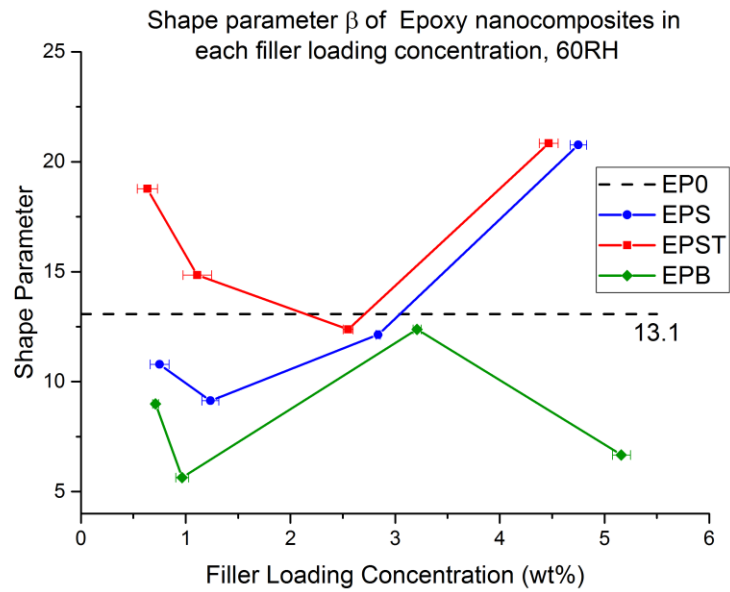


Figure 6-22 Shape parameter  $\beta$  of EP0, EPS, EPST and EPB in different filler load concentrations, 60RH.

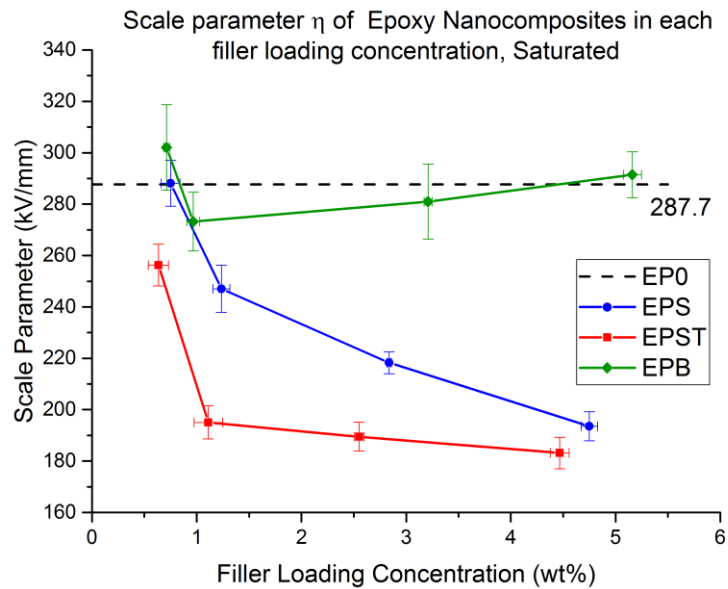


Figure 6-23 Scale parameter  $\eta$  ( $\text{kV} \cdot \text{mm}^{-1}$ ) of EP0, EPS, EPST and EPB in different filler load concentrations, saturated.

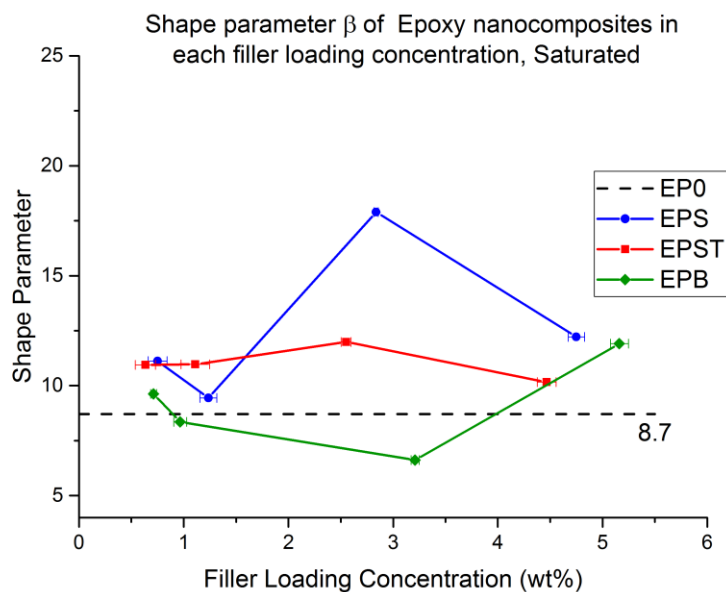


Figure 6-24 Shape parameter  $\beta$  of EP0, EPS, EPST and EPB in different filler load concentrations, Saturated.

Moreover, according to Table 6-5 and Figure 6-25, there are significant increases in reduction percentages once RH varies from 60RH to the saturated condition. If the assumption of EPS/EPST sharing the same thickness of water shell in different loadings under a certain RH condition is correct, the thickness of the water shell may be different and become larger with the growth of humidity, which will be proved in the next chapter.

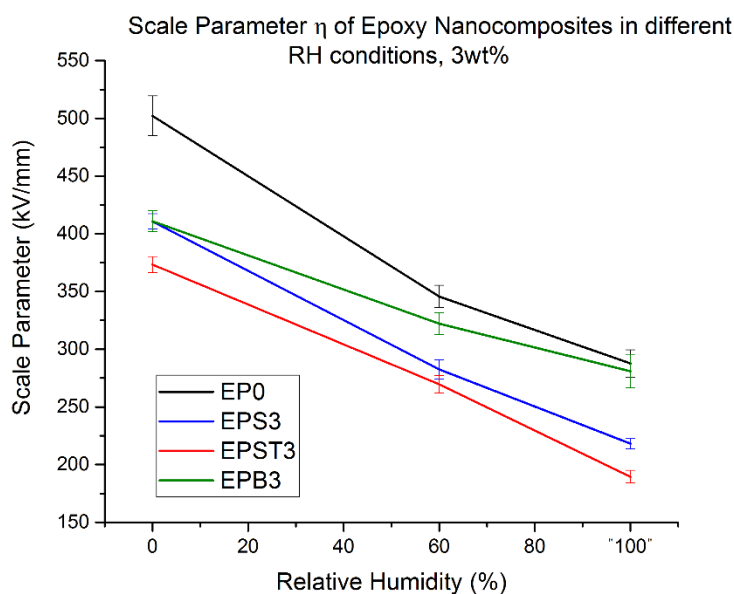


Figure 6-25 Scale parameter  $\eta$  ( $\text{kV} \cdot \text{mm}^{-1}$ ) of EP0, EPS, EPST and EPB in different relative humidity conditions, 3 wt%.

## 6.4 Chapter Summary

Dielectric breakdowns (AC and DC) of epoxy and its nanocomposites were investigated and analysed by two-parameter Weibull distribution. According to the work in this chapter, the following conclusions can be made:

1. In AC breakdown tests, agglomerations of particles/aggregates, observed in Chapter 4, have little influence on the reduction of AC breakdown strength. The presence of particles led to the enhancement of the mobility of charge carriers and thus a reduction of breakdown strength, which became more obvious with the growth of filler loadings. Moreover, the shape of particles also had a significant impact on the AC breakdown strength and that was why the plate-like BN particle based nanocomposites showed the lowest breakdown strength value.
2. In DC breakdown tests, the accumulation of charges around aggregates and resulting enhancement of electrical intensity is the main reason why the BD strength became worse. The growth of filler loadings led to a decrease of inter-particle/aggregate distances. Thus the percolation of charge carriers in the whole bulk could become easier and resulted in the reduction of DC BD strength, of which the dispersion and distribution of particles/aggregates in Chapter 4 supply qualitative support. Last, the presence of moistures resulted in an overall reduction of DC breakdown strength, which deteriorated with the growth of RH conditions.



# Chapter 7 Dielectric Spectroscopy of Epoxy Nanocomposites

## 7.1 Dielectric Spectroscopy Technique

### 7.1.1 Dielectric Spectroscopy

Dielectric spectroscopy is a commonly used method for evaluating the effect of using dielectric materials in a circuit, an electronic circuit or a high-voltage transmission system, and to help investigate the dipolar process [90]. The processes include very low-frequency processes, dipolar or orientation relaxation processes, and electronic and atomic polarisation. The very low-frequency processes can provide information about charge transport processes while relaxation processes are associated with dipole reorientation.

The first study on dielectric materials was presented by *Debye* in the 1910s. *Debye* introduced a theory based on the dielectric losses that are related to the relaxation of dielectric polarisation. However, later studies show that the model is not able to explain the case of solid materials [157]. Instead, *Dissado-Hill* theory has been developed to analyse the dielectric response so as to investigate the interaction between the material and the applied electric field. In many studies, the measurement results are shown in response to time-dependent signals, because this approach is better able to facilitate understanding of the results, particularly where non-linear processing is involved [158]. However, there is also another method, which is based on the response to harmonic excitation [159]. Such research can provide theoretical and practical advantages. Considering frequency-dependent response, the mathematical expression of a given function of time-based on the Fourier transformation can be written as a Fourier transform, as shown in Equation 7.1 [157]:

$$F[G(t)] = \varphi(\omega) = 2\pi^{\frac{1}{2}} \int_{-\infty}^{\infty} G(t) \exp(-i \cdot \omega t) dt \quad (7.1)$$

where  $\varphi(\omega)$  is the frequency spectrum of the time-dependent function  $G(t)$ . The  $i$  inclusion of in the equation means that both real and imaginary parts are taken into account. In this case, both the magnitude and phase behaviour of the material sample have been considered.

## 7.1.2 Dielectric Response

### 7.1.2.1 Dielectric Polarisation

When an electric field is applied to a dielectric material, instead of flowing through the dielectric material, the charges will tend to move a little bit. This is called dielectric polarisation. All the investigations of dielectric properties are based on the dielectric polarisation inside the material. Owing to such polarisation, the positive and negative charges move along the electric field in the opposite direction. This movement will produce an internal electric field with a direction opposite to the external electric field.

Different polarisation mechanisms have been used to study the reactions of materials to the applied electric field. The main types are electronic polarisation, ionic polarisation, orientation polarisation and interfacial polarisation as shown in Figure 7-1. Those dielectric mechanisms can be classified into either relaxation or resonance processes.

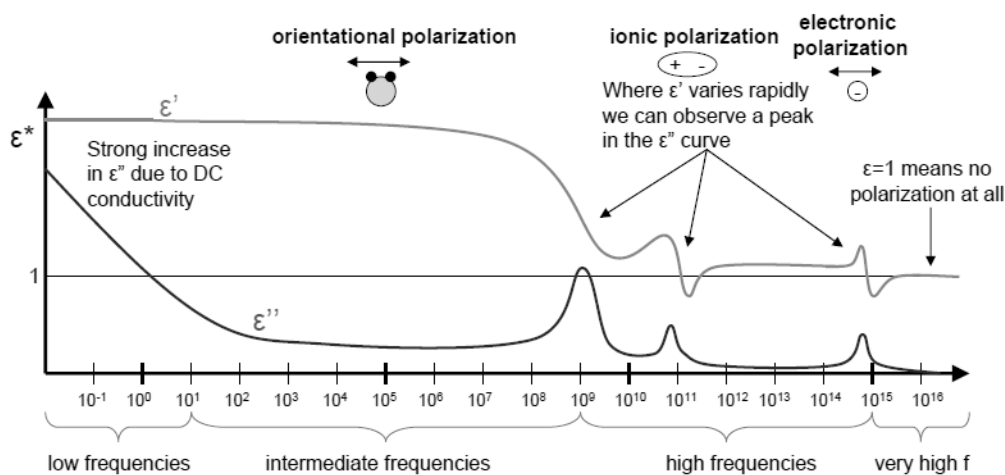


Figure 7-1 The polarisation spectrum with orientation, ionic and electronic polarisation mechanisms [3].

Orientation polarisation is the primary mechanism in the low-frequency range. In general, orientation polarisation is a slow process in solid dielectric material, as a dipole motion will be restricted by potential barriers from the inner structures of the dielectric material. Some changes can be observed as well, for example, because of the adding fillers; moreover, it is influenced by the frequency and its effect will be reduced at higher frequencies. The orientation polarisation under the application of an electric field is shown in Figure 7-2.

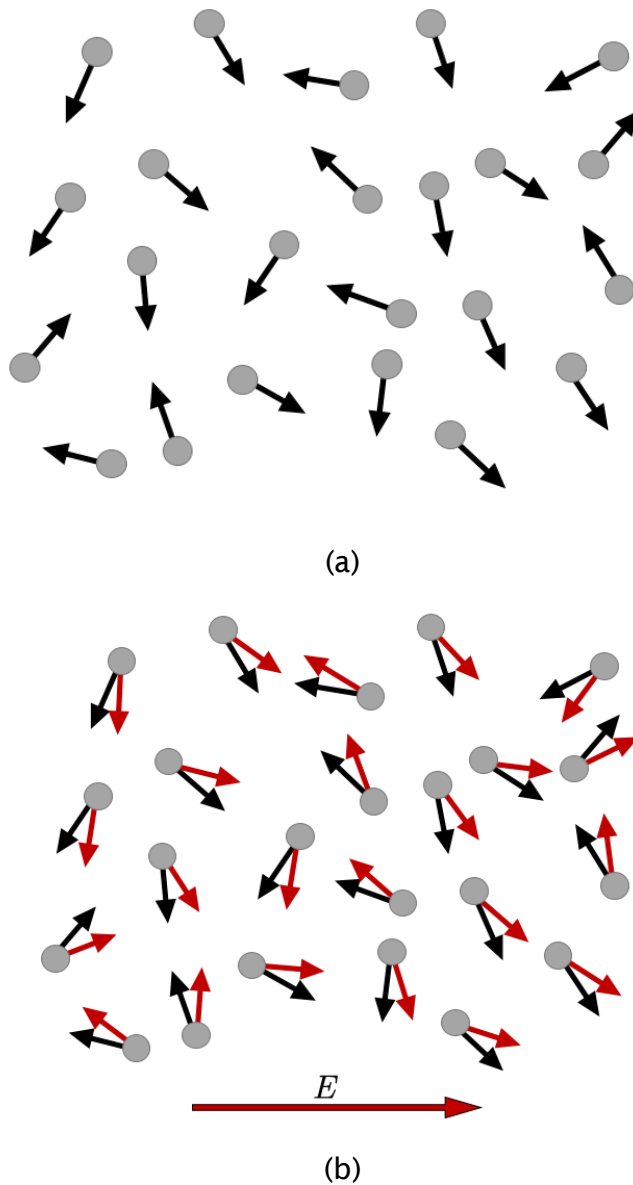


Figure 7-2 Illustration of orientation polarisation: (a) without electric field; (b) after applying electric field.

As the name suggests, ionic polarisation happens in ionic materials. Assume there is a molecule consisting of two atoms, Red and Blue, as shown in Figure 7-3. The red atom is ready to give some of its valence electrons to the blue one in order to make the outermost shells of both atoms more fully completed. This tendency is, in fact, the force that produces the so-called ionic bond. In this case, the red atom is more electropositive and the blue one more electronegative in term of ions. In the absence of an electric field  $E$ , the distance between the ions is  $d_0$ . When an electric field is applied to such a molecule, their positive and negative ions displace further in the opposite direction and the interionic separation increases until the bonding force stops the process.

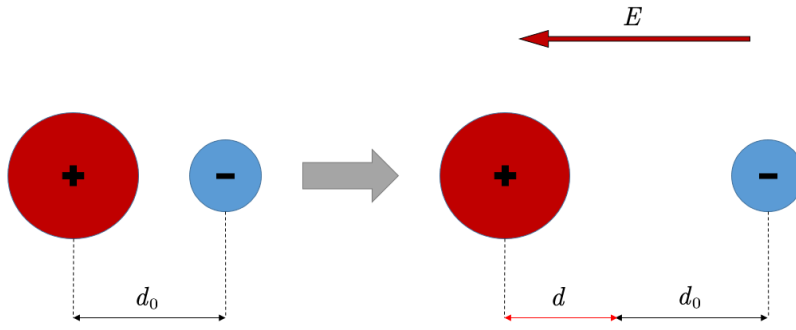


Figure 7-3 Illustration of the ionic polarisation.

The electronic polarisation is based on a resonance mechanism. The length of time it takes for these two processes to occur is very short and about  $10^{-16} \sim 10^{-12}$  s.

As mentioned above, the total polarisation of the material will be the sum of electronic polarisation, ionic polarisation and orientation polarisation. The total polarisation  $P$  can be written as Equation 7.2:

$$P = N \cdot \alpha E_i \quad (7.2)$$

where  $N$  is the number of dipoles per volume,  $\alpha$  is the charge polarizability, and  $E_i$  is the inner electric field which is caused by injected charges and other dipoles, resulting from the total electric field.

#### 7.1.2.2 Interfacial and Maxwell-Wagner-Sillars (MWS) Polarization

There are two aspects of the induced polarisation that may help to facilitate people understanding of and explain the experimental results: the first one is electrode polarisation, which is due to the accumulation of ions at the interface between polymer and electrodes, while the second is the polarisation caused by the accumulation of charge in the interphase or at the interface between components that share different characteristics. This polarisation is termed 'interfacial' or 'space charge' polarisation, and arises due to the local accumulation of charges and their drifting through the material. Thus, interfacial polarisation is different from the three forms of polarisation discussed in the previous section that are due to the displacement of bound charges.

Maxwell [160] was the first to develop a theory to explain the properties of materials containing filler particles with a volume fraction  $\varphi_f$  and a frequency-independent dielectric constant  $\epsilon_f^*$ , which is dispersed into a matrix medium with



a dielectric constant  $\epsilon_m^*$  (c.f. Figure 7-4). This approach was later generalised by Wagner [161], who considered the effects of conducting phases. Finally, Sillars [162] extended the theory to filler particles of a more general, ellipsoidal shape. The resulting theory, which is known as the Maxwell-Wagner-Sillars (MWS) theory, predicts the polarisation process resulting from the difference in the conductivity and dielectric constant of the components. Therefore, interfacial polarisation is commonly called MWS polarisation.

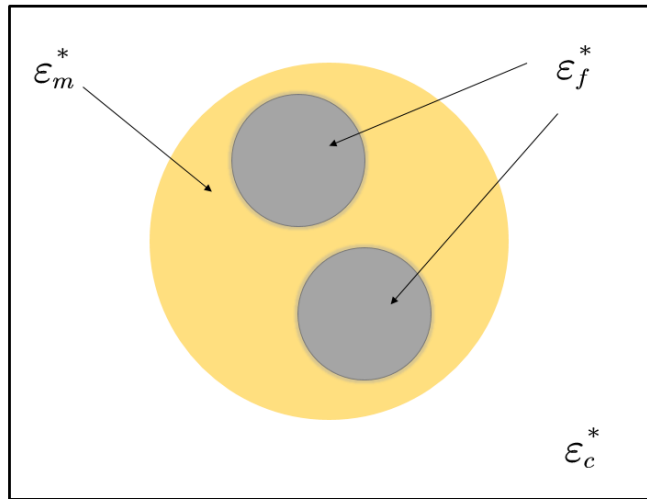


Figure 7-4 Heterogeneous material contains the matrix and fillers, which both have complex permittivity.

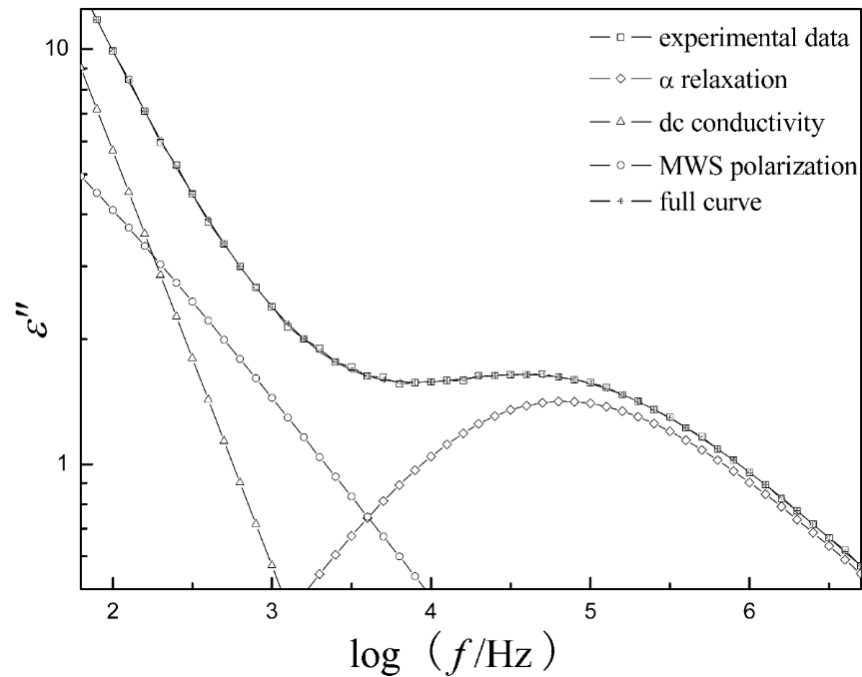


Figure 7-5 Curve fitting of the experimental  $\epsilon''$  to the sum of the  $\alpha$  relaxation, MWS relaxation, and the DC conductivity [163].

### 7.1.2.3 Alternating Electric Field-Dependent Dielectric Response

When an external electric field is applied to the dielectric material, the bound charge will be separated slightly under the applied field. The dielectric displacement  $D$  under a small electric field can be written as Equation 7.3:

$$D = \varepsilon^* \varepsilon_0 \cdot E \quad (7.3)$$

where  $\varepsilon_0$  is the permittivity of vacuum and  $\varepsilon^*$  is the complex relative permittivity [164]. Moreover, a periodic electric field can be defined via Equation 7.4:

$$E(t) = E_m \cdot \exp(-i \cdot \omega t) \quad (7.4)$$

where  $E_m$  is the amplitude of the applied field and  $\omega$  is the angular frequency. Owing to relaxation polarisation, there is a phase difference  $\delta$  between the electric displacement  $D$  and the applied electric field  $E$ : the electric displacement  $D$  can be described using Equation 7.5:

$$D = D_m \cdot e^{i(\omega t - \delta)} \quad (7.5)$$

where  $D_m$  is the amplitude of displacement. Hence its complex relative permittivity:

$$\begin{aligned} \varepsilon^* &= D/(\varepsilon_0 E) = D_m/(\varepsilon_0 E_m) \cdot e^{-i\delta} = \bar{\varepsilon} \cdot (\cos \delta - i \sin \delta) \\ &= \varepsilon' - i\varepsilon'' \end{aligned} \quad (7.6)$$

where  $\varepsilon'$  is the real part of complex relative permittivity, which is the lossless permittivity and  $\varepsilon''$  the imaginary part of the complex relative permittivity due to bound charge and dipole relaxation phenomena, which results in energy loss. The dielectric displacement, which is due to the response of dielectric materials under the external applied electric field only, is known as the polarisation.

Dielectric spectroscopy is used to measure the response of materials under an externally applied field with varying frequency. When an external AC field is applied to the material, polarisations due to different mechanisms occur in the material. The direction of polarisation changes as the applied field changes. There is a delay between the change of the field and the change of polarization direction. This phase-lag is known as the phase angle  $\delta$ . The dielectric loss tangent, which can be defined as the ratio of energy loss, can be written as Equation 7.7:

$$\tan \delta \approx \varepsilon''/\varepsilon' \quad (7.7)$$

Figure 7-6 shows that a real capacitor can be treated as a lossless capacitor in series with an equivalent series resistance (ESR). The dielectric loss angle can be defined as the angle between the impedance of the capacitor and the negative reactance.

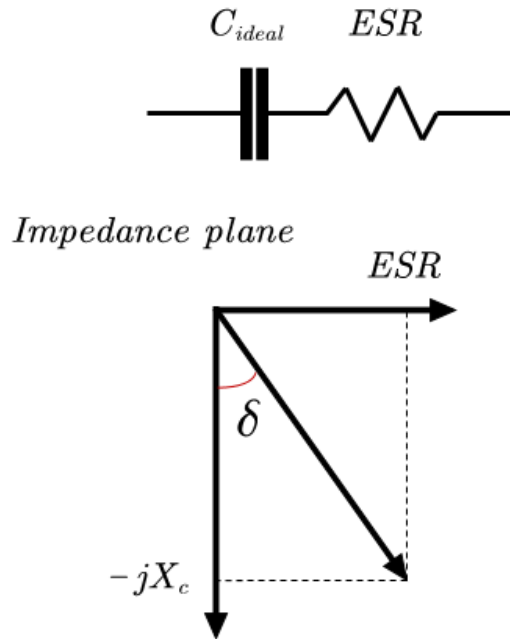


Figure 7-6 Illustration of loss tangent.

## 7.2 Dielectric Spectroscopy Measurement Results

### 7.2.1 Dielectric Response of Pure Epoxy Resin and Temperature Effect

Both of the relative real and imaginary permittivity values of pure samples (EP0) are shown in Figures 7-7 to 7-9. It can be observed from Figure 7-7 that the real relative permittivity has higher values at a low-frequency range for three different temperatures. There is a continuous drop in relative permittivity as the frequency increases to 0.1 MHz. The results show that the pure epoxy resin is frequency dependent at the measured frequency range (0.01 Hz - 0.1 MHz).

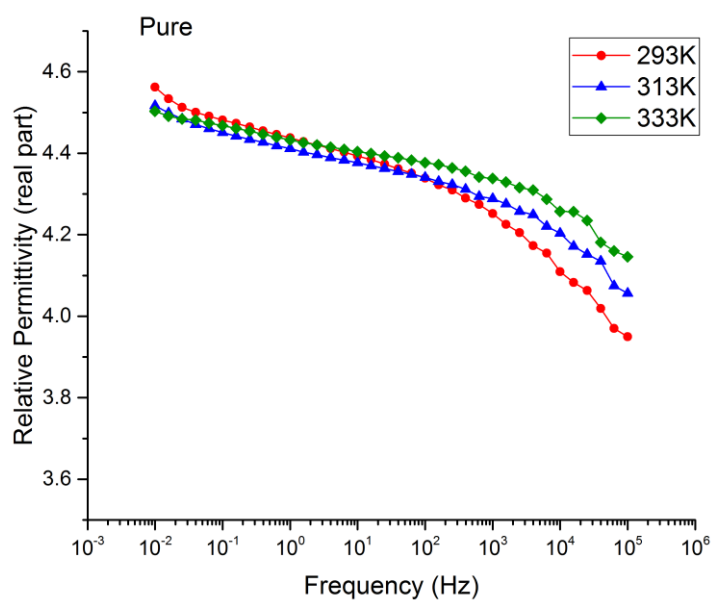


Figure 7-7 Relative permittivity (real) of pure epoxy resins, 293K-333K.

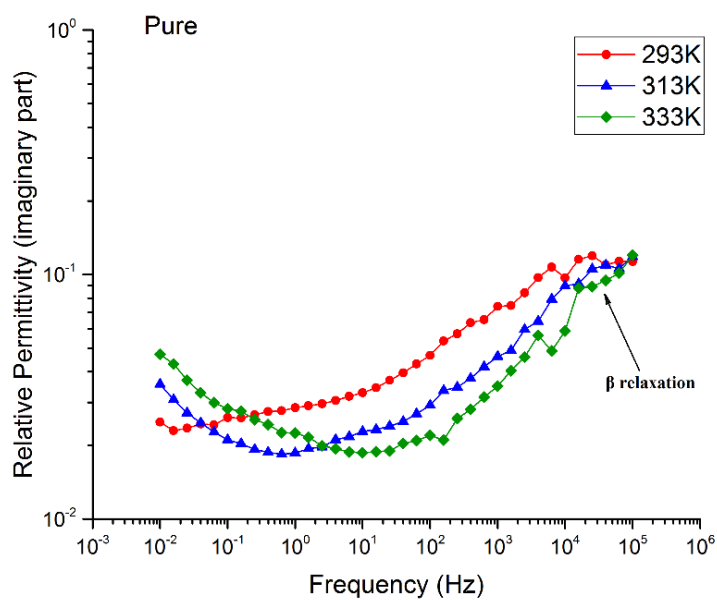


Figure 7-8 Relative permittivity (imaginary) of pure epoxy resins, 293K-333K.

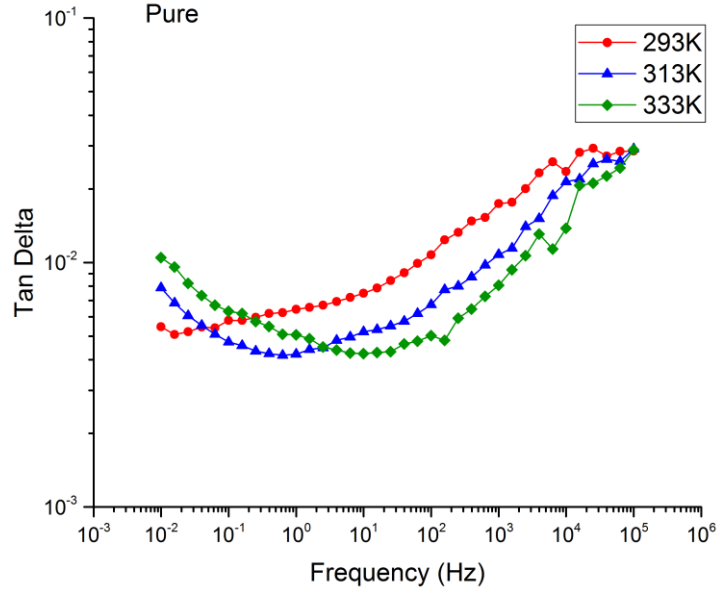


Figure 7-9  $\tan \delta$  of pure epoxy resins, 293K-333K.

The  $\tan \delta$  is used to describe the dielectric materials' ability to dissipate energy. The permittivity of dielectric materials under time-varying fields has both real and imaginary components, and it can be written as Equation 7.7 in section 7.1.2.2. The real part of permittivity  $\epsilon'$  is the lossless permittivity that is given by the product of relative permittivity  $\epsilon_r$  and permittivity in free space  $\epsilon_0$ . The imaginary part of permittivity  $\epsilon''$ , on the other hand, represents the energy loss. When an alternating electric field is applied to the sample, the value of  $\tan \delta$  can also be defined as follows:

$$\epsilon' = \epsilon_{\infty} + (\epsilon_s - \epsilon_{\infty}) / [1 + (\omega\tau)^2] \quad (7.8)$$

$$\epsilon'' = \gamma / (\omega\epsilon_0) + (\epsilon_s - \epsilon_{\infty}) \cdot \omega\tau / [1 + (\omega\tau)^2] \quad (7.9)$$

where  $\omega$  is the phase,  $\gamma = Ae^{-B/T}$  refers to the relationship between conductivity and temperature,  $\tau$  is the relaxation time,  $\epsilon_s$  is the static permittivity of samples,  $\epsilon_{\infty}$  is the permittivity of electronic polarisation, and  $\epsilon_0$  is the permittivity of vacuum.

Moreover,

$$g = \epsilon_0 \cdot \omega^2 \tau \cdot (\epsilon_s - \epsilon_{\infty}) / [1 + (\omega\tau)^2] \quad (7.10)$$

where  $g$  is the conductivity of the sample. Thus, it can be seen from the above equation that under the alternating electric field, the  $\tan\delta$  of polymer materials depends on not only the frequency and temperature, but also the conductivity and the relaxation time of large molecular chains. The dielectric loss of polymer materials could be due to both conductivity losses when the charge carriers travel across the materials under the applied field and the orientation polarisation of large molecular chains under the applied field. The resistivity of the epoxy resin is approximately  $10^{13}\sim 10^{14} \Omega \cdot m$ : thus, the conductive epoxy loss is small. Moreover, the epoxy resin tends to form a large three-dimensional cross-linked network during the curing process, and leading to a large number of large molecules. The orientation polarisation is mainly caused by the direction of polar groups and this three-dimensional network structure limits the orientation polarization. Therefore, relaxation loss will be mainly caused by such a polar group in epoxy resin [4].

Considering the influence of temperature upon permittivity, the temperature will influence the movement of molecules, which can determine the foundation of relaxation polarisation (which is dominant in the low-frequency range). That is to say, higher temperature will result in a shorter relaxation time. However, the electronic polarisation does not respond to temperature that is dominant in the high-frequency range. Permittivity will present as  $\varepsilon_{\infty}$  and  $\varepsilon_s$  at high and low-frequency ranges respectively. Thus, as shown in Figure 7-10 (a), with increasing temperature, both  $\varepsilon'$  and  $\varepsilon''$  will move towards the high-frequency range with a small decrease of  $\varepsilon_s$  (at the low-frequency range) and  $\varepsilon''_{\max}$ . As it is easier to form electronic polarization at a higher temperature,  $\varepsilon'$  (act as  $\varepsilon_{\infty}$  at high frequency) increases as the temperature rises. Both are also reflected in the experimental results shown in Figures 7-7 and 7-8. Moreover, as shown in Figure 7-10 (b),  $\varepsilon'$  reflects the changes in  $\varepsilon_s$  and  $\varepsilon_{\infty}$  versus temperature at low and high frequencies respectively. In addition,  $\varepsilon'$  will show growth at the mid-frequency level (0.1~100 Hz) with increases in temperature.

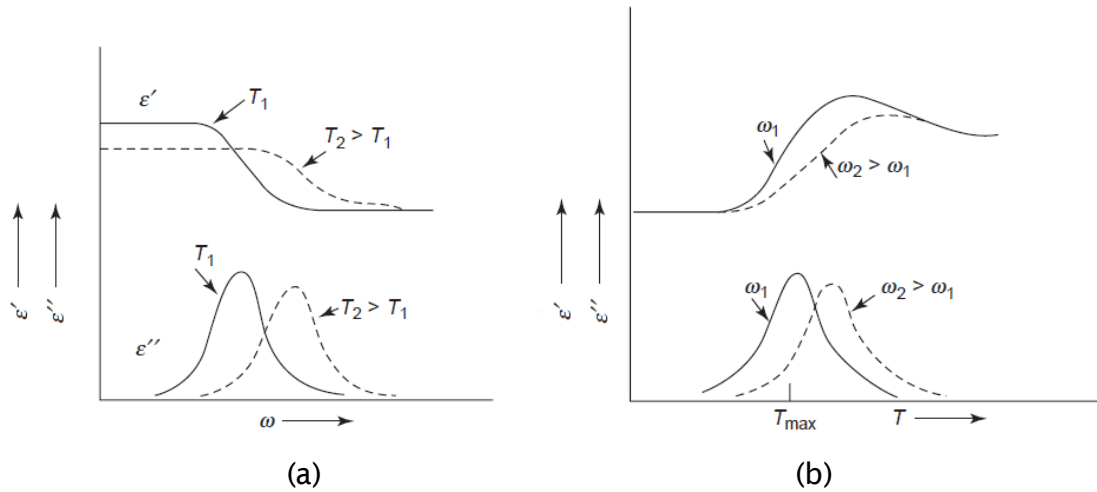


Figure 7-10 Real and imaginary relative permittivity curve versus frequency and temperature [165].

Considering the influence of temperature,  $\tan \delta$  can be written via Equation 7.11:

$$\tan \delta = \gamma / (\epsilon \epsilon_0 \cdot \omega) = A / (\epsilon \epsilon_0 \cdot \omega) \cdot e^{-B/T} \quad (7.11)$$

Thus,  $\tan \delta$  can be shown as in Figure 7-11, where  $\omega_2 > \omega_1$ . Under different temperatures, the relaxation time will be different. The increase and decrease of temperature will lead to reduction and growth of relaxation time, as represented by the fact that the peak of  $\tan \delta$  will move towards higher and lower frequency ranges, respectively, which is shown by the movement of the curves as in Figure 7-11.

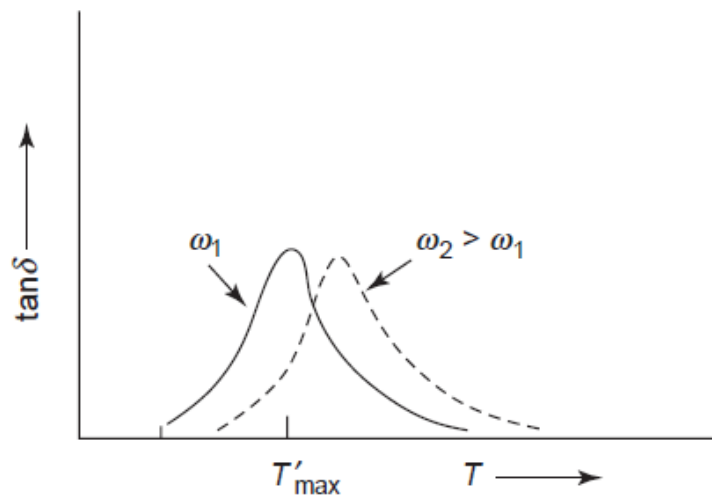


Figure 7-11  $\tan \delta$  curves versus frequency and temperature [165].

It can be seen from Figure 7-9 that  $\tan\delta$  decreases as the frequency decreases. The rapid decrease in value of  $\tan\delta$  in the high-frequency range is believed to be due to the increase in relaxation loss of polar groups of epoxy resins under the high-frequency field. Moreover, the increase in the  $\tan\delta$  value at the low-frequency range is believed to be due to the dipole and space charge polarisation discussed earlier. Orientation polarisation occurs in the high-frequency range and leads to an increase in  $\tan\delta$ .

### 7.2.2 Dielectric Response of Epoxy Nanocomposites and Temperature Effect

#### 7.2.2.1 Effects of Nanofillers, Filler Types and Filler Loading Concentrations

Real and imaginary relative permittivity are plotted in Figures 7-12, 7-13 and 7-14 as a function of frequency, filler types in different loading concentrations at 293K. There is a clear reduction in  $\varepsilon'$  with the increase in frequency in the range of this study, as shown in Figure 7-15. In a typical resin system, the  $\varepsilon'$  of epoxy is determined by the number of orientable dipoles within the system and their ability to orient under an applied electric field [14, 166]. It can be seen from figures that the  $\varepsilon'$  of most nanocomposites is lower than that of the unfilled epoxy resin with the loading concentration up to a certain value when the nano-sized fillers are added, and that  $\varepsilon'$  of EPS and EPST samples seems to decrease as the loading concentration increases, however, as the filler loading concentration increases further, the permittivity then begins to increase. There are also similar observations in the literature [34, 167, 168]. Such reduction of  $\varepsilon'$  with the increase in filler loadings means that the polarisations inside the composites are decreased. It is known that the  $\varepsilon'$  of the epoxy and its nanocomposites is governed by the polarisation associated with epoxy and nano-SiO<sub>2</sub>/hBN particles and is strongly influenced by the interfacial polarization at the interface between the matrix and nanoparticles. Thus, when a small amount of nanofillers is loaded into epoxy, due to one of the two effects introduced in [167] and corresponding to the inner layer of the multi-core model [56], the interaction between nano-filler and polymer chains restricts the chain mobility of epoxy in the vicinity of nanoparticles and thus reduces the polarisation within the composites [169]. As the loading concentration increases, more immobile layers are formed and the mobility of epoxy chains decreases continuously, resulting in a reduction of permittivity of nanocomposites



as shown in Figures 7-12 (a) and 7-13 (a). According to another effect discussed in [167], the presence of more nanoparticles with higher permittivity (3.5-7.0 of  $\text{SiO}_2$ ) than the matrix leads to the increase in  $\varepsilon'$ , as shown in Figure 7-14 (a). Moreover, EPST shows higher  $\varepsilon'$  than EPS in all loading concentrations. This is firstly due to the additional mobile charges introduced by surface treatment which increases the polarisation in bulk [68]. Secondly, as C8 chains on the particle surface are not firmly bonded to matrix structures, the higher mobility of chain segments at interphase could further lead to higher  $\varepsilon'$  than that of EPS.

However, the EPB samples do not show similar results. The  $\varepsilon'$  of EPB decreases with the growth of filler loading concentrations, whereas the EPB05 sample has a higher  $\varepsilon'$  than EP0. According to the discussion in SEM characterisation, the presence of layered structures would result in many shorter chains. Under same applied voltage, these chains more easily become polarized than those in EPS and EPST samples, even in EP0, thus leading to a higher  $\varepsilon'$ , which was also found in [167]. However, with an increase in filler loadings, the effect of intercalated macroscopic layer structures becomes more and more obvious and restricts the mobility of chain segment in the vicinity of particles. Thus, the  $\varepsilon'$  of EPB undergoes a reduction, as shown in Figures 7-12 (a) and 7-13 (a). Moreover, due to the similar  $\varepsilon'$  of hBN (4.0-4.5) itself compared to the matrix, the result of the second effect is not obvious.

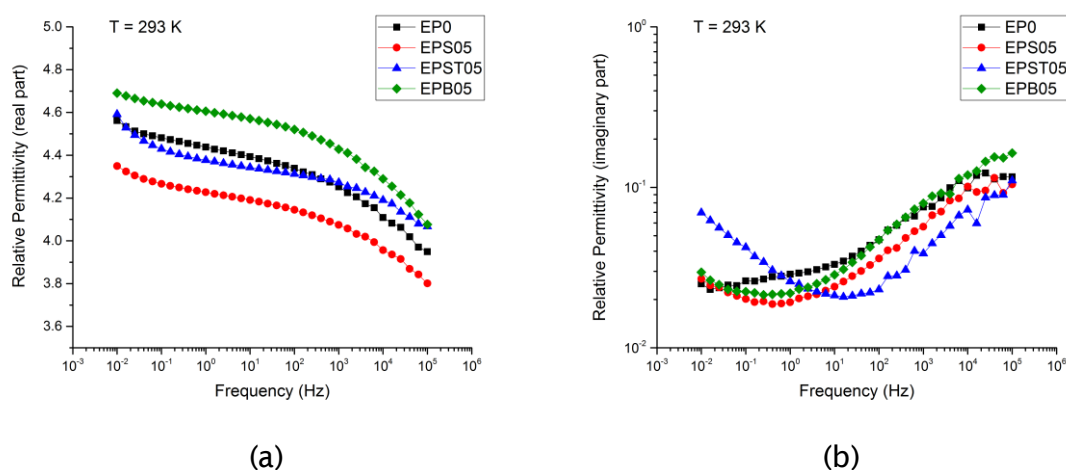


Figure 7-12 Relative permittivity in EP0, EPS, EPST, and EPB samples, filler loading concentration of 0.5 wt%, dry, 293K: (a) real part; (b) imaginary part.

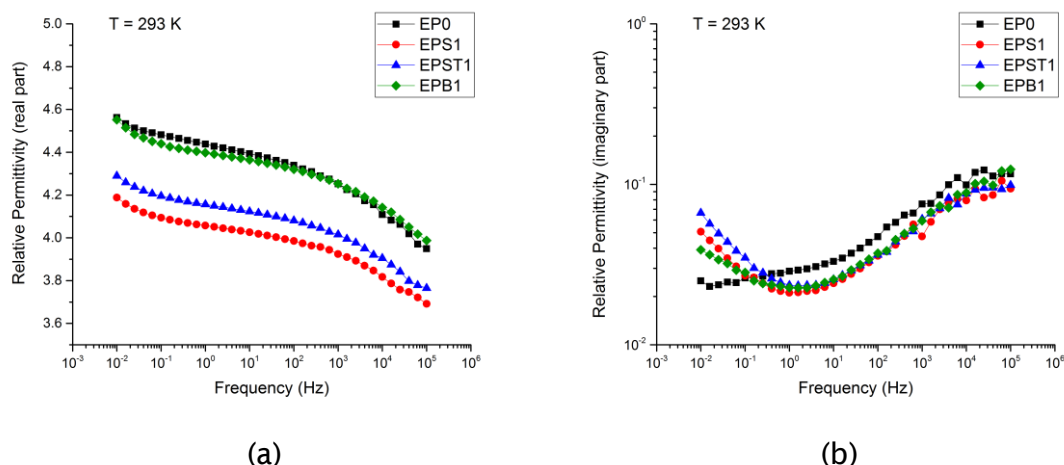


Figure 7-13 Relative permittivity in EP0, EPS, EPST, and EPB samples, filler loading concentration of 1 wt%, dry, 293K: (a) real part; (b) imaginary part.

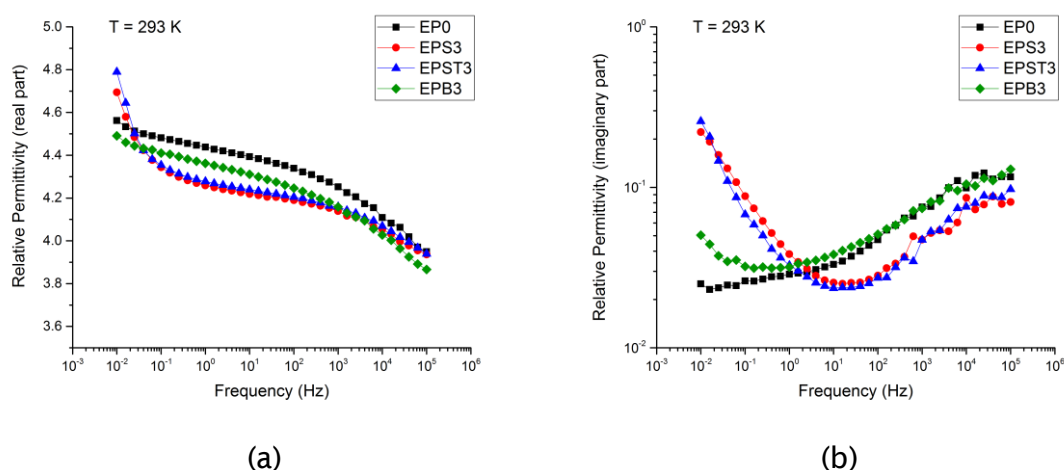


Figure 7-14 Relative permittivity in EP0, EPS, EPST, and EPB samples, filler loading concentration of 3 wt%, dry, 293K: (a) real part; (b) imaginary part.

In the high-frequency range, it shows a typical  $\beta$  relaxation of local motions of epoxy chains/dipoles in the vicinity of particles. The higher mobility will lead to the movement of the peak to the high-frequency range [165]. Thus, within nanocomposites, it can be obviously seen that the mobility of chain segments in the vicinity of particles is highest in EPST samples followed by EPS and EPB samples as shown in Figures 7-12 (b), 7-13 (b) and 7-14 (b). This is consistent with the analyses in the previous part. In the low-frequency range, the  $\epsilon''$  of nanocomposites shows different levels of increase at the low-frequency area which is always, reported as a “surge”, especially in EPST, due to the surface treatment (as discussed before). It is noted that the surge of  $\text{SiO}_2$ -based composites becomes obvious with the increase in filler loading concentration. This may be caused by the overlapped third layer containing shallow traps, which could lead to an increase in

the electrical conductivity of nanocomposites and result in an increase in  $\varepsilon''$  [164] as shown in Figures 7-13 (b) and 7-14 (b). However, hBN platelets seem to restrict the motions of charges within bulks when compared to  $\text{SiO}_2$  of spherical structure, thus leading to the small increase in the surge of EPB samples due to the introduced charges with lower mobility.

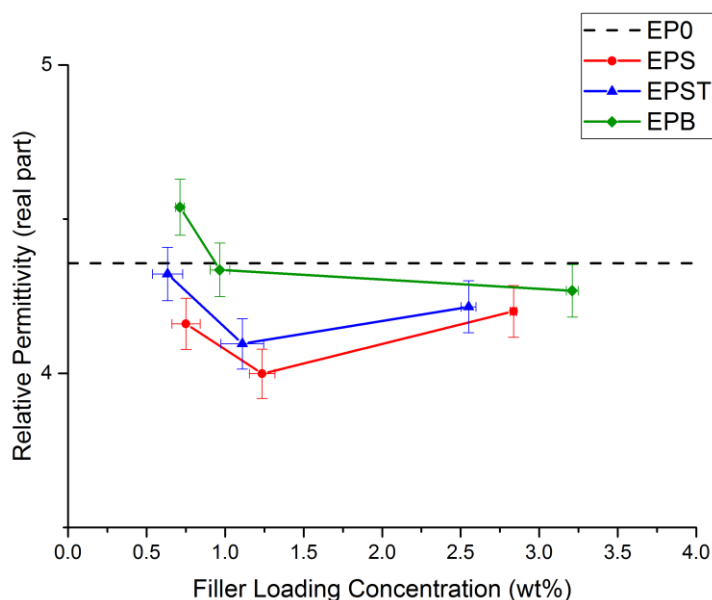


Figure 7-15 Comparison of real relative permittivity between EP0, EPS, EPST, and EPB samples at 50Hz, filler loading concentrations of 0.5, 1 and 3 wt%, dry, 293K.

### 7.2.2.1 Effects of Temperature

Considering the influence of temperature upon  $\varepsilon'$  and  $\varepsilon''$ , the results of EPS, EPST and EPB samples of 3 wt% at different temperature are shown in Figures 7-16, 7-17 and 7-18. Given that the surge of  $\varepsilon'$  of EPS and EPST in the low frequency range at 293K should be related to introduced charges, this seems to be further proved at higher temperatures where charges have higher mobility (see in Figures 7-16 (a) and 7-17 (a)). The process of  $\varepsilon''$  can be seen to be related to temperature as well, as shown in Figure 7-16 (b) and Figure 7-17 (b). For both EPS3 and EPST3 at 333K, composites filled with 0.5 wt% particles do not exhibit any peak as presented in samples of 3 wt%. It can be concluded that the relaxation in 3 wt% of  $\text{SiO}_2$ -based nanocomposites is related to the volume fraction of nanoparticles/ interfacial areas and can be further proved to be Maxwell-Wagner-Sillars (MWS) polarisation. As there are a number of deep/shallow traps located at the interface, the charges inside will be thermally activated and show higher mobility. Thus, the shifting of the

## Chapter 7 Dielectric Spectroscopy

relaxation peak towards the high-frequency range of EPS and EPST is easy to explain. Moreover, according to the differences between the activation energy of EPS3 and EPST3 in Table 7-1 that result from the Arrhenius plot, 0.6 eV higher value of EPST3 may indicate that additional traps have been introduced in the interfacial layers due to the presence of C8 chains, as this value is equal to the trap depth  $\omega$  for the hopping mobility of charges in polyethylene [10]. However, EPB3 exhibits anomalous behaviour of  $\varepsilon'$  at 333K.

Table 7-1 Charge transport activation energy.

Sample	Activation Energy (eV)
EPS3	2.07
EPST3	2.67

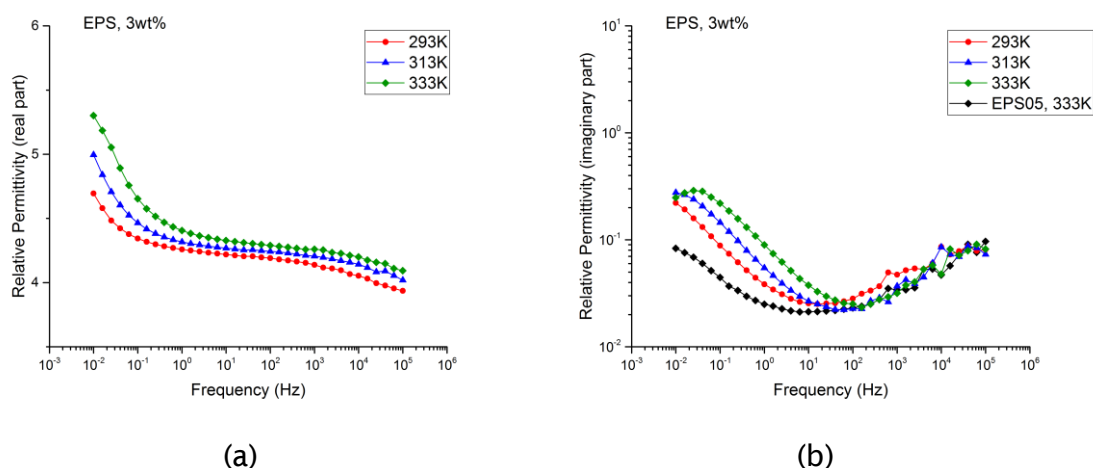


Figure 7-16 Relative permittivity in EP0, EPS samples, filler loading concentration of 3 wt%, dry, at 293, 313, 333K: (a) real part; (b) imaginary part.

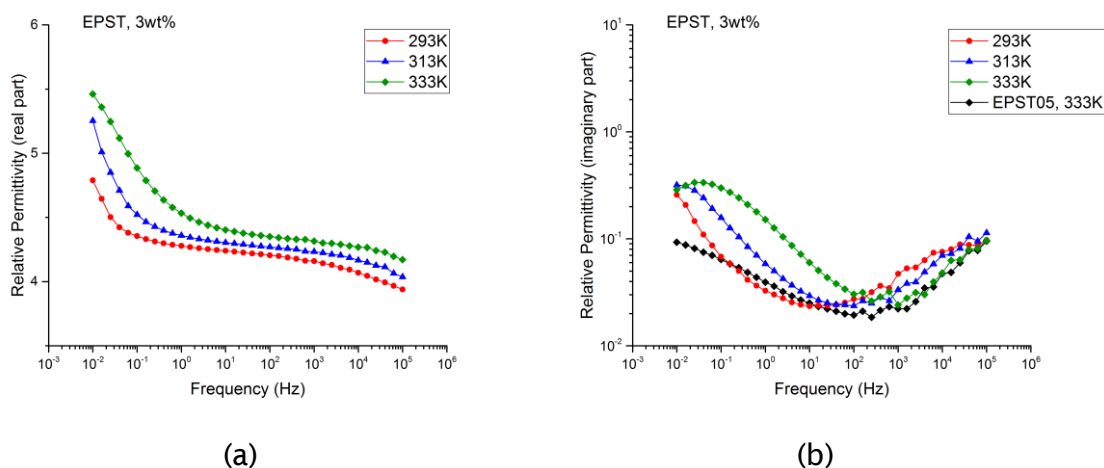


Figure 7-17 Relative permittivity in EP0, EPST samples, filler loading concentration of 3 wt%, dry, at 293, 313, 333K: (a) real part; (b) imaginary part.

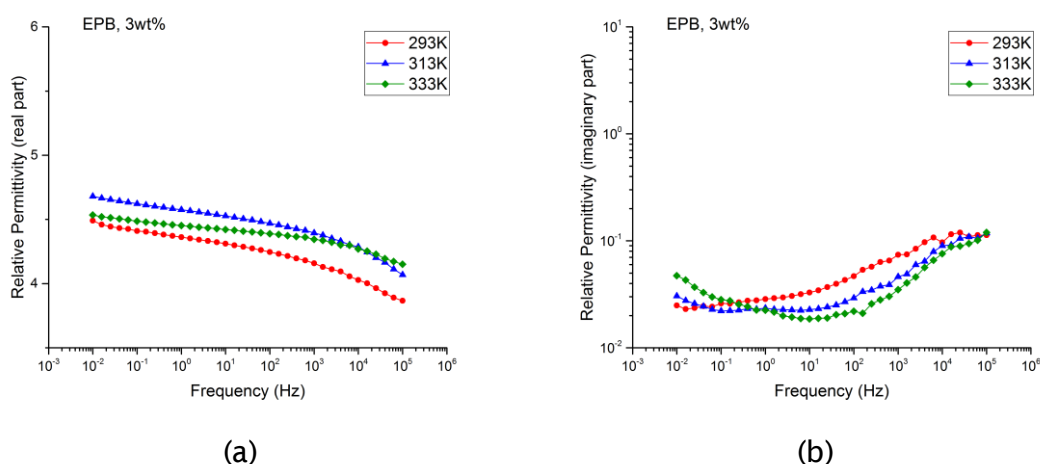
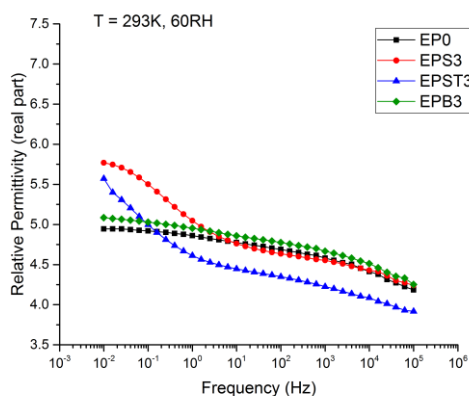


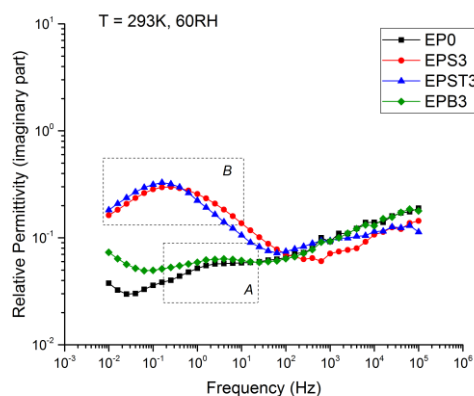
Figure 7-18 Relative permittivity in EP0, EPB samples, filler loading concentration of 3 wt%, dry, at 293, 313, 333K: (a) real part; (b) imaginary part.

### 7.2.3 Effect of Moisture on Dielectric Response of Epoxy Nanocomposites

The real and imaginary relative permittivity of 3 wt% are plotted in Figures 7-19 and 7-20 as a function of frequency, filler types in different RH conditions at 293K. As shown in Figure 7-14 (a), Figure 7-19 (a) and Figure 7-20 (a), as relative humidity increases, the  $\epsilon'$  of EPS, EPST and EPB samples also shows an increase, which is caused by the resultant growth of the volume fraction of water, itself related to the growth of water uptake. Moreover, it is noted that a large increase in the  $\epsilon'$  of EPS and EPST at low frequencies, which becomes more obvious with the growth of RH value. However, this is not shown in the results for EPB. This is likely due to the increased movement ability of charges through the water shell/matrix in  $\text{SiO}_2$ -based nanocomposites, whereas hBN acts to impair the motions of charges as discussed above. Moreover, the  $\epsilon'$  of EPS is higher than that of EPST under 60 RH conditions, which is contrary to saturated samples. Similar phenomena were also observed in filler loadings of 0.5 and 1 wt%.

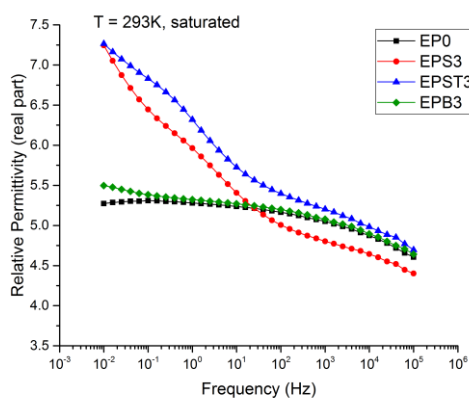


(a)

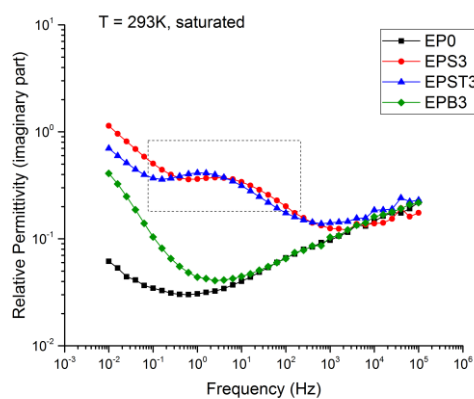


(b)

Figure 7-19 Relative permittivity in EP0, EPS, EPST, and EPB samples, filler loading concentration of 3 wt%, 60 RH, 293K: (a) real part; (b) imaginary part.

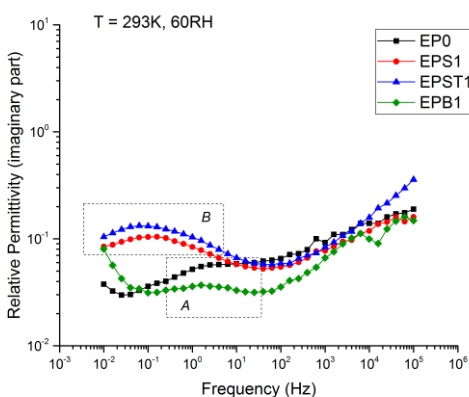


(a)

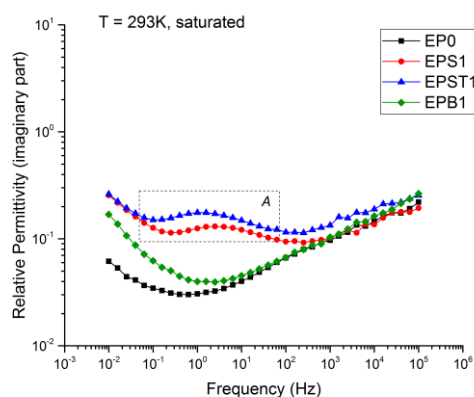


(b)

Figure 7-20 Relative permittivity in EP0, EPS, EPST, and EPB samples, filler loading concentration of 3 wt%, saturated, 293K: (a) real; (b) imaginary part.



(a)



(b)

Figure 7-21 Relative imaginary permittivity in EP0, EPS, EPST, and EPB samples, filler loading concentration of 1 wt%, 293K: (a) 60 RH; (b) saturated.

There are obvious relaxation peaks in the results of  $\varepsilon''$  shown in Figures 7-19, 7-20 and 7-21. As seen in Rectangle A of Figure 7-10 (b), EPB shows a similar relaxation peak compared to EP0 under 60 RH, which is also evident in 0.5 wt% and 1 wt% as shown in Figure 7-21 (a) but different in magnitude. It may be concluded that they both have similar structures of bonded water on the matrix chains. However, this type of peak disappeared in the saturated samples as shown in Figures 7-20 (b) and 7-21 (b). This is believed to be due to the shifting of the relaxation peaks towards high frequencies [96] and merging into the  $\beta$  relaxation peaks. Moreover, the responses of EPS and EPST are quite different. These peaks should be related to the bonded water reported in [18, 70, 96, 170, 171]. The observed loss peaks are probably due to Maxwell-Wagner-Sillars (MWS) losses from water at interface acting as a conducting layer [172, 173]. At this moment, it can be regarded as an interfacial layer between the fillers and matrix according to the interlayer model [174]. Thus, the  $\varepsilon^*$  of composites can be expressed by Equation 7.12 [174]:

$$\varepsilon_C^*(\omega) = \frac{\varepsilon_f^*(\omega)\varphi_f + \varepsilon_l^*(\omega)\varphi_l R^* + \varepsilon_m^*(\omega)\varphi_m S^*}{\varphi_f + \varphi_l R^* + \varphi_m S^*} \quad (7.12)$$

with

$$R^* = \frac{[(1-n)\varepsilon_l^* + n\varepsilon_f^*]}{\varepsilon_l^*} \quad (7.13)$$

$$S^* = \frac{[(1-n)\varepsilon_m^* + n\varepsilon_l^*][(1-n)\varepsilon_l^* + n\varepsilon_f^*] + dn(1-n)(\varepsilon_l^* - \varepsilon_m^*)(\varepsilon_f^* - \varepsilon_l^*)}{\varepsilon_l^* \varepsilon_m^*} \quad (7.14)$$

$$d = \frac{\varphi_f}{\varphi_f + \varphi_l} \quad (7.15)$$

where  $\varepsilon(m, f, l)$  and  $\varphi(m, f, l)$  represent the  $\varepsilon^*$  and volume fraction of the matrix, filler and interfacial layer respectively.  $n$  is the depolarisation factor of particles in the direction of the field related to the filler shape. When the particle is spherical,  $n$  is equal to 1/3. Once  $\varepsilon_l^*$  is small enough, Equation 7.12 can present a Debye-like relaxation according to Equations 7.16 and 7.17 [175]:

$$\varepsilon^*(\omega) = \varepsilon_\infty + \frac{\varepsilon_s - \varepsilon_\infty}{1 + i\omega\tau} \quad (7.16)$$

where

$$\tau = \left( \frac{\varphi_f}{1 - \varphi_f} \right) \left( \frac{\varepsilon_0}{n(1 - n)\sigma_i\varphi_i} \right) [(n\varepsilon_f + (1 - n)\varepsilon_m) - n(\varepsilon_f - \varepsilon_m)\varphi_f] \quad (7.17)$$

According to Equation 7.17, the frequency of the peak of the relaxation process is proportional to the volume fraction  $\varphi_i$  of the interfacial layer [175]. This explains the difference between Figures 7-19 (b) and 7-20 (b), which is due to the increase in RH. Moreover, the surge of  $\varepsilon''$  in all epoxy nanocomposites is found to be due to an increase in the motion of charges while water is present, especially in high RH conditions. The overlapping of the water shell and resultant conductive path should also contribute to the surge in  $\varepsilon''$  of EPS and EPST [70].

In order to further understand the influence of the water shell, which is calculated based on Equation 7.17, the Monte Carlo method is used to calculate the average thickness of the water shell of epoxy SiO<sub>2</sub> nanocomposites in all filler loadings under 60 RH and saturated conditions with 100 runs. If it is assumed that all the particles in saturated EPS/EPST samples are surrounded by water shells and only part of the particles in the samples under 60 RH conditions have water shells around, the ratio between them can be reflected by introducing an index  $k$  ( $k=1$  in saturated samples) which is calculated based on water uptake results in section 3.4, as expressed by Equation 7.18:

$$k = \frac{M_{i\_60} - M_{0\_60}}{M_{i\_s} - M_{0\_s}} \quad (7.18)$$

where  $M_{i\_60/s}$  and  $M_{0\_60/s}$  are the water uptake of epoxy nanocomposites and pure resins under 60 RH and saturated conditions respectively, and  $i$  refers to the filler loading concentration of EPS/EPST samples. Then,  $k \times \varphi_i$  is used to represent the volume fraction of water shells of nanocomposites under 60RH/saturated conditions. The conductivity here is  $0.01 \text{ S} \cdot \text{m}^{-1}$ , which was also used in [174, 175]. The resultant is Equation 7.19 as shown below:

$$\tau = \left( \frac{\varphi_f}{1 - \varphi_f} \right) \left( \frac{3\varepsilon_0}{2k\sigma_i\varphi_i} \right) [(\varepsilon_f + 2\varepsilon_m) - (\varepsilon_f - \varepsilon_m)\varphi_f] \quad (7.19)$$

According to Equation 2.11, the volume fraction of particles  $\varphi_f$  can be obtained, and then volume fraction of the water shell  $\varphi_i$  in EPS/EPST of different filler loadings can be calculated via Equation 7.19 based on the relaxation time extracted



from experiment results in Figures 7-19 to 7-21, which is used to generate the average thickness of water shell (ATWS) under 60RH/saturated condition, as shown in Table 7-2. It is noted that ATWS is revealed to be much higher in saturated samples, where 53.4 nm is very close to the simulation result of 50 nm in [15, 19]. Thus, it can be concluded that ATWS in EPS/EPST will increase obviously under RH conditions, which was qualitatively reported in [176]. Moreover, based on Equation 7.19 and the results presented in Table 7-2, plots of filler loading concentration versus relaxation time for silica nanocomposites are shown in Figure 7-22, in which  $\tau(m)$  and  $\tau(c)$  are measured and calculated (using ATWS) relaxation time respectively. From the figures, here could propose this method to be a relatively reliable way to estimate the ATWS or related relaxation peak of epoxy nanocomposites with spherical particles.

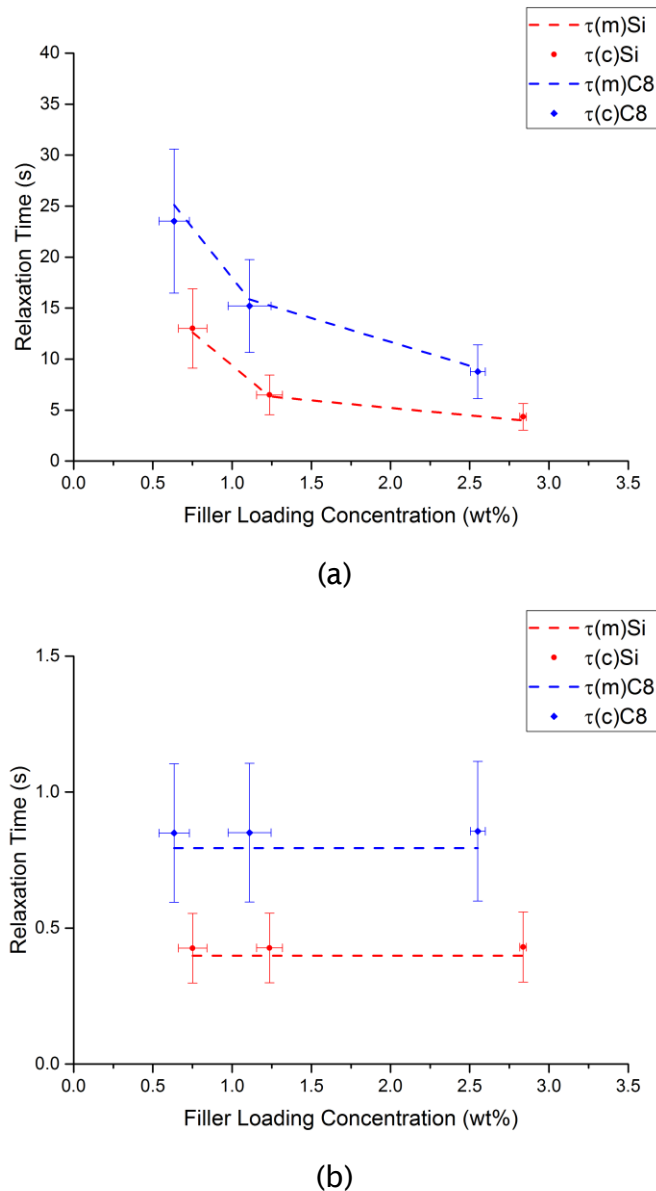


Figure 7-22 Measured and calculated relaxation time of silica nanocomposites: (a) 60 RH; (b) saturated.

Table 7-2 Average thickness of water shell under different RH environment

Sample	Thickness(nm)/60RH	Thickness(nm)/Saturated
EPS	$23.7 \pm 4.6$	$53.4 \pm 10.3$
EPST	$21.4 \pm 4.3$	$42.1 \pm 8.4$

The difference in ATWS between EPS and EPST samples conditioned under a 60RH environment is found to be  $2.3 \pm 0.3$  nm in value, which is almost the same as the average thickness of the surface-treated layer at  $\sim 2.13$  nm calculated in section 5.1.1. However, this increases to  $11.3 \pm 1.9$  nm. The major difference between these two particles is believed to be due to their surface characteristics as bonded water and hydrophobic treated layer. In saturated samples, the bonded water on the particle surface of EPS seems to attract more water molecules via Van de Waals forces [15]; accordingly, ATWS in EPST is much smaller due to the lack of hydroxyl groups, tightly bonded water and corresponding attracting ability. Therefore, the existence of two layers of tightly and loosely bonded water could be demonstrated, and the former can be removed by surface treatment. However, the second layer of water still exists due to hydroxyl groups on polymer chains and free volume in this region [70]. Thus, although surface modification could remove the hydroxyl groups and does reduce water uptake, the influences of water shell still exist, although they are mitigated. The schematic diagram shown in Figure 7-23 aims to illustrate the water shell around the particles. The dashed circle represents the average thickness of the water shell in 60RH conditioning samples; owing to the higher RH conditions, the ATWS of saturated samples increases and is shown by the dotted circled area. There is a tightly bonded layer in both EPS and EPST samples, with tightly bonded water via hydroxyl groups acting as the first layer of water shell and hydrophobic C8 chains respectively. Under the 60RH condition, the difference between EPS and EPST samples is dominated by the tightly bonded layer as discussed above. Although there should also be some water located beyond the dashed boundary, it is not able to show conductive behaviour and thus not to be regarded as part of the water shell. Once more moisture appears due to higher RH conditioning, the areas between dashed and dotted circles become conductive.

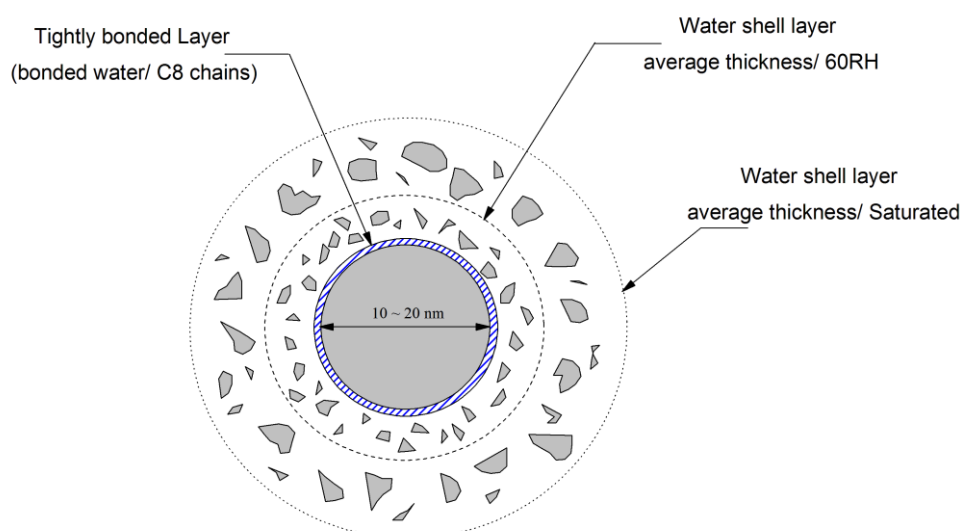


Figure 7-23 Illustration of water shell under different relative humidity conditions.

Regarding the EPB samples, despite the fact that the depolarisation factor  $n$  of BN particles is hard to determine at this point, if there is a conductive layer of water formed around its particles, the similar Debye-like relaxation processes of silica nanocomposites should appear. However, only a relaxation of bonded water similar to that in pure samples can be observed, thus, it could be concluded that there is no water shell formed in hBN-based nanocomposites. This should, first, be due to that there are only a very small amount of hydroxyl groups on hBN particles located on edge planes with [111] rather than upper/lower sides of the plates; secondly, as the molecule structures of interphases in the parallel and vertical direction of particle planes is different [178], there would be no similar continuous structures to form the water shells that are present around spherical particles. Additionally, the increase in water uptake with filler loading concentrations in saturated EPB samples may mainly result from the growth of cracks/voids [98, 178].

### 7.3 Chapter Summary

The work presented in this Chapter can be summarised as follows:

1. Water absorption was highly influenced by the surface of and structure around particles. The surface treatment reduced the water uptake and introduced deeper traps in the interfacial layers when compared to the untreated samples. However, there was no obvious impact on modifying the dielectric properties, owing to the limitation of the thickness of the tightly bonded layer and water in the second layer of the multi-core/water shell model. Moreover, the frequently reported relaxation peaks due to bonded water that appeared in the mid-frequency range were proven to be related to Maxwell-Wagner-Sillars polarisation within water shells around spherical particles rather than to bonded water on the particle surface as reported in the previous literature [19, 48].
2. The addition of inorganic nanoparticles is a solution to modify the dielectric properties of epoxy composites. However, absorbed moisture is a problem that is difficult to solve. While getting rid of hydroxyl groups on the surface of silica particles, water shells still appeared and led to similar dielectric properties as those for composites filled with untreated particles. Moreover, the “hydrophobic” performance of BN nanocomposites was found to be much better than for silica ones, especially as concerns the lack of formation of a water shell around the particles. It can thus be concluded that hBN-filled epoxy nanocomposites would be suitable for an environment with moisture; however, other demands of the application should still be considered.

## Chapter 8 DC Conductivity and Space Charge Behaviour of Epoxy Nanocomposites

### 8.1 DC Conductivity of Epoxy Nanocomposites

#### 8.1.1 DC Conductivity

##### 8.1.1.1 Concept of Conductivity

When a voltage  $V$  is applied between two sides of a material, an electric field is then established. The electric field may or may not be uniform depending on the geometry of the electrode and other factors. Charged carriers/particles will be forced under the electric field by an electrostatic force that is the product of their charge,  $e$  (in Coulombs, C) and the electric field. This force shares the same direction as the electric field. Once carriers/particles are forced, this results in the movement (so-called ‘drift’) and they transport in the material, though this transport could also be caused by the random *diffusion* of carriers/particles. The rate of charge carrier transporting ( $C \cdot s^{-1}$ ) is named the electric current,  $I(A)$ , and its equivalent system property in the material is the current density,  $J (A \cdot m^{-2})$ . Due to Ohm's law, the current  $I$  through a conductor based on the drift to the applied voltage can be expressed as Equation 8.1:

$$I = \frac{V}{R} \quad (8.1)$$

where  $R(\Omega)$  is the resistance of the conductor. Moreover, Ohm's law can also be expressed according to the properties of the material, the applied field  $E$  and current density  $J$  as Equation 8.2:

$$J = \left( \frac{1}{\rho} \right) \cdot E = \sigma E \quad (8.2)$$

where  $\rho$  is the resistivity of the material ( $[\Omega \cdot m]$ ) and  $\sigma = 1/\rho$  is the conductivity ( $[\Omega \cdot m]^{-1}$  or  $S \cdot m^{-1}$ ). Equation 8.2 expresses the proportional relationship between the average velocity of the charged carriers/particles (called ‘drift velocity’) and the applied field  $E$ .

## Chapter 8 DC Conductivity and Space Charge Behaviour

Materials exhibit a very wide range of conductivities, and some typical polymers (as good insulators) are in the approximate range  $10^{-16} \sim 10^{-20} \text{ S} \cdot \text{m}^{-1}$  [179]. Thus, the current in these insulators may be extremely difficult to measure. Moreover, their conductivity also depends on temperature, sample preparation and some other parameters. Therefore, the factors affecting the conductivity of materials will be introduced here. The conductivity of a material due to charge carriers in a material can be expressed as Equation 8.3:

$$\sigma_i = n_i e_i \mu_i \quad (8.3)$$

where  $n_i$  is the concentration ( $\text{m}^{-3}$ ) of the charge carrier type  $i$ ,  $e_i$  is the electric charge (C) on each carrier, and  $\mu_i$  is the mobility ( $\text{m}^2 \text{V}^{-1} \text{s}^{-1}$ ), which is defined as the drift velocity per unit field:

$$\mu = \frac{v_d}{E} \quad (8.4)$$

Generally, there will be more than one type of charge carrier contributing to the conductivity of the material. Thus, if there are  $N$  types of carriers, the resulting conductivity can be expressed as Equation 8.5:

$$\sigma = \sum_i^N \sigma_i = \sum_i^N |n_i e_i \mu_i| \quad (8.5)$$

The concentration of charge carriers  $n$  is in the range from almost zero to more than one per atom ( $< \sim 10^{29} \text{ m}^{-3}$ ). This should result in a large range of conductivities [179]. Moreover, the value of mobility  $\mu$  may only have very small magnitude; however, under certain conditions,  $n \times \mu$  will vary significantly. Based on this, it is thus possible to assume a constant carrier concentration  $n$ . In addition, the energy band theory has been introduced to provide insight into the carrier concentration of polymers, as well as, the band transport of carriers of materials [165, 180, 181].

### 8.1.1.2 Ionic and Electronic Conduction

The band theory may be able to explain charge transport along all or part of the polymer chains, both as holes and electrons. This section aims to provide an overview of the types of carriers and typical conduction mechanisms in solid materials. Charge transport may be classified based on the type of charge carrier [179]. Two main types are ionic (including protonic) transport and electronic

(including hole) transport. Moreover, the type of charge carrier (in terms of conduction phenomena) mainly depends on the chemical and physical properties of the materials, the applied field's frequency and the temperature.

*Ionic transport* is mass transport, and metallic electrodes can only provide electrons or recombination sites for holes. Ionic transport depends primarily on the creation, movement and destruction of ions, although there are already some ions existing in the material. All of these ions could be generated by electrolytic action at interface of the electrode and the insulating material or by decomposition of the material. The movement of ions and resulting current flow will form the ionic conduction. Moreover, ionic transport can be further divided into two types of ionic conduction: first, *intrinsic ionic conductivity* is carried out along the dissociated main chain or side groups and is followed by a proton and/or electron transfer through the hydrogen bond network; second, *extrinsic ionic conduction* is caused by ions that are not part of the chemical structure (most exist as additives or impurities).

*Electronic transport* through a band structure is also known as electron and hole transport. This transport of carriers can proceed along the length of the polymer chain. Electrons and holes are likely to be trapped in a localised state between the molecular and chain defects. Electrons/holes can be trapped by acceptors/donors or ionised donors/acceptors. Once the charges have been trapped, this may lead to the local polarisation and distortion of the lattice structure, which will further result in the deformation of the local energy band and makes it hard for trapped charges to escape. Therefore, the carriers must overcome the large potential barriers with the help of thermal/phonon excitation to leave the traps. Moreover, this process may also be affected by applying high electric fields and other factors [179]. Once the carriers become free, they will be attracted and then enter its "potential well."

One of the mechanisms for electronic transport is known as *thermally activated hopping* from one trap to another, where the electron/hole gained sufficient energy could overcome the potential barrier by thermal fluctuations to reach. Another mechanism is that an electron/hole can move from one trap to a close adjacent one by means of *quantum mechanical tunnelling*, as an electron is not only well-defined as a particle and the electron-wave can tunnel through narrow barriers by simply 'appearing' to a nearby trap [182]. Regarding conduction in polymer insulators, taking PE as an example, it is believed to be dominated by electrons and the

transport of carriers takes place along the amorphous regions and is limited by whereby traps [183, 184].

### 8.1.2 DC Conductivity Measurement Results and Analysis

#### 8.1.2.1 Effects of Filler Loading Concentration

The DC conductivity of pure, EPS, EPST and EPB samples in each loading concentration at 293K are plotted in Figures 8-1 to 8-3 as a function of time. All the data in the last 600s of each curve are plotted, with an error bar also included. It is noted that, in all kinds of nanocomposites, conductivity increases with the growth of filler loading concentrations. EPS05 shows slightly lower conductivity than pure samples; this is likely due to morphology changes caused by the presence of nanoparticles, as discussed in section 4.2 and [147]. Changes in the chemical structures of polymers may lead to an increased presence of traps in bulk, especially near the surface [165]; this could hinder the charge injection, thus reducing the mobility of charge carriers and finally resulting in a reduction in conductivity [185]. However, with an increase of filler loadings, more nanofillers will lead to a far greater impact on polymer structures and thus a higher density of traps; this means the average distance between arbitrary traps should be lower in samples with higher filler loadings and that charge carriers will require less energy when moving from one to another. The resulting increased carrier mobility will lead to higher conductivity.

Moreover, if regarding nanofillers as recombination centres [105], the shorter average surface distance between nanoparticles (shown in Table 4-2 in section 4.3), should also result in a higher conductivity value. EPST and EPB samples should share the similar mechanism. However, it should be noted that the variation of EPB samples is obvious smaller than that of SiO<sub>2</sub> samples. This is likely due to the vastly more complex morphology in bulk (as has been shown in section 4.2) and the enormous traps adjacent to the surface, which significantly reduce the amount of injected charges.



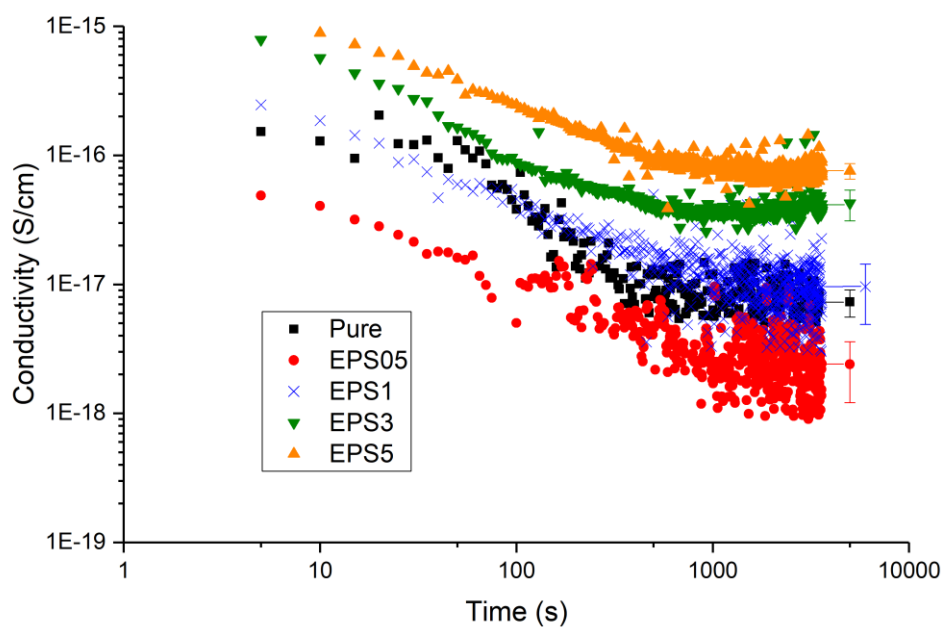


Figure 8-1 DC conductivity of EP0 and EPS samples in each filler loading concentration, dry, 293K.

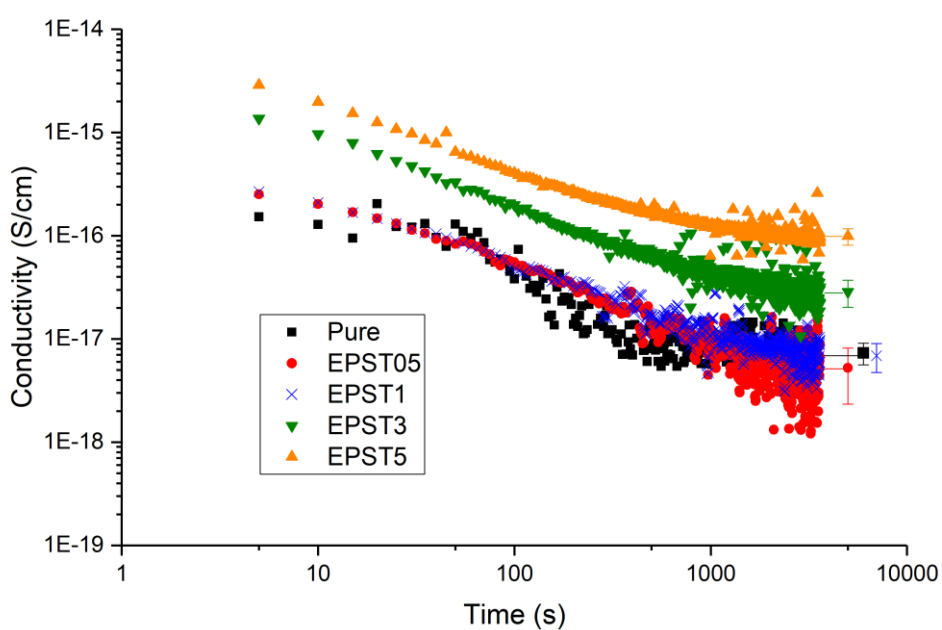


Figure 8-2 DC conductivity of EP0 and EPST samples in each filler loading concentration, dry, 293K.

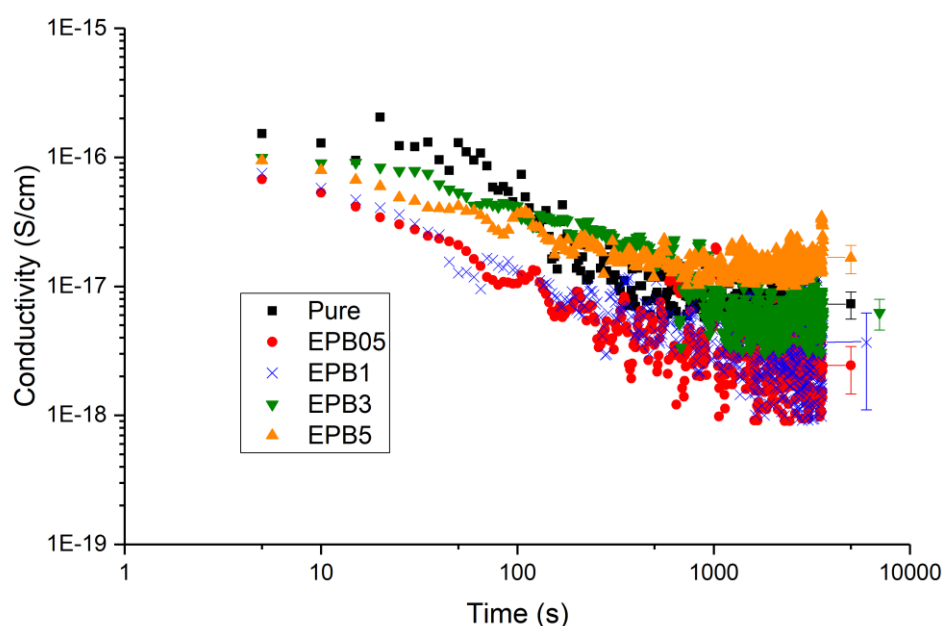


Figure 8-3 DC conductivity of EP0 and EPB samples in each filler loading concentration, dry, 293K.

### 8.1.2.2 Effects of Filler Type

The DC conductivity of pure, EPS, EPST and EPB samples in 1 and 3 wt% are shown in Figures 8-4 and 8-5. It is noted that EPST1 samples have similar, slightly higher conductivity when compared to EPS1 samples, which becomes more obvious at 3 wt%. This is likely to be caused by the residues of solvents from the surface treatment, which acts as additional charge carriers, resulting in high conductivity. The samples with higher loading concentrations clearly contain larger amounts of this kind of carrier; our experiment is consistent with analysis, which is also reported in [10]. However, water absorption should cause an increase of conductivity after 1000s in EPS1 and EPS3 samples during the test, that is the reason why the conductivity of EPS in the last 600s is higher than that of EPST in both 1 and 3 wt%. Moreover, morphology and more traps as mentioned in section 5.2.2 and 6.3.2.1 respectively due to the presence of plate-like nano-hBN fillers seem to act as barriers for charges, leading to lower conductivity.

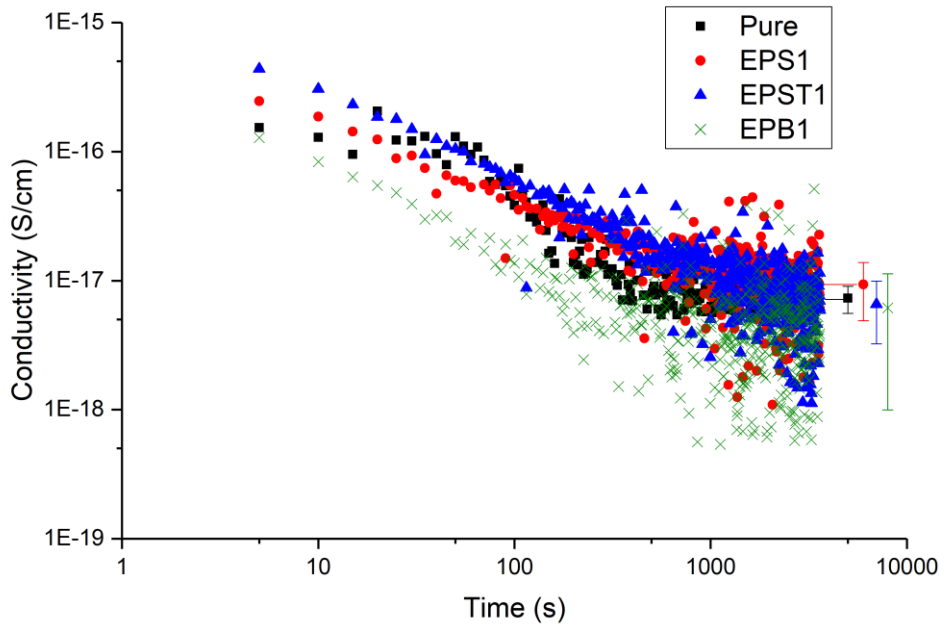


Figure 8-4 DC conductivity of epoxy and its nanocomposites (1 wt%), dry, 293K.

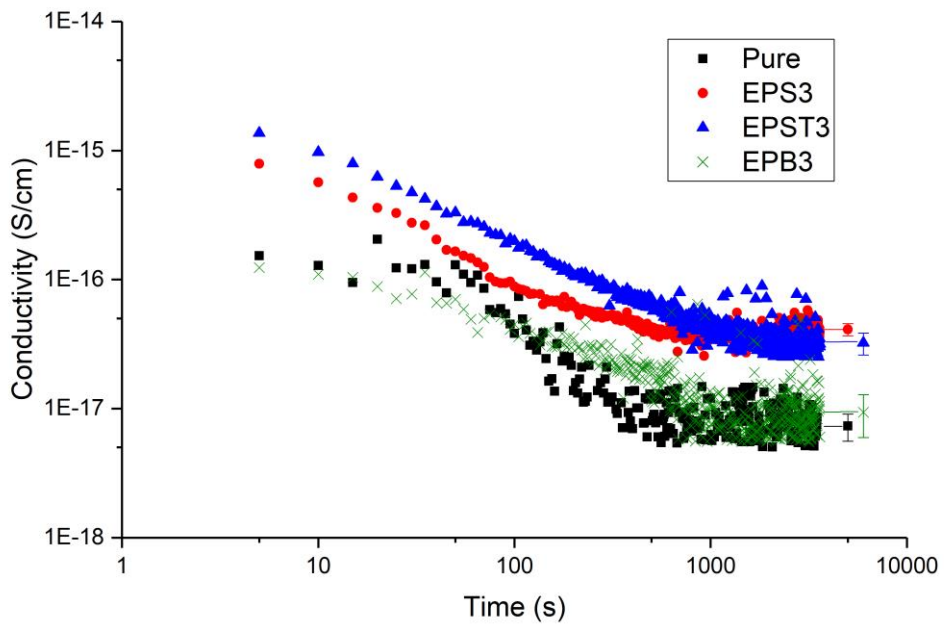


Figure 8-5 DC conductivity of epoxy and its nanocomposites (3 wt%), dry, 293K.

### 8.1.3 Effects of Moisture on DC Conductivity Measurement and Analysis

The effect of moisture on pure epoxy samples is shown in Figure 8-6. The conductivity rises with the increase in filler loading due to the enhancement of the mobility of charge carriers. The ratios of conductivity in A. RH, 60RH and saturated

## Chapter 8 DC Conductivity and Space Charge Behaviour

samples appear similar to that of the water uptake percentage measured in section 3.4, as they are 0.40%, 0.52% and 1.86% respectively.

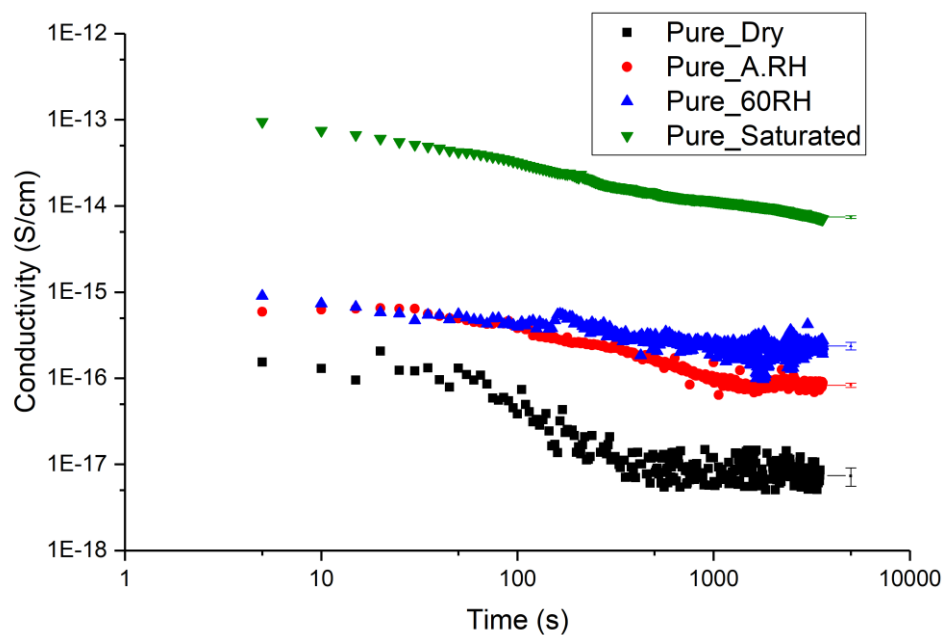


Figure 8-6 DC conductivity of pure epoxy resins in each RH condition, 293K.

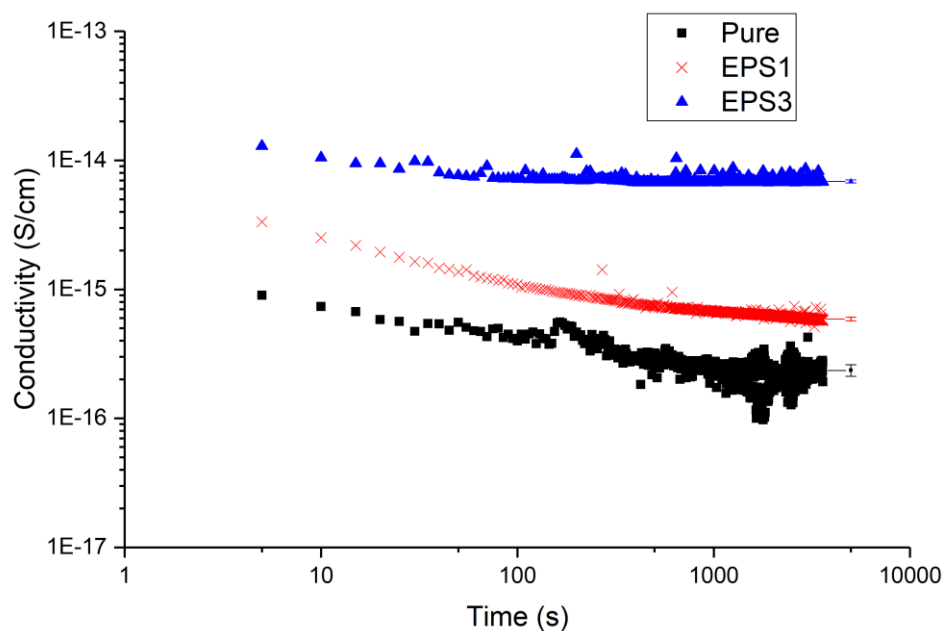


Figure 8-7 DC conductivity of EP0 and EPS samples in 1 and 3 wt%, 60RH, 293K.

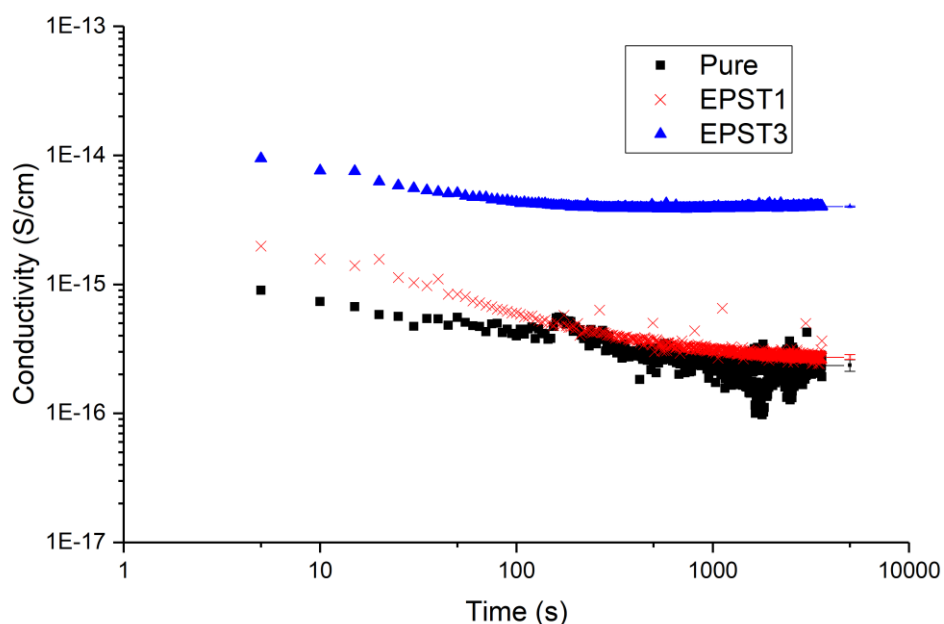


Figure 8-8 DC conductivity of EP0 and EPST samples in 1 and 3 wt%, 60RH, 293K.

Regarding the moisture effect on EPS and EPST samples at different filler loadings, increased conductivity is evident in samples of higher filler loadings. Firstly, this is due to the presence of more water, leading to higher mobility values of charge carriers in both base materials and within traps/particles. Secondly, to consider the effect of the shorter distance between particles, the surface distances of EPS and EPST samples in each RH condition based on the water-shell model and shell thickness analysis in section 7.2.3 are presented in Table 8-1. It is obvious that shorter average surface distance is evident in samples with higher water content and filler loadings; this will make it easier for carriers to move from one to another if particles are regarded as recombination centres [105]. Moreover, because the presence of particles could create traps at interphases coming from the end of chains [105], the effect of hopping and quantum tunnelling processes may be more obvious in higher RH conditions, as hopping distance may be larger than the distance stated in Table 8-1. Thus, it is assumed that the tunnelling effect may become much more significant due to the presence of moisture. Some researchers have reported various tunnelling distances between traps, and one has quantified it as  $\sim 10$  nm [186]. If this value is taken as the threshold of tunnelling, the percentages of the surface distances between one particle and the closest one that are smaller than 10 nm in each RH condition are listed in Table 8-2; this is based on the proposed quantification method in Chapter 4.

Table 8-1 Weighted surface distance of EPS and EPST samples in 1, 3 wt% in each RH condition.

Sample Code	Dry (nm)	60RH (nm)	Saturated (nm)
EPS1	180.43	157.93	137.09
EPS3	155.27	134.92	115.50
EPST1	257.35	239.58	224.29
EPST3	200.08	178.22	155.31

Table 8-2 Percentage of weighted surface distance &lt;10 nm of EPS and EPST samples in 1, 3 wt% in each RH condition.

Sample Code	Dry (%)	60RH (%)	Saturated (%)
EPS1	17.25	48.61	65.57
EPS3	18.50	49.73	70.32
EPST1	14.57	40.13	51.79
EPST3	16.54	48.48	62.88

As shown in Table 8-2, it is noted that, under the dry condition, the percentages of both EPS and EPST are lower than 20% and increase slightly with the growth of filler loadings. Moreover, the slightly smaller ones in the EPST samples are likely due to the surface treatment. With the presence of moisture, the percentages show significant increases of ~30% in samples under 60RH condition and a further increase ~10-15% in saturated ones. A similar ratio is also found in the experimental results of the conductivity of 3 wt% samples, as is shown in Figures 8-8 and 8-9, rather than the ratio of water uptake between these two RH conditions. Results for 1 wt% show similar trends. Thus, the tunnelling effect may become more obvious in samples with moisture, thus increasing the conductivity of epoxy SiO<sub>2</sub> samples.

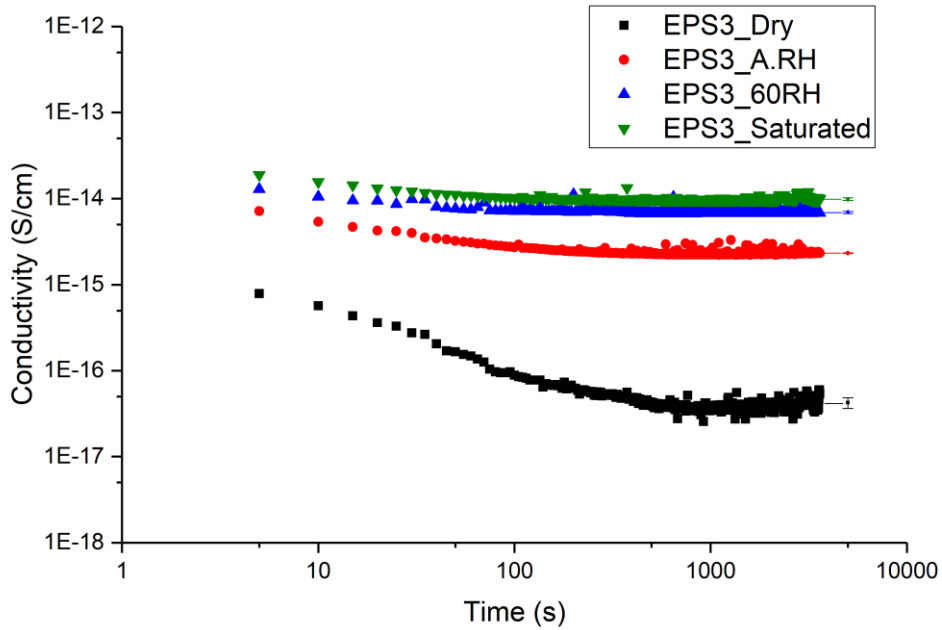


Figure 8-9 DC conductivity of EP0 and EPS3 in each RH condition, 293K.

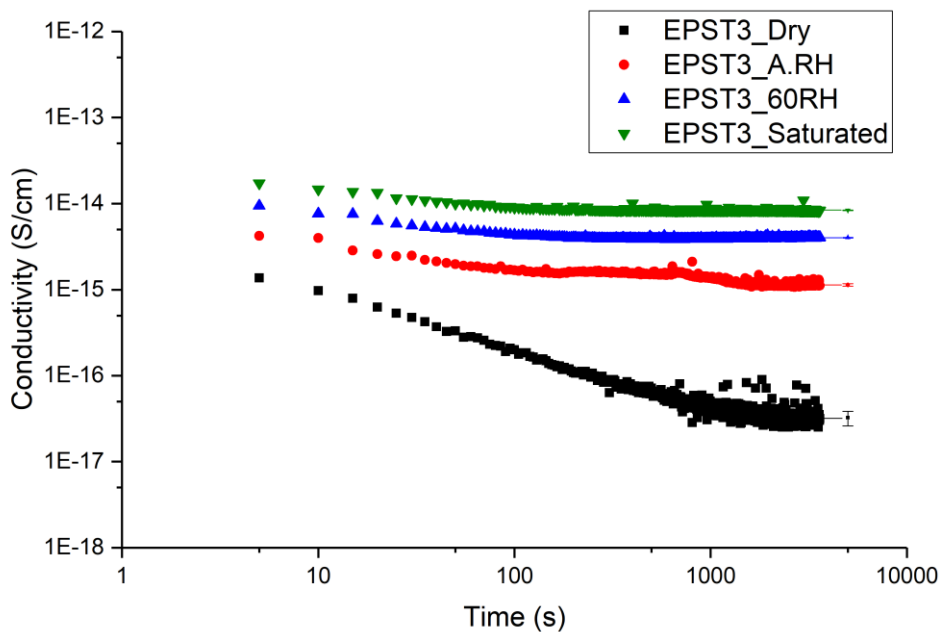


Figure 8-10 DC conductivity of EP0 and EPST3 in each RH condition, 293K.

However, EPB samples in all RH conditions (with samples in 60RH shown in Figure 8-11 as an example) exhibit opposite trends when compared to EPS and EPST samples, showing lower conductivity in 3 wt% even though conductivity still increases under RH conditions. This behaviour could be due to the fact that the barrier effect of resulting morphology from the presence of nano-hBN particles is more dominant than moisture on the conductivity of EPB samples.

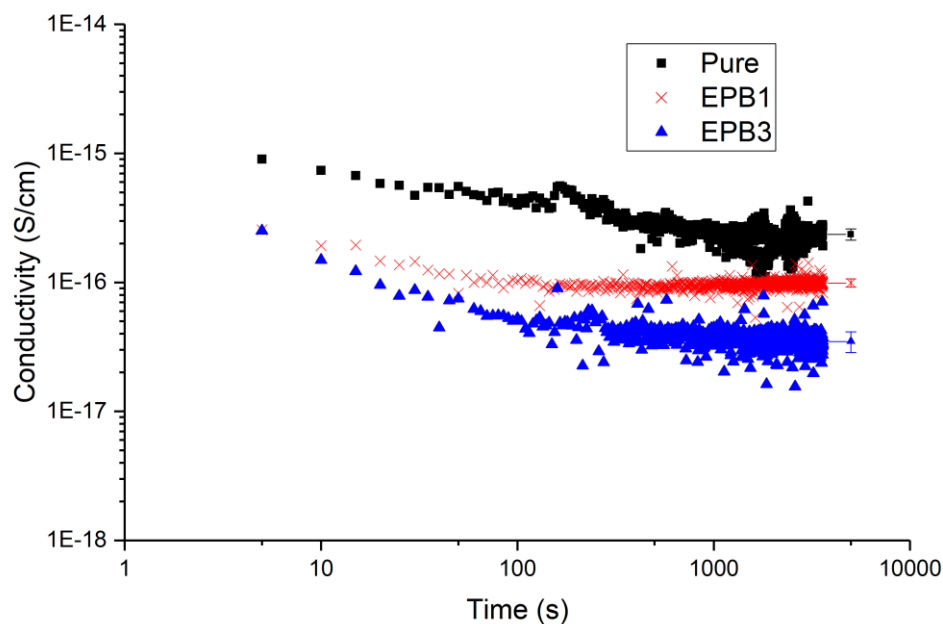


Figure 8-11 DC conductivity of EP0 and EPB samples in 1 and 3 wt%, 60RH, 293K.

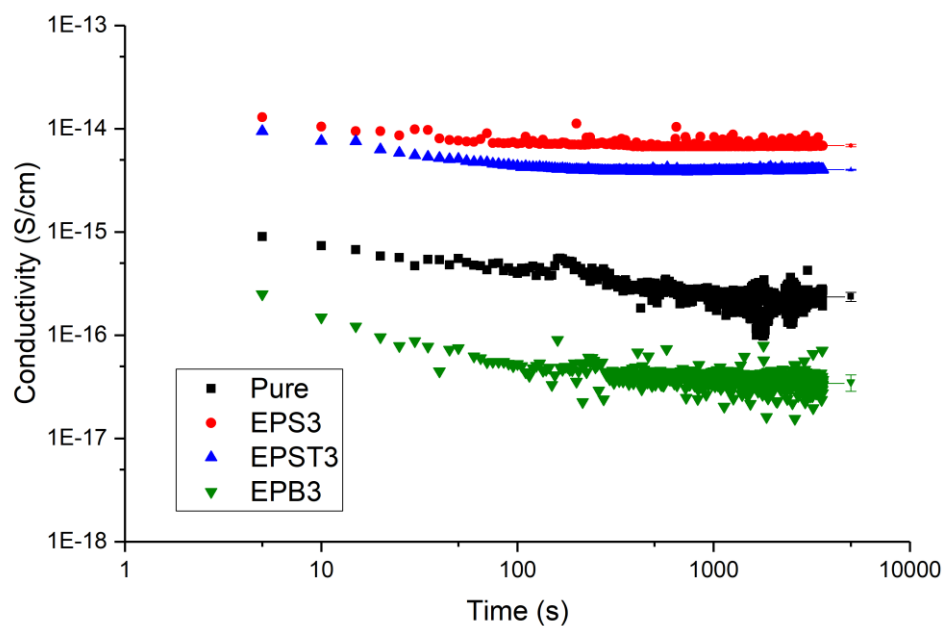


Figure 8-12 DC conductivity of epoxy and its nanocomposites (3 wt%), 60RH.

As shown in Figure 8-12, the difference between EPS3 and EPST 3 samples is likely to primarily result from the inter-particle surface distance (see also Table 8-1). If nanoparticles are regarded as recombination centres [105], the shorter distance in EPS samples would allow charges to transport from one to another, thus leading to higher conductivity. BN particles and the resulting morphology seem to act as



barriers or to play a role in hindering the injection and formation of channels for charges and carriers in each RH condition, which are consistent with the analysis in previous part of this section. The same trend seen in Figure 8-12 is also observed in A.RH and saturated samples' results.

## **8.2 Space Charge Behaviour of Epoxy Nanocomposites**

### **8.2.1 Space Charge and Measurement Method**

When a sufficiently high electric field is applied to epoxy resins, charges can be injected into the bulk of materials, and these could also travel across the material under an external electric field. In this case, the electrical properties of the epoxy resin would also be changed. This change is not only due to the high applied field, but also the temperature, the electrode and polymer interface. For example, earlier studies have shown that many phenomena are observed in the polymer insulator [187]. Earlier studies have also found that charge trapping, tunnelling and hopping conduction determine the charge transport in polymer materials [188-190].

#### **8.2.1.1 Concept of Space Charge**

As space charge has significant effects upon solid dielectric materials, studies on this subject have been carried out continuously. Space charge is a surplus of charge carriers, including electrons, ions and holes distributed into the polymer material. These charges are moving around and trapped in the material. The trapped charges could lead to space charge limited current (SCLC), which causes electrical breakdown or aging problems of the polymer when the applied electric field is high enough [188]. Space charge usually occurs in dielectric material and is one of the most important factors that will decide the dielectric properties of the material [190]. Earlier studies have also shown that the presence of nanofillers in the epoxy resin influences the accumulation of space charge. When compared to pure epoxy, epoxy nanocomposites with nanofillers seem to have less accumulated charges. It has also been reported that the dynamics of charges in epoxy nanocomposites result in faster charging intensity, especially for negative charges. The space charge injection mainly comes from the electrode and is generated within the polymer materials [165]. The reasons for the formation of space charge in the polymer can be divided into the following mechanisms: charge injection from external electrodes, the orientation of dipole movements inside dielectric materials resulting from the applied electric field, and ionisation of impurities inside the dielectric materials resulting from the applied electric field.

The dominant mechanism for charge emission in most polymer dielectric materials is the injecting electrons from the cathode and the extracting electrons from the anode (hole injection). This mechanism, which can also be described as electrons being injected from the cathode and holes being injected from the anode, is widely used to explain the movement of charge carriers in polymer dielectric material. Considering the charge injection from the external electrode, the electrons and holes will travel through the interface of the polymer and electrodes and be injected into the bulk dielectric. Thus, defects and impurities in the interfacial areas will affect the charge injection [191-194].

When an external electric field is applied to the polymer dielectric, the dipole will be oriented under the field within the polymer dielectric. This is called dipole polarisation or orientation polarisation. The movement of dipoles will cause space charge accumulation in a range inside the polymer dielectric material. Moreover, another reason for the accumulation of space charge is that it is mainly caused by the ionisation of chemical species in bulk of the dielectric material, such as cross-linked residues and impurities [193]. The applied voltage and temperature also have significant effects on the distribution of space charge when applying high voltage. Thus, the space charge distribution can vary even in the same sample [191, 193]. Moreover, the space charge density as a combination of both current density and inhomogeneous resistivity over a range of space, can be summarised as follows:

$$\zeta(x) = J \cdot \varepsilon \frac{d\rho(x)}{dx} \quad (8.6)$$

where  $\zeta$  is the space charge density,  $J$  is the current density,  $\varepsilon = \varepsilon_0 \cdot \varepsilon_r$  is the absolute permittivity and  $\rho$  is the electrical resistivity [195].

### 8.2.1.2 Homocharge and Heterocharge

Homocharge and heterocharge are usually used to describe polarities when analysing the formation of space charge. Homocharge is space charge that has the same polarity as the nearby electrode, while heterocharge is space charge that has the opposite polarity. Figure 8-5 (a) and (b) depict the homocharge and heterocharge respectively. As space charge accumulation inside polymer dielectric material will affect the local electric field, the net space charge distribution within polymer dielectric material will be important, because the breakdown strength of

material will change with the variation of the local electric field; this can make it difficult to predict the lifetime of the polymer insulators.

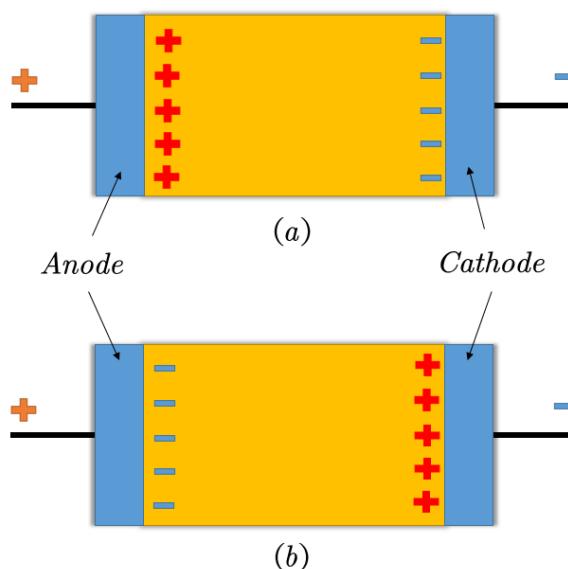


Figure 8-13 Illustration of (a) Homocharge and (b) heterocharge.

The charge injection from the electrode will generate homocharges around the electrode. These charges will increase the electric stress in the bulk of samples, therefore, electric stress at the electrode interface will be reduced. Heterocharges may be caused by the ionisation process of small molecules, and are expected to have the opposite effect when compared to the homocharges. Moreover, PEA measurement can only measure the distribution of net charges, when both homo- and heterocharges exist in the material at the same time. That is to say, this measurement can only observe the net charge presents in the material. Therefore, homocharges and heterocharges in the results are the net charges of both positive and negative charges.

### 8.2.2 PEA Measurement Results and Analysis-Dry

“Volts-on” measurements are taken in the experiments, meaning that the readings will be taken by applying a pulse when a voltage is applied to the samples. Before the measurements, a reference measurement also needs to be taken. For the epoxy resin samples, the voltage for reference measurement is set to 1.5 kV. The applied voltage during the volts-on measurements is ~5 to 6 kV, while the sample thickness is  $145 \pm 10 \mu\text{m}$ . Thus, the applied electric field is maintained at  $40 \text{ kV}\cdot\text{mm}^{-1}$ . The readings are taken using a software package called “Easy Data” at 0 seconds, 120 seconds, 300 seconds, 600 seconds, 1200 seconds, 1800 seconds, 2400 seconds, 3000 seconds and 3600 seconds. After this measurement is complete, a test of

space charge decay is also processed: data is collected at 0 seconds, 30 seconds, 60 seconds, 90 seconds, 120 seconds, 150 seconds, and 180 seconds. In the interests of clarity, only selected data are presented in the results. Space charge formation in the dielectric material is closely related to the applied electric stress. A typical distribution of space charge measurement when there is no bulk charge in the sample is presented in Figure 8-6. The space charge will begin to occur if the applied voltage is high enough.

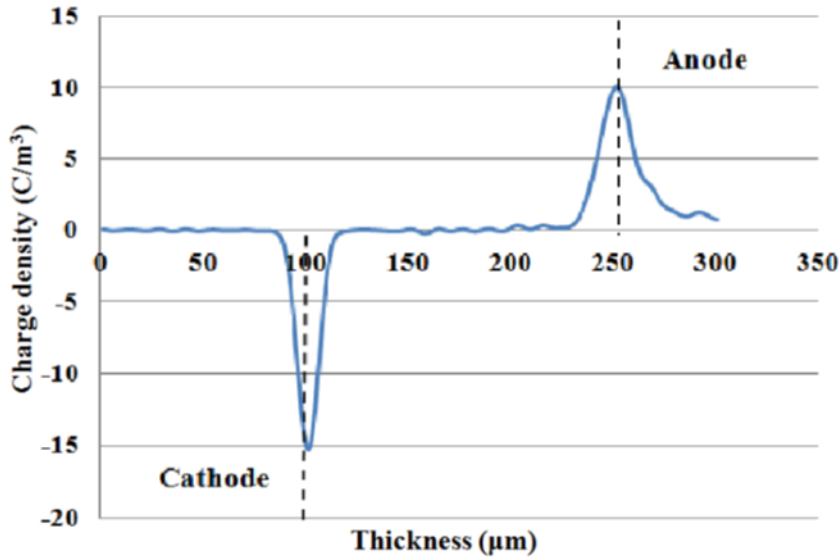


Figure 8-14 A typical waveform of space charge measurement [4].

Moreover, the results of volts-on measurement cannot be used directly. Thus, a subtraction method can be employed to remove the capacitive charges from the electrodes. In this method, the reference data is multiplied by the ratio between the applied voltage and a reference voltage; this can be considered as the charge density data at the applied voltage without the effect of space charges in bulk. The actual measured charge density data obtained from the volts-on measurement minus the multiplied, will reveal the injected charges in the sample and its induced charge at the electrodes. This can be expressed as [196]:

$$\rho_{acc}(x) = \rho_{app}(x) - \frac{V_{app}}{V_{ref}} \cdot \rho_{ref}(x) \quad (8.7)$$

where  $V_{ref}$  and  $V_{app}$  are the reference and applied voltages,  $\rho_{acc}(x)$  is the space charge density after subtraction, and  $\rho_{app}(x)$  and  $\rho_{ref}(x)$  represent the charge density at the applied voltage and reference voltage respectively. Moreover, the total charge amount and charge density within the bulk of the sample can be calculated using Equations 8.8 and 8.9, as follows:

$$Q = \int_0^d (|n_p(x)| + |n_n(x)|) \cdot A dx \quad (8.8)$$

$$n = Q / (A \cdot d \cdot q) \quad (8.9)$$

where  $n_p(x)$  and  $n_n(x)$  are the charge density of positive and negative charges respectively,  $A$  is the electrode area equal to 50.265 mm<sup>2</sup> (with a radius of 4 mm),  $d$  is the thickness of samples ( $145 \pm 10$  μm),  $Q$  is the total charge amount,  $q = 1.602 \times 10^{-19} C$  and  $n$  is total charge density in bulk.

### 8.2.2.1 Space Charge Built-up—Volts-on”

#### A. Effects of Filler Loading Concentration

Results of the “volts-on” space charge measurement on pure specimens are shown in Figures 8-15 and 8-16, which are the original and subtracted data respectively.

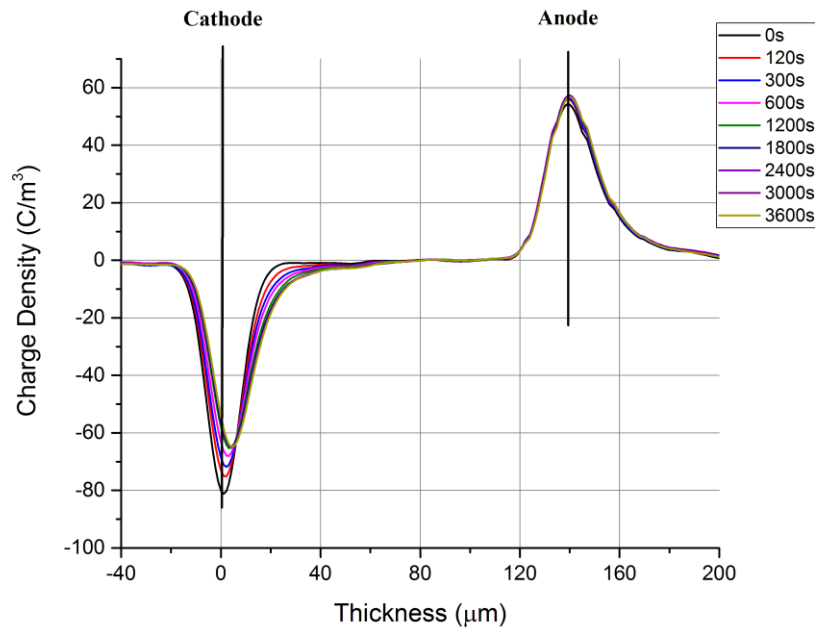


Figure 8-15 Original space charge profile of EP0 at 40 kV·mm<sup>-1</sup>, dry.

In Figure 8-15, it is obvious that some homocharges present adjacent to the cathode in pure epoxy and that the amount of homocharges increases with time. Charges are dictated by homocharges, and the presence can be attributed to charge injection from both electrodes in the form of electrons and holes [197]. Heterocharges may occur due to the charge separation process in the specimen but play only a minimal role. However, as the PEA system only measures the net

charges, this might be covered by the charge injection. Thus, the subtraction method was applied in an attempt to reflect more details of the charge distribution in bulk, as shown in Figure 8-16.

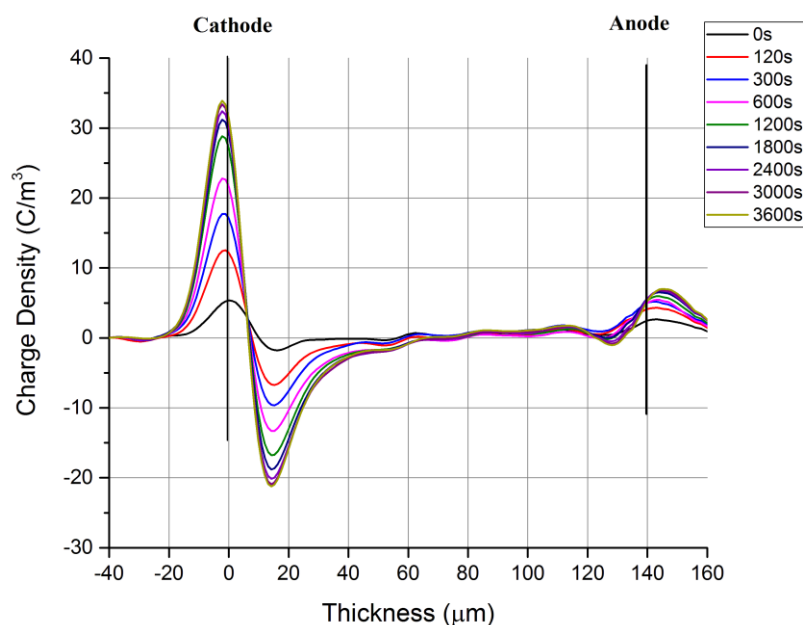


Figure 8-16 Subtracted space charge profile of EP0 at  $40 \text{ kV} \cdot \text{mm}^{-1}$ , dry.

When compared to EP0, the original and subtracted space charge distribution in the EPS samples are shown in Figures 8-17 and 8-18, while the total charge amount for each filler loading is plotted in Figure 8-19. The magnitude of homocharges in EPS05 near the cathode increases gradually and can be seen to be higher than EP0. According to the lower total charge amount of EPS05 in Figure 8-19, fillers in EPS05 samples appear to suppress charge injection which could also prove that the conductivity of EPS05 is lower than that of EP0 measured in section 8.1.2. As filler loadings increase, there is an obvious negative charge injection in the EPS1 samples; moreover, EPS3 and EPS5 samples exhibit anomalous charge distribution behaviour, as there are a large number of heterocharges distributed near both electrodes.

In the EPS5 sample, as shown in Figure 8-18, a large amount of charge injection can be observed. First, near the anode, the homocharges moving towards the cathode indicate the injection of positive charges, although the magnitude first increases and then decreases (this may be caused by the neutralisation with negative charges); second, adjacent to the cathode, the magnitude of heterocharges increases with time, and the peaks move towards the anode, which may be the result of the continuous injection of negative charges; third, in

*Rectangle A*, the peaks decrease as they move towards the cathode and then increase as they move towards the anode, which may indicate that the charge built up in this region is first dominated by positive charges and then by negative charges. Based on this analysis, the heterocharges appearing adjacent to both electrodes should be the injected charges from the opposite side of the samples and neutralise the homocharges located at the space they occupied, which does not happen in EPS05 or EPS1. A similar observation was made in [20]. According to Tables 4-1 and 4-2, the inter-particle distances of EPS5 are lower than those of EPS1; this could make the percolation of charge carriers easier, and they may even reach the other side of the sample. The same phenomena shown in EPS3 should share the same mechanism due to their very similar behaviour, although the injection and neutralisation are lesser in the bulk of EPS3, which is qualitatively consistent with the inter-particle distances of both EPS3 and EPS5.

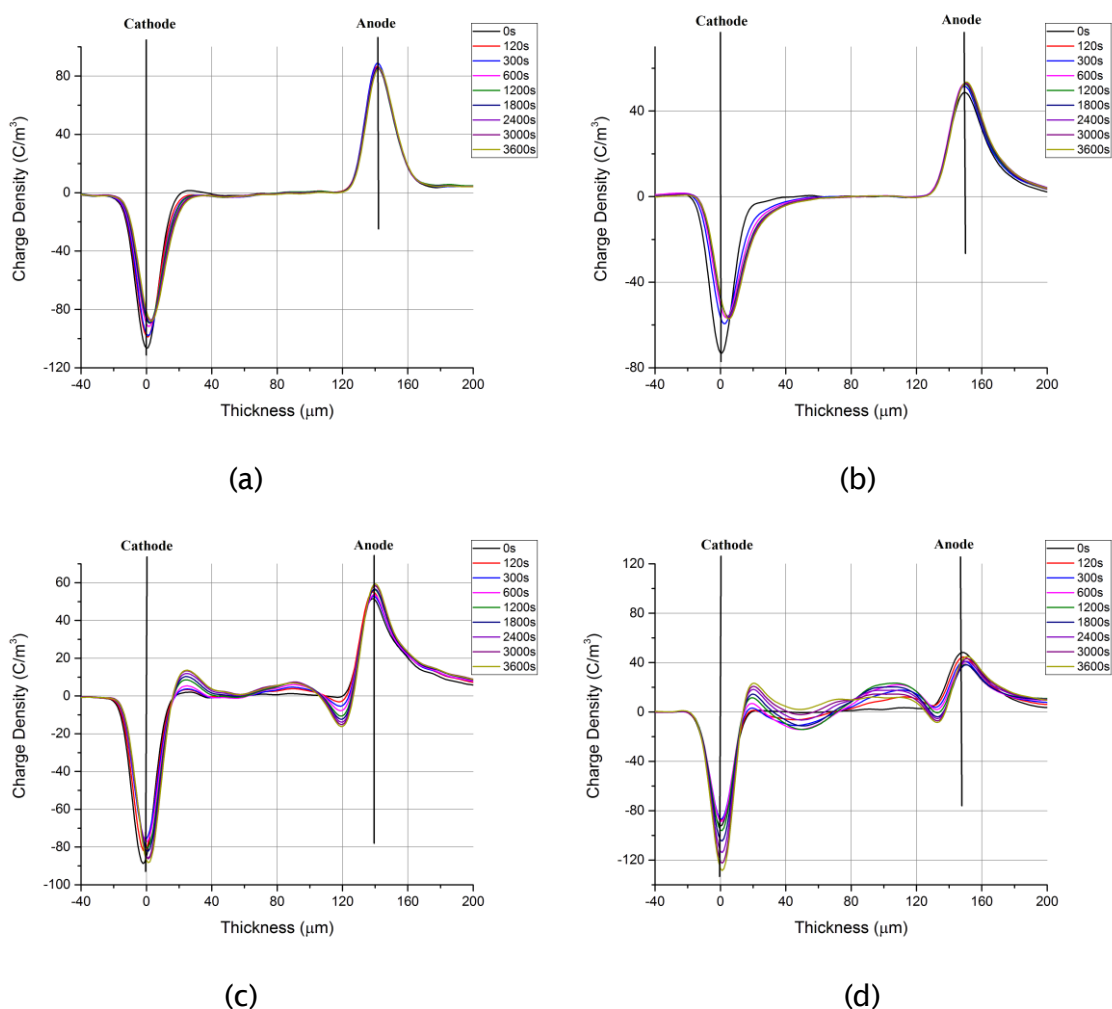


Figure 8-17 Original space charge profile of EPS at 40 kV·mm<sup>-1</sup>: (a) 0.5 wt%; (b) 1 wt%; (c) 3 wt%; (d) 5 wt%, dry.

## Chapter 8 DC Conductivity and Space Charge Behaviour

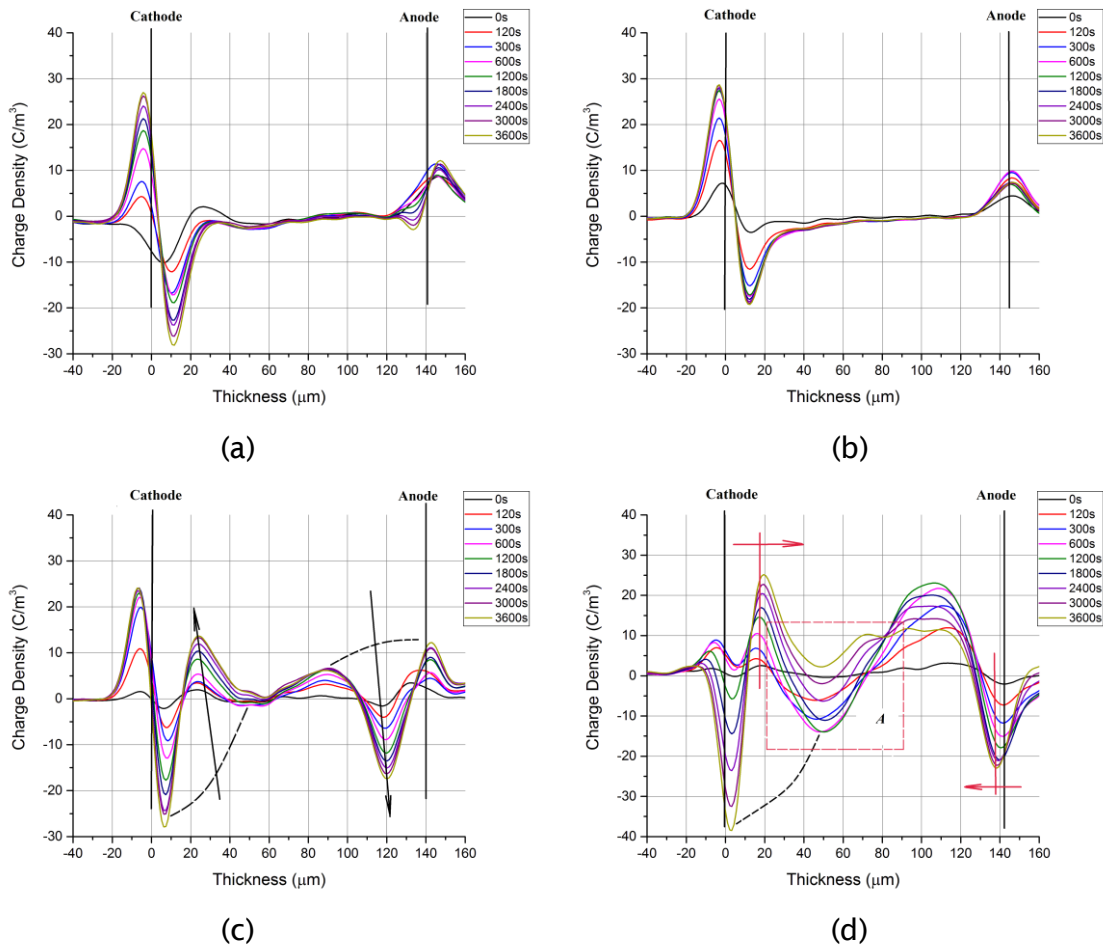


Figure 8-18 Subtracted space charge profile of EPS at 40 kV·mm<sup>-1</sup>: (a) 0.5 wt%; (b) 1 wt%; (c) 3 wt%; (d) 5 wt%, dry (dash curves indicate the ideal charge distributions without neutralization).

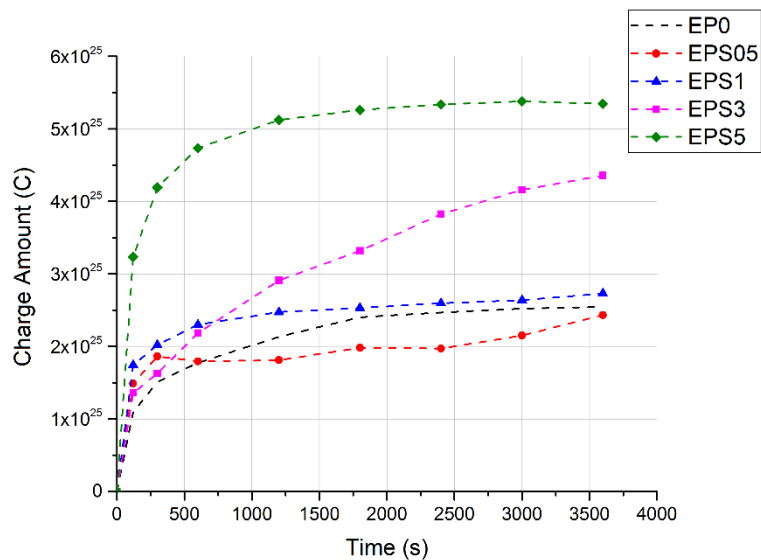


Figure 8-19 Total charge amount in bulk of EP0 and EPS in each filler loading concentration, dry.



Moreover, since the PEA technique can only show the net charge distribution in bulk, the total charge amount of EPS3 before 750s is lower than that of EPS05 and EPS1 (as shown in Figure 8-19), which is due to the neutralisation at both electrodes. The analysis above suggests that samples filled with more untreated  $\text{SiO}_2$  particles will have a larger charge injection and higher charge mobility in bulk. In other words, as conductivity is the product of charge carrier concentration  $n$  and mobility  $\mu$ , they will have higher conductivity. This is consistent with the results observed in section 8.1.2.

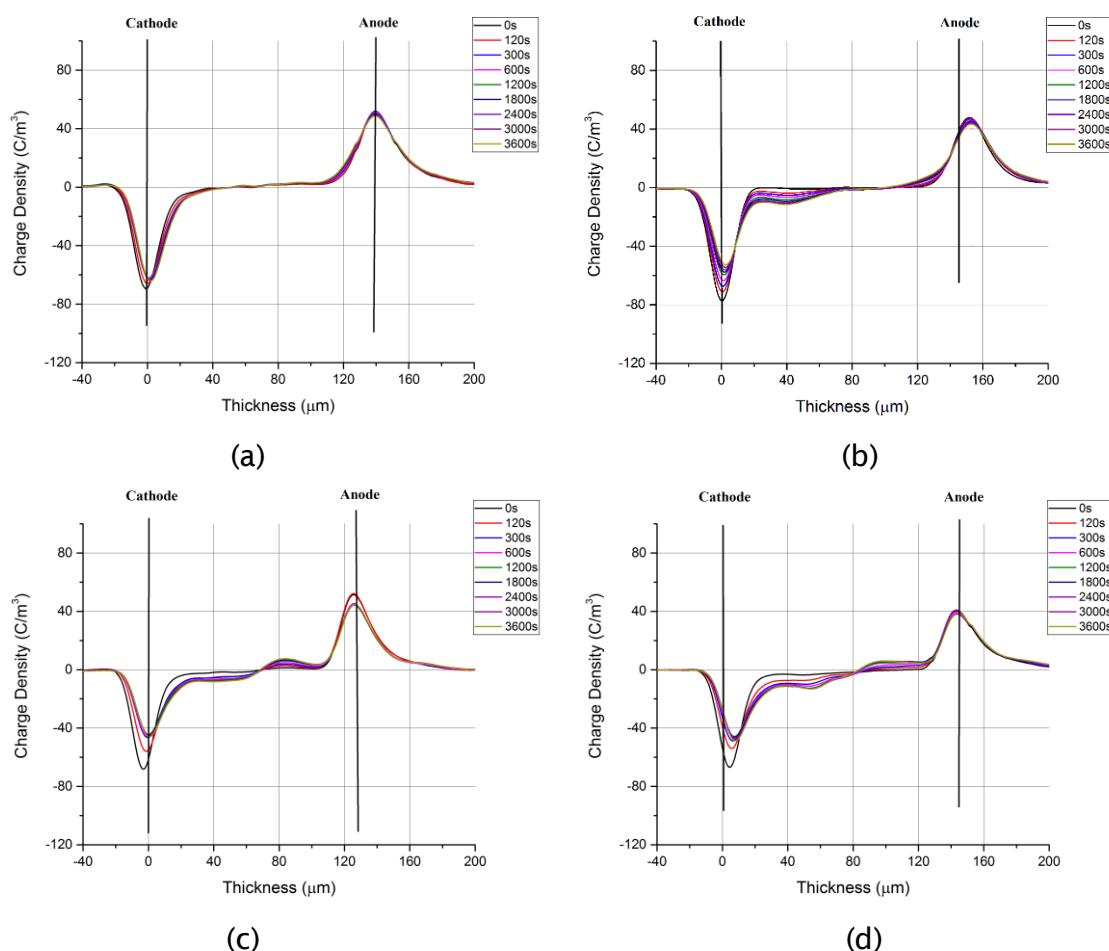


Figure 8-20 Original space charge profile of EPST at  $40 \text{ kV} \cdot \text{mm}^{-1}$ : (a) 0.5 wt%; (b) 1 wt%; (c) 3 wt%; (d) 5 wt%, dry.

The original and subtracted space charge distribution in the EPST samples are shown in Figures 8-20 and 8-21, while the total charge amount for each filler loading is plotted in Figure 8-22. When compared to the pure sample, the space charge distribution in the EPST05 samples exhibits similar behaviour to that of the magnitude and charge injection. This is not the same as the behaviour in EPS05, which demonstrates the fillers' effect of suppressing charge injection. In EPST1, homocharges are present at both electrodes and move towards the middle of the

sample. Moreover, as shown in Figure 8-22, the lower charge injection rate of EPST1 at the beginning when compared to EPST05 may be evidence for deep traps introduced by the surface treatment, which would restrict the charge mobility in bulk.

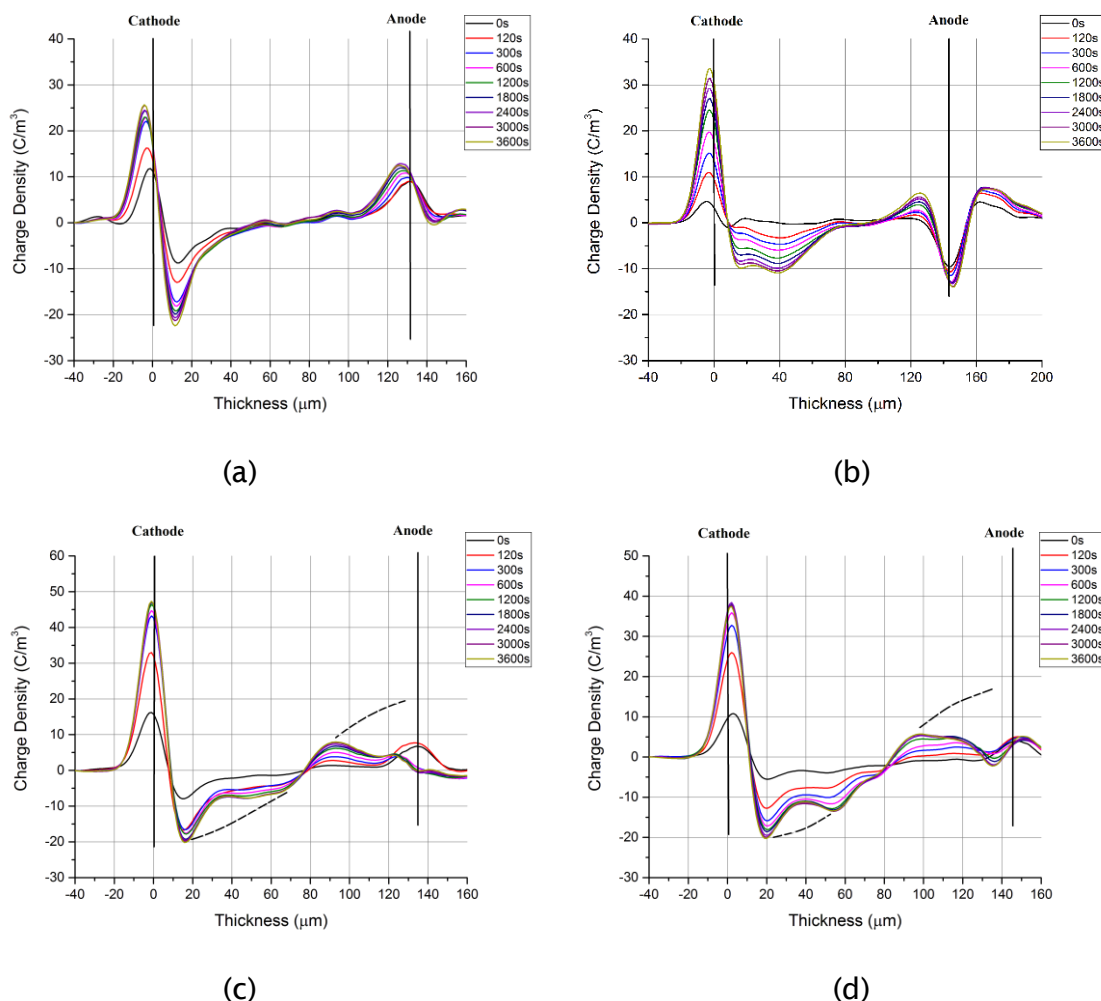


Figure 8-21 Subtracted space charge profile of EPST at  $40 \text{ kV} \cdot \text{mm}^{-1}$ : (a) 0.5 wt%; (b) 1 wt%; (c) 3 wt%; (d) 5 wt%, dry.

However, reduction in the distance of arbitrary deep traps related to the inter-particle distance may result in trapped charges passing through the potential well via the quantum tunnelling mechanism [198], which contributes to the obvious increase in the initial built-up charge of EPST3. The higher probability of EPST3 relative to EPST1 in Table 8-2 also supports this analysis. Moreover, with the increase of filler loadings, fast initial charge built-up and similar charge neutralisation phenomena as in EPS3 and EPS5 are observed in EPST5. However, the injected charges traveling through the whole bulk are not as numerous as those in the EPS3 and EPS5 samples, which consequently show heterocharges at both electrodes.

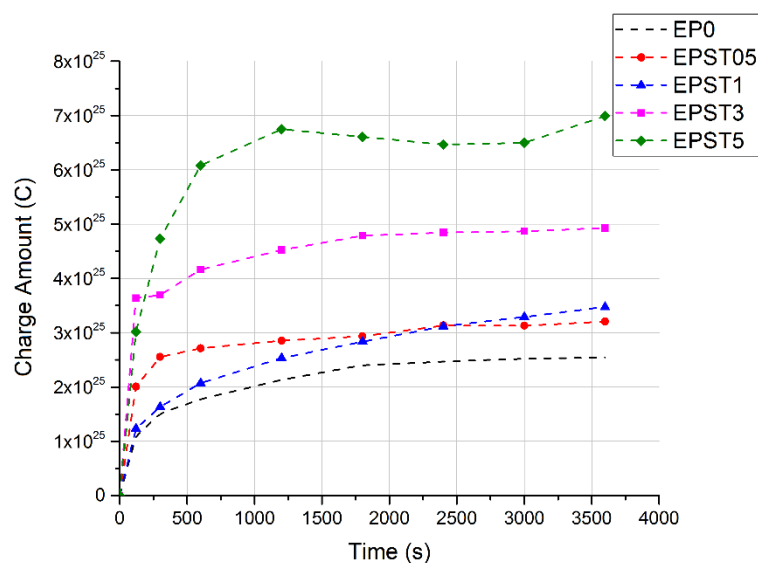


Figure 8-22 Total charge amount in bulk of EP0 and EPST in each filler loading concentration, dry.

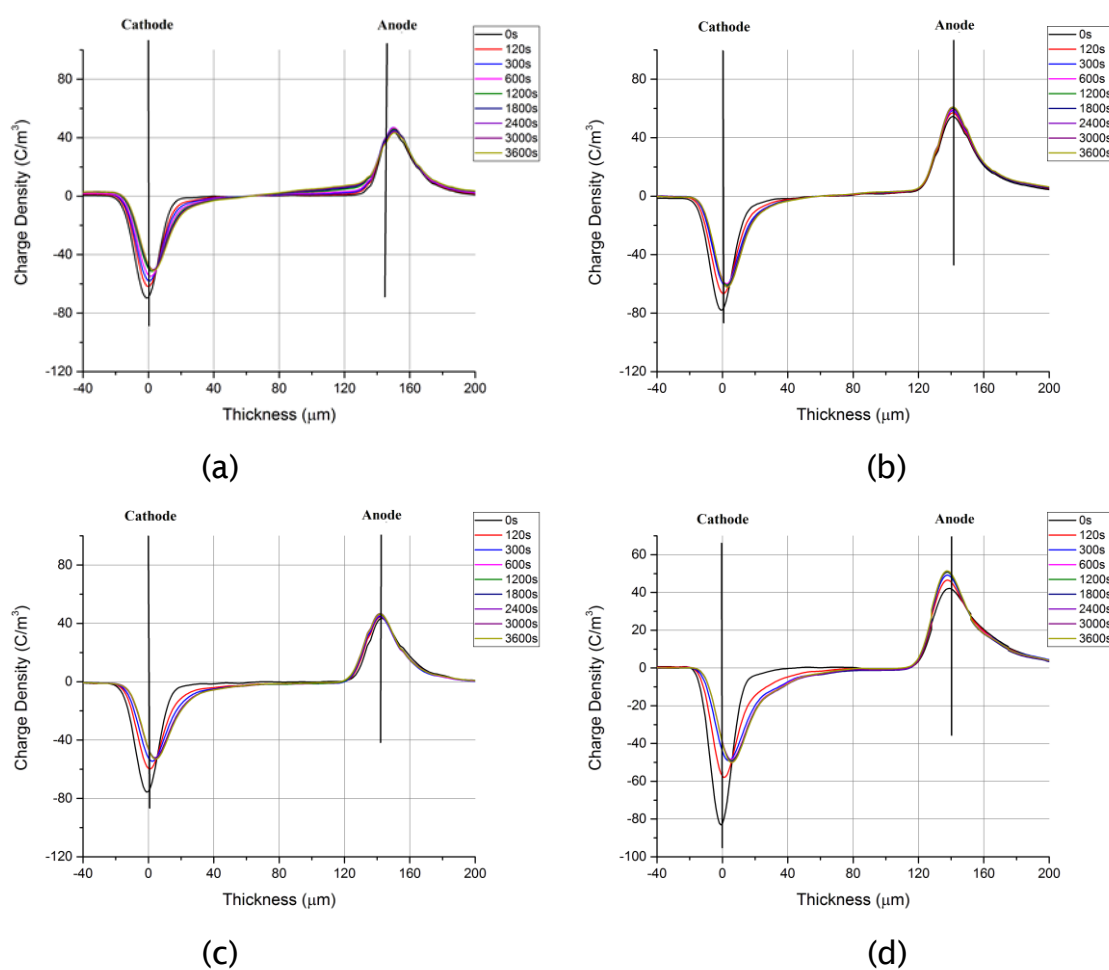


Figure 8-23 Original space charge profile of EPB at  $40 \text{ kV}\cdot\text{mm}^{-1}$ : (a) 0.5 wt%; (b) 1 wt%; (c) 3 wt%; (d) 5 wt%, dry.

## Chapter 8 DC Conductivity and Space Charge Behaviour

Figures 8-23 and 8-24 show the original and subtracted space charge accumulation in nano-hBN samples for each loading concentration. Obviously, in EPB samples, charges are dominated by homocharges. It can be seen that the injected negative charges gradually increase and move towards the middle of the bulk with the growth of loading concentrations. Figure 8-25 clearly shows suppressed injection in EPB05 samples and an obvious increase in initial built-up charge with the growth of filler loadings, which may refer to the presence of shallow traps in bulk [198].

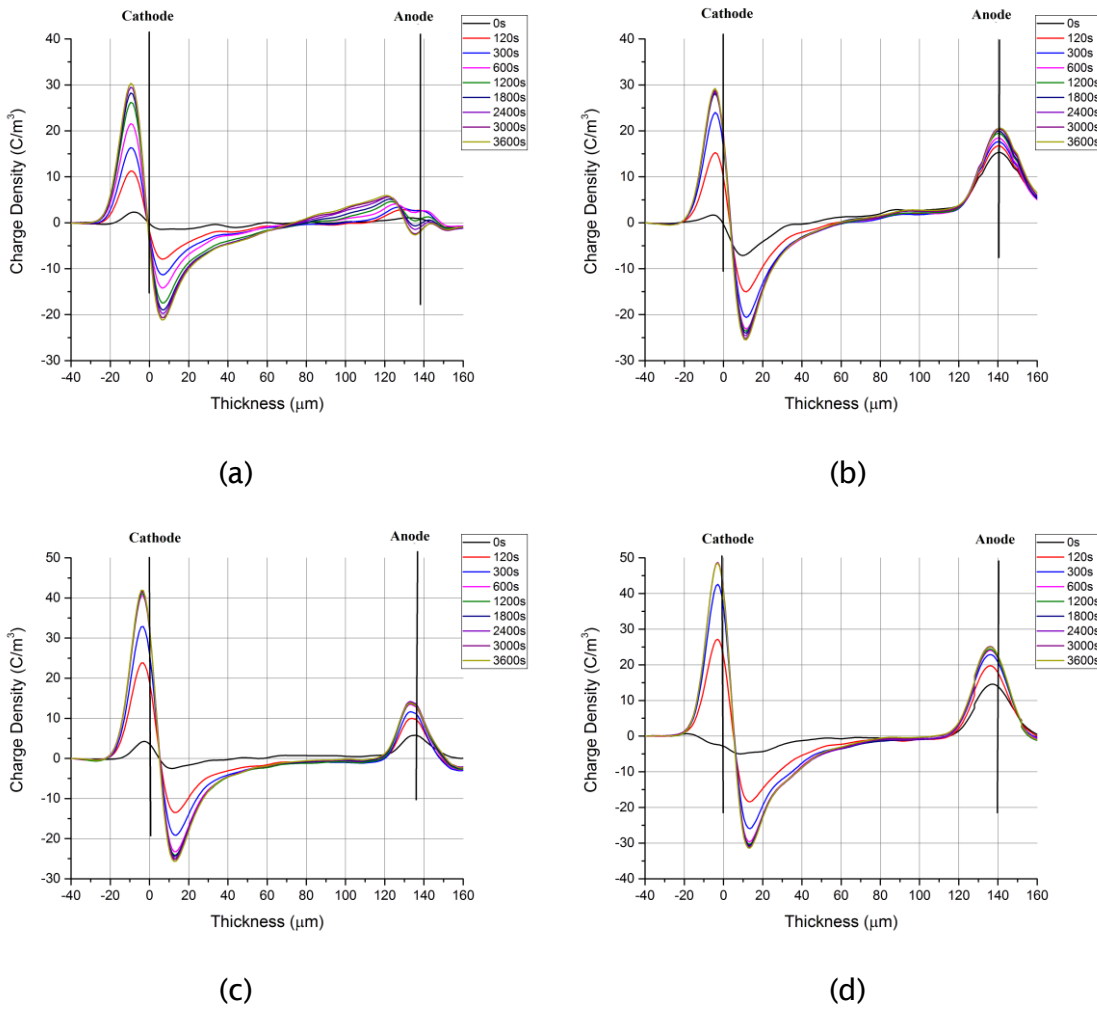


Figure 8-24 Subtracted space charge profile of EPB at 40 kV·mm<sup>-1</sup>: (a) 0.5 wt%; (b) 1 wt%; (c) 3 wt%; (d) 5 wt%, dry.

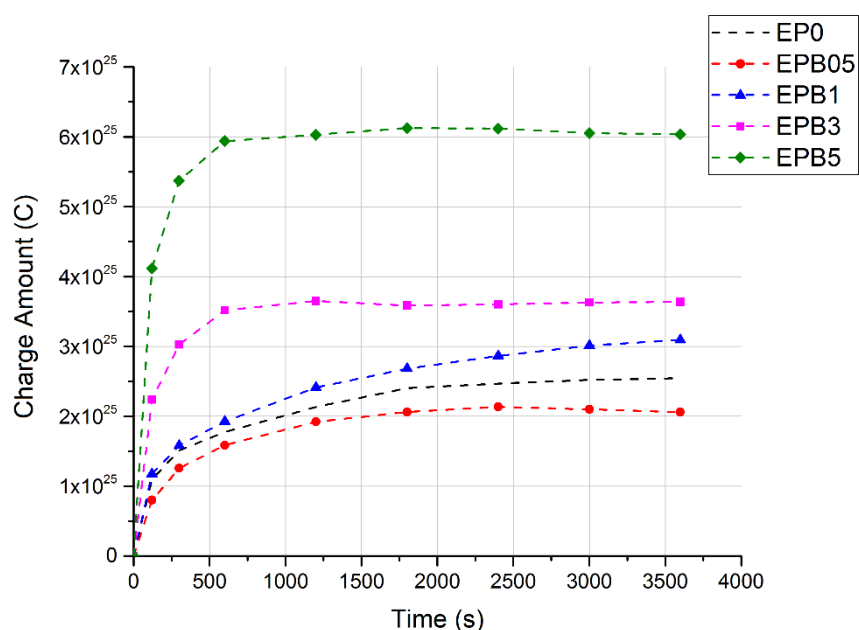


Figure 8-25 Total charge amount in bulk of EP0 and EPB in each filler loading concentration, dry.

### ***B. Effects of Filler Type and Surface Treatment***

Figure 8-26 presents comparisons between all kinds of samples at each filler concentration. In EPS samples, the low total charge amount in EPS05 and EPS1 indicates that the presence of nanoparticles could hinder the charge injection to some extent, although the initial injection rate becomes more rapid than other kinds of samples from 1 wt%. However, the rate and the total charge amount are lower at 3 wt% and 5 wt% respectively. This is believed to be caused by large numbers of heterocharges traveling from the opposite electrode across the bulk. As a result, the amount of net charges becomes smaller, and most are neutralised.

Compared to EPS samples, EPST samples show an overall higher total charge amount at each filler loading and an injection rate increase along with the filler loading increase. First, this is consistent with the conductivity being higher than EPS, as measured in section 8.1.2, due to the solvent residues. Second, more charges in bulk may imply that there are more traps in the bulk of EPST samples. As mentioned in section 7.2.2, the surface treatment should lead to additional deep traps at interphase and thus result in a higher total charge amount in EPST samples. Third, these additional deep traps could make it difficult for the trapped charges to overcome the potential barrier, thus influencing their mobility and leading to a lower rate of initial charge injection compared to EPS samples (see Figure 8-26 (b)).

In EPB samples, charge injection and distribution behaviour are very similar to that of EPST, though their amounts are smaller in each filler loadings. This may indicate that there are a large number of traps in bulk of EPB samples; however, it is hard to determine whether they are shallow or deep ones at this point.

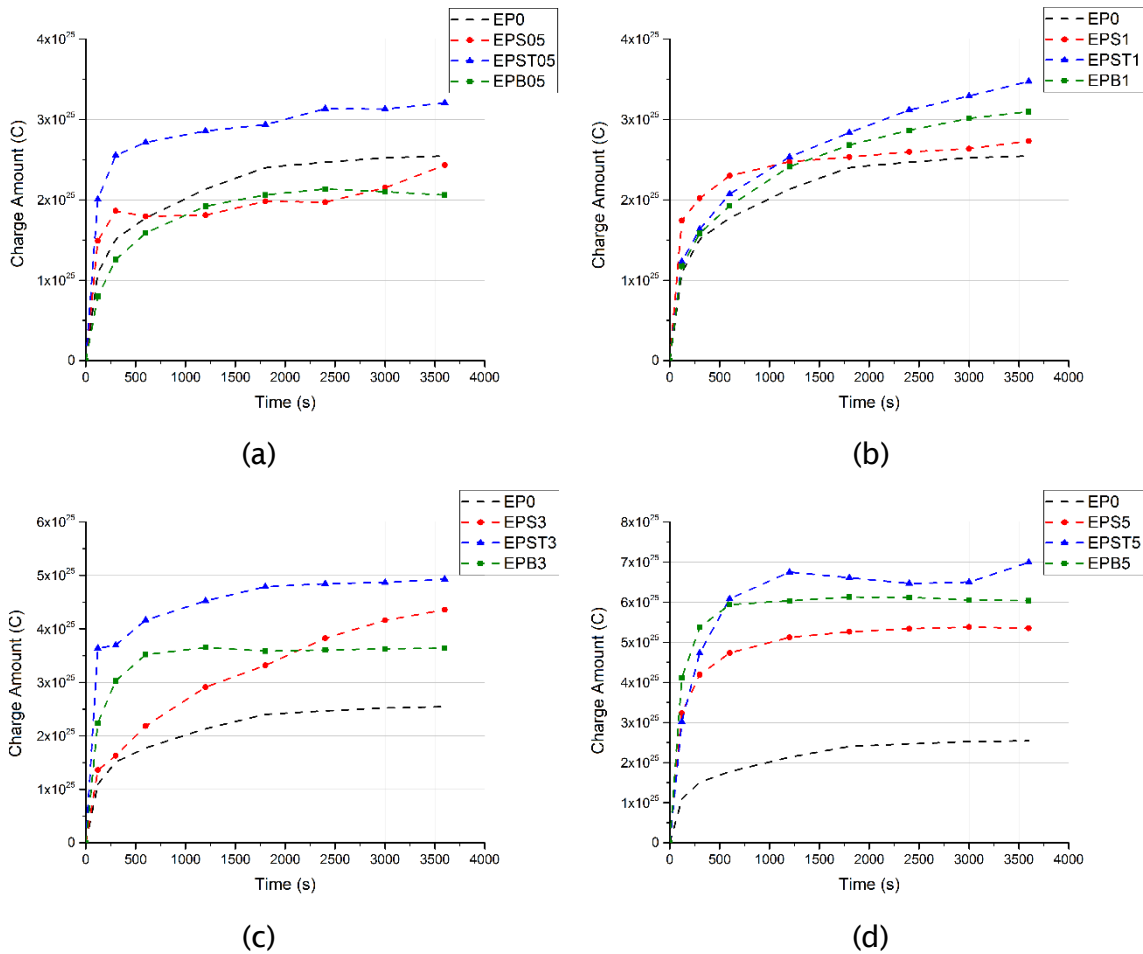


Figure 8-26 Comparison of total charge amount in epoxy and its nanocomposites samples at 40 kV·mm<sup>-1</sup>: (a) 0.5 wt%; (b) 1 wt%; (c) 3 wt%; (d) 5 wt%, dry.

### 8.2.2.2 Space Charge Decay

The space decay of pure, EPS, EPST and EPB samples is presented in Appendix D. The total charge amounts are then summarised in Figures 8-27~8-30, while space charge decay rates are calculated and shown in Table 8-3. Among all types of samples, the residual charges increase as filler loading concentration increases and could indicate more traps in samples due to the addition of more fillers. EPS samples show a gradually rising decay rate as loadings increase, which provides evidence for the existence of traps due to the presence of nanofillers. However, EPST samples show a contrary trend: the decay rate decreases, while the residual charge amount in bulk is the highest among all samples types for each filler loading. This is caused by the additional deep traps in the EPST samples, since charges

decay slower from deep traps, which are usually related to chemical changes in bulk, than from shallow traps, which are caused by the physical defects [199], Thus, it can be concluded that the presence of nano-SiO<sub>2</sub> fillers could lead to physical changes and resultant shallow traps in bulk, while surface treatments act as chemical changes that will introduce deep traps.

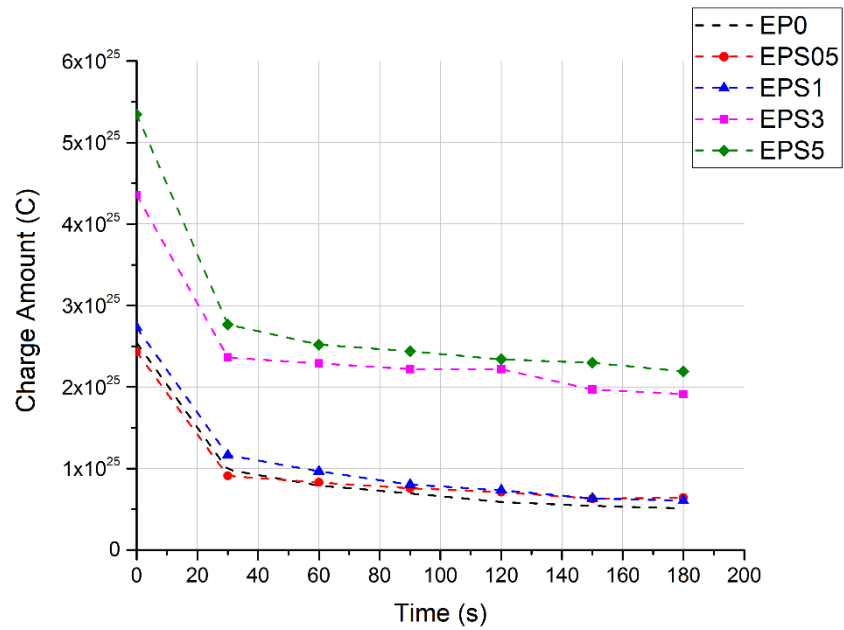


Figure 8-27 Decay of total charge amount in bulk of EP0 and EPS in each filler loading concentration, dry.

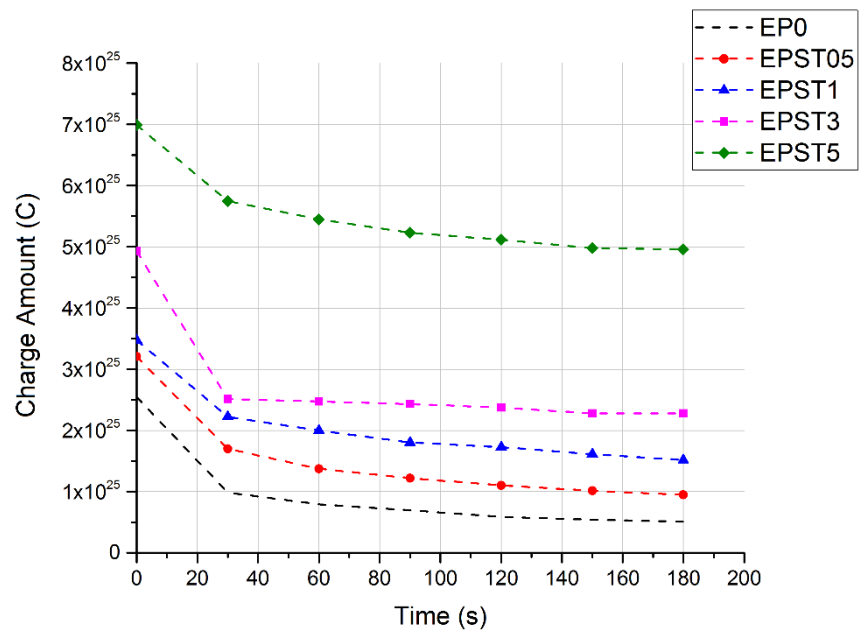


Figure 8-28 Decay of total charge amount in bulk of EP0 and EPST in each filler loading concentration, dry.

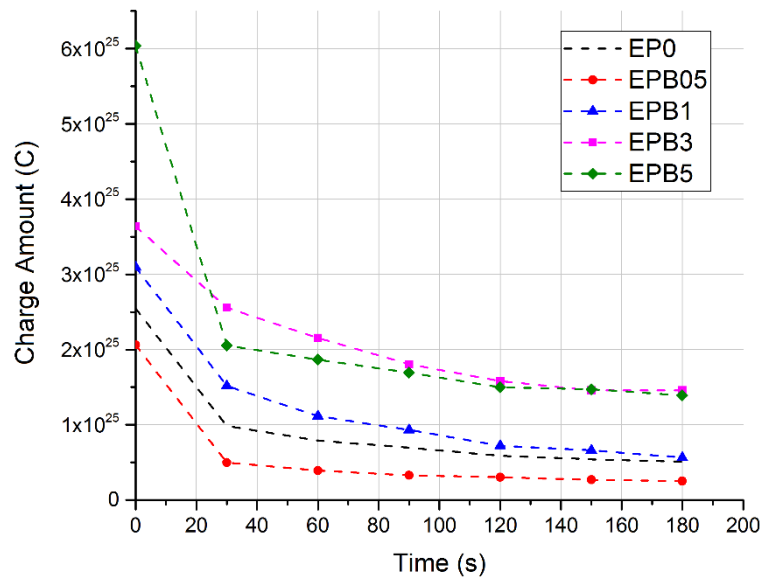
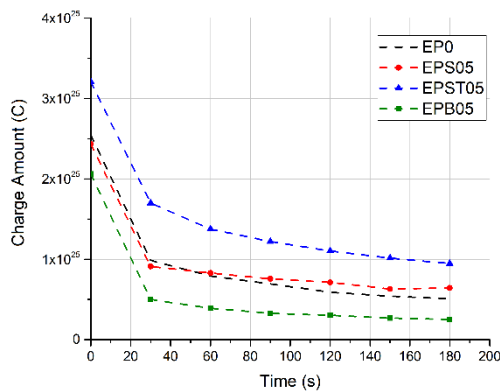
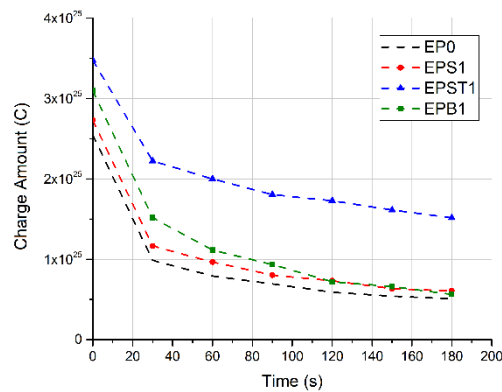


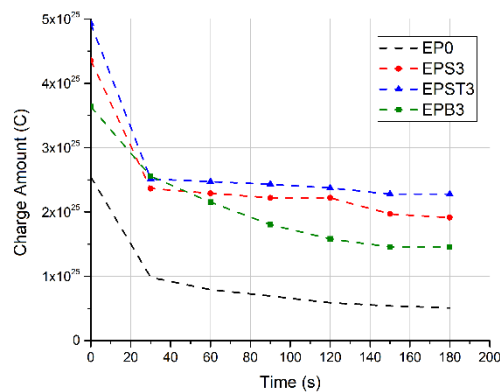
Figure 8-29 Decay of total charge amount in bulk of EP0 and EPB in each filler loading concentration, dry.



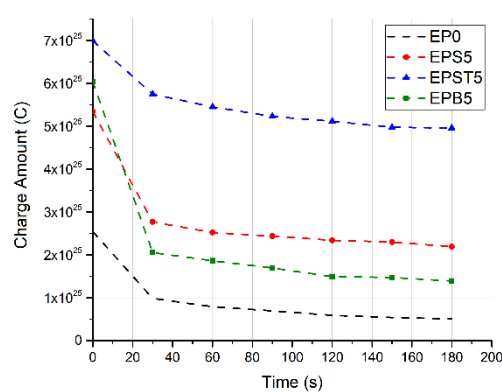
(a)



(b)



(c)



(d)

Figure 8-30 Comparison of decay of total charge amount in bulk of epoxy and its nanocomposites in each filler loading concentration, dry.



Regarding the EPB sample, residual charge amounts in bulk are the lowest compared to EPS and EPST (shown in Figure 8-30), and the space charge decay rates increase with the growth of filler loadings, especially in EPB5 (shown in Table 8-3). Thus, according to the previous analysis, the traps in EPB samples are likely to be shallow traps. As mentioned in the above discussion of the morphology of EPB samples (see Section 4.2), these traps are due to the presence of hBN particles, which result in physical defects [199] such as layered structures/cracks.

Table 8-3 Space charge decay rate ( $C \cdot s^{-1}$ ) of epoxy and its nanocomposites, dry.

Sample Code	Filler Loading Concentration				
	0 wt%	0.5 wt%	1 wt%	3 wt%	5 wt%
EP	1.13E+23	–	–	–	–
EPS	–	0.99E+23	1.18E+23	1.36E+23	1.75E+23
EPST	–	1.25E+23	1.13E+23	1.47E+23	1.09E+23
EPB	–	1.01E+23	1.41E+23	1.21E+23	2.58E+23

## 8.2.3 Effects of Moisture on PEA Measurement and Analysis

### 8.2.3.1 Space Charge Built-up—“Volts-on”

The “volts-on” PEA measurement results, along with the total charge amount of epoxy and its nanocomposites under ambient and 60% relative humidity conditions, are shown in Figures 8-31 to 8-39. In Figure 8-31, EP0 show that the homocharge injection and initial charge build-up rate significantly increases with moisture. However, the magnitude near the cathode decreases and shows an increase at the anode with the growth of the RH condition. In Figure 8-32, it is explicitly noted that more charges are injected into bulk, and that the presence of moisture results in the injected charge amounts and mobilities. Moreover, negative charges present in the middle of samples under both RH conditions and seem to contain more in bulk of samples under 60RH. This should first be attributed to the water molecules that produce ions ( $OH^-$ ,  $H_3O^+$ ) and holes coming from the anode [15, 200]. More water content means that more ionised charges will be present in the bulk of samples. Second, as electrons can travel through inter-chain spaces

[105, 192] where water could locate, negative charges obviously appear in the bulk of RH conditioned samples and even neutralise some positive charges at the anode from 600s onwards (see Figure 8-31 (b)), which could indicate that negative charges are more dominant in samples with water uptake. Moreover, there is also a presence of neutralisation near the cathode at later times, indicating the movement of positive charges. The neutralisation process of 60RH-conditioned samples at both electrodes can be further proven by Figure 8-32, in which the pure sample contains a lower initial injection rate before the 1500s and exhibits a decreasing trend of the charge amount.

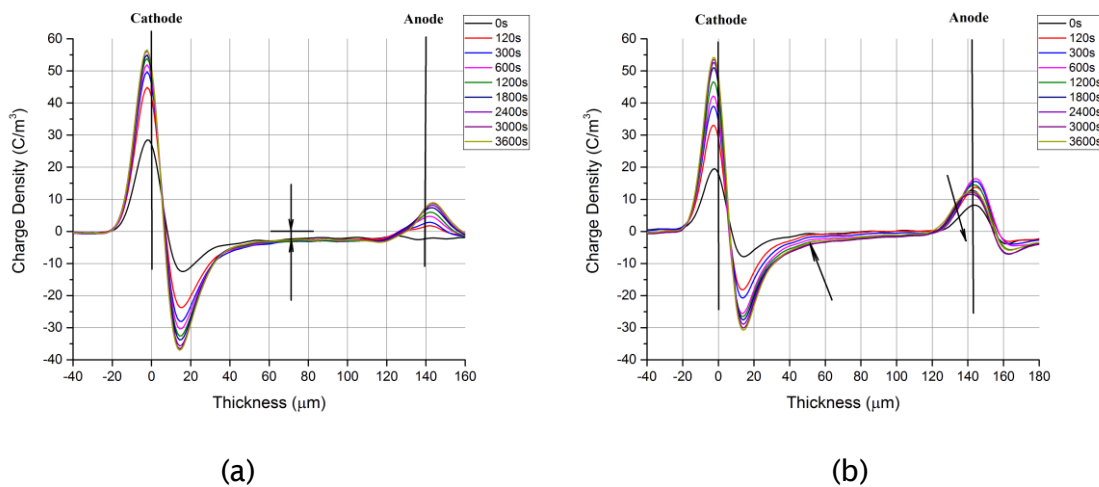


Figure 8-31 Subtracted space charge profile of EP0 at  $40 \text{ kV} \cdot \text{mm}^{-1}$ : (a) A.RH; (b) 60RH.

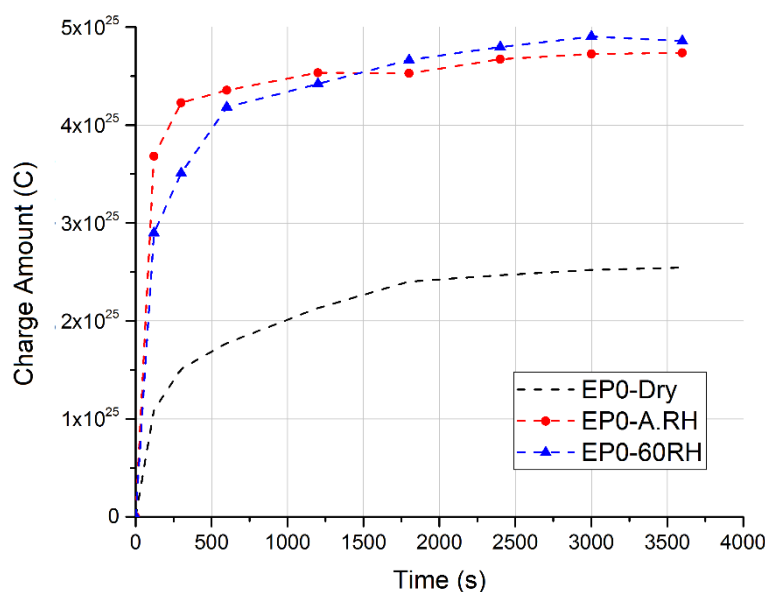


Figure 8-32 Total charge amount in bulk of pure samples in different RH conditions.

As shown in Figure 8-33, for EPS1 and EPS3, the initial injection rate and neutralisation phenomena become quicker and more obvious with the growth of RH conditions, indicating the higher mobility of both positive and negative charges. Moreover, more obvious increases in the magnitude of heterocharges near the anode than those adjacent to the cathode indicate the dominance of negative charges (mostly as injected electrons) in the 60RH condition due to the presence of water in the matrix, which is also found in pure samples and leads to higher mobility. As shown in Figure 8-34, the charge amount of EPS1 decreases with RH conditions and is higher than that of EPS3 samples under both conditions. This provides further evidence for neutralisation. Moreover, heterocharges near the cathode are more relevant to the filler loadings, while the amount increases with the growth of the RH condition. As discussed in the previous section, the presence of untreated  $\text{SiO}_2$  could introduce shallow traps in bulk. Thus, positive charges are likely to transport along these shallow traps or along conductive percolation channels due to water uptake in samples with higher filler loadings.

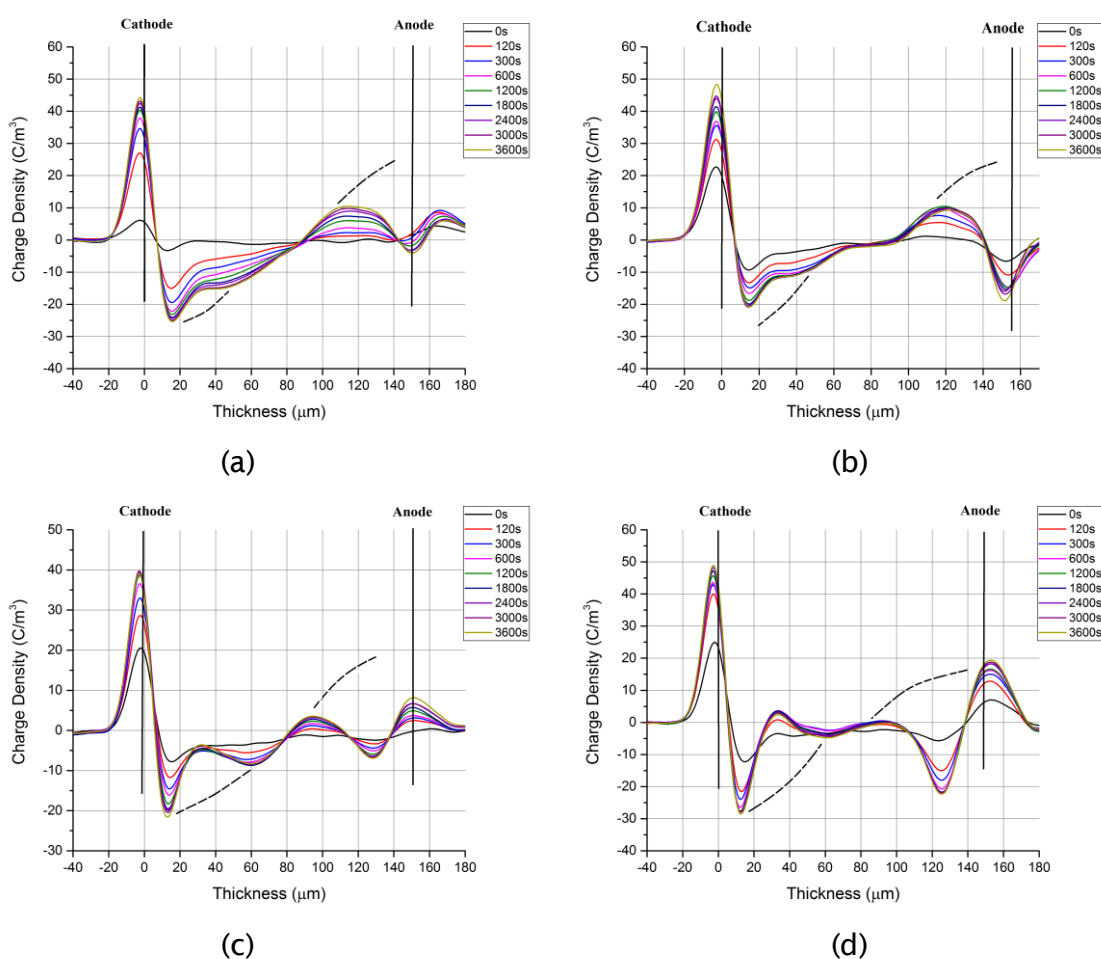
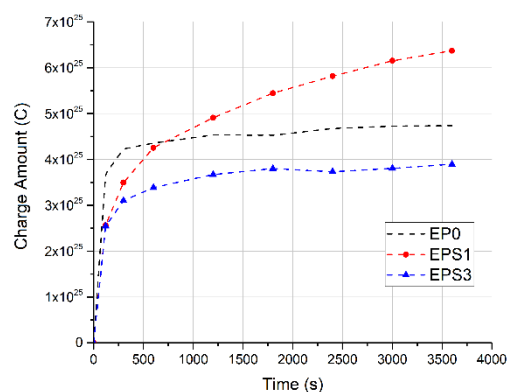
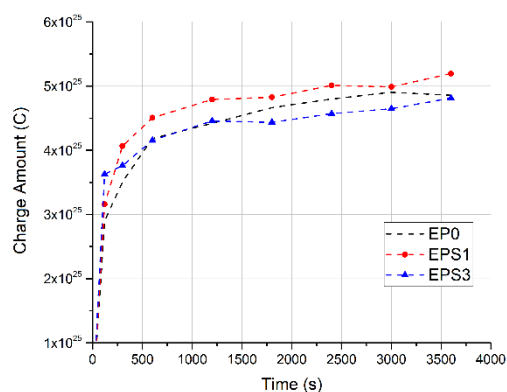


Figure 8-33 Subtracted space charge profile of EPS at 40 kV·mm<sup>-1</sup>: (a) 1 wt%, A.RH; (b) 1 wt%, 60RH; (c) 3 wt%, A.RH; (d) 3 wt%, 60RH.

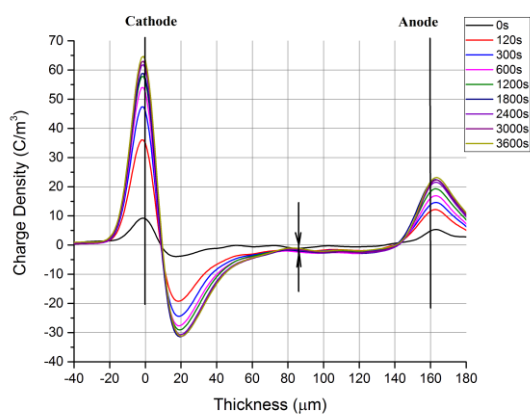


(a)

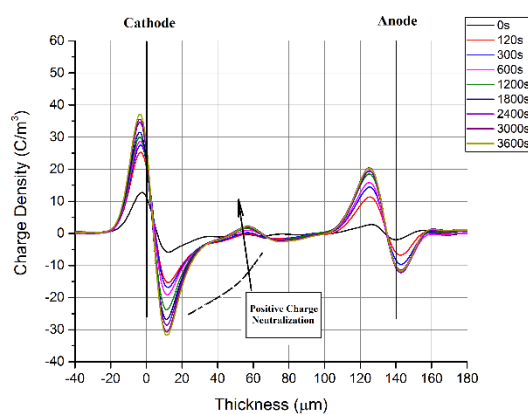


(b)

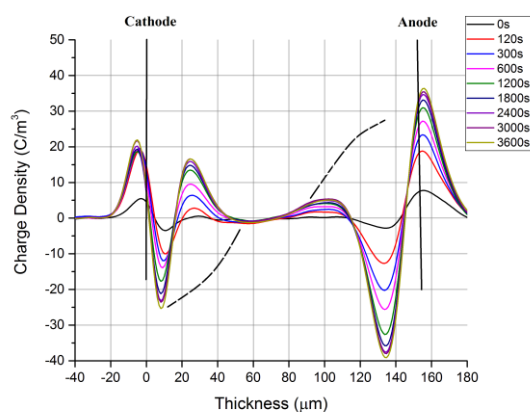
Figure 8-34 Total charge amount in bulk of EP0 and EPS in each filler loading concentration: (a) A.RH; (b) 60RH.



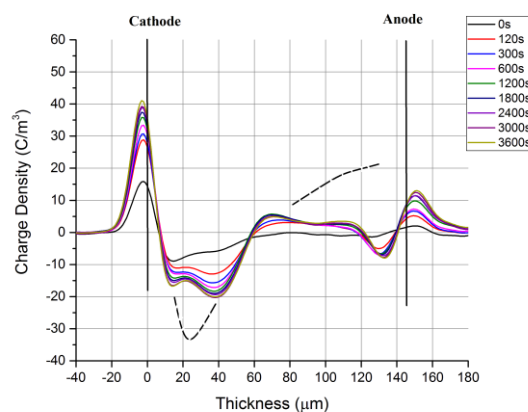
(a)



(b)



(c)



(d)

Figure 8-35 Subtracted space charge profile of EPST at  $40 \text{ kV} \cdot \text{mm}^{-1}$ : (a) 1 wt%, A.RH; (b) 1 wt%, 60RH; (c) 3 wt%, A.RH; (d) 3 wt%, 60RH.

In the case of EPST samples, as shown in Figure 8-35 (a) and (b), the charge distribution of EPST1 is dominated by negative charges, while positive charge neutralisation happens in both RH conditions. Unlike the presence of neutralisation in EPS samples, it appears in the sample with lower filler loadings. As surface treatment introduces additional deep traps, positive charges can travel along these traps while becoming more mobile as water uptake increases. To an extent, positive charges/holes should transport along shallow and deep traps in the bulk of SiO<sub>2</sub>-based nanocomposites. EPS3 samples exhibit similar behaviour, and there are obvious heterocharges near both electrodes. There is also evidence for neutralisation; see Figure 8-36.

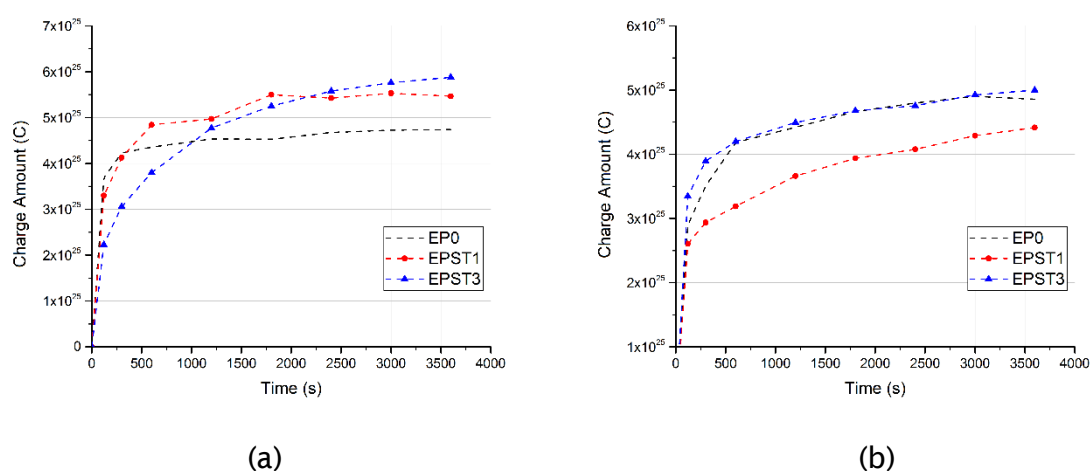


Figure 8-36 Total charge amount in bulk of EP0 and EPST in each filler loading concentration: (a) A.RH; (b) 60RH.

As can be seen in Figure 8-37 (a) and (c), EPB samples only show homocharge in bulk, and there is an increase of magnitude near the cathode as water content rises; this is also reflected in Figure 8-38. Moreover, there are negative charges in the middle of samples under the 60RH condition. One possible source could be the ions from water ( $\text{H}_3\text{O}^+$  and  $\text{OH}^-$ ), while another more important source is the increased injection in the form of negative charges. Moreover, when comparing between Figures 8-37(a) and (c) or (b) and (d), the move-in of the positive peak near the anode and the neutralisation in samples with higher filler loadings indicate the increase in mobility of positive charges, a phenomenon also found in EPS and EPST samples. This is likely to be due to the presence of water and more shallow traps in bulk, which could contribute to the movement of positive charges [105].

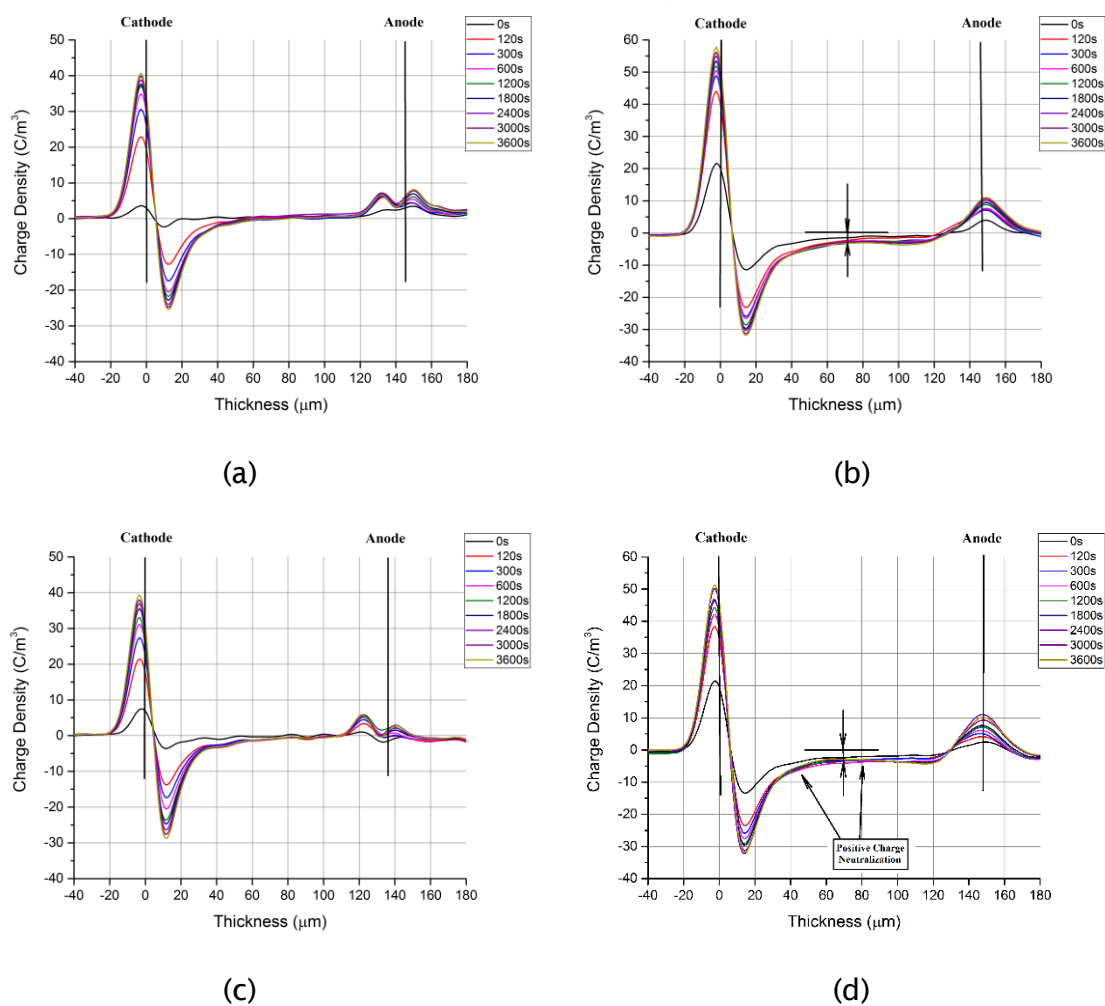


Figure 8-37 Subtracted space charge profile of EPB at 40 kV·mm<sup>-1</sup>: (a) 1 wt%, A.RH; (b) 1 wt%, 60RH; (c) 3 wt%, A.RH; (d) 3 wt%, 60RH.

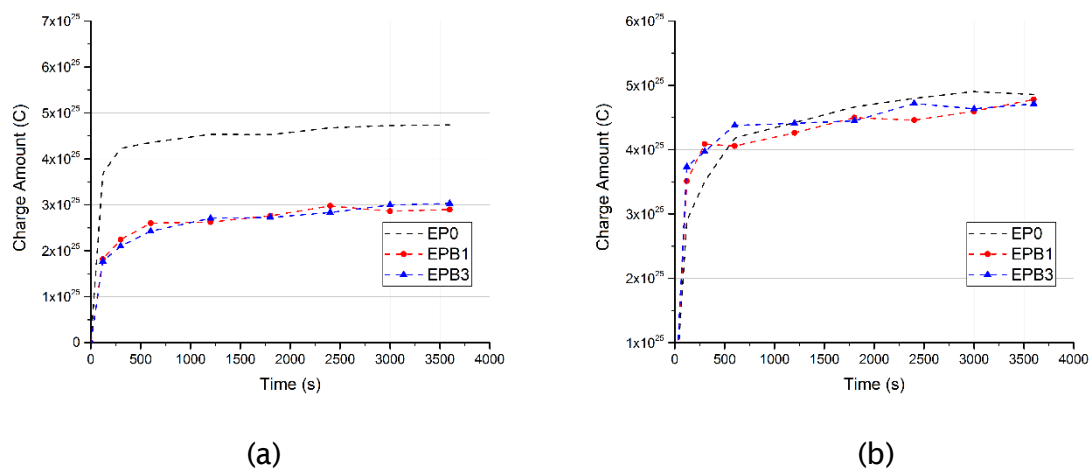


Figure 8-38 Total charge amount in bulk of EP0 and EPB in each filler loading concentration: (a) A.RH; (b) 60RH.

As shown in Figure 8-39(a), the final charge amount of EPST1 samples is smaller than that for EPS1, indicating less injection. Due to the surface treatment, there is less water absorption and more deep traps in the bulk of EPST samples, both of which will limit the transport of charges; the charges accumulated near the cathode will then hinder the charge injection and thus lead to the final amount of charges in bulk [165]. Similar results are also shown in Figure 8-39(b). However, the results in samples with higher loadings are different, a result likely to be due to the much more significant neutralisation process. Moreover, in most cases, EPB samples show the lowest charge amount value and no significant charge injection, as in SiO<sub>2</sub>-based nanocomposites under either dry or moisture conditions. This implies that BN particles could act as barriers for the charge injection. As conductivity is determined by the product of  $n \times \mu$ , at this stage, the space charge behaviour can be qualitatively consistent with the results and analysis of conductivity presented in sections 8.1.2 and 8.1.3, where EPB samples exhibit the lowest conductivity among epoxy and its nanocomposites.

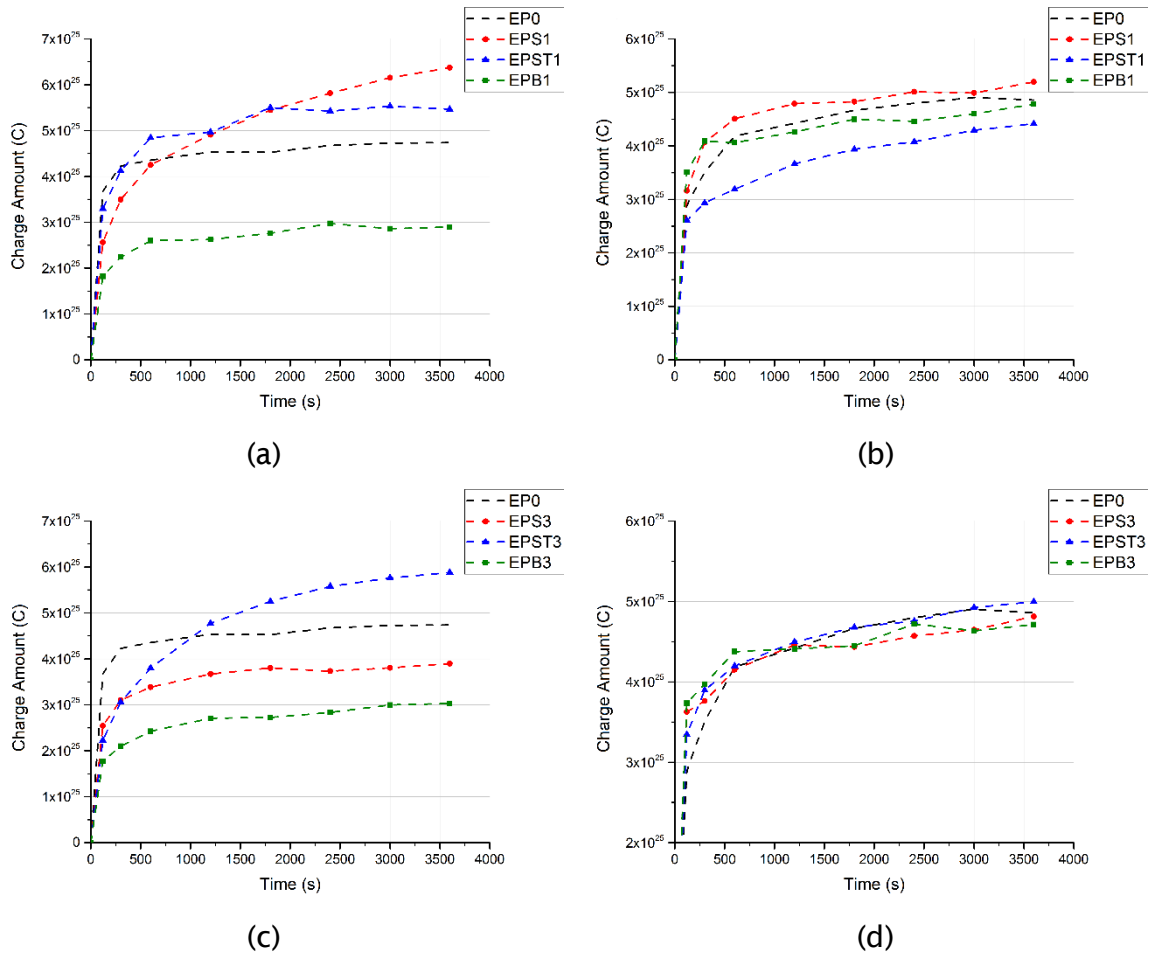


Figure 8-39 Comparison of total charge amount in epoxy and its nanocomposites samples at 40 kV·mm<sup>-1</sup>: (a) 1 wt%, A.RH; (b) 1 wt%, 60RH; (c) 3 wt%, A.RH; (d) 3 wt%, 60RH.

## 8.2.3.2 Space Charge Decay

The space charge decay of pure, EPS, EPST and EPB samples is presented in Appendix D. The total charge amount is summarised in Figures 8-40 to 8-43, while the decay rates are listed in Table 8-4. The lower decay rate of pure samples in higher RH conditions may be due to the presence of heterocharges at both electrodes, which thus form a so-called ‘barrier’ to hinder the decay of charges. Similar behaviour was also identified in [201]. Among all kinds of nanocomposites, the behaviour is similar to that in their dry conditions. However, the rate of decay is larger and increases significantly as water content rises.

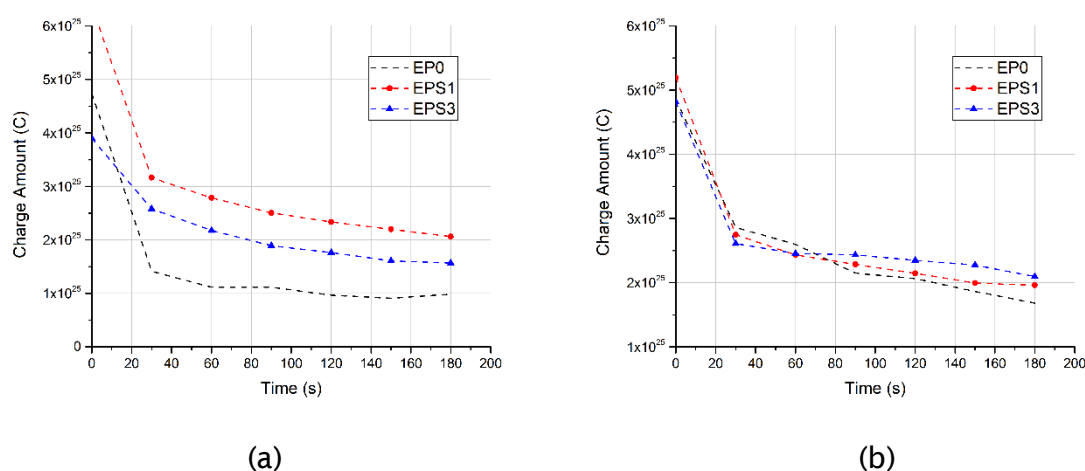


Figure 8-40 Decay of total charge amount in bulk of EP0 and EPS in each filler loading concentration: (a) A.RH; (b) 60RH.

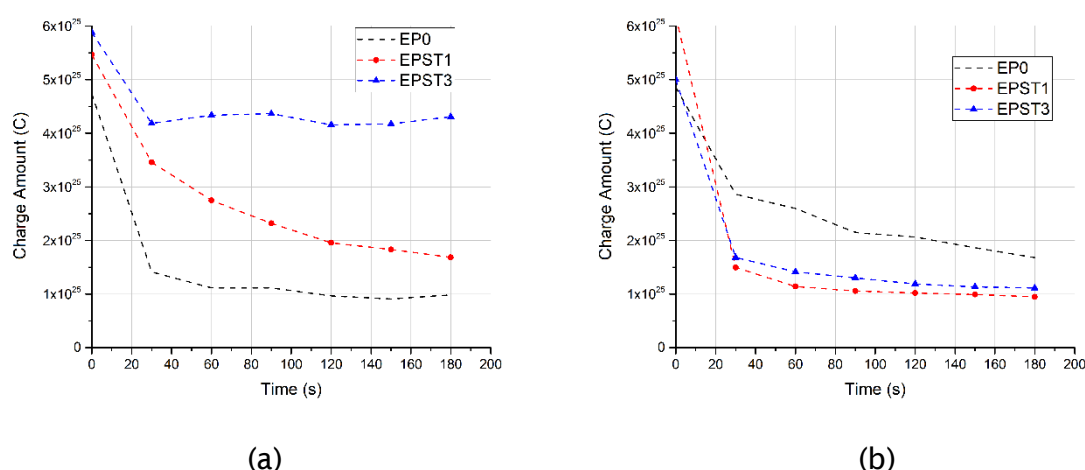


Figure 8-41 Decay of total charge amount in bulk of EP0 and EPST in each filler loading concentration: (a) A.RH; (b) 60RH.



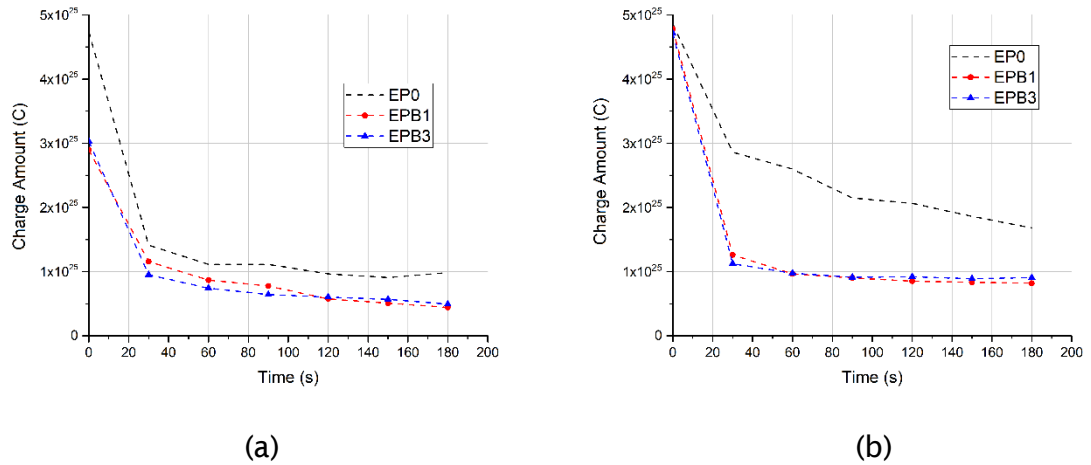


Figure 8-42 Decay of total charge amount in bulk of EP0 and EPB in each filler loading concentration: (a) A.RH; (b) 60RH.

As shown in Figure 8-43, under the A.RH condition, the deep traps due to the surface treatment of EPST samples lead to higher residual charge amounts than is the case for EPS samples. However, in Figure 8-44, 60RH conditioned samples can be seen to exhibit the opposite results; this mechanism should be the same in pure samples, in which heterocharges hinder the decay process. The fact that the overall lowest value is for EPB samples further proves that charges in bulk contain shallow traps.

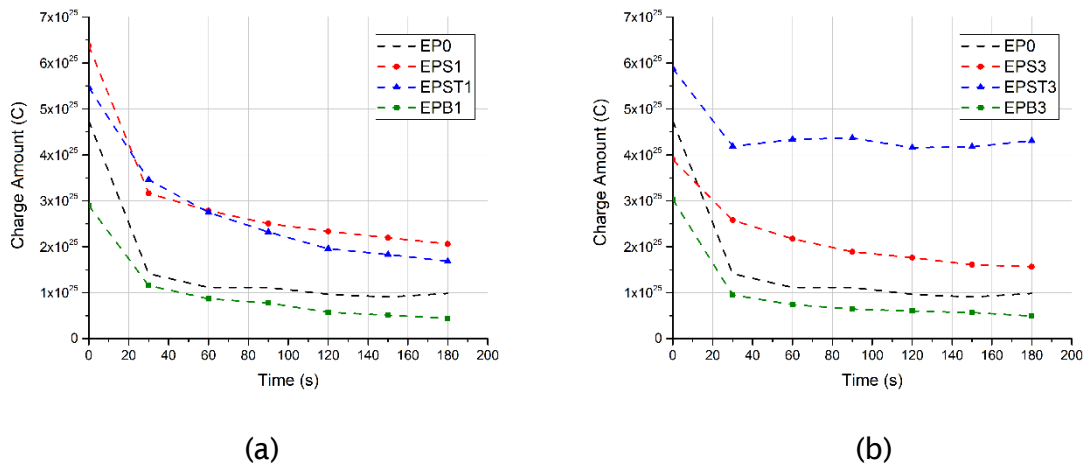


Figure 8-43 Comparison of decay of total charge amount in bulk of epoxy and its nanocomposites: (a) 1 wt%, A.RH; (b) 3 wt%, A.RH.

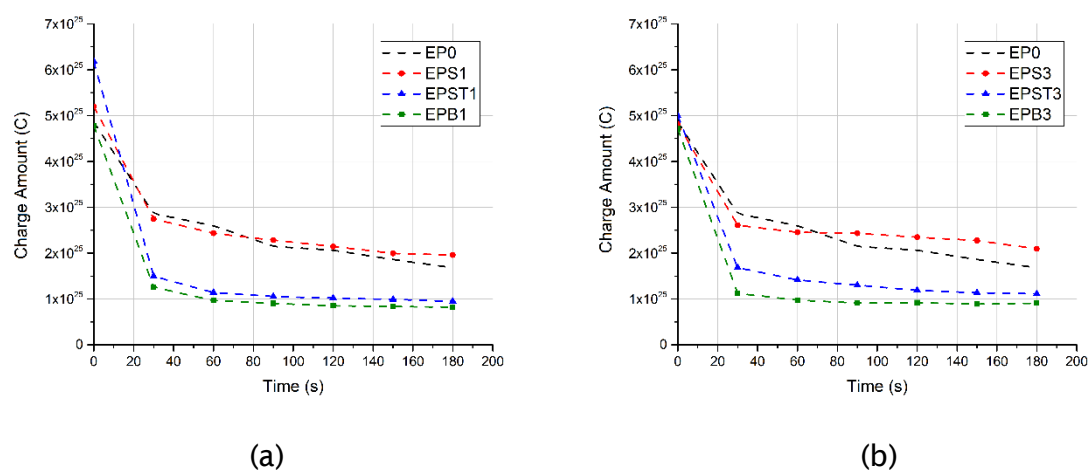


Figure 8-44 Comparison of decay of total charge amount in bulk of epoxy and its nanocomposites: (a) 1 wt%, 60RH; (b) 3 wt%, 60RH.

Table 8-4 Space charge decay rate ( $C \cdot s^{-1}$ ) of epoxy and its nanocomposites with moisture.

Sample Code	Filler Loading Concentration					
	A.RH			60RH		
	0 wt%	1 wt%	3 wt%	0 wt%	1 wt%	3 wt%
EP	2.09E+23	–	–	1.76E+23	–	–
EPS	–	2.40E+23	1.29E+23	–	1.80E+23	1.51E+23
EPST	–	2.10E+23	0.87E+23	–	2.91E+23	2.16E+23
EPB	–	1.36E+23	1.41E+23	–	2.20E+23	2.11E+23

### 8.3 Chapter Summary

The work presented in this Chapter can be summarised as follows:

1. Combining all analysis on dry samples and samples with moisture gave us a clear view on the influence of adding nanoparticles to epoxy resins and the characteristics of the movement of positive and negative charges in bulk. Based on this analysis, the DC conductivity and space charge measurement were found to be consistent with each other. The presence of nanoparticles resulted in morphology changes, mostly in the form of physical defects, as noted in Chapter 4. These changes in polymers led to an increased presence of shallow traps in bulk, which hindered the charge injection and reduced the mobility of charge carriers, and thus contributed to the reduction of DC conductivity. Moreover, the surface treatment of  $\text{SiO}_2$  particles introduced deep traps, while hBN particles resulted in shallow traps, with a significant amount due to the resultant layered structures. In addition, positive charges/holes will transport along shallow and deep traps in the bulk of  $\text{SiO}_2$ -based nanocomposites, while plate-like nano-hBN fillers seem to act as barriers to charge injection and movement.
2. However, with the increase of filler loadings, the addition of more nanofillers further affected polymer structures and thus caused a higher density of traps, meaning that the average distance between arbitrary traps (either shallow or deep ones) should be lowered and that charge carriers require less energy when moving from one to another by hopping or the quantum tunnelling mechanism. The resultant higher mobility of carriers consequently led to larger conductivities. Moreover, if particles are regarded as recombination centres, the reduction of inter-particle distances in higher filler loadings also contributed to higher conductivity in silica-based nanocomposites.
3. The presence of water firstly produced more charge carriers as ions ( $\text{OH}^-$ ,  $\text{H}_3\text{O}^+$ ) due to polarisation and led to an increase in charge injection. Secondly, the presence of water resulted in the higher mobility of charge carriers in both base materials and within traps/particles, which was based on quantitative results in Chapters 4 and 7. Moreover, water shells around spherical particles contributed to a higher probability of the quantum tunnelling process and the formation of conductive percolation channels. So far, the space charge resulting under the moisture condition is consistent with that of DC conductivity.



## Chapter 9 Conclusions and Future Work

### 9.1 Conclusions

The investigation of this thesis used a range of techniques to chemically and electrically analyse the properties of epoxy and its nanocomposites. The aim of the study is first to develop a method to describe the morphology of nanofillers in the nanocomposites more precisely and find out how presence of these fillers will influence the physical and chemical properties of epoxy resins. Second, it is to investigate the effect of presence of nanofillers and resultant interfacial regions between the matrix and nanofillers on the dielectric and electrical properties of epoxy nanocomposites. Third, influences of water absorption on the dielectric/electrical properties of epoxy and its composites are worthwhile to be thoroughly investigated.

Consequently, the thesis firstly proposed a combined method to quantitatively evaluate the dispersion and distribution of particles/aggregates in epoxy nanocomposites, which was based on the Equivalent Diameter and Monte Carlo Method, 1st Nearest Neighbour Distance Method and Quadrat-Based Method. However, due to the presence of hBN particles and resultant unclear images of morphology, it was not possible to quantify the mixing state of nano hBN-based epoxy nanocomposites; instead, this method was found to be more suitable for spherical particle-based samples. According to the proposed quantification method, epoxy nanocomposites with surface-treated particles showed overall better dispersion and distribution of particles/aggregates than those with untreated particles. Moreover, the poor mixing state resulted in an adverse impact on the morphology of the epoxy matrix with creating some physical defects (e.g., cracks and cavities). In hBN-based samples, particles were more likely to exist individually and they, therefore, have a larger effect on the matrix. All results were used to help the investigation of the structural and dielectric/electrical properties of epoxy nanocomposites. Two modelling methods using Matlab were also proposed, which aimed to simulate the real dispersion and distribution of particles/aggregates in polymer nanocomposites based on the quantification method. These methods were intended to provide a deeper understanding and a foundation of simulation research for the dielectric properties of nanocomposites informed by measured morphology.

## Chapter 9 Conclusions and Future Work

The chemical structures and thermal properties of epoxy and its nanocomposites were also investigated. The presence of nano-SiO<sub>2</sub> and hBN particles both led to a decrease in cross-linking density during the curing of epoxy resins, and further resulted in poorer thermal stability than was the case for the pure samples. However, the particles acted as flame retardants for polymers and postponed the initiation of decomposition by hindering/slowing the oxidation. In two SiO<sub>2</sub>-based samples, surface treatment modified the cross-linking density in the interfacial areas by getting rid of some surface groups, like hydroxyl groups found in EPS samples; however, unsuitable surface treatment led to the higher mobility of chain segments at the interface and thus the reduction of  $T_g$ . Moreover, the morphology of hBN-based nanocomposites had a great impact on its thermal properties: in TGA measurement, shorter chains resulted in better performance while decomposition; in DSC measurement, the exfoliated and intercalated macroscopic layer structures of hBN-based nanocomposites, which were observed in Chapter 4, restricted the mobility of chain segment in the vicinity of particles and led to the increase of  $T_g$  in samples with higher filler loadings. This analysis demonstrates that the cross-linking density of samples mainly affected the results of TGA, whereas the mobility of chain segments played the main role in influencing the glass transition temperature of polymer composites.

In order to relate the characterised morphology to the dielectric properties of epoxy nanocomposites, dielectric breakdowns (AC and DC) of epoxy and its nanocomposites were investigated and analysed by means of two-parameter Weibull distribution. As nanoparticles in bulk mostly acted as impurities, the AC and DC breakdown strength of epoxy nanocomposites showed an overall reduction when compared to unfilled ones. In AC breakdown tests, agglomerations of particles/aggregates, as observed in Chapter 4, had little influence on the reduction of AC breakdown strength. The presence of particles led to the increase in the mobility of charge carriers and thus the reduction of breakdown strength, which became more obvious as filler loadings increased. In addition, the shape of particles also had a significant impact on AC breakdown strength; thus, plate-like BN particle-based nanocomposites showed the lowest breakdown strength value. In DC breakdown tests, the accumulation of charges around aggregates and the resultant enhancement of electrical intensity were the main reasons behind the worsening of BD strength. Moreover, as increased filler loadings led to a decrease in inter-particle/aggregate distances, the percolation of charge carriers in the whole bulk became easier and resulted in the reduction of DC BD strength, where the

dispersion and distribution of particles/aggregates investigated in Chapter 4 provided qualitative support.

Furthermore, adding nanoparticles physically and chemically affected the base material and influenced the dielectric responses; this, it is a solution for modifying the dielectric properties of epoxy composites. Moreover, as the dielectric response was affected by the existence of moisture in the sample, this provided a method for extracting the influence of water absorption on dielectric properties; subsequently, a relatively reliable method was proposed by using Monte Carlo simulation to estimate the average thickness of the water shell or the related relaxation peak of epoxy nanocomposites with spherical particles. This experimentally demonstrated the existence of a two-layer water shell structure and calculated the thickness of the water shell of  $\text{SiO}_2$ -based nanocomposites under different humidity conditions. According to the analysis of the water uptake of epoxy nanocomposites, surface treatment can reduce water uptake; however, there was no obvious impact on modifying effects on dielectric properties due to the limitation of the thickness of the tightly bonded layer. The “hydrophobic” performance of BN nanocomposites is far better than that of the silica ones, especially because of the lack of formation of water shells around the particles, meaning that it could be more suitable for applications in environments with humidity.

From the combined analysis of DC conductivity and space charge measurements, the influence of adding nanoparticles in epoxy resins and the characteristics of the movement of positive and negative charges in bulk were clearly noted. As the presence of nanoparticles resulted in morphology changes, mostly in the form of physical defects while the surface treatment introducing deeper traps at the interface, there were more shallow traps presenting in bulk; this hindered the charge injection and reduced the mobility of charge carriers, and as a consequence, reduced the DC conductivity. However, with the increase of filler loadings, there was a greater effect on polymer structures and thus a higher density of traps, meaning that the average distance between arbitrary traps (either shallow or deep) is lowered and, consequently, charge carriers are required less energy when moving from one to another by hopping or via the quantum tunnelling mechanism. The resultant higher mobility of carriers consequently led to higher conductivities. Moreover, if particles were regarded as recombination centres, the reduction of inter-particle distances in higher filler loadings also contributed to increased conductivity in silica-based nanocomposites. This also gave support to the concept

of reduction in DC breakdown strength with the growth of filler loadings. In addition, the presence of plate-like nano-hBN created complex microstructure in epoxy resins and acted as a barrier for charge injection and movement. Thus, more traps near the surface and within the bulk of nanocomposites. This led to the increased DC breakdown strength as filler loadings rose.

According to the quantitative results in Chapter 4 and 7, the presence of water caused an increase in charge injection, higher mobility of charge carriers (both in base materials and within traps/particles) and an obvious reduction in DC breakdown results. Moreover, water shells around spherical particles contributed to the higher probability of the quantum tunnelling process and the formation of conductive percolation channels. Therefore, the DC conductivity and space charge measurements on dry and wet samples were consistent with each other, which supported the results of analyses of the dielectric breakdown experiments.

### 9.2 Future Work

The investigation in this thesis with utilizing a range of analysis techniques has indicated that epoxy nanocomposite systems are significantly complex, where a number of assumptions have been made and some work has not been done due to the limitation of time. Thus, with reference to the present work, some directions for future work are suggested and listed below:

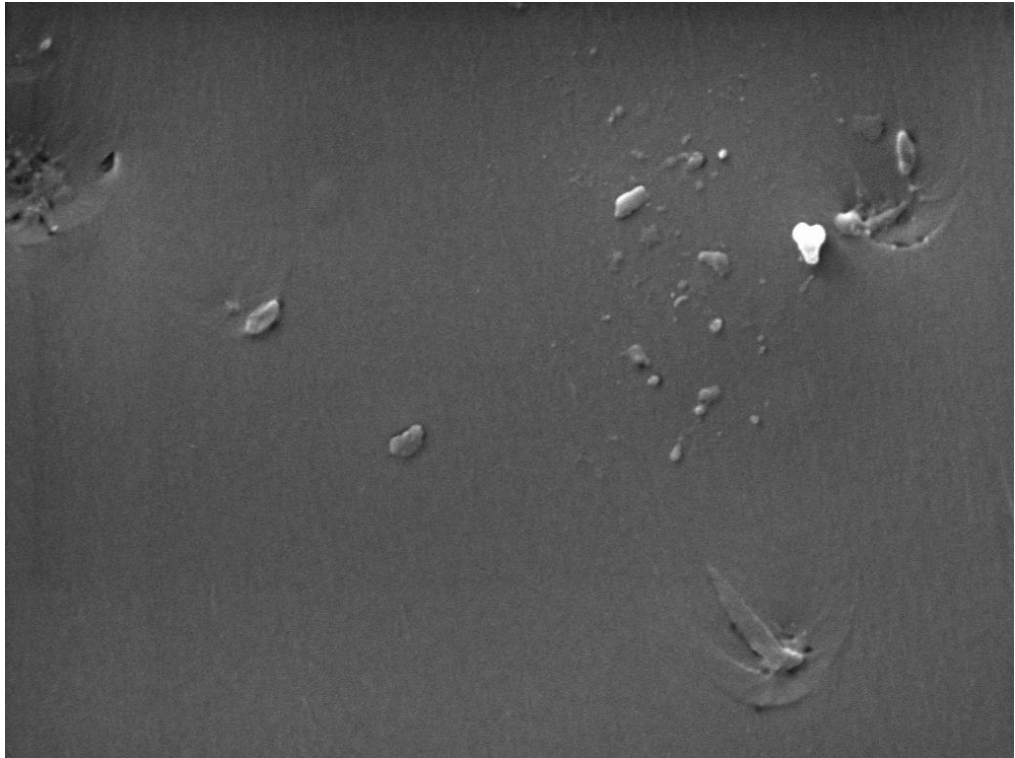
- In order to arrive at a deeper understanding of the dielectric/electrical properties of spherical/ellipsoidal particle-based nanocomposites, it may be possible to link the simulation of dispersion and distribution of particles/aggregates based on the measured morphology of nanocomposites to existing models, such as charge transport, percolation and inner electric field intensity;
- As the surface treatment on nano-SiO<sub>2</sub> particles in this work is not suitable without tightly bound to the structures of the matrix, a more appropriate one must be implemented in the future. The resulting material should be tested according to the experiments in this work, after which comparisons can be drawn to find out the differences and mechanisms involved;



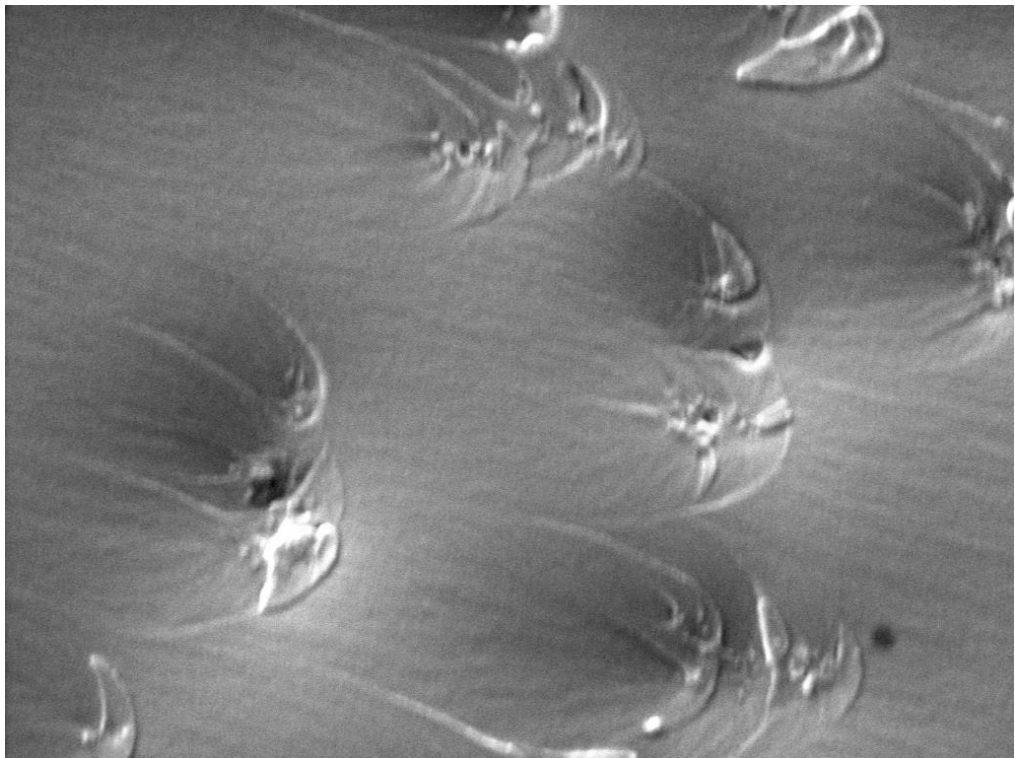
- Most of the analyses of DC conductivity and space charge measurements in this work are qualitative. Future work could provide a quantitative description and more precise analyses, which may include a study of the influences of particles and moisture on hopping, tunnelling or the mobility of charges carriers;
- Effects of moisture on thermal and electrical properties, based on the alternating electric field of epoxy nanocomposites, could also be investigated in the future.



## Appendix A SEM Image Processing and Histograms of Main Data

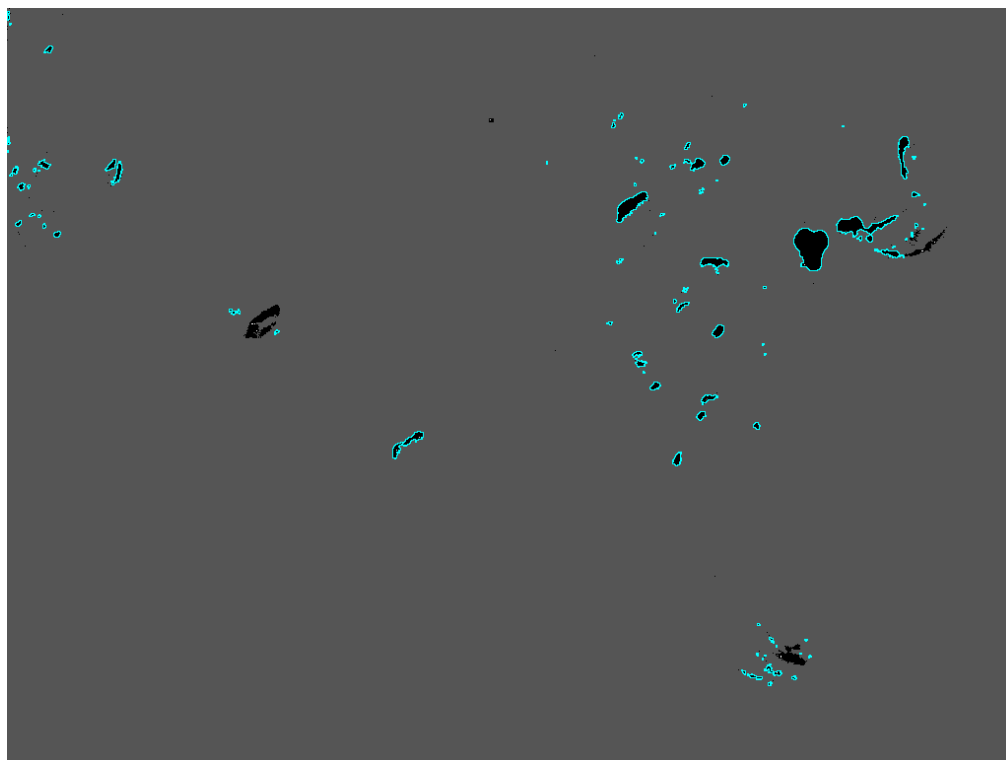


(a)

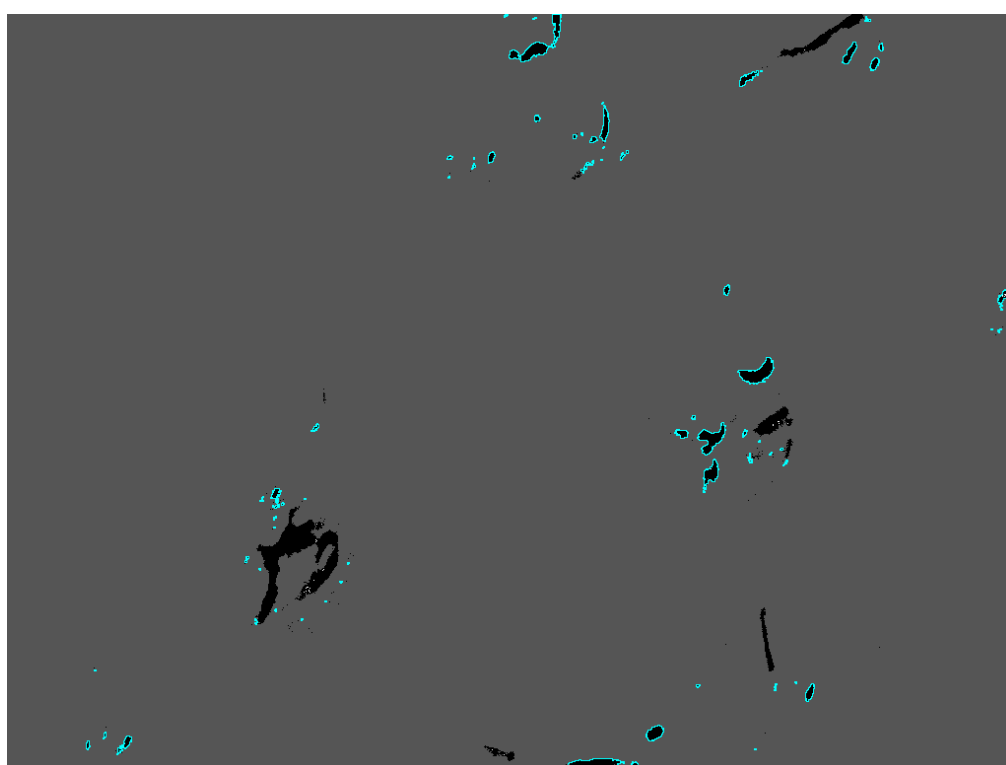


(b)

Figure A-1 Original SEM images of EPS1 samples,  $\times 15000$ .



(a)



(b)

Figure A-2 Processed SEM images with highlighted particles of EPS1 samples,  $\times 15000$ .

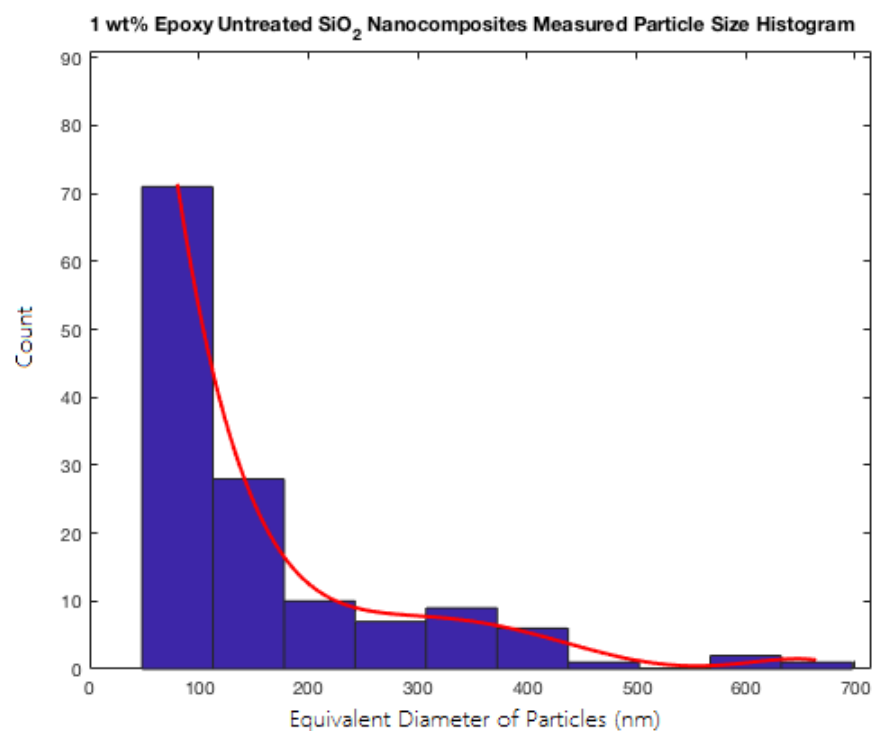


Figure A-3 Histogram of measured particle/aggregate size of EPS1 samples.

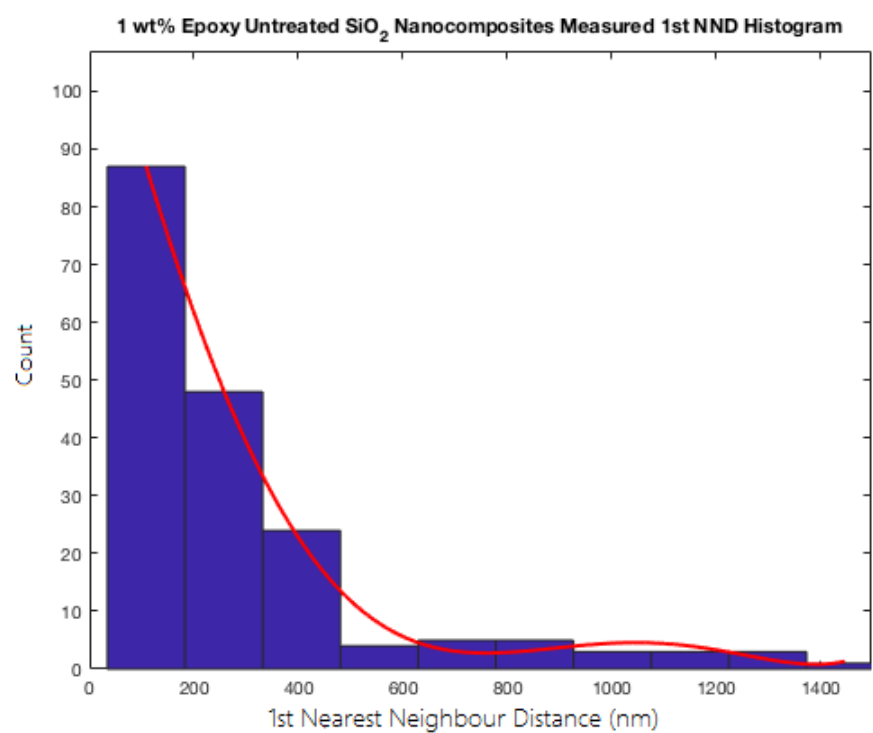
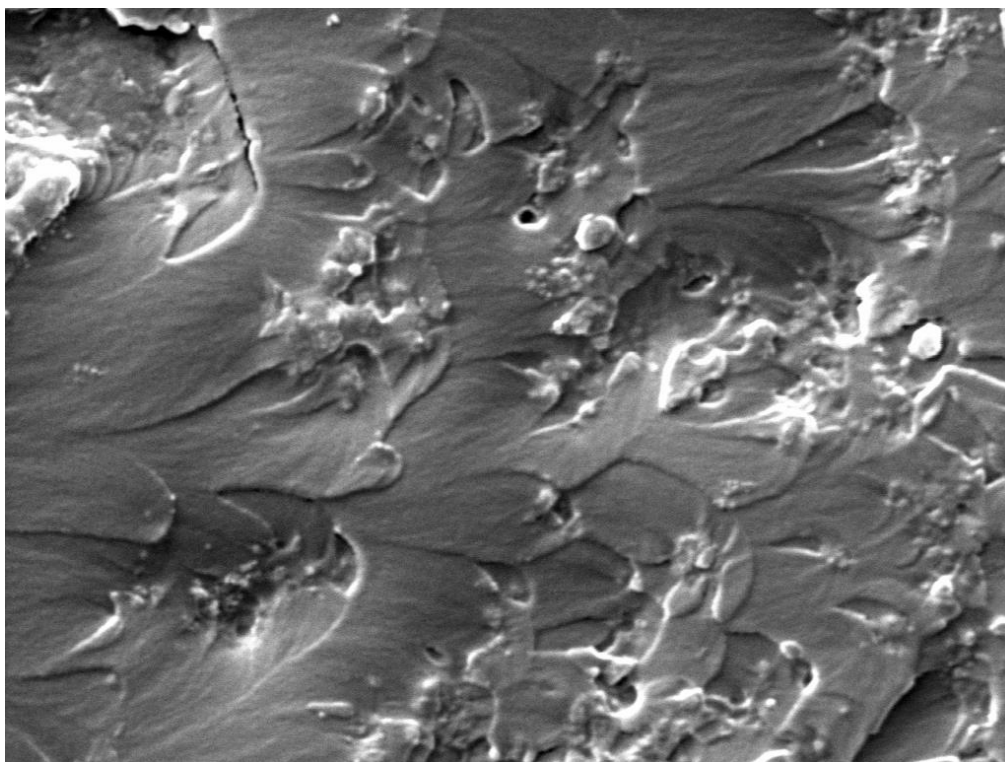
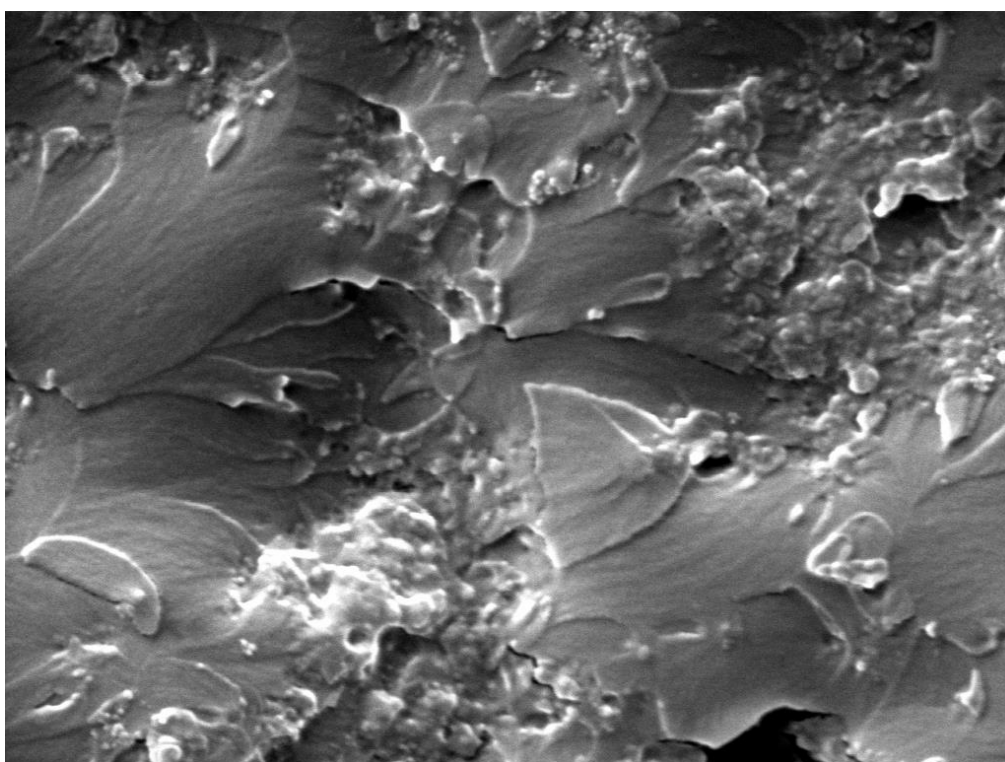


Figure A-4 Histogram of measured 1st Nearest Neighbour Distance of EPS1 samples.

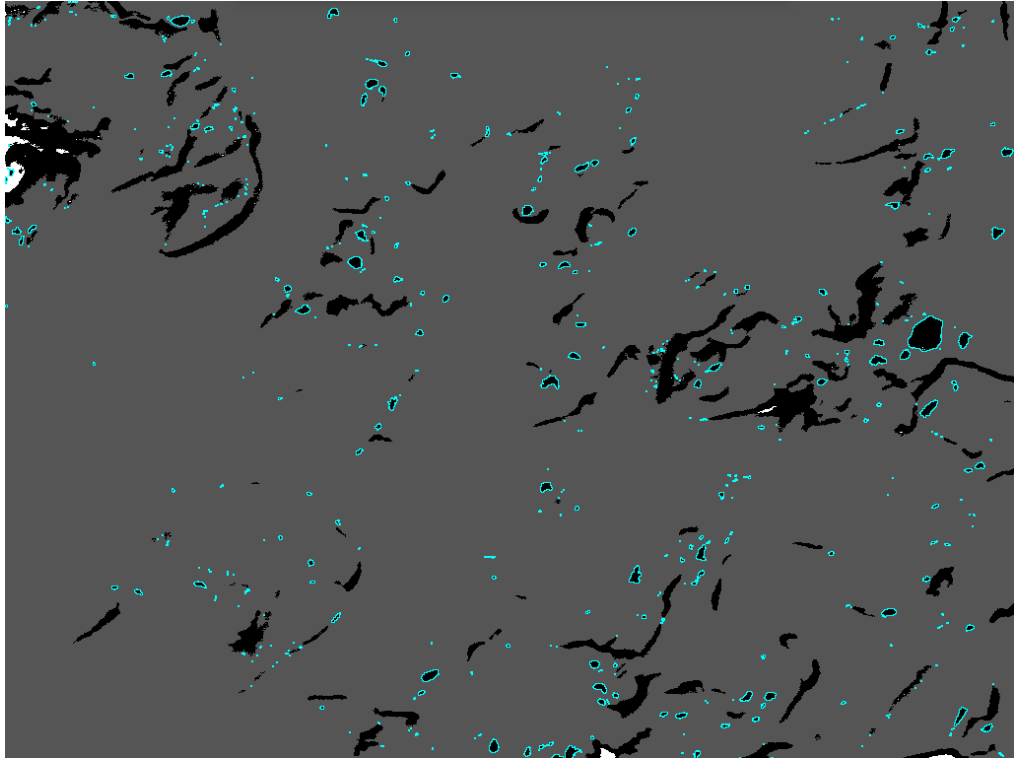


(a)

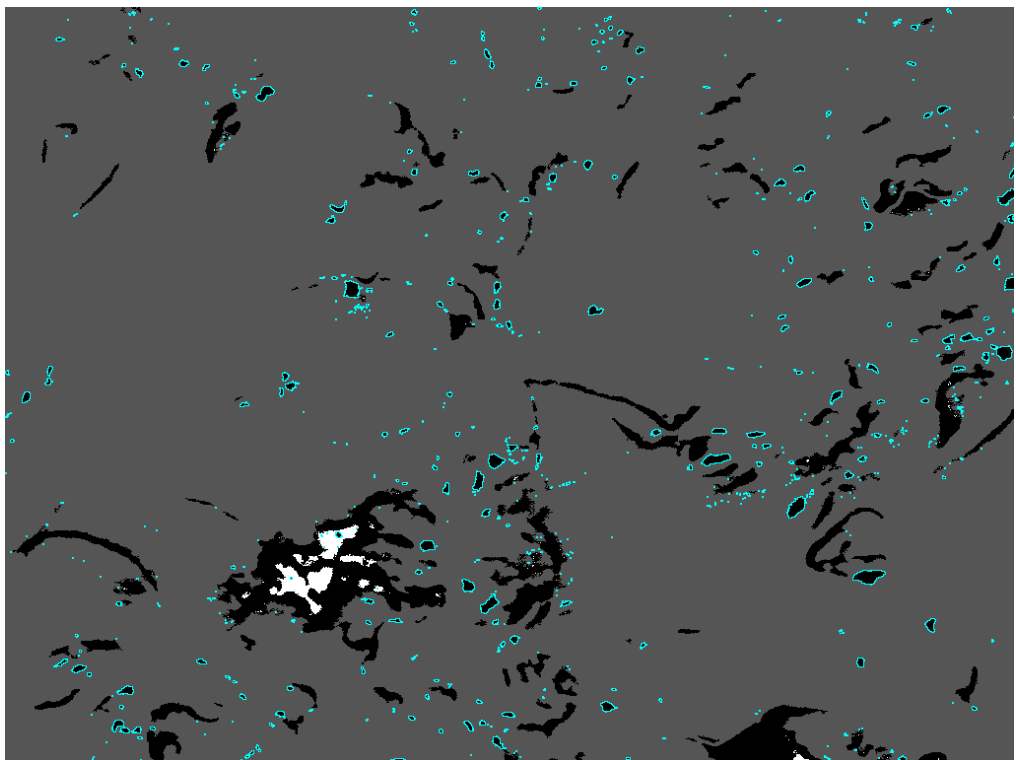


(b)

Figure A-5 Original SEM images of EPS5 samples,  $\times 15000$ .



(a)



(b)

Figure A-6 Processed SEM images with highlighted particles of EPS5 samples,  
×15000.

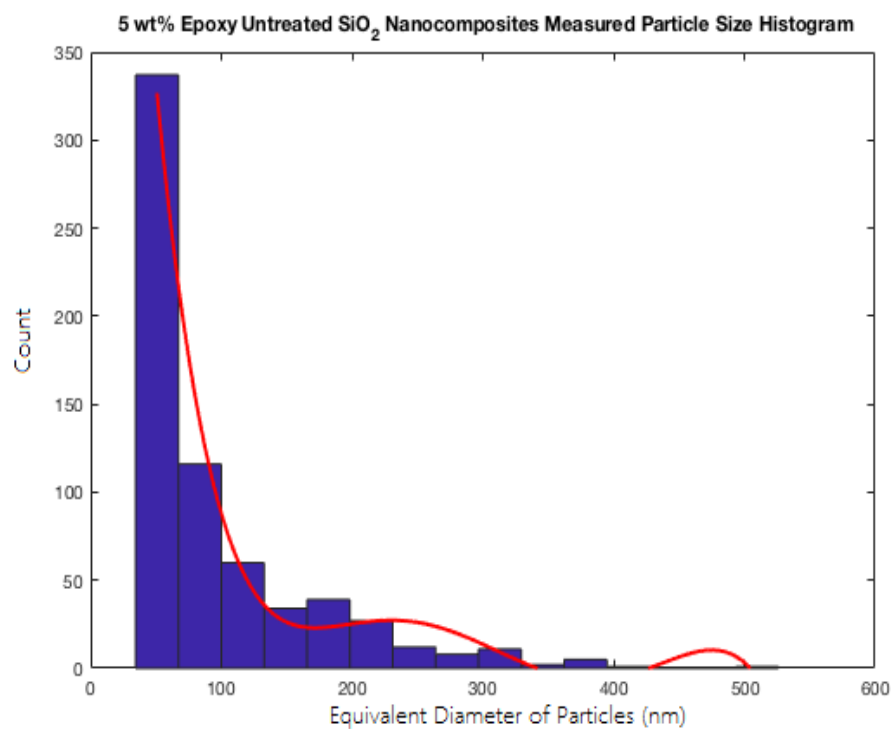


Figure A-7 Histogram of measured particle/aggregate size of EPS5 samples.

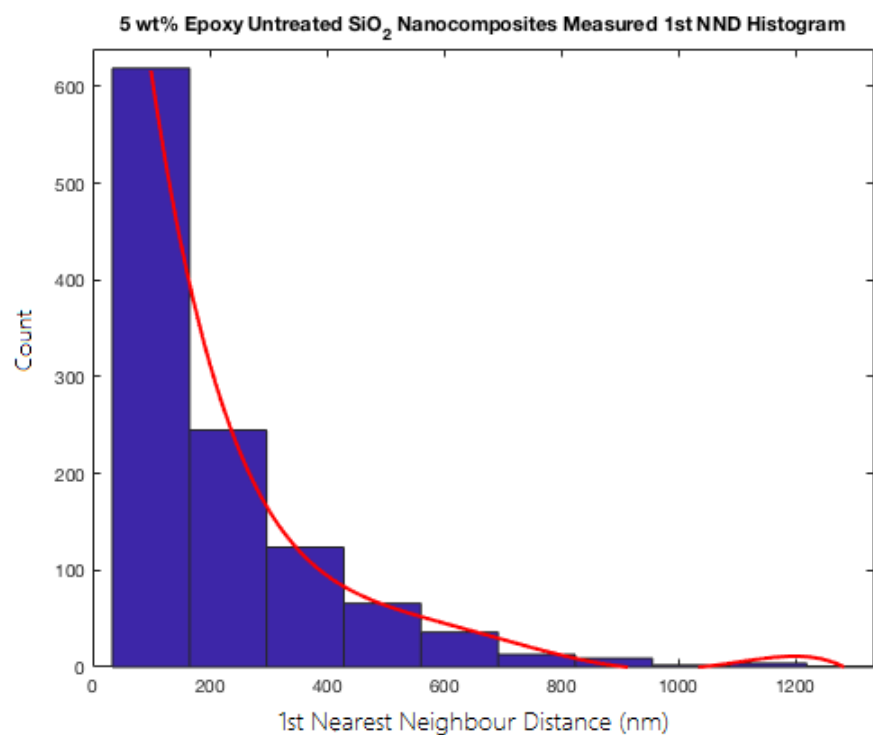
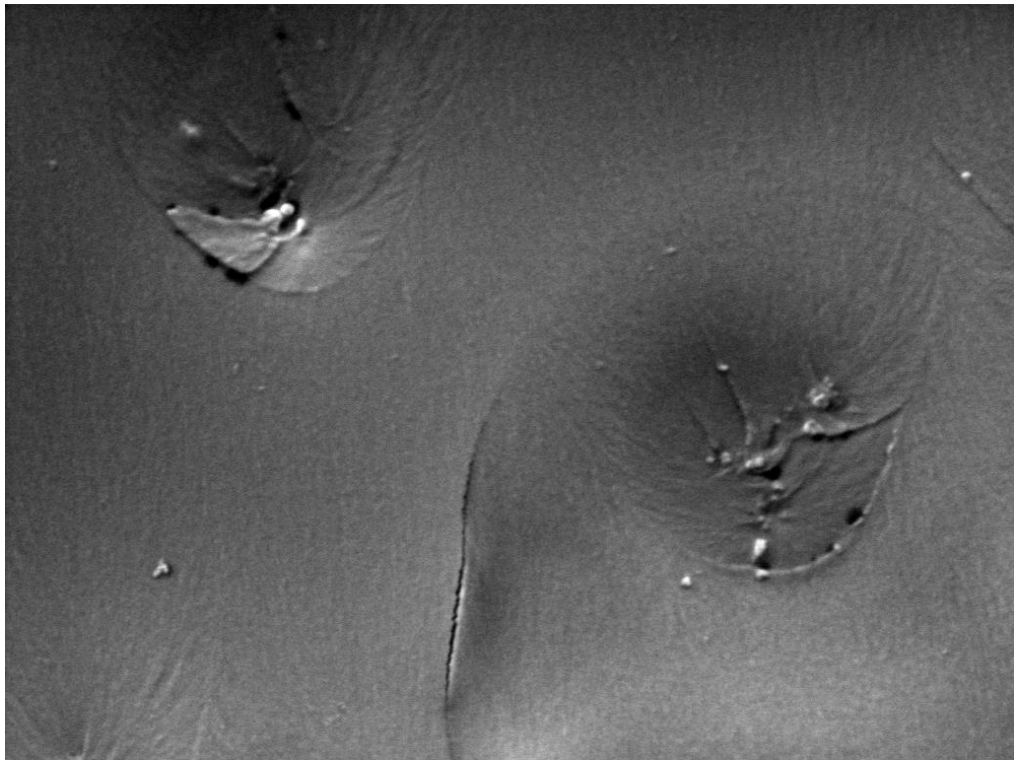
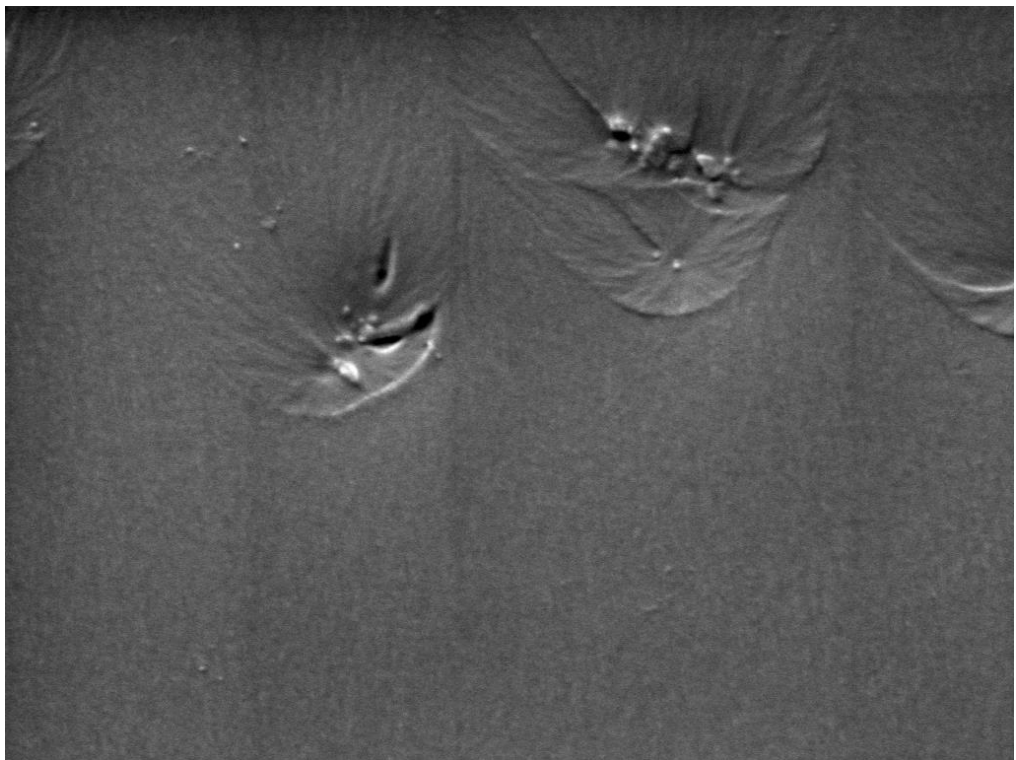


Figure A-8 Histogram of measured 1st Nearest Neighbour Distance of EPS5 samples.



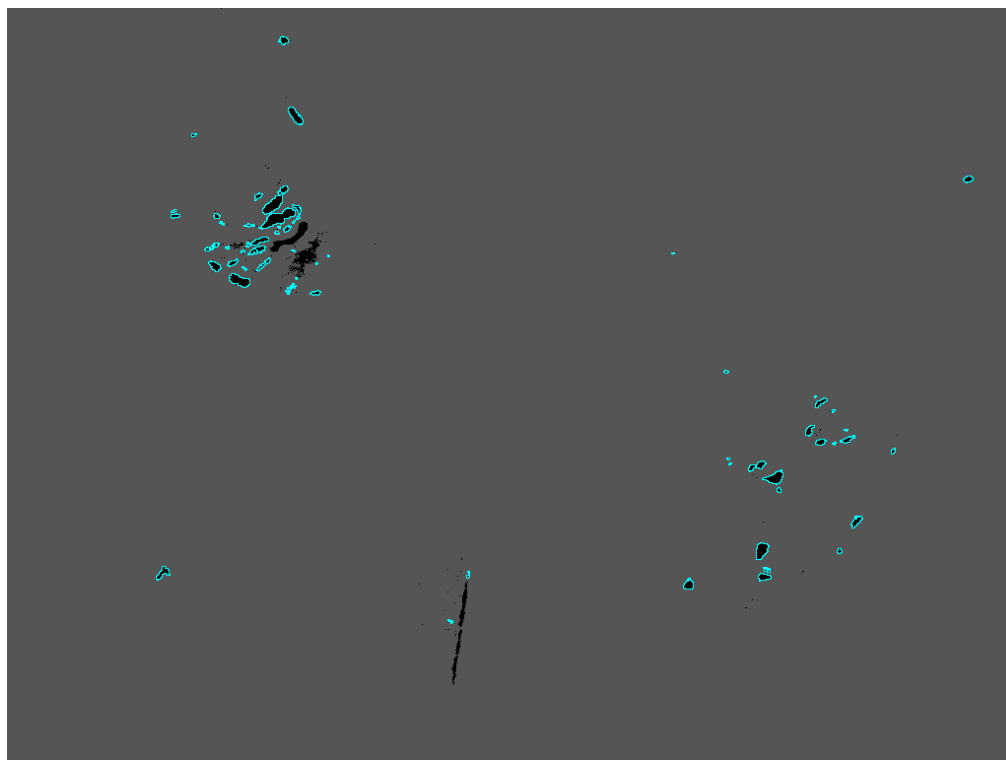


(a)

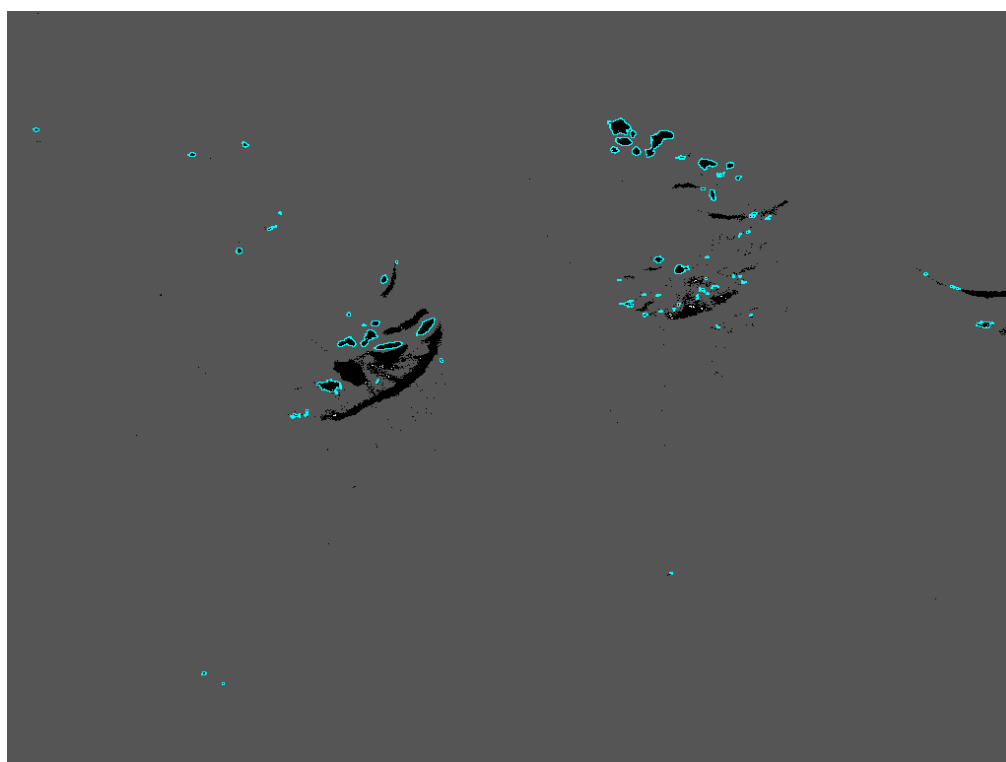


(b)

Figure A-9 Original SEM images of EPST1 samples,  $\times 15000$ .



(a)



(b)

Figure A-10 Processed SEM images with highlighted particles of EPST1 samples,  $\times 15000$ .

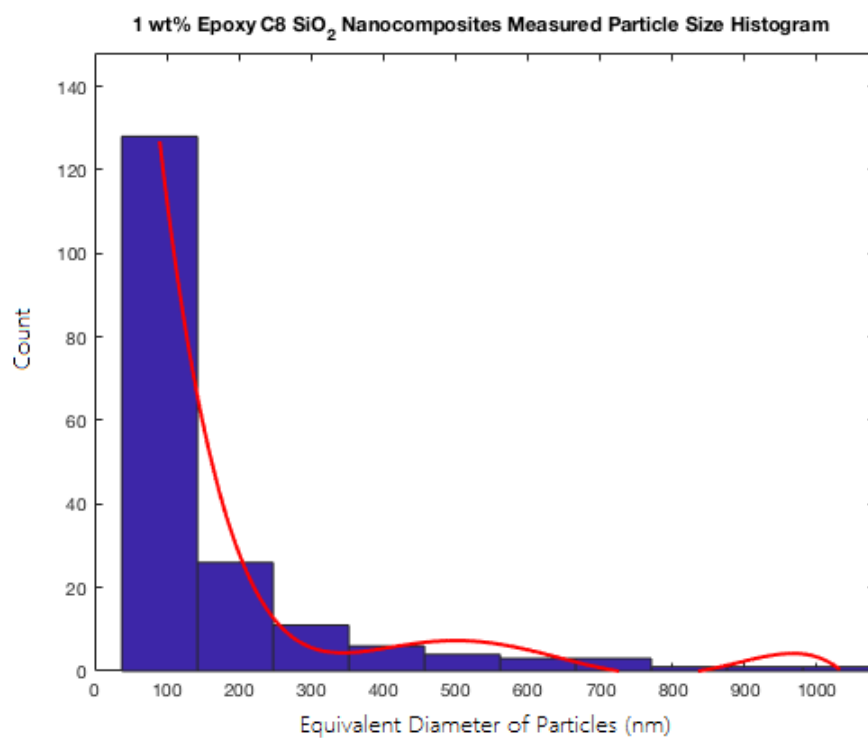


Figure A-11 Histogram of measured particle/aggregate size of EPST1 samples.

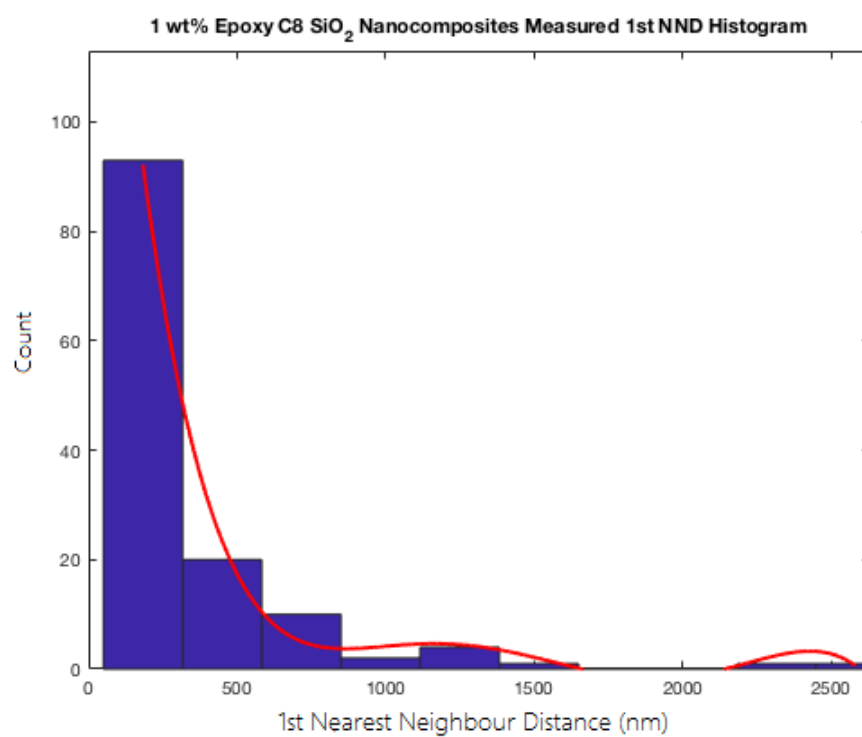
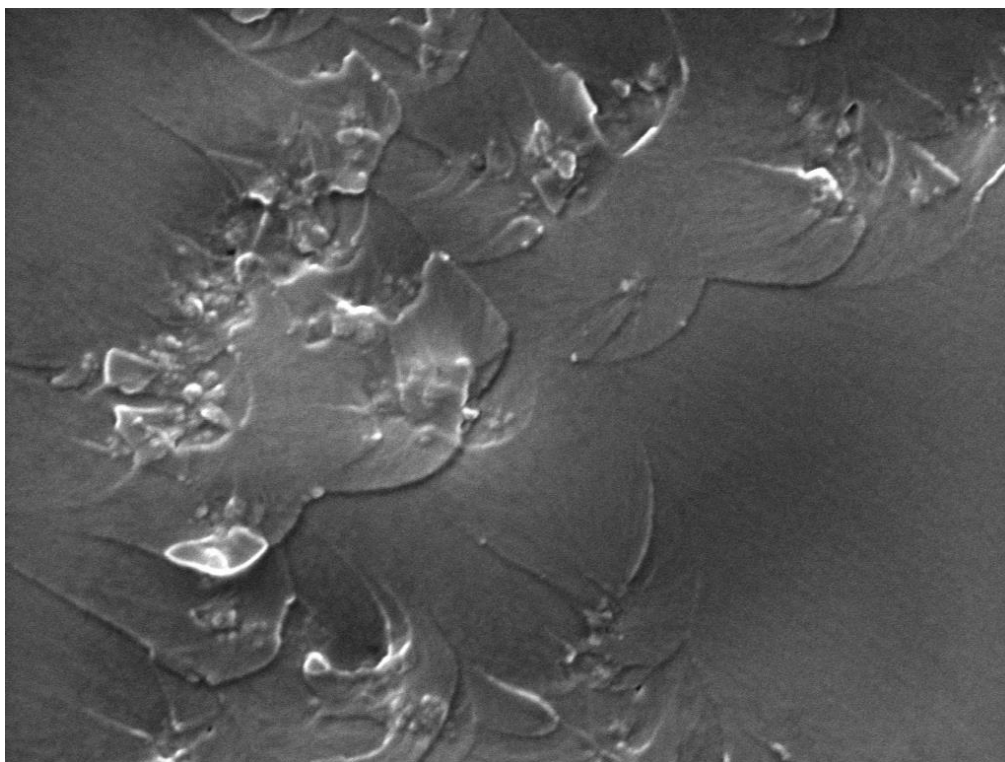
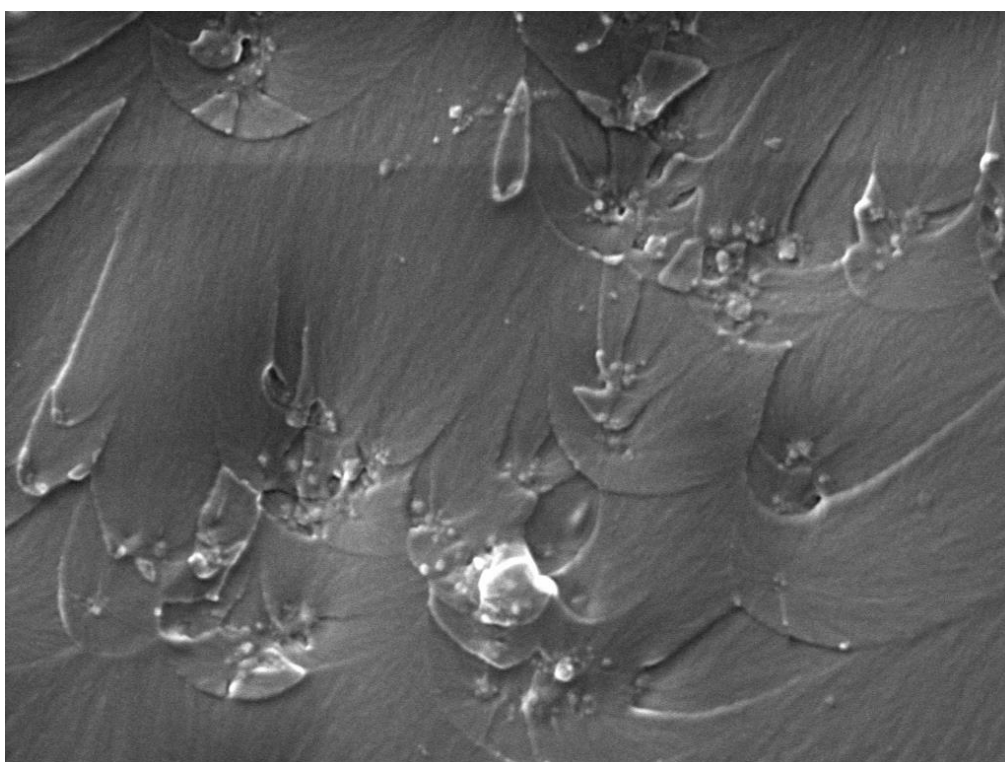


Figure A-12 Histogram of measured 1st Nearest Neighbour Distance of EPST1 samples.

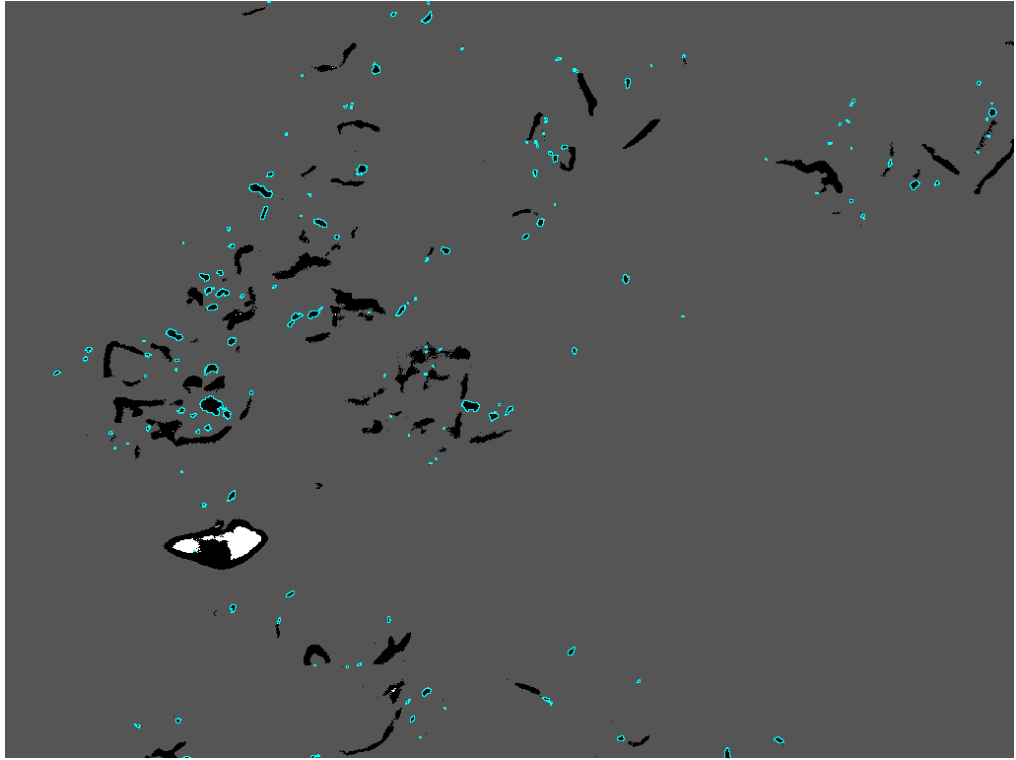


(a)

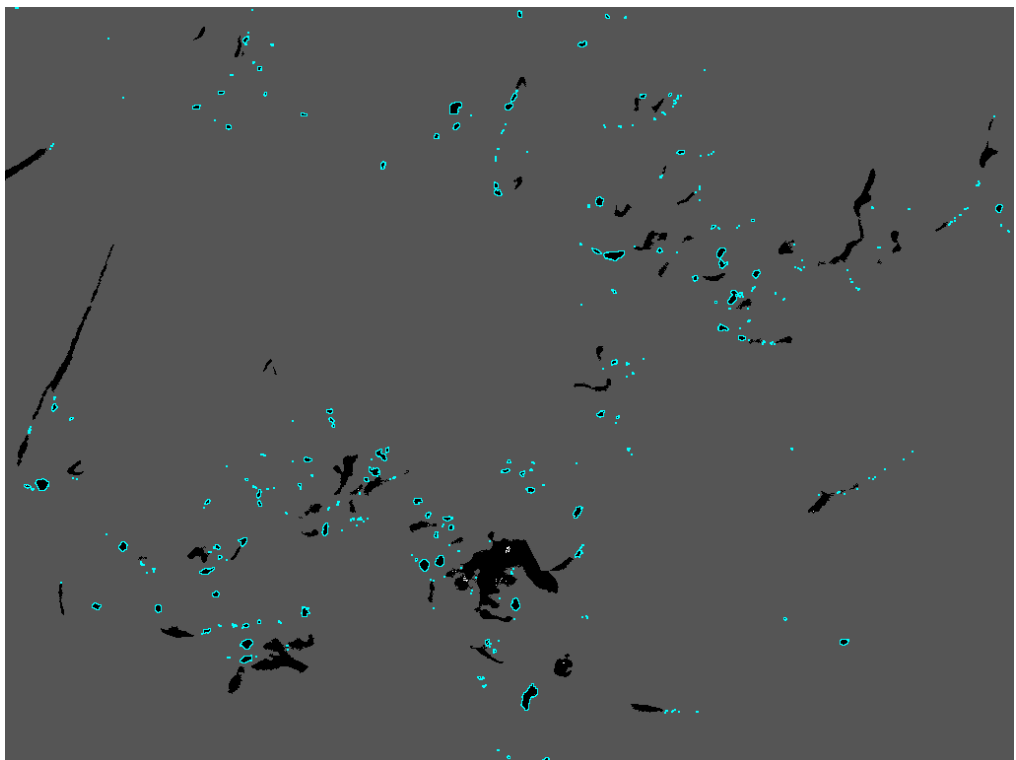


(b)

Figure A-13 Original SEM images of EPST3 samples,  $\times 15000$ .



(a)



(b)

Figure A-14 Processed SEM images with highlighted particles of EPST3 samples,  $\times 15000$ .

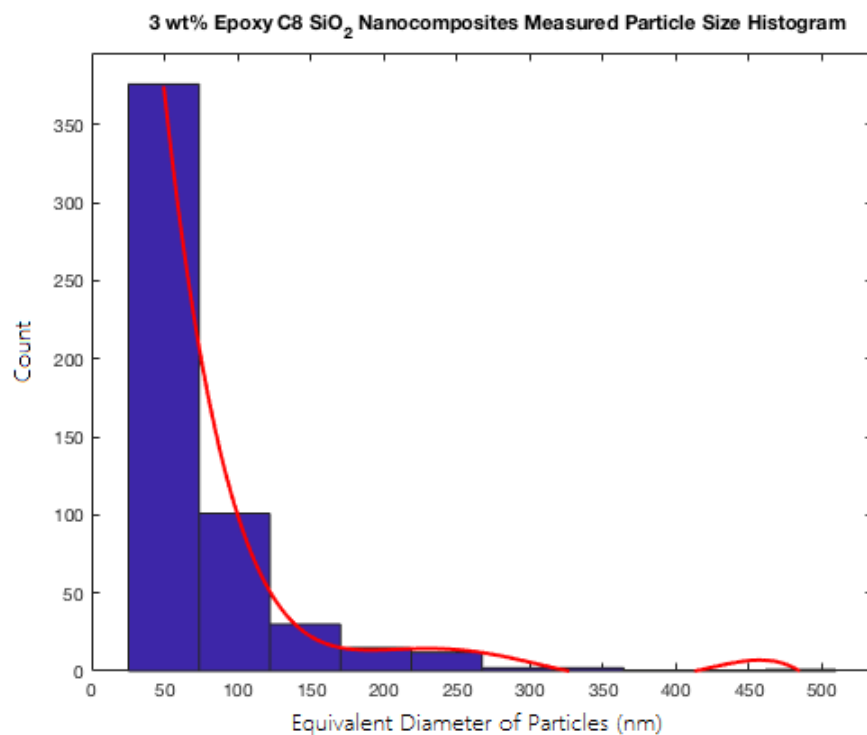


Figure A-15 Histogram of measured particle/aggregate size of EPST3 samples.

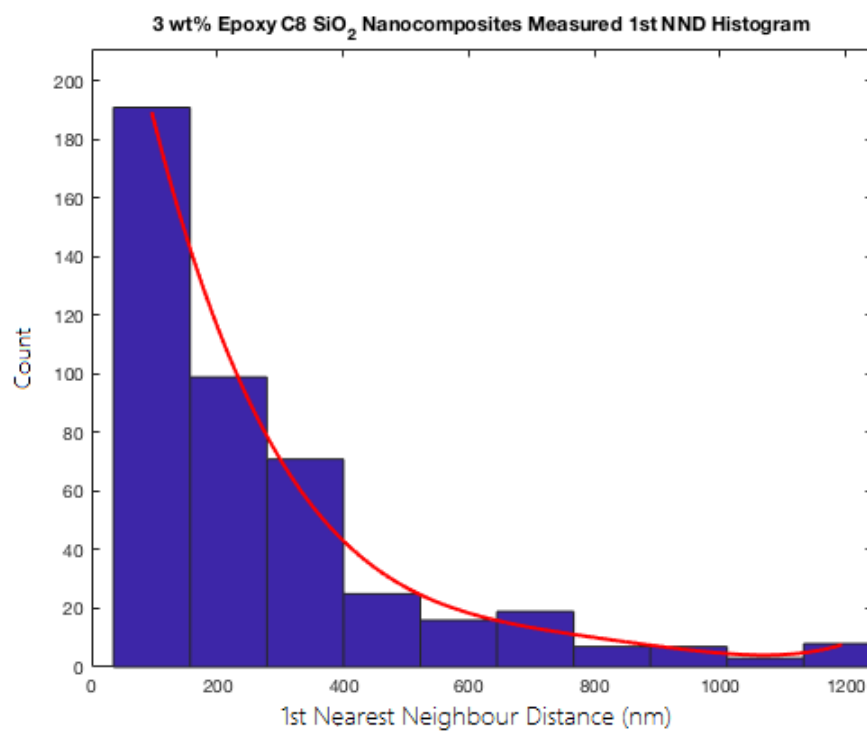
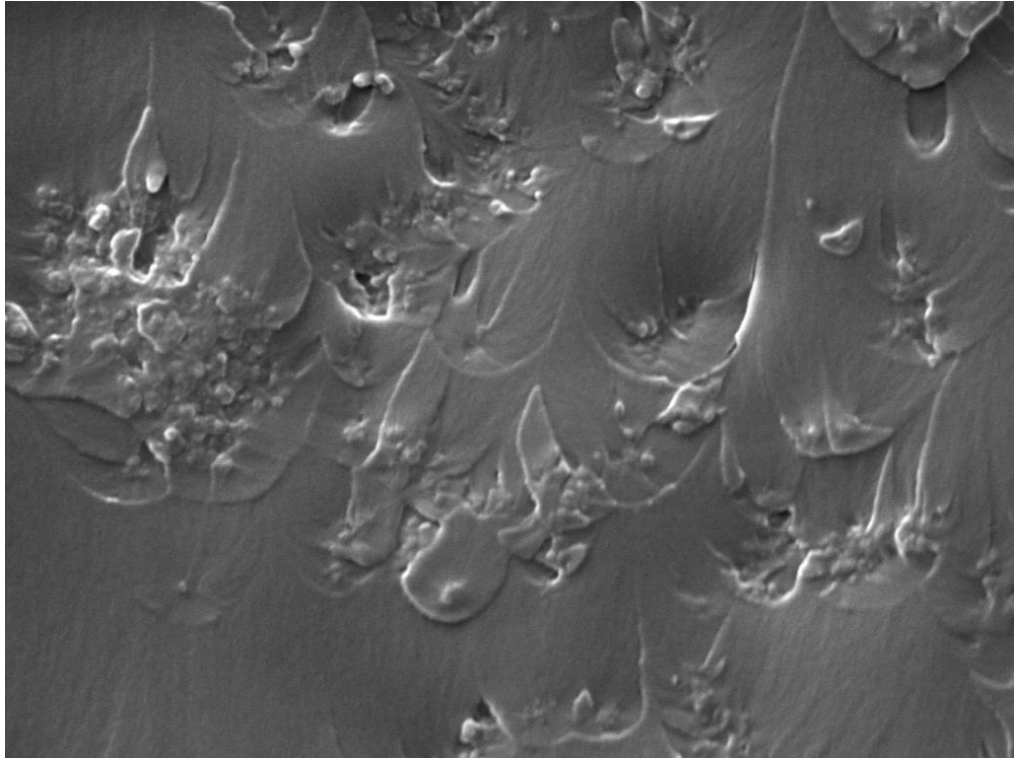
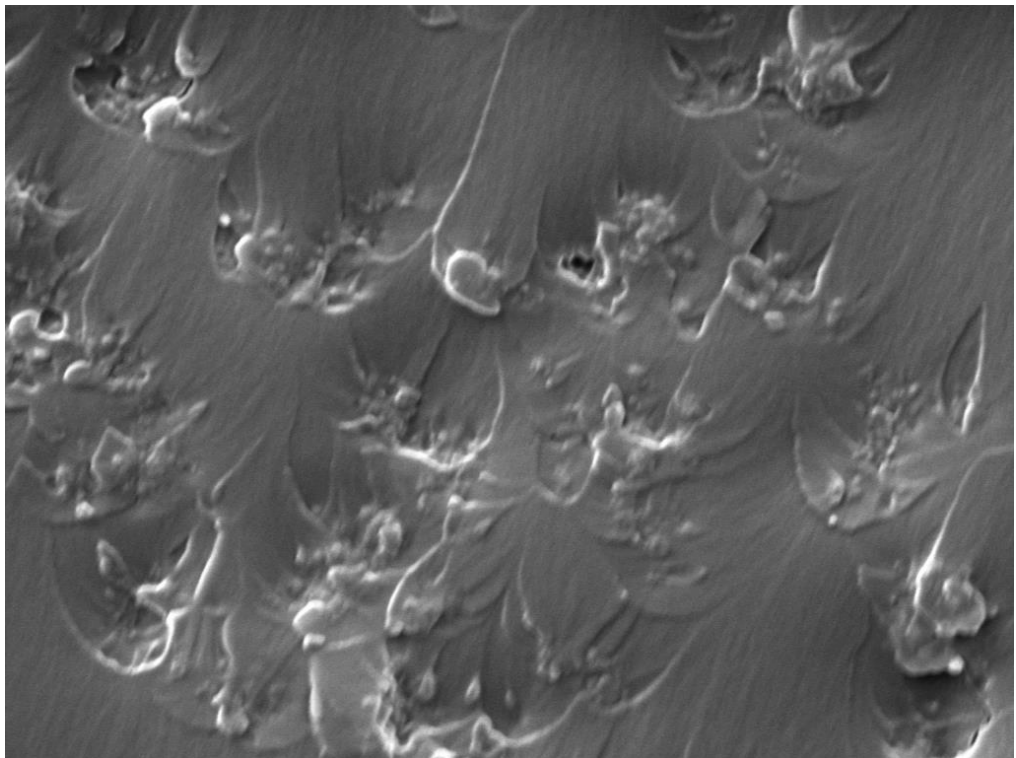


Figure A-16 Histogram of measured 1st Nearest Neighbour Distance of EPST3 samples.

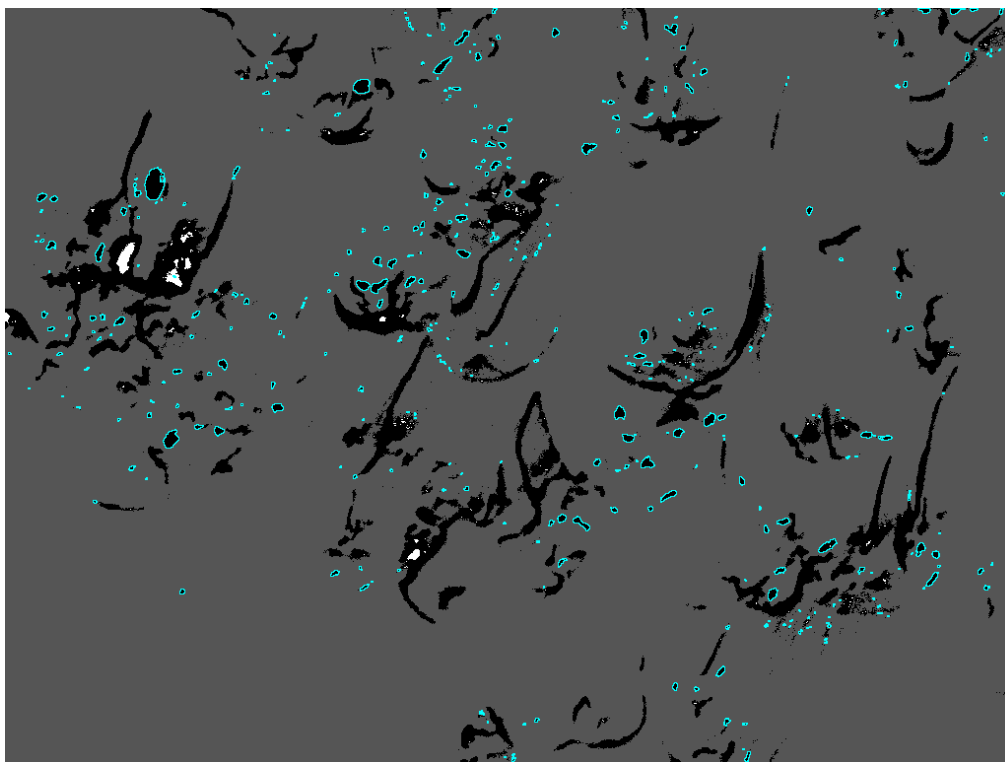


(a)

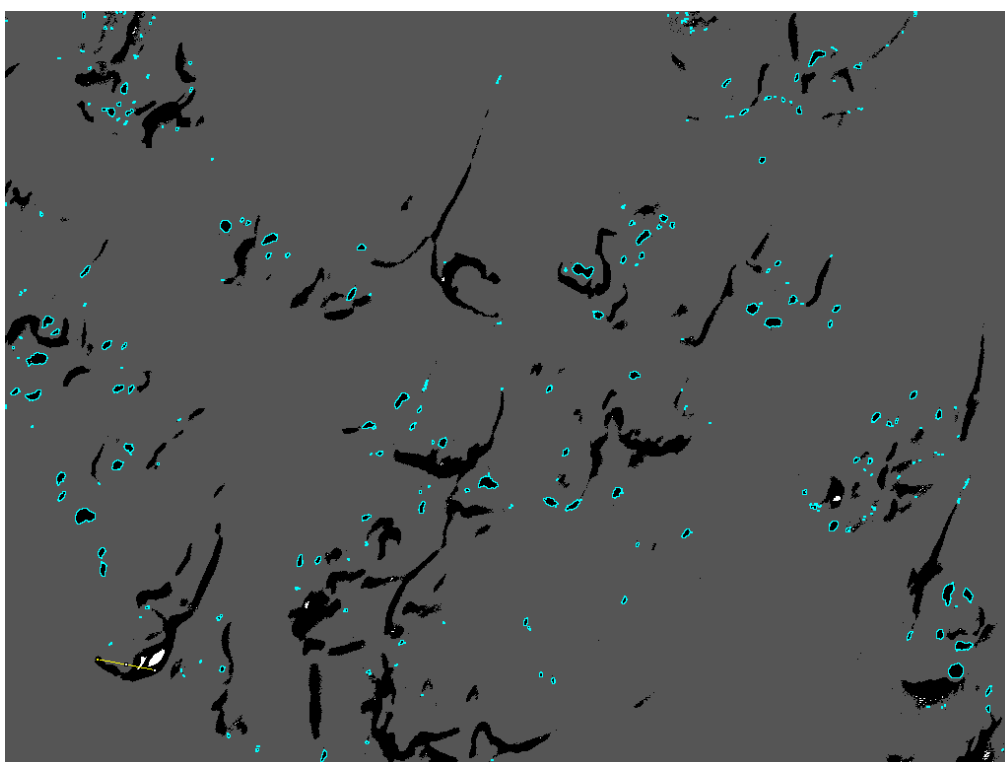


(b)

Figure A-17 Original SEM images of EPST5 samples,  $\times 15000$ .



(a)



(b)

Figure A-18 Processed SEM images with highlighted particles of EPST5 samples,  $\times 15000$ .



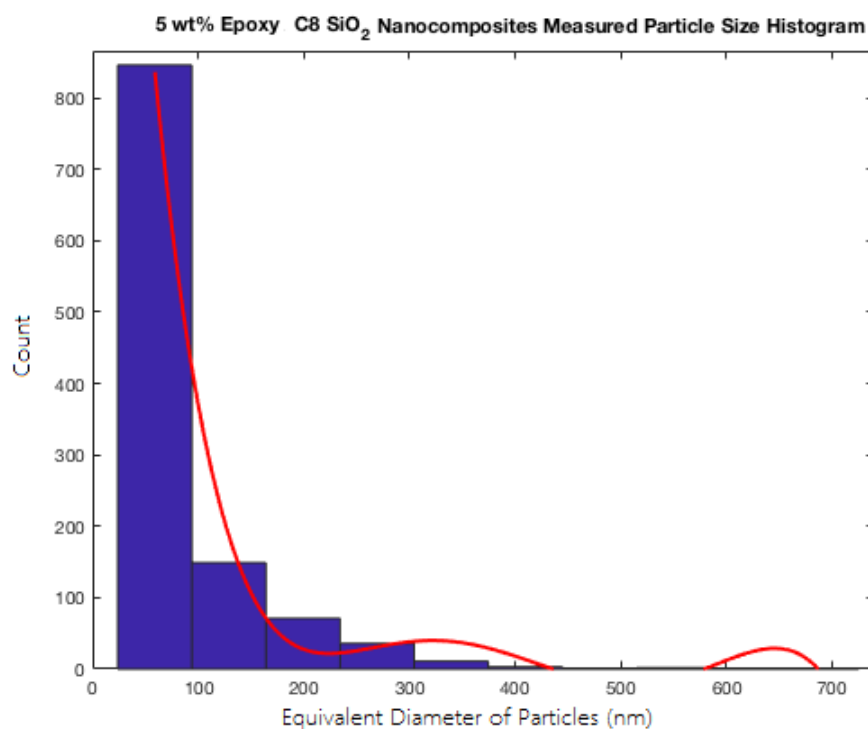


Figure A-19 Histogram of measured particle/aggregate size of EPST5 samples.

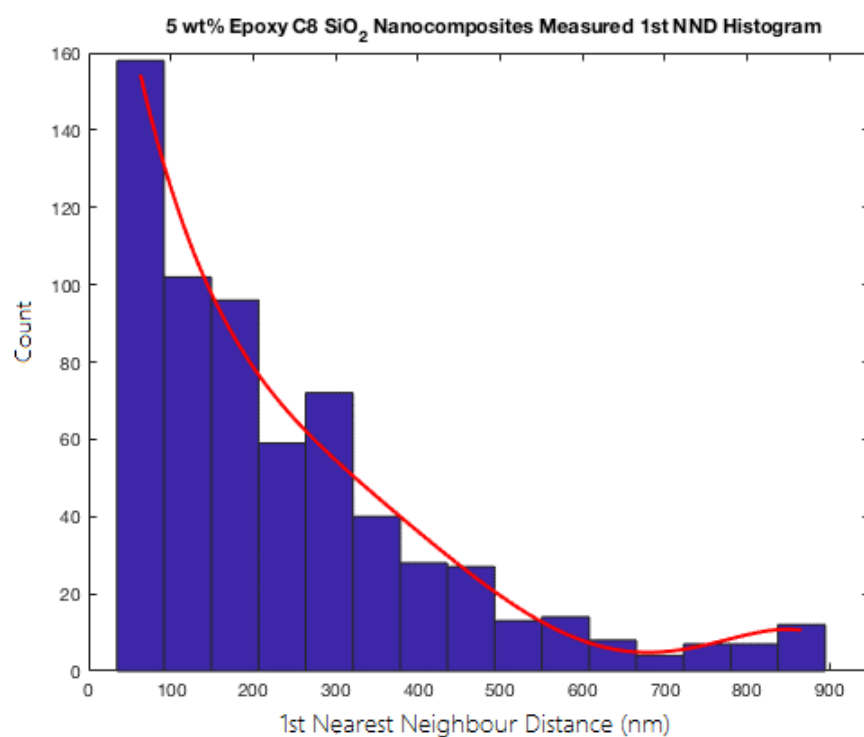


Figure A-20 Histogram of measured 1st Nearest Neighbour Distance of EPST5 samples.



## Appendix B Particle/Aggregate Dispersion and Distribution Matlab Code

The code followed is for Probability Distribution Method while calculating 1st NND Distribution (from line 43 to 77), which can be replaced by the Matlab code for the Histogram Method.

```

1      clear all;
2      clc;
3      warning off;
4      %Define;
5      Vf=1.42; %give value to volume fraction of 3 wt%: 5 wt% is 2.35 and 1 wt% is 0.47;
6      Skewness = [];
7      %Size Distribution;
8      %for u=1:1:100 %Monte Carlo Method for 100 runs;
9      u
10     Diff = [];
11     Vfr = [];
12     R1 = [];
13     RNew=[];
14     RMatrix=[];
15     for NumBall = 1:1:500;
16     for j = 1:NumBall
17     x = 12.6:7.5:254.9; %radius parameter, min value, interval & max value;
18     l = length(x);
19     for i = 1:l
20     y(i) = real(0.9617*exp(-0.0129*2*x(i))); %give the size distribution function of particles;
21     z(i) = sum(y(1:i));
22     end
23     h = sum(y)*rand (1);
24     zz = h*ones(1,l)-z;
25     i=1;
26     while(zz(i)>0)
27     i=i+1;
28     end
29     R(j) = x(i);
30     R1=[R1,R(j)];%record all random radius;
31     end
32     Vi=4/3*pi*R.^3;
33     Vt=sum(Vi);
34     Vfr=[Vfr;Vt*100/(3000*3000*3000)];
35     Diff=abs(Vfr-Vf);
36     end
37     [minimum index] = min(Diff(:,1));%get the number of particles that can fulfill the volume fraction
    the most which is named as INDEX;

```

## Appendix B Particle/Aggregate Dispersion and Distribution Matlab Code

```

38 Vf_real=Vfr(index);
39 i=index;
40 A1=((i-1)^2+i+1)/2;
41 A2=(i^2+i)/2;
42 RMatrix(1,:)=R1(A1:A2);%get the random radius under INDEX number
43 %1st NND Distribution-Probability Distribution Method;
44 syms x
45 %Give Measured 1st NND Probability Distribution Function;
46 f_x= 0.6568*exp(-0.00480*x); %give PDF of 1st NND;
47 xx=28.2:25:1080; % interval of 1st NND;
48 n=length(xx);
49 %Use intergral of PDF to calculate the probability in each interval;
50 for i=1:n-1
51 yy(i)=double(int(f_x,xx(i),xx(i+1)));
52 end
53 %point location given;
54 N=index; %give the number of particles;
55 %caluculate the number of particles in each interval based on their probability;
56 num=round(N*yy./sum(yy));
57 %make sure the number of particles equal to the N;
58 num(1)=N-sum(num(2:end));
59 d = [];
60 %generate a random start point of partcles, distacnes based on the calculated intervals;
61 for i=1:n-1
62 temp=xx(i)+25*rand(1,num(i));
63 d=[d temp];
64 end
65 %searching the partcls location fulfill the 1st NND, update, error of 1st NND allowrance within [-1
66 1];
67 for i=1:length(d)
68 xyz=3000*rand (3,1);
69 dis=sqrt(xyz'*xyz);
70 while dis>d(i)+1&dis<d(i)-1
71 xyz=3000*rand (3,1);
72 dis=sqrt(xyz'*xyz);
73 end
74 %generate 1st NND particles and Point Location Given;
75 xt(i)=xyz(1);
76 yt(i)=xyz(2);
77 zt(i)=xyz(3);
78 end
79 %Skewness;
80 L=3000;H=3000;W=3000;%give definition of scale;
81 V=L*H*W;
82 indexS=20; %give definition of size of each cubic;
83 v=L*H*W/(indexS*indexS*indexS);
84 L0=L/indexS;H0=H/indexS;W0=W/indexS;
85 Count=zeros(indexS*indexS,indexS);
86 for i=1:1:length(xtN)

```

## Appendix B Particle/Aggregate Dispersion and Distribution Matlab Code

```

86     for n=0:1:indexS-1
87         if n*L0<=ztN(i) && ztN(i)<(n+1)*L0
88             for j=0:1:indexS-1
89                 for k=0:1:indexS-1
90                     if j*L0<=xtN(i) && xtN(i)<(j+1)*L0 && k*H0<=ytN(i) && ytN(i)<(k+1)*H0
91                         Count(j*indexS+k+1,n+1)=Count(j*indexS+k+1,n+1)+1;
92                     else if j*L0<=xtN(i) && xtN(i)<(j+1)*L0 && ytN(i)==H
93                         Count((j+1)*indexS,n+1)=Count((j+1)*indexS,n+1)+1;
94                     else if xtN(i)==L && k*H0<=ytN(i) && ytN(i)<(k+1)*H0
95                         Count(indexS*(indexS-1)+k+1,n+1)=Count(indexS*(indexS-1)+k+1,n+1)+1;
96                     end
97                 end
98             end
99         end
100     end
101     else if ztN(i)==L
102         for j=0:1:indexS-1
103             for k=0:1:indexS-1
104                 if j*L0<=xtN(i) && xtN(i)<(j+1)*L0 && k*H0<=ytN(i) && ytN(i)<(k+1)*H0
105                     Count(j*indexS+k+1,indexS)=Count(j*indexS+k+1,indexS)+1;
106                 else if j*L0<=xtN(i) && xtN(i)<(j+1)*L0 && ytN(i)==H
107                     Count((j+1)*indexS,indexS)=Count((j+1)*indexS,indexS)+1;
108                 else if xtN(i)==L && k*H0<=ytN(i) && ytN(i)<(k+1)*H0
109                     Count(indexS*(indexS-1)+k+1,indexS)=Count(indexS*(indexS-1)+k+1,indexS)+1;
110                 end
111             end
112         end
113     end
114 end
115 end
116 end
117 end
118 end
119 A = [];
120 for i=1:indexS
121     for k=1:indexS*indexS
122         A=[A;Count(k,i)];
123     end
124 end
125 Sum=sum(A);
126 LA=length(A);
127 Aver=Sum/LA;
128 Std=std(A);
129 B = [];
130 for i=1:LA
131     B=[B;(A(i)-Aver) ^3/(Std)^3];
132 end
133 Skewness = [Skewness; LA/((LA-1) * (LA-2))*sum(B)];
134 %Plot Drawing of Simulated particles;

```

## Appendix B Particle/Aggregate Dispersion and Distribution Matlab Code

```
135     figure;
136     [x y z] = sphere (100);
137     for k=1:index;
138         RNew(k)=RMatrix(k); %where can define the thickness of water shell;
139         surf(RNew(k)*x+xt(k), RNew(k)*y+yt(k), RNew(k)*z+zt(k))
140         colormap([0.5,0.5,0.5]);
141         hold on;
142     end
143     axis equal
144     axis ([0 3000 0 3000 0 3000])
145     camlight;
146     alpha (1);
147     shading interp;
148     title ('3 wt% Epoxy Untreated SiO2 Nanocomposites Particle Simulated Dispersion and
    Distribution');%give the title name;
149     %close all;
150     %clearvars -except Skewness Vf u;
151     %end
```

### **1st NND Distribution-Histogram Method Code**

```
d1 = load('data_NND.txt'); % give measured 1st NND data;
N = index; %give number of particles;
k = length(d);
idx = randperm(ceil(N/k)*k,N);
idx = mod(idx,k)+1;
d = d(idx);
n = length(d);
D = repmat(d,[1 n]);
minErr = inf;
for k = 1:100
    k
    for nlter = 1:10
        D = D+k*rand(n,n);
        D = triu(D,0) + tril(D',-1);
        for i = 1:n, D(i,i) = 0; end
        data = mdscale(D,3,'criterion','strain');
        mind = computeMinDis(data);
        [N1,X] = hist(d1,10);
        N2 = hist(mind,X);
        N1 = N1/sum(N1); N2 = N2/sum(N2);
        err = norm(N1-N2,1);
        if err<minErr
            minErr = err;
            bestX = data;
            bestK = k;
        end
    end
end
for nlter = 1:1000
```

```

nIter
D = D+bestK*rand(n,n);
D = triu(D,0) + tril(D',-1);
for i = 1:n, D(i,i) = 0; end
data = mdscale(D,3,'criterion','strain');
mind = computeMinDis(data);
[N1,X] = hist(d1,10);
N2 = hist(mind,X);
N1 = N1/sum(N1); N2 = N2/sum(N2);
err = norm(N1-N2,1);
if err<minErr
    minErr = err;
    bestX = data;
end
end
bestX = bestX-repmat(min(bestX,[],1),[size(bestX,1) 1]);
mind = computeMinDis(bestX);
%Point location Given;
xt=bestX(:,1);
yt=bestX(:,2);
zt=bestX(:,3);

```

### 1st NND Calculation Function in Histogram Method;

```

function minD = computeMinDis(points)
D = pdist2(points,points);
for i = 1:size(D,1)
    D(i,i) = inf;
end
minD = min (D, [],2);

```





## Appendix C DC Breakdown Strength of Epoxy and its Nanocomposites with Moisture

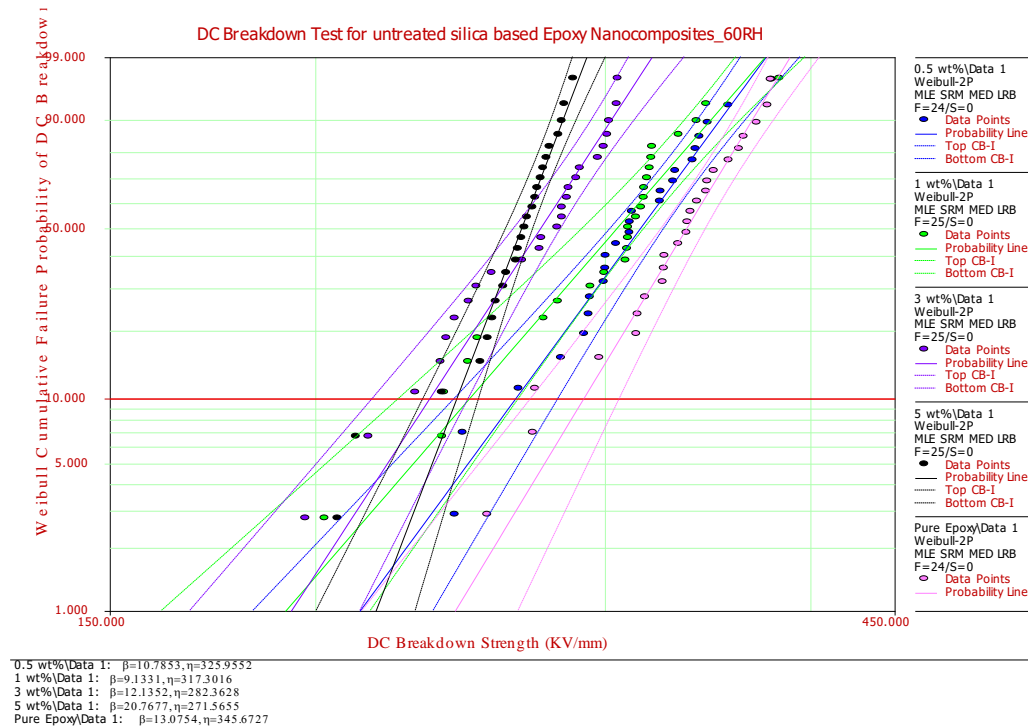


Figure C-1 Weibull plot of EPS samples in different loading concentrations on DC breakdown strength, 60RH.

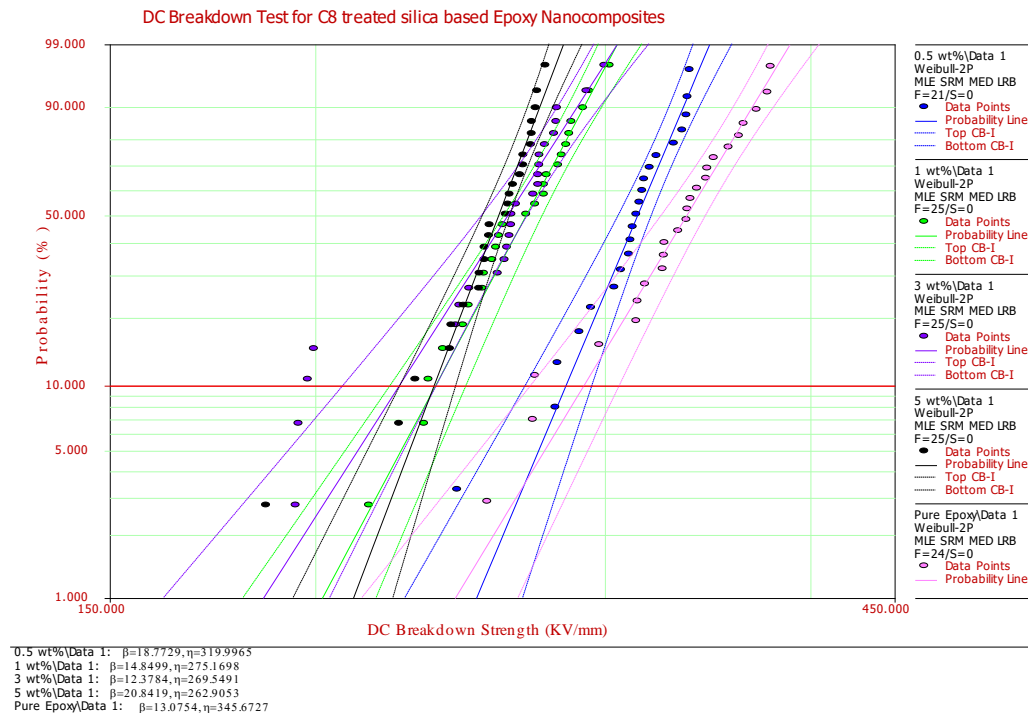


Figure C-2 Weibull plot of EPST samples in different loading concentrations on DC breakdown strength, 60RH.

## Appendix C DC BD Strength of Epoxy and its Nanocomposites with Moisture

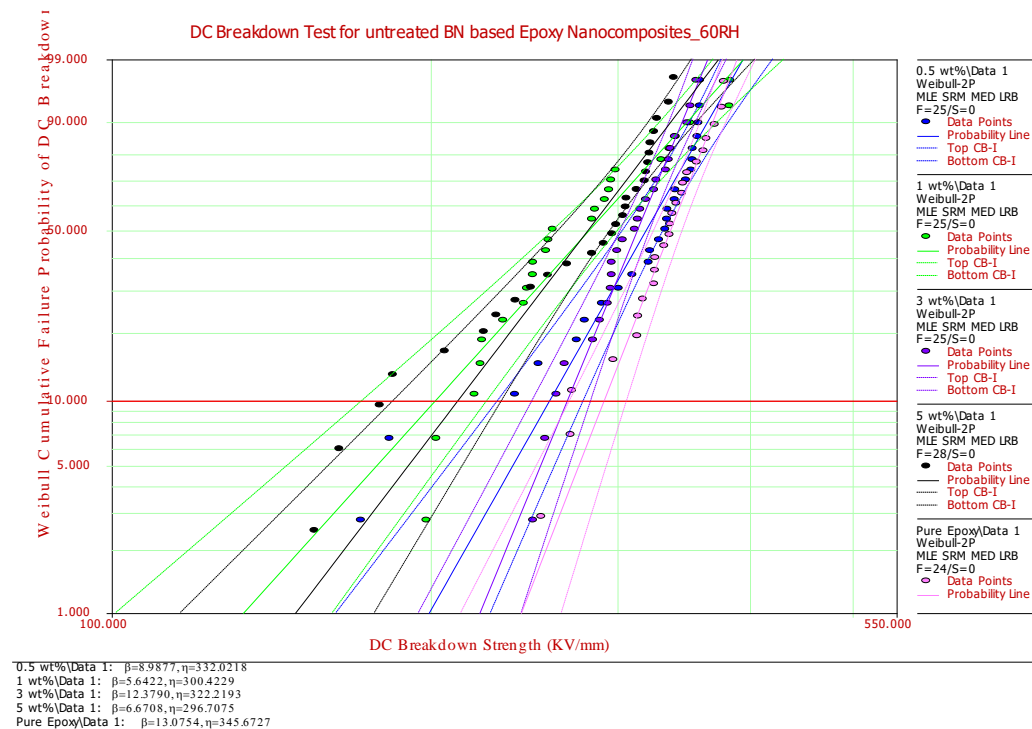


Figure C-3 Weibull plot of EPB samples in different loading concentrations on DC breakdown strength, 60RH.

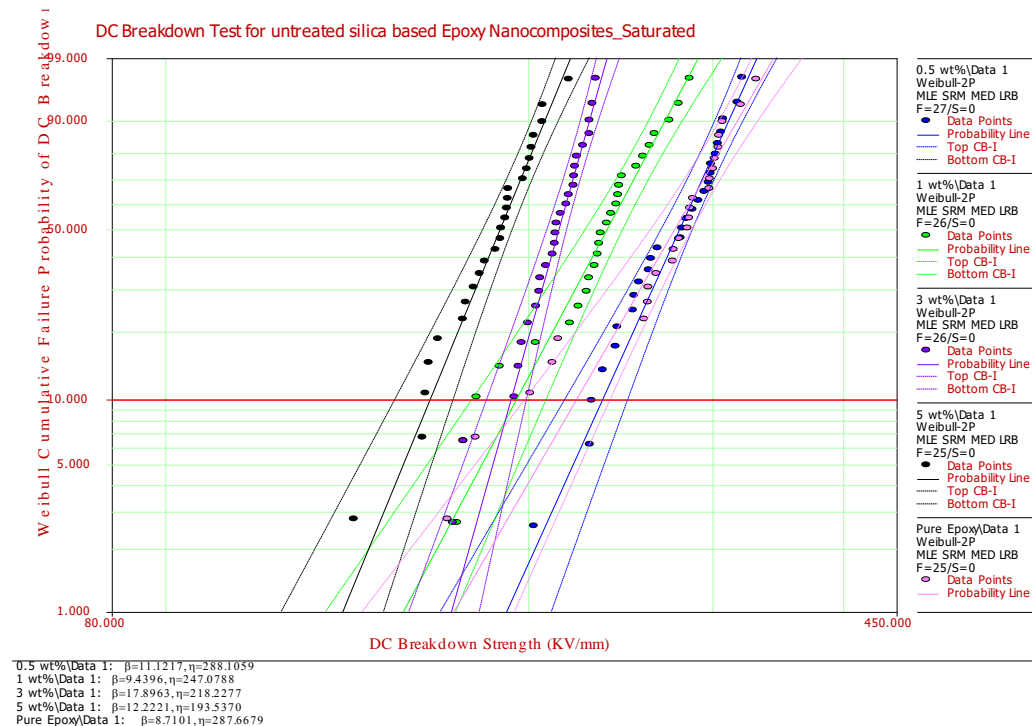


Figure C-4 Weibull plot of EPS samples in different loading concentrations on DC breakdown strength, saturated.

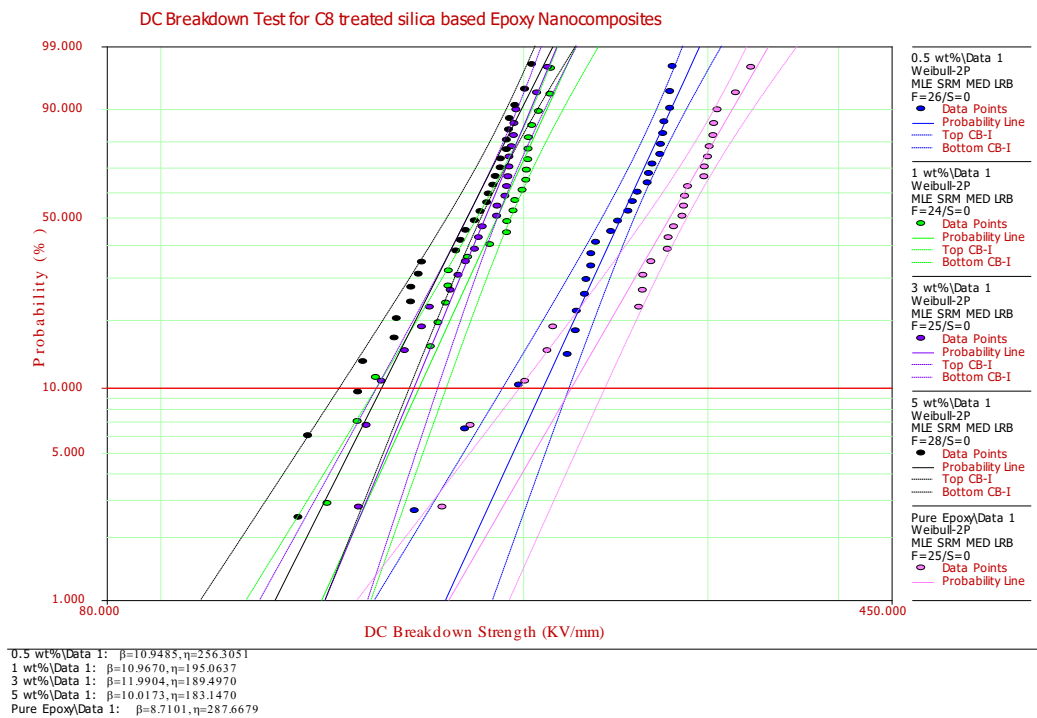


Figure C-5 Weibull plot of EPST samples in different loading concentrations on DC breakdown strength, saturated.

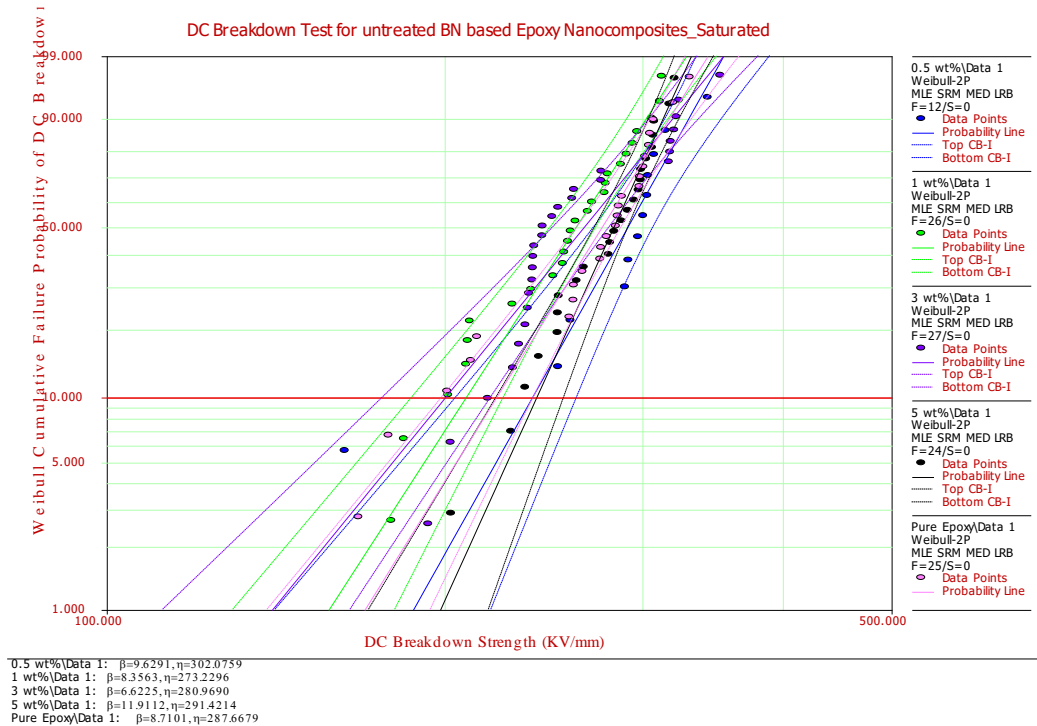


Figure C-6 Weibull plot of EPB samples in different loading concentrations on DC breakdown strength, saturated.



## Appendix D Space Charge Decay in Epoxy and its Nanocomposites

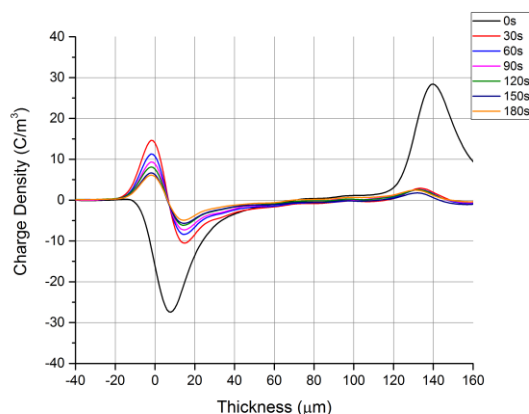
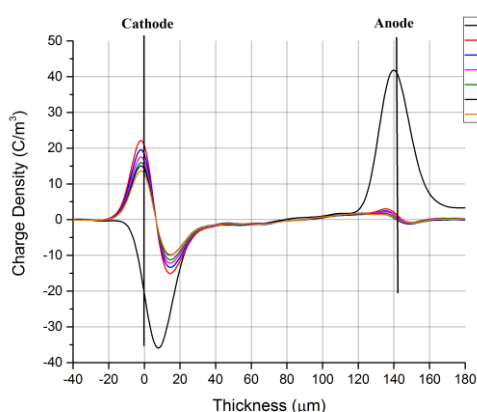
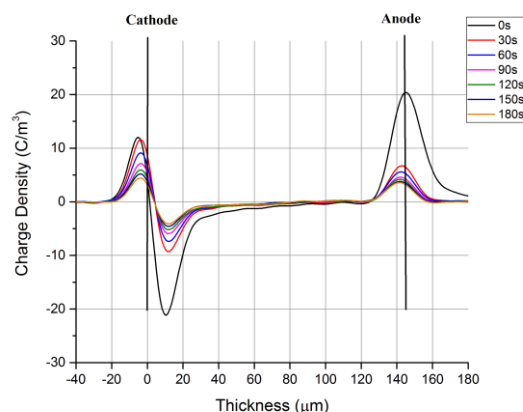


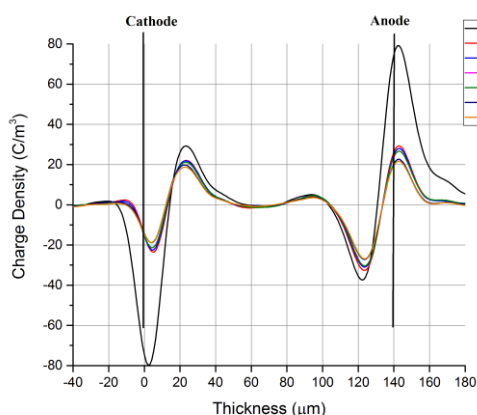
Figure D-1 Space charge decay in pure epoxy samples at  $40 \text{ kV} \cdot \text{mm}^{-1}$ , dry.



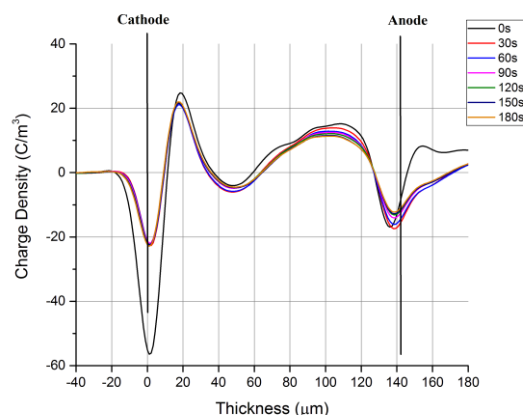
(a)



(b)



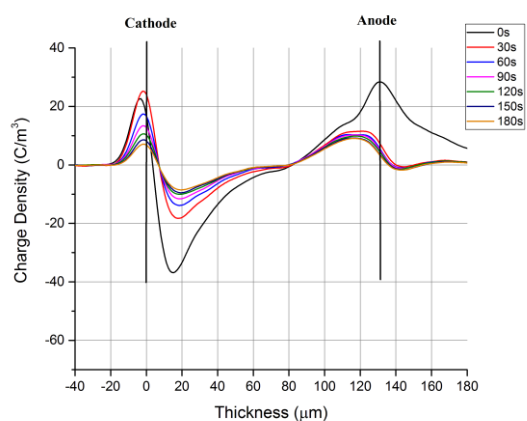
(c)



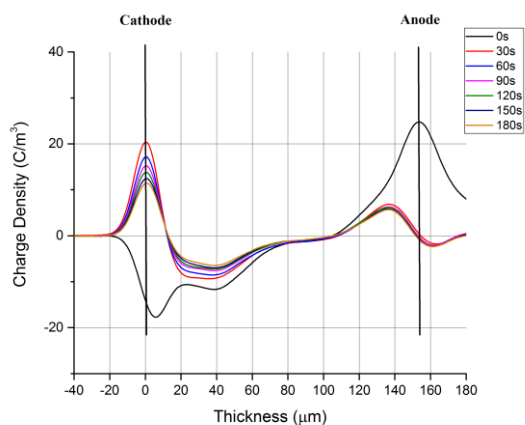
(d)

Figure D-2 Space charge decay in EPS samples at  $40 \text{ kV} \cdot \text{mm}^{-1}$ : (a) 0.5 wt%; (b) 1 wt%; (c) 3 wt%; (d) 5 wt%, dry.

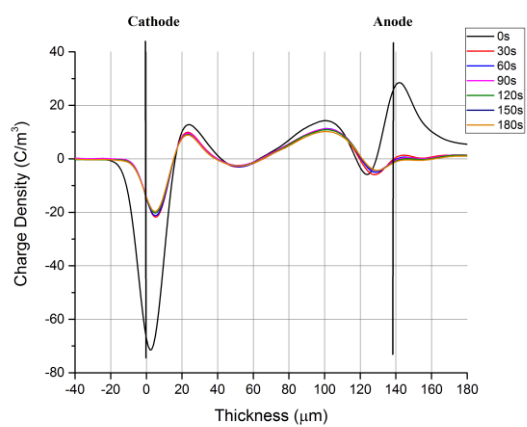
## Appendix D Space Charge Decay in Epoxy and its Nanocomposites



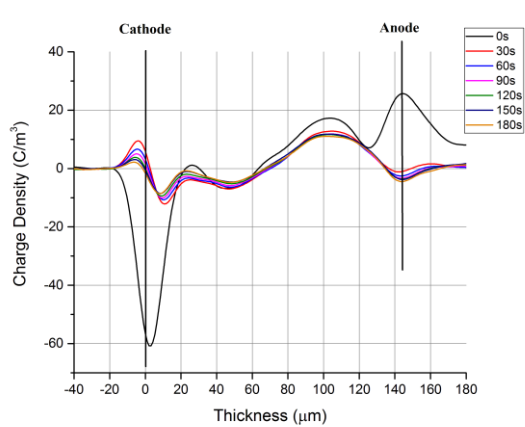
(a)



(b)

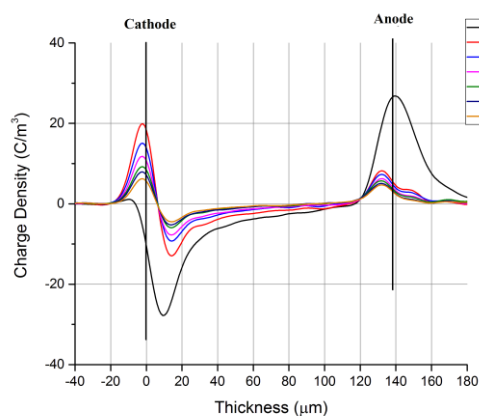


(c)

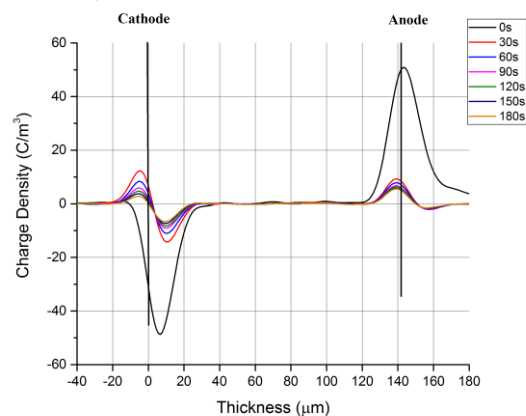


(d)

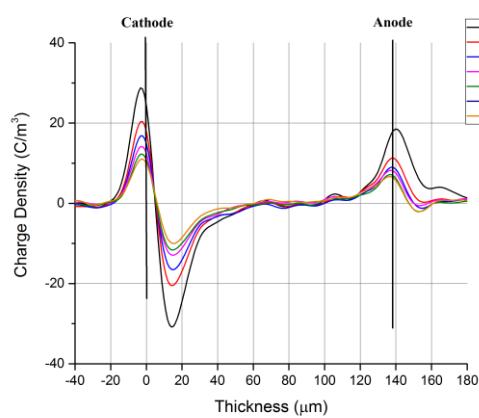
Figure D-3 Space charge decay in EPST samples at  $40 \text{ kV} \cdot \text{mm}^{-1}$ : (a) 0.5 wt%; (b) 1 wt%; (c) 3 wt%; (d) 5 wt%, dry.



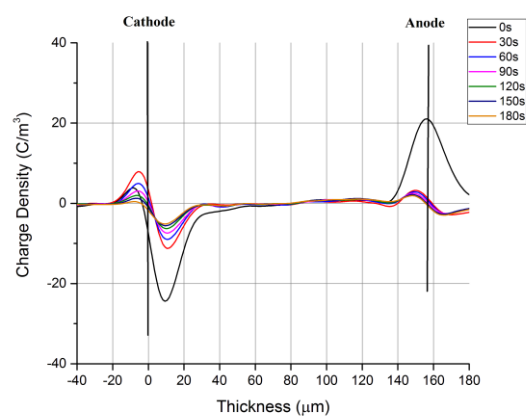
(a)



(b)



(c)



(d)

Figure D-4 Space charge decay in EPB samples at 40 kV·mm<sup>-1</sup>: (a) 0.5 wt%; (b) 1 wt%; (c) 3 wt%; (d) 5 wt%, dry.

## Appendix D Space Charge Decay in Epoxy and its Nanocomposites

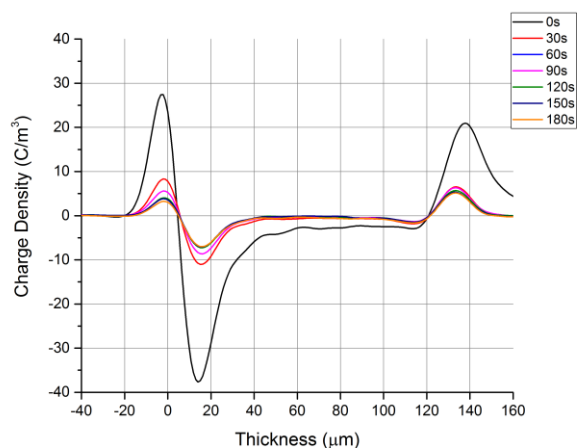
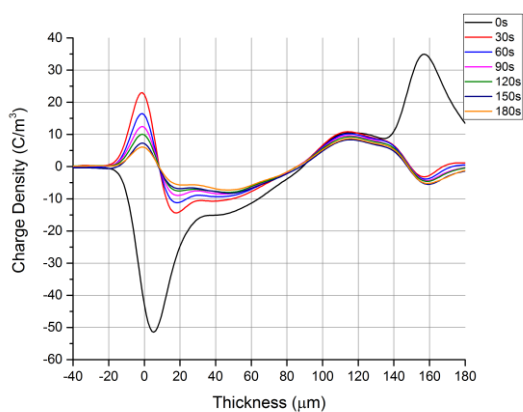
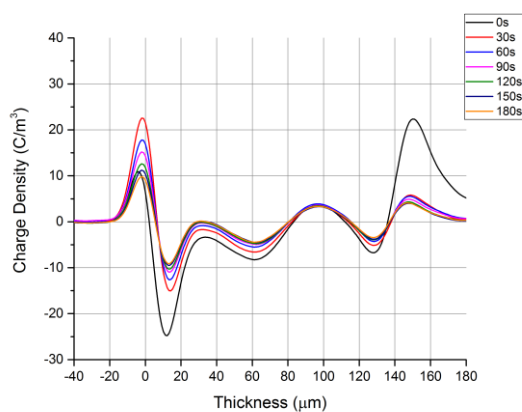


Figure D-5 Space charge decay in pure epoxy samples at  $40 \text{ kV}\cdot\text{mm}^{-1}$ , A.RH.

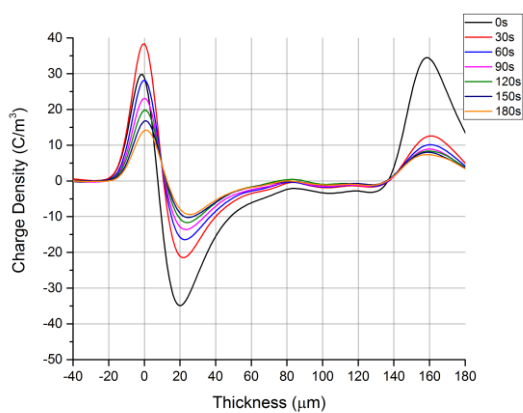


(a)

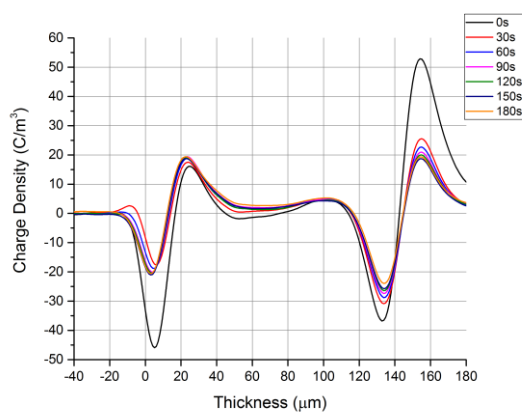


(b)

Figure D-6 Space charge decay in EPS samples at  $40 \text{ kV}\cdot\text{mm}^{-1}$ : (a) 1 wt%; (b) 3 wt%, A.RH.



(a)

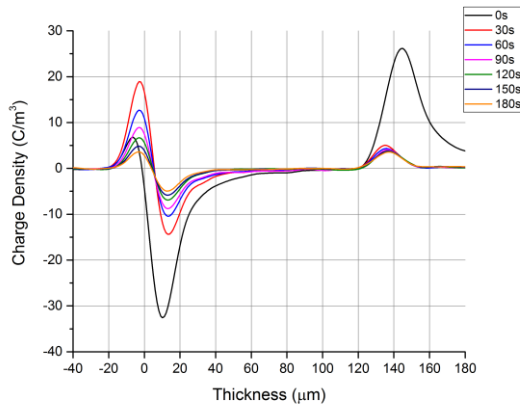


(b)

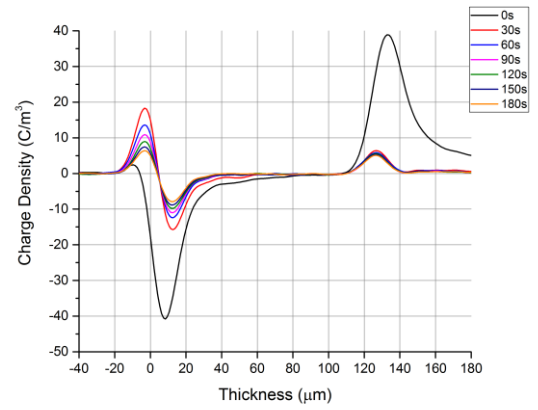
Figure D-7 Space charge decay in EPST samples at  $40 \text{ kV}\cdot\text{mm}^{-1}$ : (a) 1 wt%; (b) 3 wt%, A.RH.



## Appendix D Space Charge Decay in Epoxy and its Nanocomposites



(a)



(b)

Figure D-8 Space charge decay in EPB samples at  $40 \text{ kV}\cdot\text{mm}^{-1}$ : (a) 1 wt%; (b) 3 wt%, A.R.H.

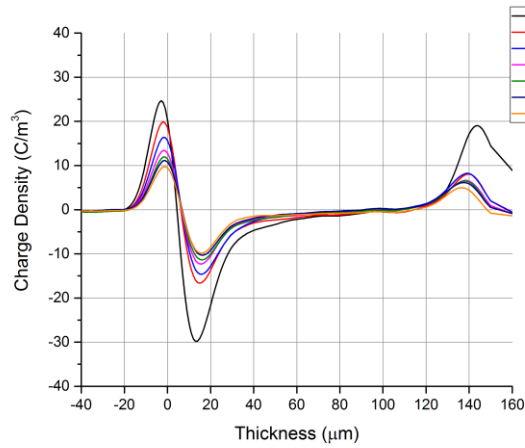
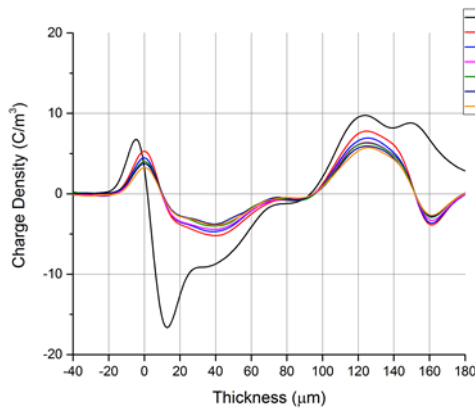
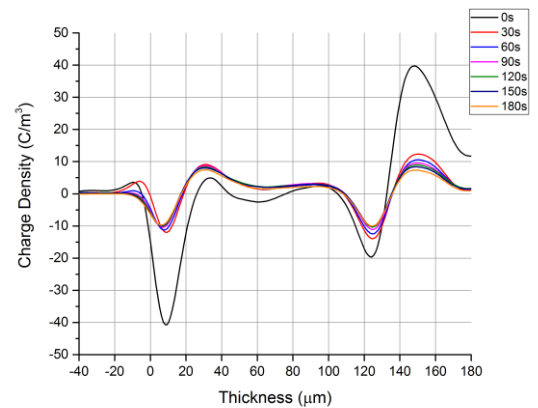


Figure D-9 Space charge decay in pure epoxy samples at  $40 \text{ kV}\cdot\text{mm}^{-1}$ , 60RH.



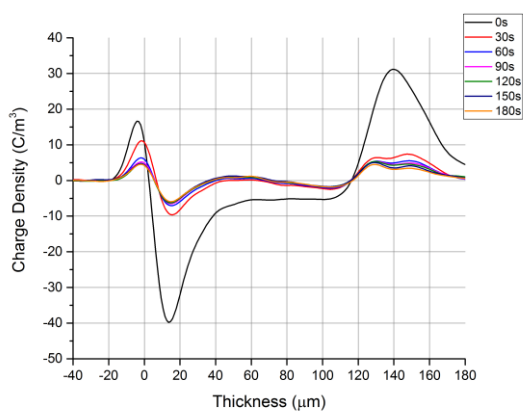
(a)



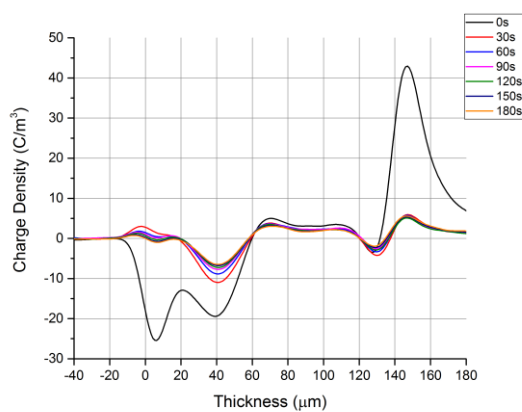
(b)

Figure D-10 Space charge decay in EPS samples at  $40 \text{ kV}\cdot\text{mm}^{-1}$ : (a) 1 wt%; (b) 3 wt%, 60RH.

## Appendix D Space Charge Decay in Epoxy and its Nanocomposites

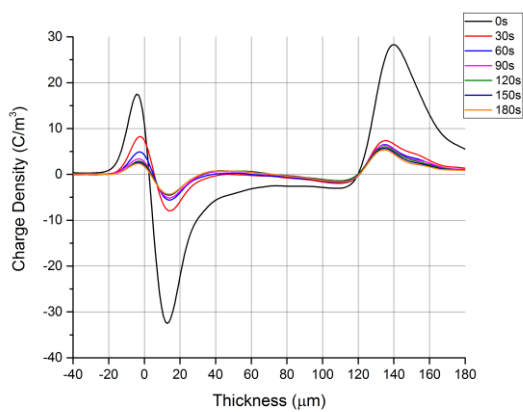


(a)

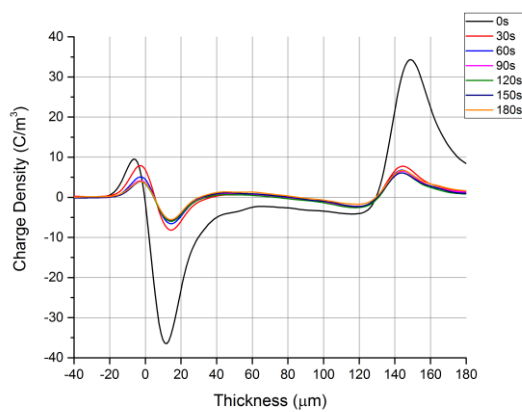


(b)

Figure D-11 Space charge decay in EPST samples at  $40 \text{ kV}\cdot\text{mm}^{-1}$ : (a) 1 wt%; (b) 3 wt%, 60RH.



(a)



(b)

Figure D-12 Space charge decay in EPB samples at  $40 \text{ kV}\cdot\text{mm}^{-1}$ : (a) 1 wt%; (b) 3 wt%, 60RH.

## Bibliography

- [1] J. L. Hedrick, I. Yilgör, G. L. Wilkes, and J. E. McGrath, "Chemical modification of matrix Resin networks with engineering thermoplastics," *Polymer Bulletin*, vol. 13, no. 3, pp. 201-208, 1985/03/01 1985.
- [2] C. Gao, "Effects of nanometer material and their application," *Journal of Jiangsu University of Science and Technology*, vol. 22, no. 06, pp. 63-70, 2001.
- [3] T. Andritsch, "Epoxy Based Nanodielectrics for High Voltage DC-Applications: Synthesis, Dielectric Properties and Space Charge Dynamics," Delft University of Technology, 2010.
- [4] Q. Wang, "The effect of nano size fillers on electrical performance of epoxy resin," University of Southampton, 2012.
- [5] S. K. Kumar, B. C. Benicewicz, R. A. Vaia, and K. I. Winey, "50th Anniversary Perspective: Are Polymer Nanocomposites Practical for Applications?," *Macromolecules*, vol. 50, no. 3, pp. 714-731, 2017/02/14 2017.
- [6] S. Rawal, J. Brantley, and N. Karabudak, "Development of carbon nanotube-based composite for spacecraft components," in *Recent Advances in Space Technologies (RAST), 2013 6th International Conference on*, 2013, pp. 13-19: IEEE.
- [7] G. Chen, S. Li, and L. Zhong, "Space charge in nanodielectrics and its impact on electrical performance," in *Properties and Applications of Dielectric Materials (ICPADM), 2015 IEEE 11th International Conference on the*, 2015, pp. 36-39: IEEE.
- [8] C. Cheng, "Nanostructured material's special effects and its applications," *Journal of Anhui Institute of Architecture*, vol. 4, p. 018, 2005.
- [9] T. Lewis, "Interfaces are the dominant feature of dielectrics at the nanometric level," *IEEE Transactions on Dielectrics and Electrical Insulation*, vol. 11, no. 5, pp. 739-753, 2004.
- [10] K. Y. Lau, "Structure and electrical properties of silica-based polyethylene nanocomposites," University of Southampton, 2013.
- [11] H. Gu *et al.*, "An overview of multifunctional epoxy nanocomposites," *Journal of Materials Chemistry C*, vol. 4, no. 25, pp. 5890-5906, 2016.
- [12] T. Andritsch, R. Kochetov, P. H. Morshuis, and J. J. Smit, "Dielectric properties and space charge behavior of MgO-epoxy nanocomposites," in *Solid Dielectrics (ICSD), 2010 10th IEEE International Conference on*, 2010, pp. 1-4: IEEE.
- [13] J. C. Fothergill, J. K. Nelson, and M. Fu, "Dielectric properties of epoxy nanocomposites containing TiO<sub>2</sub>, Al<sub>2</sub>O<sub>3</sub> and ZnO fillers," in *Electrical Insulation and Dielectric Phenomena, 2004. CEIDP'04. 2004 Annual Report Conference on*, 2004, pp. 406-409: IEEE.

## Bibliography

- [14] L. Zhang, H. Zhang, G. Wang, C. Mo, and Y. Zhang, "Dielectric behaviour of nano - TiO<sub>2</sub> bulks," *physica status solidi (a)*, vol. 157, no. 2, pp. 483-491, 1996.
- [15] L. Hui, L. S. Schadler, and J. K. Nelson, "The influence of moisture on the electrical properties of crosslinked polyethylene/silica nanocomposites," *IEEE Transactions on Dielectrics and Electrical Insulation*, vol. 20, no. 2, pp. 641-653, 2013.
- [16] G. Xiao and M. Shanahan, "Water absorption and desorption in an epoxy resin with degradation," *Journal of Polymer Science Part B: Polymer Physics*, vol. 35, no. 16, pp. 2659-2670, 1997.
- [17] K. Lau, A. Vaughan, G. Chen, I. Hosier, and A. Holt, "On the dielectric response of silica-based polyethylene nanocomposites," *Journal of Physics D: Applied Physics*, vol. 46, no. 9, p. 095303, 2013.
- [18] M. Praeger, I. Hosier, A. Vaughan, and S. Swingler, "Calcined silica for enhanced polyethylene nano composites," *Applied Physics Letters*, pp. 1-4, 2015.
- [19] I. L. Hosier, M. Praeger, A. S. Vaughan, and S. G. Swingler, "The Effects of Water on the Dielectric Properties of Silicon-Based Nanocomposites," *IEEE Transactions on Nanotechnology*, vol. 16, no. 2, pp. 169-179, 2017.
- [20] Q. Wang, P. Curtis, and G. Chen, "Effect of nano-fillers on electrical breakdown behavior of epoxy resin," in *Electrical Insulation and Dielectric Phenomena (CEIDP), 2010 Annual Report Conference on*, 2010, pp. 1-4: IEEE.
- [21] G. Tesoro, "Epoxy resins - chemistry and technology, Clayton A. May, Ed., Marcel Dekker, New York, 1988, 1,288 pp. Price: \$195.00," *Journal of Polymer Science Part C: Polymer Letters*, vol. 26, no. 12, pp. 539-539, 1988.
- [22] N. Tagami *et al.*, "Effects of curing and filler dispersion methods on dielectric properties of epoxy nanocomposites," in *2007 Annual Report - Conference on Electrical Insulation and Dielectric Phenomena*, 2007, pp. 232-235.
- [23] A. Jaya, H. Berahim, T. Tumiran, and R. Rochmadi, "The Performance of High Voltage Insulator Based on Epoxy-Polysiloxane and Rice Husk Ash Compound in Tropical Climate Area," *Electrical and Electronic Engineering*, vol. 2, no. 4, pp. 208-216, 2012.
- [24] M. Beneš, "Kinetics of curing of epoxy resins.," 2006.
- [25] T. Blecha and J. Pihera, "Epoxy resin curing process evaluation based on signal frequency analysis from interdigital structure sensor," in *Electronic System-Integration Technology Conference (ESTC), 2010 3rd*, 2010, pp. 1-4: IEEE.
- [26] C. Y. Shigue, R. G. dos Santos, C. A. Baldan, and E. Ruppert-Filho, "Monitoring the epoxy curing by the dielectric thermal analysis method," *IEEE transactions on applied superconductivity*, vol. 14, no. 2, pp. 1173-1176, 2004.

- [27] S. Sourour and M. Kamal, "Differential scanning calorimetry of epoxy cure: isothermal cure kinetics," *Thermochimica Acta*, vol. 14, no. 1-2, pp. 41-59, 1976.
- [28] S. Tatsumiya, K. Yokokawa, and K. Miki, "A dynamic DSC study of the curing process of epoxy resin," *Journal of Thermal Analysis and Calorimetry*, vol. 49, no. 1, pp. 123-129, 1997.
- [29] J. Pihera and A. Hamáček, "Monitoring of epoxy curing-using impedance sensors," *Research report*, 2009.
- [30] R. Roy, S. Komarneni, and D. Roy, "Multi-phasic ceramic composites made by sol-gel technique," *MRS Online Proceedings Library Archive*, vol. 32, 1984.
- [31] P. M. Ajayan, L. S. Schadler, and P. V. Braun, *Nanocomposite science and technology*. John Wiley & Sons, 2006.
- [32] C. Granqvist and R. Buhrman, "Ultrafine metal particles," *Journal of applied Physics*, vol. 47, no. 5, pp. 2200-2219, 1976.
- [33] C.-S. Wang and M.-C. Lee, "Multifunctional naphthalene containing epoxy resins and their modification by hydrosilation for electronic application," *Polymer Bulletin*, vol. 40, no. 6, pp. 623-630, 1998.
- [34] S. Singha and M. J. Thomas, "Dielectric properties of epoxy nanocomposites," *IEEE Transactions on Dielectrics and Electrical Insulation*, vol. 15, no. 1, 2008.
- [35] T. Tanaka, "Dielectric nanocomposites with insulating properties," *IEEE Transactions on Dielectrics and Electrical Insulation*, vol. 12, no. 5, pp. 914-928, 2005.
- [36] K. J. Klabunde and R. Richards, *Nanoscale materials in chemistry*. Wiley Online Library, 2001.
- [37] N. Hayakawa, H. Maeda, S. Chigusa, and H. Okubo, "Partial discharge inception characteristics of LN 2/epoxy composite insulation system under thermal bubble condition," *Cryogenics*, vol. 40, no. 3, pp. 167-171, 2000.
- [38] S. Kang, S. I. Hong, C. R. Choe, M. Park, S. Rim, and J. Kim, "Preparation and characterization of epoxy composites filled with functionalized nanosilica particles obtained via sol-gel process," *Polymer*, vol. 42, no. 3, pp. 879-887, 2001.
- [39] P. L. Teh *et al.*, "The properties of epoxy resin coated silica fillers composites," *Materials Letters*, vol. 61, no. 11, pp. 2156-2158, 2007.
- [40] T. Lewis, "Interfaces and nanodielectrics are synonymous," in *Solid Dielectrics, 2004. ICSD 2004. Proceedings of the 2004 IEEE International Conference on*, 2004, vol. 2, pp. 792-795: IEEE.
- [41] J. Nelson and Y. Hu, "Nanocomposite dielectrics—properties and implications," *Journal of Physics D: Applied Physics*, vol. 38, no. 2, p. 213, 2005.
- [42] M. Okazaki, M. Murota, Y. Kawaguchi, and N. Tsubokawa, "Curing of epoxy resin by ultrafine silica modified by grafting of hyperbranched

## Bibliography

- polyamidoamine using dendrimer synthesis methodology," *Journal of applied polymer science*, vol. 80, no. 4, pp. 573-579, 2001.
- [43] M. F. Shafee and M. Jaafar, "Effect of Boron Nitride Nano Filler Filled Epoxy Composites for Underfill Application," *Journal of Engineering Science*, vol. 9, pp. 89-98, 2013.
  - [44] F. Guastavino *et al.*, "Electrical characterization of polymer-layered silicate nanocomposites," in *Electrical Insulation and Dielectric Phenomena, 2005. CEIDP'05. 2005 Annual Report Conference on*, 2005, pp. 175-178: IEEE.
  - [45] G. C. Montanari, D. Fabiani, F. Palmieri, D. Kaempfer, R. Thomann, and R. Mulhaupt, "Modification of electrical properties and performance of EVA and PP insulation through nanostructure by organophilic silicates," *IEEE Transactions on Dielectrics and Electrical Insulation*, vol. 11, no. 5, pp. 754-762, 2004.
  - [46] T. Imai, F. Sawa, T. Ozaki, Y. Inoue, T. Shimizu, and T. Tanaka, "Comparison of insulation breakdown properties of epoxy nanocomposites under homogeneous and divergent electric fields," in *Electrical Insulation and Dielectric Phenomena, 2006 IEEE Conference on*, 2006, pp. 306-309: IEEE.
  - [47] Q. Wang and G. Chen, "Effect of pre-treatment of nanofillers on the dielectric properties of epoxy nanocomposites," *IEEE Transactions on Dielectrics and Electrical Insulation*, vol. 21, no. 4, pp. 1809-1816, 2014.
  - [48] C. Zou, J. C. Fothergill, and S. W. Rowe, "The effect of water absorption on the dielectric properties of epoxy nanocomposites," *IEEE Transactions on Dielectrics and Electrical Insulation*, vol. 15, no. 1, 2008.
  - [49] D. Kim, J. S. Lee, C. M. Barry, and J. L. Mead, "Microscopic measurement of the degree of mixing for nanoparticles in polymer nanocomposites by TEM images," *Microscopy research and technique*, vol. 70, no. 6, pp. 539-546, 2007.
  - [50] W. Zhou, J. Zuo, X. Zhang, and A. Zhou, "Thermal, electrical, and mechanical properties of hexagonal boron nitride-reinforced epoxy composites," *Journal of Composite Materials*, vol. 48, no. 20, pp. 2517-2526, 2014.
  - [51] H. Domminghaus, "The plastics and their properties," *VDI Verlag*, 1992.
  - [52] S. Nilsson, T. Hjertberg, and A. Smedberg, "The Effect of Crosslinking on the Electrical Properties of LDPE," in *21st Nordic Insulation Symposium, June 15-17, 2009 Gothenburg, Sweden*, 2009.
  - [53] E. Urbaczewski - Espuche, J. Galy, J. F. Gerard, J. P. Pascault, and H. Sautereau, "Influence of chain flexibility and crosslink density on mechanical properties of epoxy/amine networks," *Polymer engineering & science*, vol. 31, no. 22, pp. 1572-1580, 1991.
  - [54] G. Tsagaropoulos and A. Eisenberg, "Dynamic mechanical study of the factors affecting the two glass transition behavior of filled polymers. Similarities and differences with random ionomers," *Macromolecules*, vol. 28, no. 18, pp. 6067-6077, 1995.
  - [55] F. W. Starr, T. B. Schröder, and S. C. Glotzer, "Effects of a nanoscopic filler on the structure and dynamics of a simulated polymer melt and the

- relationship to ultrathin films," *Physical Review E*, vol. 64, no. 2, p. 021802, 2001.
- [56] T. Tanaka, M. Kozako, N. Fuse, and Y. Ohki, "Proposal of a multi-core model for polymer nanocomposite dielectrics," *IEEE Transactions on Dielectrics and Electrical Insulation*, vol. 12, no. 4, pp. 669-681, 2005.
  - [57] S. Raetzke and J. Kindersberger, "Role of interphase on the resistance to high-voltage arcing, on tracking and erosion of silicone/SiO<sub>2</sub> nanocomposites," *IEEE Transactions on Dielectrics and Electrical Insulation*, vol. 17, no. 2, 2010.
  - [58] S. Rätzke, *Zur Wirkungsweise von nanoskaligen Füllstoffpartikeln in polymeren Isolierwerkstoffen der Hochspannungstechnik*. VDI-Verlag, 2009.
  - [59] M. G. Todd and F. G. Shi, "Complex permittivity of composite systems: A comprehensive interphase approach," *IEEE Transactions on Dielectrics and Electrical Insulation*, vol. 12, no. 3, pp. 601-611, 2005.
  - [60] M. G. Todd and F. G. Shi, "Validation of a novel dielectric constant simulation model and the determination of its physical parameters," *Microelectronics journal*, vol. 33, no. 8, pp. 627-632, 2002.
  - [61] M. G. Todd and F. G. Shi, "Characterizing the interphase dielectric constant of polymer composite materials: effect of chemical coupling agents," *Journal of applied physics*, vol. 94, no. 7, pp. 4551-4557, 2003.
  - [62] M. G. Todd and F. G. Shi, "Molecular basis of the interphase dielectric properties of microelectronic and optoelectronic packaging materials," *IEEE Transactions on Components and Packaging Technologies*, vol. 26, no. 3, pp. 667-672, 2003.
  - [63] G. Pike and C. Seager, "Percolation and conductivity: A computer study. I," *Physical review B*, vol. 10, no. 4, p. 1421, 1974.
  - [64] C.-H. Kuo and P. K. Gupta, "Rigidity and conductivity percolation thresholds in particulate composites," *Acta metallurgica et materialia*, vol. 43, no. 1, pp. 397-403, 1995.
  - [65] S. Wang and A. Ogale, "Continuum space simulation and experimental characterization of electrical percolation behavior of particulate composites," *Composites science and technology*, vol. 46, no. 2, pp. 93-103, 1993.
  - [66] Y.-B. Yi and A. Sastry, "Analytical approximation of the two-dimensional percolation threshold for fields of overlapping ellipses," *Physical Review E*, vol. 66, no. 6, p. 066130, 2002.
  - [67] T. Andritsch, R. Kochetov, Y. Gebrekiros, U. Lafont, P. Morshuis, and J. Smit, "Synthesis and dielectric properties of epoxy based nanocomposites," in *Electrical Insulation and Dielectric Phenomena, 2009. CEIDP'09. IEEE Conference on*, 2009, pp. 523-526: IEEE.
  - [68] T. Andritsch, R. Kochetov, P. Morshuis, and J. Smit, "Proposal of the polymer chain alignment model," in *Electrical Insulation and Dielectric Phenomena (CEIDP), 2011 Annual Report Conference on*, 2011, pp. 624-627: IEEE.

## Bibliography

- [69] J. Clayden, N. Greeves, S. Warren, and P. Wothers, "Organic Chemistry", ed: Oxford University Press, 2001.
- [70] C. Zou, M. Fu, J. C. Fothergill, and S. W. Rowe, "Influence of absorbed water on the dielectric properties and glass-transition temperature of silica-filled epoxy nanocomposites," in *Electrical Insulation and Dielectric Phenomena, 2006 IEEE Conference on*, 2006, pp. 321-324: IEEE.
- [71] S. Rätzke, "About the mechanism of action of nanoscale filler particles in polymeric materials for high voltage insulations," Technische Universität München, 2009.
- [72] M. Kozako, S.-I. Kuge, T. Imai, T. Ozaki, T. Shimizu, and T. Tanaka, "Surface erosion due to partial discharges on several kinds of epoxy nanocomposites," in *Electrical Insulation and Dielectric Phenomena, 2005. CEIDP'05. 2005 Annual Report Conference on*, 2005, pp. 162-165: IEEE.
- [73] M.-I. Baraton, F. Chancel, and L. Merhari, "In situ determination of the grafting sites on nanosized ceramic powders by FT-IR spectrometry," *Nanostructured Materials*, vol. 9, no. 1, pp. 319-322, 1997.
- [74] J. C. Fothergill, "Ageing, space charge and nanodielectrics: ten things we don't know about dielectrics," in *Solid Dielectrics, 2007. ICSD'07. IEEE International Conference on*, 2007, pp. 1-10: IEEE.
- [75] Huntsman, "Technical Bulletin JEFFAMINE® D-230 Polyetheramine," 2007.
- [76] Sigma-Aldrich, "Product Number: 31185, Safety data Sheet," Revision Date June 2016, Version 5.3.
- [77] Sigma-Aldrich, "Product Number: 637238, Safety data Sheet," Revision Date Oct. 2013. Version 5.1.
- [78] Momentive, "Condensed Product Bulletin-Boron Nitride Powders NX Grades," April 2016. MPM 300-201-00E-GL.
- [79] M. Reading, Z. Xu, A. S. Vaughan, and P. L. Lewin, "The thermal and electrical properties of nano-silicon dioxide filled epoxy systems for use in high voltage insulation," in *Electrical Insulation Conference (EIC), 2011*, 2011, pp. 493-497: IEEE.
- [80] A. Coats and J. Redfern, "Thermogravimetric analysis. A review," *Analyst*, vol. 88, no. 1053, pp. 906-924, 1963.
- [81] J. Tarrío-Saavedra, J. López-Beceiro, S. Naya, and R. Artiaga, "Effect of silica content on thermal stability of fumed silica/epoxy composites," *Polymer Degradation and Stability*, vol. 93, no. 12, pp. 2133-2137, 2008.
- [82] Y.-L. Liu, W.-L. Wei, K.-Y. Hsu, and W.-H. Ho, "Thermal stability of epoxy-silica hybrid materials by thermogravimetric analysis," *Thermochimica Acta*, vol. 412, no. 1, pp. 139-147, 2004.
- [83] S.-J. Park, H.-C. Kim, H.-I. Lee, and D.-H. Suh, "Thermal stability of imidized epoxy blends initiated by N-benzylpyrazinium hexafluoroantimonate salt," *Macromolecules*, vol. 34, no. 22, pp. 7573-7575, 2001.
- [84] W. J. Sichina, "National Marketing Manager, Characterization of Epoxy Resins Using DSC," in "thermal analysis," PerkinElmer, Inc., Printed in U.S.A.2000.



- [85] J. M. a. C. Mortimer, "Differential scanning calorimetry,," Norwalk: Perkin-Elmer Corporation.
- [86] C. G. a. P. Norman, "The use of Differential Scanning Calorimetry(DSC) in the prediction of metal composition and polymer characterization," 1996.
- [87] E. T. Inc, "Tg - Glass Transition Temperature for Epoxies," 2012.
- [88] M. Reading, "An investigation into the structure and properties of polyethylene oxide nanocomposites," University of Southampton, 2010.
- [89] G. Gherbaz, "Nanostructured polymers: morphology and properties," University of Southampton, 2009.
- [90] A. Volkov and A. Prokhorov, "Broadband dielectric spectroscopy of solids," *Radiophysics and quantum electronics*, vol. 46, no. 8, pp. 657-665, 2003.
- [91] M. Kadhim, A. Abdullah, I. Al-Ajaj, and A. Khalil, "Dielectric properties of epoxy/Al<sub>2</sub>O<sub>3</sub> nanocomposites," *Int. J. Appl. Innov. Eng. Manag*, vol. 3, pp. 468-477, 2014.
- [92] Y. Li, M. Yasuda, and T. Takada, "Pulsed electroacoustic method for measurement of charge accumulation in solid dielectrics," *IEEE Transactions on Dielectrics and Electrical Insulation*, vol. 1, no. 2, pp. 188-195, 1994.
- [93] G. Chen, Z. Xu, and L. Zhang, "Measurement of the surface potential decay of corona-charged polymer films using the pulsed electroacoustic method," *Measurement Science and Technology*, vol. 18, no. 5, p. 1453, 2007.
- [94] L.-R. Bao, A. F. Yee, and C. Y.-C. Lee, "Moisture absorption and hygrothermal aging in a bismaleimide resin," *polymer*, vol. 42, no. 17, pp. 7327-7333, 2001.
- [95] P. Bonniau and A. Bunsell, "A comparative study of water absorption theories applied to glass epoxy composites," *Journal of Composite Materials*, vol. 15, no. 3, pp. 272-293, 1981.
- [96] P. Gonon, T. P. Hong, O. Lesaint, S. Bourdelais, and H. Debruyne, "Influence of high levels of water absorption on the resistivity and dielectric permittivity of epoxy composites," *Polymer testing*, vol. 24, no. 6, pp. 799-804, 2005.
- [97] L. Li *et al.*, "Water transportation in epoxy resin," *Chemistry of materials*, vol. 17, no. 4, pp. 839-845, 2005.
- [98] M. Saha *et al.*, "Effect of non-ionic surfactant assisted modification of hexagonal boron nitride nanoplatelets on the mechanical and thermal properties of epoxy nanocomposites," *Composite Interfaces*, vol. 22, no. 7, pp. 611-627, 2015.
- [99] L. Hui, R. C. Smith, X. Wang, J. K. Nelson, and L. S. Schadler, "Quantification of Particulate Mixing in Nanocomposites," in *2008 Annual Report Conference on Electrical Insulation and Dielectric Phenomena*, 2008, pp. 317-320.
- [100] Y. Zhou, J. Hu, X. Chen, F. Yu, and J. He, "Thermoplastic polypropylene/aluminum nitride nanocomposites with enhanced thermal

## Bibliography

- conductivity and low dielectric loss," *IEEE Transactions on Dielectrics and Electrical Insulation*, vol. 23, no. 5, pp. 2768-2776, 2016.
- [101] J. W. Leggoe, "Nth-nearest neighbor statistics for analysis of particle distribution data derived from micrographs," *Scripta materialia*, vol. 53, no. 11, pp. 1263-1268, 2005.
- [102] P. J. Diggle, "Statistical analysis of spatial point processes," *Academic, London*, 1983.
- [103] J. Seiler and J. Kindersberger, "Insight into the interphase in polymer nanocomposites," *IEEE Transactions on Dielectrics and Electrical Insulation*, vol. 21, no. 2, pp. 537-547, 2014.
- [104] A. P. Kumar, D. Depan, N. S. Tomer, and R. P. Singh, "Nanoscale particles for polymer degradation and stabilization—trends and future perspectives," *Progress in polymer science*, vol. 34, no. 6, pp. 479-515, 2009.
- [105] T. Lewis, "Polyethylene under electrical stress," *IEEE Transactions on Dielectrics and Electrical Insulation*, vol. 9, no. 5, pp. 717-729, 2002.
- [106] A. Gu and G. Liang, "Thermal degradation behaviour and kinetic analysis of epoxy/montmorillonite nanocomposites," *Polymer Degradation and Stability*, vol. 80, no. 2, pp. 383-391, 2003.
- [107] P. C. Ma, J.-K. Kim, and B. Z. Tang, "Effects of silane functionalization on the properties of carbon nanotube/epoxy nanocomposites," *Composites Science and Technology*, vol. 67, no. 14, pp. 2965-2972, 2007.
- [108] R. Mueller, H. K. Kammler, K. Wegner, and S. E. Pratsinis, "OH Surface Density of SiO<sub>2</sub> and TiO<sub>2</sub> by Thermogravimetric Analysis," *Langmuir*, vol. 19, no. 1, pp. 160-165, 2003/01/01 2003.
- [109] G. Thiele, M. Poston, and R. Brown, "A case study in sizing nanoparticles," *Micromeritics Analytical Services*, vol. 1, 2010.
- [110] J. Macan, I. Brnardić, S. Orlić, H. Ivanković, and M. Ivanković, "Thermal degradation of epoxy-silica organic-inorganic hybrid materials," *Polymer Degradation and Stability*, vol. 91, no. 1, pp. 122-127, 2006.
- [111] Y.-L. Liu, C.-Y. Hsu, W.-L. Wei, and R.-J. Jeng, "Preparation and thermal properties of epoxy-silica nanocomposites from nanoscale colloidal silica," *Polymer*, vol. 44, no. 18, pp. 5159-5167, 2003.
- [112] M. Preghenella, A. Pegoretti, and C. Migliaresi, "Thermo-mechanical characterization of fumed silica-epoxy nanocomposites," *Polymer*, vol. 46, no. 26, pp. 12065-12072, 2005.
- [113] Z. Jin-Cheng *et al.*, "High thermal conductivity of hexagonal boron nitride laminates," *2D Materials*, vol. 3, no. 1, p. 011004, 2016.
- [114] M. Lines. (2001). *Silica - Silicon Dioxide (SiO<sub>2</sub>)*. Available: <https://www.azom.com/article.aspx?ArticleID=1114>
- [115] M. Modesti, A. Lorenzetti, D. Bon, and S. Besco, "Thermal behaviour of compatibilised polypropylene nanocomposite: Effect of processing conditions," *Polymer Degradation and Stability*, vol. 91, no. 4, pp. 672-680, 2006.

- [116] T. G. Fox and P. J. Flory, "Second - Order Transition Temperatures and Related Properties of Polystyrene. I. Influence of Molecular Weight," *Journal of Applied Physics*, vol. 21, no. 6, pp. 581-591, 1950/06/01 1950.
- [117] H. Markovitz, "Thomas G. Fox 1921-1977," *Rheologica Acta*, journal article vol. 17, no. 3, pp. 207-209, May 01 1978.
- [118] Y. Sun, Z. Zhang, K.-S. Moon, and C. P. Wong, "Glass transition and relaxation behavior of epoxy nanocomposites," *Journal of Polymer Science Part B: Polymer Physics*, vol. 42, no. 21, pp. 3849-3858, 2004.
- [119] C. E. Corcione and M. Frigione, "Characterization of nanocomposites by thermal analysis," *Materials*, vol. 5, no. 12, pp. 2960-2980, 2012.
- [120] T. J. Lewis, "Interfaces and nanodielectrics are synonymous," in *Proceedings of the 2004 IEEE International Conference on Solid Dielectrics, 2004. ICSD 2004.*, 2004, vol. 2, pp. 792-795 Vol.2.
- [121] B. J. Ash, L. S. Schadler, and R. W. Siegel, "Glass transition behavior of alumina/polymethylmethacrylate nanocomposites," *Materials Letters*, vol. 55, no. 1, pp. 83-87, 2002/07/01/ 2002.
- [122] A. M. Mayes, "Softer at the boundary," *Nature Materials*, vol. 4, p. 651, 09/01/online 2005.
- [123] J. K. Nelson and Y. Hu, "The impact of nanocomposite formulations on electrical voltage endurance," in *Proceedings of the 2004 IEEE International Conference on Solid Dielectrics, 2004. ICSD 2004.*, 2004, vol. 2, pp. 832-835 Vol.2.
- [124] Z. Lin, Y. Liu, K.-s. Moon, and C.-P. Wong, "Enhanced thermal transport of hexagonal boron nitride filled polymer composite by magnetic field-assisted alignment," in *Electronic Components and Technology Conference (ECTC), 2013 IEEE 63rd*, 2013, pp. 1692-1696: IEEE.
- [125] Z. Lin, Y. Liu, S. Raghavan, K.-s. Moon, S. K. Sitaraman, and C.-p. Wong, "Magnetic alignment of hexagonal boron nitride platelets in polymer matrix: toward high performance anisotropic polymer composites for electronic encapsulation," *ACS applied materials & interfaces*, vol. 5, no. 15, pp. 7633-7640, 2013.
- [126] H. Shen, C. Cai, J. Guo, Z. Qian, N. Zhao, and J. Xu, "Fabrication of oriented hBN scaffolds for thermal interface materials," *RSC Advances*, vol. 6, no. 20, pp. 16489-16494, 2016.
- [127] C. Esposito Corcione, G. Mensitieri, and A. Maffezzoli, "Analysis of the structure and mass transport properties of nanocomposite polyurethane," *Polymer Engineering & Science*, vol. 49, no. 9, pp. 1708-1718, 2009.
- [128] A. v. Hippel, "Der Mechanismus des „elektrischen “Durchschlages in festen Isolatoren. I," *Zeitschrift für Physik A Hadrons and Nuclei*, vol. 67, no. 11, pp. 707-724, 1931.
- [129] A. Von Hippel, "Electric breakdown of solid and liquid insulators," *Journal of Applied Physics*, vol. 8, no. 12, pp. 815-832, 1937.
- [130] A. v. Hippel, "Elektrische Festigkeit und Kristallbau," *Zeitschrift für Physik A Hadrons and Nuclei*, vol. 75, no. 3, pp. 145-170, 1932.

## Bibliography

- [131] E. Forster, "Research in the dynamics of electrical breakdown in liquid dielectrics," *IEEE Transactions on Electrical Insulation*, no. 3, pp. 182-185, 1980.
- [132] A. Sharbaugh, J. Devins, and S. Rza, "Review of past work on liquid breakdown," *IEEE Transactions on Electrical Insulation*, no. 3, pp. 167-170, 1980.
- [133] M. Nagao, T. Kimura, Y. Mizuno, M. Kosaki, and M. Ieda, "Detection of joule heating before dielectric breakdown in polyethylene films," *IEEE transactions on electrical insulation*, vol. 25, no. 4, pp. 715-722, 1990.
- [134] M. Hikita, S. Tajima, I. Kanno, G. Sawa, and M. Ieda, "New approach to breakdown study by measuring pre-breakdown current in insulating materials," *Japanese Journal of Applied Physics*, vol. 23, no. 12A, p. L886, 1984.
- [135] P. Salovaara and K. Kannus, "Increasing the dielectric breakdown strength of polypropylene using polyaniline additive," in *IASTED Conf. on Energy and Power Systems*, 2006, pp. 234-239.
- [136] R. Buehl and A. Von Hippel, "The electrical breakdown strength of ionic crystals as a function of temperature," *Physical Review*, vol. 56, no. 9, p. 941, 1939.
- [137] W. Weibull, "Wide applicability," *Journal of applied mechanics*, vol. 103, no. 730, pp. 293-297, 1951.
- [138] H. Pham and C.-D. Lai, "On recent generalizations of the Weibull distribution," *IEEE transactions on reliability*, vol. 56, no. 3, pp. 454-458, 2007.
- [139] R. B. Abernethy, *The New Weibull handbook: reliability and statistical analysis for predicting life, safety, supportability, risk, cost and warranty claims*. Dr. Robert B. Abernethy, 2004.
- [140] Y. Hu, R. C. Smith, J. K. Nelson, and L. S. Schadler, "Some mechanistic understanding of the impulse strength of nanocomposites," in *Electrical Insulation and Dielectric Phenomena, 2006 IEEE Conference on*, 2006, pp. 31-34: IEEE.
- [141] T. Tanaka, "Interpretation of several key phenomena peculiar to nano dielectrics in terms of a multi-core model," in *Electrical Insulation and Dielectric Phenomena, 2006 IEEE Conference on*, 2006, pp. 298-301: IEEE.
- [142] M. F. Fréchet *et al.*, "Nanodielectrics: A "universal" panacea for solving all electrical insulation problems?," in *Solid Dielectrics (ICSD), 2010 10th IEEE International Conference on*, 2010, pp. 1-3: IEEE.
- [143] C. Zhou and G. Chen, "Space charge and AC electrical breakdown strength in polyethylene," *IEEE Transactions on Dielectrics and Electrical Insulation*, vol. 24, no. 1, pp. 559-566, 2017.
- [144] X. Huang, Z. Ma, Y. Wang, P. Jiang, Y. Yin, and Z. Li, "Polyethylene/aluminum nanocomposites: Improvement of dielectric strength by nanoparticle surface modification," *Journal of applied polymer science*, vol. 113, no. 6, pp. 3577-3584, 2009.

- [145] M. Roy, J. K. Nelson, R. MacCrone, and L. Schadler, "Candidate mechanisms controlling the electrical characteristics of silica/XLPE nanodielectrics," *Journal of Materials Science*, vol. 42, no. 11, pp. 3789-3799, 2007.
- [146] S. Li, D. Min, W. Wang, and G. Chen, "Linking traps to dielectric breakdown through charge dynamics for polymer nanocomposites," *IEEE Transactions on Dielectrics and Electrical Insulation*, vol. 23, no. 5, pp. 2777-2785, 2016.
- [147] K. Lau, A. Vaughan, G. Chen, I. Hosier, A. Holt, and K. Y. Ching, "On the space charge and DC breakdown behavior of polyethylene/silica nanocomposites," *IEEE Transactions on Dielectrics and Electrical Insulation*, vol. 21, no. 1, pp. 340-351, 2014.
- [148] K. Lau *et al.*, "Modeling of polymer nanocomposites: Permittivity vs. electric field intensity," in *Power and Energy (PECon), 2014 IEEE International Conference on*, 2014, pp. 140-145: IEEE.
- [149] M. Sharip, K. Lau, and D. Zaidel, "Modeling of Nanocomposite Structures to Evaluate the Effect of Nanoplatelet Interphase Region on Electric Field Intensity," *Journal of Telecommunication, Electronic and Computer Engineering (JTEC)*, vol. 8, no. 12, pp. 147-152, 2016.
- [150] W. Kim, J. W. Bae, I. D. Choi, and Y. S. Kim, "Thermally conductive EMC (epoxy molding compound) for microelectronic encapsulation," *Polymer Engineering & Science*, vol. 39, no. 4, pp. 756-766, 1999.
- [151] J. Zeng, R. Fu, Y. Shen, H. He, and X. Song, "High thermal conductive epoxy molding compound with thermal conductive pathway," *Journal of applied polymer science*, vol. 113, no. 4, pp. 2117-2125, 2009.
- [152] Z.-L. Hou, M.-S. Cao, J. Yuan, X.-Y. Fang, and X.-L. Shi, "High-temperature conductance loss dominated defect level in h-BN: Experiments and first principles calculations," ed: AIP, 2009.
- [153] K. Yung and H. Liem, "Enhanced thermal conductivity of boron nitride epoxy - matrix composite through multi - modal particle size mixing," *Journal of Applied Polymer Science*, vol. 106, no. 6, pp. 3587-3591, 2007.
- [154] K. Lau, A. Vaughan, G. Chen, and I. Hosier, "Polyethylene nanodielectrics: The effect of nanosilica and its surface treatment on electrical breakdown strength," in *Electrical Insulation and Dielectric Phenomena (CEIDP), 2012 Annual Report Conference on*, 2012, pp. 21-24: IEEE.
- [155] J.-W. Zha, Z.-M. Dang, H.-T. Song, Y. Yin, and G. Chen, "Dielectric properties and effect of electrical aging on space charge accumulation in polyimide/TiO<sub>2</sub> nanocomposite films," *Journal of Applied Physics*, vol. 108, no. 9, p. 094113, 2010.
- [156] Y. Tanaka, G. Chen, Y. Zhao, A. Davies, A. Vaughan, and T. Takada, "Effect of additives on morphology and space charge accumulation in low density polyethylene," *IEEE Transactions on Dielectrics and Electrical Insulation*, vol. 10, no. 1, pp. 148-154, 2003.
- [157] A. Jonscher, "Dielectric relaxation in solids," ed. Chelsea Dielectric Press: London, 1983.

## Bibliography

- [158] M. F. Frechette, M. L. Trudeau, H. Alamdar, and S. Boily, "Introductory remarks on nanodielectrics," *IEEE Transactions on Dielectrics and Electrical Insulation*, vol. 11, no. 5, pp. 808-818, 2004.
- [159] J. Martinez, M. Boulouz, C. Mayoux, and C. Lacabanne, "Thermally stimulated creep for the study of ageing in insulating polymers under electric field," in *Electrical Insulation, Conference Record of the 1992 IEEE International Symposium on*, 1992, pp. 62-65: IEEE.
- [160] J. C. Maxwell, *A treatise on electricity and magnetism*. Clarendon press, 1881.
- [161] K. Wagner, "The after effect in dielectrics," *Arch. Electrotech*, vol. 2, no. 378, p. e394, 1914.
- [162] R. Sillars, "The properties of a dielectric containing semiconducting particles of various shapes," *Institution of Electrical Engineers-Proceedings of the Wireless Section of the Institution*, vol. 12, no. 35, pp. 139-155, 1937.
- [163] P. Xu and X. Zhang, "Investigation of MWS polarization and dc conductivity in polyamide 610 using dielectric relaxation spectroscopy," *European Polymer Journal*, vol. 47, no. 5, pp. 1031-1038, 2011.
- [164] A. S. a. W. L. F. Kremer, *Broadband Dielectric Spectroscopy*. Springer-Verlag, 2002.
- [165] K. C. Kao, *Dielectric phenomena in solids*. Academic press, 2004.
- [166] J. P. Eloundou, "Dipolar relaxations in an epoxy-amine system," *European Polymer Journal*, vol. 38, no. 3, pp. 431-438, 2002.
- [167] R. Kochetov, T. Andritsch, P. H. F. Morshuis, and J. J. Smit, "Anomalous behaviour of the dielectric spectroscopy response of nanocomposites," *IEEE Transactions on Dielectrics and Electrical Insulation*, vol. 19, no. 1, pp. 107-117, 2012.
- [168] C. Pan, K. Kou, Q. Jia, Y. Zhang, G. Wu, and T. Ji, "Improved thermal conductivity and dielectric properties of hBN/PTFE composites via surface treatment by silane coupling agent," *Composites Part B: Engineering*, vol. 111, pp. 83-90, 2017.
- [169] S. Singha and M. J. Thomas, "Permittivity and tan delta characteristics of epoxy nanocomposites in the frequency range of 1 MHz-1 GHz," *IEEE Transactions on Dielectrics and Electrical Insulation*, vol. 15, no. 1, 2008.
- [170] P. Steeman, J. Baetsen, and F. Maurer, "Temperature dependence of the interfacial dielectric loss process in glass bead - filled polyethylene," *Polymer Engineering & Science*, vol. 32, no. 5, pp. 351-356, 1992.
- [171] P. Steeman, F. Maurer, and M. Van Es, "Dielectric monitoring of water absorption in glass-bead-filled high-density polyethylene," *Polymer*, vol. 32, no. 3, pp. 523-530, 1991.
- [172] L. Paquin, H. St-Onge, and M. Wertheimer, "The Complex Permittivity of Polyethylene/Mica Composites," *IEEE Transactions on Electrical Insulation*, no. 5, pp. 399-404, 1982.

- [173] M. Woo and M. R. Piggott, "Water Absorption of Resins and Composites: III. Water Distribution as Indicated by Capacitance Measurement," *Journal of Composites, Technology and Research*, vol. 10, no. 1, pp. 16-19, 1988.
- [174] P. Steeman and F. Maurer, "An interlayer model for the complex dielectric constant of composites," *Colloid & Polymer Science*, vol. 268, no. 4, pp. 315-325, 1990.
- [175] P. Steeman and F. Maurer, "An interlayer model for the complex dielectric constant of composites: An extension to ellipsoidally shaped particles," *Colloid & Polymer Science*, vol. 270, no. 11, pp. 1069-1079, 1992.
- [176] C. Zou, J. C. Fothergill, and S. W. Rowe, "A "water shell" model for the dielectric properties of hydrated silica-filled epoxy nano-composites," in *Solid Dielectrics, 2007. ICSD'07. IEEE International Conference on*, 2007, pp. 389-392: IEEE.
- [177] J. Hou *et al.*, "Preparation and characterization of surface modified boron nitride epoxy composites with enhanced thermal conductivity," *Rsc Advances*, vol. 4, no. 83, pp. 44282-44290, 2014.
- [178] M. Tanimoto, T. Yamagata, K. Miyata, and S. Ando, "Anisotropic thermal diffusivity of hexagonal boron nitride-filled polyimide films: effects of filler particle size, aggregation, orientation, and polymer chain rigidity," *ACS applied materials & interfaces*, vol. 5, no. 10, pp. 4374-4382, 2013.
- [179] L. A. Dissado and J. C. Fothergill, *Electrical degradation and breakdown in polymers*. IET, 1992.
- [180] C. Kittel, *Introduction to solid state physics*. Wiley, 2005.
- [181] R. Pethig, "Dielectric and electrical properties of biological materials," *Journal of Bioelectricity*, vol. 4, no. 2, pp. vii-ix, 1985.
- [182] E. Merzbacher, "Quantum Mechanics," *Inc., New York*, 1998.
- [183] C. Garton and N. Parkman, "Experimental and theoretical investigation of conduction in polyethylene from 4 MV/m up to 'intrinsic' breakdown," in *Proceedings of the Institution of Electrical Engineers*, 1976, vol. 123, no. 3, pp. 271-276: IET.
- [184] S. Pelissou, H. St-Onge, and M. Wertheimer, "Electrical conduction of polyethylene below and above its melting point," *IEEE transactions on electrical insulation*, vol. 23, no. 3, pp. 325-333, 1988.
- [185] G. Chen, T. Tay, A. Davies, Y. Tanaka, and T. Takada, "Electrodes and charge injection in low-density polyethylene using the pulsed electroacoustic technique," *IEEE Transactions on Dielectrics and Electrical Insulation*, vol. 8, no. 6, pp. 867-873, 2001.
- [186] D. I. Lubyshev, P. P. González - Borrero, E. Marega, E. Petitprez, N. La Scala, and P. Basmaji, "Exciton localization and temperature stability in self - organized InAs quantum dots," *Applied Physics Letters*, vol. 68, no. 2, pp. 205-207, 1996.
- [187] M. Ieda, "Electrical conduction and carrier traps in polymeric materials," *IEEE transactions on electrical insulation*, no. 3, pp. 162-178, 1984.

## Bibliography

- [188] K. Kojima, Y. Takai, and M. Ieda, "Electronic conduction in polyethylene naphthalate at high electric fields," *Journal of applied physics*, vol. 59, no. 8, pp. 2655-2659, 1986.
- [189] T. Lewis, "The micro-physics of charge in dielectrics," *Le Vide*, vol. 53, no. 287, pp. 16-24, 1998.
- [190] T. J. Lewis, "Electrical effects at interfaces and surfaces," *IEEE transactions on electrical insulation*, no. 3, pp. 289-295, 1986.
- [191] J. C. Fothergill and L. A. Dissado, *Space charge in solid dielectrics*. Dielectrics Society, 1998.
- [192] T. Lewis, "Charge transport in polymers," in *Electrical Insulation & Dielectric Phenomena-Annual Report 1976, Conference on*, 1976, pp. 533-561: IEEE.
- [193] T. Mizutani, "Space charge measurement techniques and space charge in polyethylene," *IEEE Transactions on Dielectrics and Electrical Insulation*, vol. 1, no. 5, pp. 923-933, 1994.
- [194] T. Mizutani, H. Semi, and K. Kaneko, "Space charge behavior in low-density polyethylene," *IEEE Transactions on Dielectrics and Electrical Insulation*, vol. 7, no. 4, pp. 503-508, 2000.
- [195] S. Boggs, "A rational consideration of space charge," *IEEE Electrical Insulation Magazine*, vol. 20, no. 4, pp. 22-27, 2004.
- [196] N. Liu, C. Zhou, G. Chen, and L. Zhong, "Determination of threshold electric field for charge injection in polymeric materials," *Applied physics letters*, vol. 106, no. 19, p. 192901, 2015.
- [197] D. Fabiani, G. Montanari, A. Dardano, G. Guastavino, L. Testa, and M. Sangermano, "Space charge dynamics in nanostructured epoxy resin," in *Electrical Insulation and Dielectric Phenomena, 2008. CEIDP 2008. Annual Report Conference on*, 2008, pp. 710-713: IEEE.
- [198] G. Li, G. Chen, and S. Li, "Charge transport model in nanodielectric composites based on quantum tunneling mechanism and dual-level traps," *Applied Physics Letters*, vol. 109, no. 6, p. 062901, 2016.
- [199] T.-c. Zhou, G. Chen, R.-j. Liao, and Z. Xu, "Charge trapping and detrapping in polymeric materials: Trapping parameters," *Journal of Applied Physics*, vol. 110, no. 4, p. 043724, 2011.
- [200] L. Hui, J. Nelson, and L. Schadler, "The influence of moisture on the electrical performance of XLPE/silica nanocomposites," in *Solid Dielectrics (ICSD), 2010 10th IEEE International Conference on*, 2010, pp. 1-4: IEEE.
- [201] M. Praeger, I. Hosier, A. Holt, A. Vaughan, and S. Swingler, "On the effect of functionalizer chain length and water content in polyethylene/silica nanocomposites: Part II—Charge transport," *IEEE Transactions on Dielectrics and Electrical Insulation*, vol. 24, no. 4, pp. 2410-2420, 2017.